ISBN 978-82-326-2040-1 (printed ver.)
ISBN 978-82-326-2041-8 (electronic ver.)
ISSN 1503-8181

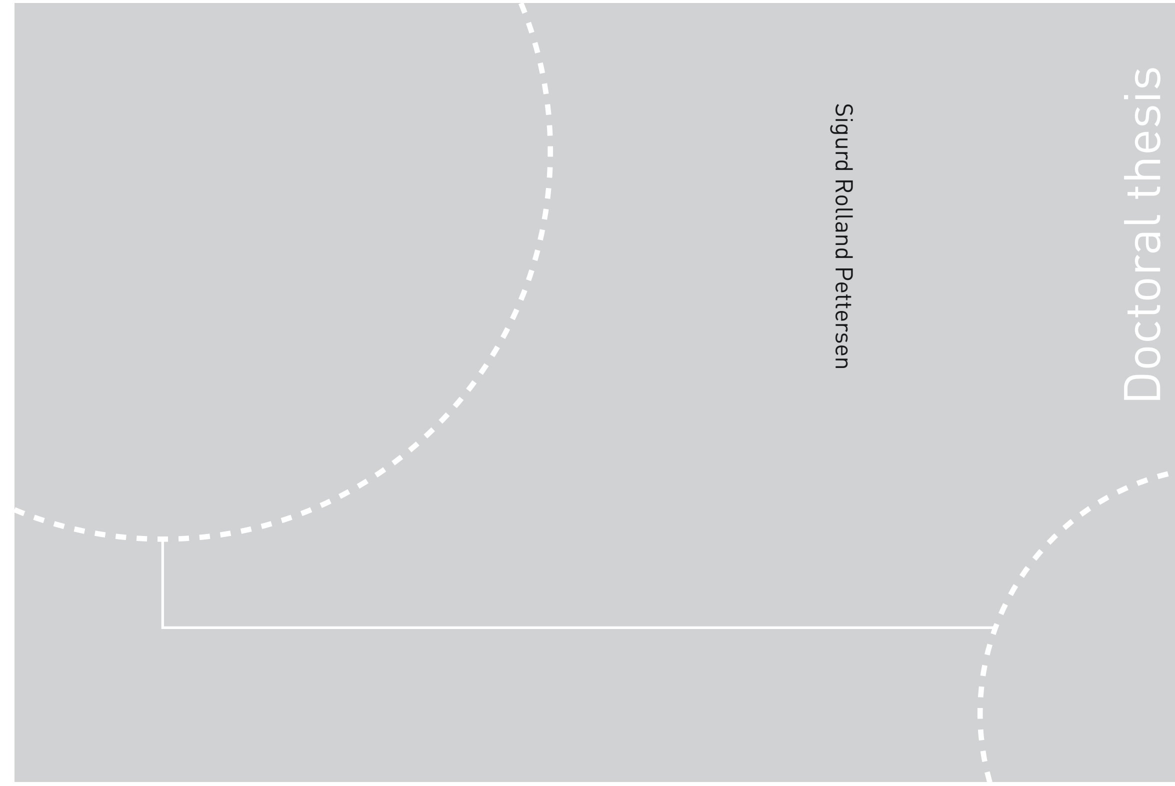

Doctoral theses at NTNU, 2016:349

NTNU
Norwegian University of Science and Technology
Thesis for the Degree of Philosophiae Doctor
Faculty of Engineering Science and Technology
Department of Structural Engineering

Doctoral theses at NTNU, 2016:349

Sigurd Rolland Pettersen

CONDUCTION MECHANISMS IN CONDUCTIVE ADHESIVES WITH METAL-COATED POLYMER SPHERES

Sigurd Rolland Pettersen

CONDUCTION MECHANISMS IN CONDUCTIVE ADHESIVES WITH METAL-COATED POLYMER SPHERES

Thesis for the Degree of Philosophiae Doctor

Trondheim, December 2016

Norwegian University of Science and Technology
Faculty of Engineering Science and Technology
Department of Structural Engineering

Norwegian University of
Science and Technology

NTNU
Norwegian University of Science and Technology

Thesis for the Degree of Philosophiae Doctor

Faculty of Engineering Science and Technology
Department of Structural Engineering

© Sigurd Rolland Pettersen

ISBN 978-82-326-2040-1 (printed ver.)
ISBN 978-82-326-2041-8 (electronic ver.)
ISSN 1503-8181

Doctoral theses at NTNU, 2016:349

Printed by NTNU Grafisk senter

Preface

This doctoral thesis is submitted to the Norwegian University of Science and Technology (NTNU) in partial fulfillment of the requirements for the degree of philosophiae doctor (PhD).

The thesis comprises an introductory section, five journal papers (three published and two submitted), and one international conference paper.

The work presented in this thesis was conducted in the period between August 2013 and September 2016 at NTNU Nanomechanical Lab (NML), Department of Structural Engineering (IKT), Faculty of Engineering Science and Technology (IVT), NTNU, Trondheim, Norway. Associated Prof. Jianying He (NTNU NML) has been my main supervisor during this work. Prof. Zhiliang Zhang (NTNU NML) and Adjunct Prof. Helge Kristiansen (NTNU NML, and Conpart AS, Skjetten, Norway) have been co-supervisors.

I have conducted much of the experimental work of this thesis outside of our department and university. Sample preparation, environmental testing, and bulk electrical characterization have been conducted at Conpart AS and Lindberg & Lund AS (Vestby, Norway). Much of the single-particle characterization was performed at NTNU NanoLab, the advanced clean-room facilities at NTNU. Ion milling and scanning electron microscopy imaging have been conducted at the Paper and Fibre Research Institute (PFI, Trondheim, Norway) and at the Electron Microscope Laboratories, Department of Materials Science and Engineering (IMT), Faculty of Natural Sciences and Technology (NT), NTNU. Some thermal measurements were conducted at the Department of Energy and Process Engineering (EPT), IVT, NTNU. In February and March 2015 I went on a research stay at the Institute of Scientific and Industrial Research (ISIR), Osaka University, Japan, which was a greatly rewarding experience, both academically and culturally.

The research was performed within the user-driven research-based innovation (BIA) project "Novel Conductive Adhesive Technology Platform for Solar Industry" (pSiCAT, Grant No. 225962/E20), in cooperation with Mosaic Solutions AS, Skjetten, Norway as well as other industrial partners, with financial support from the Research Council of Norway.

Sigurd Rolland Pettersen
Trondheim, October 2016

Abstract

Isotropic conductive adhesives (ICAs), i.e. polymer adhesives with a percolating network of filler particles embedded for conductivity, have been used as alternatives to soldering in electronic devices for decades. More recently, the photovoltaic (PV) industry have begun to show major interest in ICAs, as this is a low-temperature alternative to lead-free solders. Lower processing temperatures decrease solar cell damage and allows for the use of thinner wafers, which can be a significant contribution to the cost-reduction of PV modules. However, conventional ICAs contain large amounts (> 25 vol%) of silver, and are thus expensive.

The goal of this thesis has been to investigate the mechanisms controlling electrical and thermal conduction in a new type of ICAs, developed by our industrial partners Conpart AS and Mosaic Solutions AS. By replacing the micron-sized silver flakes and solid particles of conventional ICAs with micron-sized polymer spheres coated with silver thin films (AgPS), a conductive network can be formed throughout the adhesive matrix at silver contents in the range of ~ 0.5 – 5 vol%. The similar thermomechanical properties of the polymer cores and adhesive matrix, which together comprise > 95 vol% of the ICA, can improve the reliability of the interconnects. A major disadvantage with these ICAs is that they typically yield higher resistivities than conventional ICAs, although the silver is more efficiently used in the former. By understanding the factors limiting the electrical and thermal conductivities of the ICAs, strategies for improving these can be devised.

In this work, we have developed two distinct methods for investigating the electromechanical properties of individual AgPS. A major finding has been that for films thinner than ~ 100 nm the electrical resistivity of the silver films increase drastically. We have discovered that when incorporated into epoxy adhesive, the AgPS can form metallic contacts even when cured at room temperature, and that these are sintered into metallurgical contacts at a curing temperature of 150 °C. We found that the grains of the silver films partake in an electrochemical, size-related growth process when the ICAs are exposed to elevated heat and humidity. This growth process has a positive impact on conductivity of the ICAs in the absence of a bias voltage, and is amplified by lower cross-linking of the epoxy matrix. We also investigated the thermal properties of AgPS-based ICAs, and found that the obtained values were heavily dependent on the choice of measurement method. The work presented in this thesis is expected to have a large impact on the further development of these ICAs, especially for use in PV modules.

Acknowledgements

I would not have gotten through the many ups and downs that are an inherent part of taking a PhD without the massive support of good colleagues, friends, and family.

I would first like to thank my main supervisor, Jianying, for her enthusiastic support, friendliness and professional guidance, which have been of great value for me in my development as a scientific researcher. Zhiliang's support and advice, combined with his solid and fair leadership of our group have been very important for my work. Helge has been a never-ending source of information and interpretation, and without his guidance and deep knowledge of the field, the work in this PhD would not have been feasible. I am not a man of few written words, and I sincerely appreciate the many hours my supervisors have spent reading through long emails and manuscripts, always replying with good advice and important input.

I would also like to thank my colleagues and friends in our group and at the Department of Structural Engineering for interesting and enlightening conversations during lunch and coffee breaks, group meetings, salary beers, and trips, which have given me both social and academic support to get through my PhD. Of special importance are Molly and Emil, who have been great research partners in addition to friends. Without their contributions, this PhD thesis would have been two papers shorter.

The last three years have lead me outside my home department on many occasions, and many people have given vital contributions to the work in this PhD. Keith, Susanne, Tore, Erik, and John have all helped with sample preparation, characterization, analysis, and advice, and are gratefully recognized for their contributions. I thank Per Olav, Gary, Ken Roger, Yingda, and Ignat for giving me access to and professional training on many of the advanced characterization instruments I have used in this work. I would give a special thanks to Shijo, who gave me the opportunity of a lifetime by inviting me to Osaka and finding time in his busy schedule to be a warm and welcoming host.

I also give my heartfelt gratitude to my family; my mother, father and brothers for carrying me to the point in my life where I was able to pursue a PhD. My family-in-law have been a great contribution to my life over the last soon-to-be decade. At last, but most important, I thank my fiancée Silje for all the love, support, frustrations and joy she has given and continues to give me. You are a highly loved reminder that there are more important things in life than work.

List of papers

The following publications are included in this thesis. Papers I and II are describing experimental methods developed for investigating electrical and mechanical properties of individual metal-coated polymer spheres (MPS). In papers III-VI we are investigating the electrical and thermal conduction mechanisms of bulk isotropic conductive adhesives (ICAs) with silver-coated polymer spheres (AgPS).

(I) **Electromechanical characterization of individual micron-sized metal coated polymer particles**

Molly Bazilchuk, Sigurd R. Pettersen, Helge Kristiansen, Zhiliang Zhang, and Jianying He.

Journal of Applied Physics, 2016, **119**(24), 245102.

I developed the experimental setup presented in this study from an earlier setup in which the electrical and mechanical measurements were conducted separately by different instruments and software. M.B. performed the experiments and wrote the paper. All authors contributed in revision and discussion of the paper.

(II) **Electrical four-point probing of spherical metallic thin films coated onto micron sized polymer particles**

Sigurd R. Pettersen, August Emil Stokkeland, Helge Kristiansen, John Njagi, Keith Redford, Dan V. Goia, Zhiliang Zhang, and Jianying He.

Applied Physics Letters, 2016, **109**(4), 043103.

I had the initial idea of using the miBots to conduct four-point measurements on MPS, and conducted proof of concept studies. A.E.S. conducted the miBots measurements in the paper as a part of his master thesis. I created the finite element (FE) model, performed the analysis, and wrote the paper. H.K., Z.Z., and J.H. helped to develop the method and came with input on the analysis. J.N., K.R., and D.V.G. prepared the AgPS and performed the x-ray diffraction (XRD) measurements. All authors contributed in revision and discussion of the paper.

(III) **Contact Resistance and Metallurgical Connections between Silver Coated Polymer Particles in Isotropic Conductive Adhesives**

Sigurd R. Pettersen, Helge Kristiansen, Shijo Nagao, Susanne Helland, John Njagi, Katsuaki Suganuma, Zhiliang Zhang, and Jianying He.

Journal of Electronic Materials, 2016, **45**(7), 3734–3743.

I conducted the experimental work and wrote the paper. H.K. came up with the idea of the Figure of Merit (FoM) and contributed much on the discussion around contact resistance. J.N. prepared the AgPS, and S.H. helped to design and prepare the ICA samples. S.N. and K.S. contributed by giving me access to and training on the instruments used in the experimental work. All authors contributed in revision and discussion of the paper.

(IV) **Controlling the Conduction Mechanisms in Isotropic Conductive Adhesives with Silver-Coated Polymer Spheres**

IEEE 66th Electronic Components and Technology Conference (ECTC), Las Vegas, NV, USA, 31 May-3 June 2016. **DOI**: 10.1109/ECTC.2016.53

Sigurd R. Pettersen, Helge Kristiansen, Keith Redford, Susanne Helland, Erik Kalland, Zhiliang Zhang, and Jianying He.

I conducted the experimental work and wrote the paper. K.R. prepared the AgPS and helped with ICA preparation. K.R., H.K., S.H., and E.K contributed to the experimental design. All authors contributed in revision and discussion of the paper.

(V) **Room-temperature curing and grain growth at high humidity in conductive adhesives with ultra-low silver content**

Sigurd R. Pettersen, Keith Redford, John Njagi, Helge Kristiansen, Susanne Helland, Erik Kalland, Dan V. Goia , Zhiliang Zhang, and Jianying He.

I conducted the experimental work and wrote the paper. K.R. prepared the AgPS and helped with ICA preparation. K.R., H.K., S.H., and E.K contributed to the experimental design. J.N. and D.V.G. contributed with the XRD measurements. All authors contributed in revision and discussion of the paper.

(VI) **Investigation of thermal transport in polymer composites with percolating networks of silver thin films by the flash diffusivity method**

Sigurd R. Pettersen, Shijo Nagao, Helge Kristiansen, Susanne Helland, John Njagi, Katsuaki Suganuma, Zhiliang Zhang, and Jianying He.

I conducted the experimental work, except the MDSC measurements, and wrote the paper. I.T. (see paper acknowledgements) performed the MDSC measurements, while I performed the sample preparation and data analysis. S.N. and K.S. contributed by giving me access to and training on the instruments used in the experimental work. J.N. prepared the AgPS, and S.H. helped to design and prepare the isotropic conductive adhesive (ICA) samples. All authors contributed in revision and discussion of the paper.

In addition to the papers presented above, I have presented work relevant for this thesis at the following conferences and seminars.

(i) **Simultaneous Investigation of Conductive and Mechanical Properties of Individual, Silver Coated Polymer Particles** (poster presentation)

Sigurd R. Pettersen, Jianying He, Zhiliang Zhang, Tore Helland, and Helge Kristiansen.

Norwegian Solar Cell Conference 2014, Son, Norway, 31 May-1 June 2014.

(ii) **Multiangle approach for electromechanical characterization of silver coated polymer particles** (oral presentation)

Sigurd R. Pettersen, August Emil Stokkeland, Zhiliang Zhang, and Jianying He.

NTNU NanoLab 10 years Anniversary Symposium, Trondheim, Norway, 10-11 November 2014

(iii) **In situ, four-point electrical measurements on spherical silver thin films** (poster presentation)

Sigurd R. Pettersen, August Emil Stokkeland, Helge Kristiansen, Zhiliang Zhang, and Jianying He.

Nano Network 5th Annual Workshop, Oslo, Norway, 15-17 June 2015.

(iv) **Thermal and Electrical Properties of Novel ICA with Silver Coated Polymer Particles - A New Conduction Mechanism** (oral presentation)

Sigurd R. Pettersen, Shijo Nagao, August Emil Stokkeland, Helge Kristiansen, Susanne Helland, John Njagi, Katsuaki Suganuma, Zhiliang Zhang, and Jianying He.

Printable, Flexible and Wearable Electronic Materials and Mechanics – SANKEN Core2Core satellite symposium, Trondheim, Norway, 1 July 2015

(v) **Controlling the Conduction Mechanisms in Isotropic Conductive Adhesives with Silver-Coated Polymer Spheres** (poster presentation)

Sigurd R. Pettersen, Helge Kristiansen, Keith Redford, Susanne Helland, Erik Kalland, Zhiliang Zhang, and Jianying He.

IEEE 66th Electronic Components and Technology Conference (ECTC), Las Vegas, NV, USA, 31 May-3 June 2016.

(vi) **Grain growth and conduction mechanisms in conductive composites** (oral presentation)

Sigurd R. Pettersen, Keith Redford, John Njagi, Helge Kristiansen, Susanne Helland, Erik Kalland, Zhiliang Zhang, and Jianying He.

Nano Network 6th Annual Workshop, Trondheim, Norway, 13-15 June 2016.

List of Abbreviations

ACA	-	Anisotropic conductive adhesive
ACF	-	Anisotropic conducive film
Ag	-	Silver
AgPS	-	Silver plated polymer spheres
Al	-	Aluminum
ARC	-	Antireflective coating
Au	-	Gold
CTE	-	Coefficient of thermal expansion
CTM	-	Cell to module power loss
Cu	-	Copper
ECA	-	Electrically conductive adhesive
EVA	-	Poly(ethylene-covinyl-acetate)
ICA	-	Isotropic conductive adhesive
MPS	-	Metal plated polymer spheres
Ni	-	Nickel
nm	-	Nanometer, 1×10^{-9} m
Pb	-	Lead
PMMA	-	Poly(methyl methacrylate)
PV	-	Photovoltaic
R	-	Resistance [Ω]
RH	-	Relative humidity
S	-	Siemens, 1/ohm
Si	-	Silicon
Sn	-	Tin
vol%	-	Volume percent, fraction of the total volume
wt%	-	Weight percent, fraction of the total mass
Ø	-	Diameter
µm	-	Micrometer, 1×10^{-6} m
ρ	-	Resistivity [Ω·cm], $1/\sigma$
σ	-	Conductivity [S/cm], $1/\rho$
Ω	-	Ohm, 1/siemens

Contents

Preface i

Abstract iii

Acknowledgements v

List of papers vii

List of Abbreviations xi

Chapter 1. Introduction 1

Chapter 2. Background 3

2.1 Conductive Adhesives for Solar Module Manufacturing 3

2.1.1 Conventional solar module design 3

2.1.2 Lead-based and lead-free metallic solders 5

2.1.3 Electrically conductive adhesive (ECAs) 6

2.1.4 ICAs as solar module interconnects 9

2.2 Metal-coated polymer spheres (MPS) as ECA filler particles 13

2.2.1 Metal-coated polymer spheres 13

2.2.2 ICAs with silver-coated polymer spheres (AgPS) 16

Chapter 3. Objectives and main results 25

3.1 Aim of thesis 25

3.2 Main findings and novelty of methods 27

3.2.1 Paper I 27

3.2.2 Paper II 28

3.2.3 Paper III 28

3.2.4 Paper IV 29

3.2.5 Paper V ... 30

3.2.6 Paper VI ... 30

Chapter 4. Discussion and outlook ... 33

4.1 Decreasing ICA bulk resistivity ... 33

4.1.1 Metallic contacts ... 33

4.1.2 AgPS size and film thickness ... 35

4.2 Reliability investigations ... 36

4.2.1 Grain growth at elevated temperature and humidity ... 37

4.2.2 Thermal cycling ... 37

4.2.3 Contact resistance ... 38

4.3 Optimization of lower curing temperature adhesive systems ... 38

4.4 Further thermal transport investigations ... 39

Bibliography ... 41

Papers ... 51

Paper I ... 51

Paper II ... 61

Paper II – Supplementary Material ... 67

Paper III ... 87

Paper IV ... 99

Paper V ... 109

Paper V – Supplementary Material ... 131

Paper VI ... 139

Paper VI – Supplementary Material ... 169

PhD Publication List – Department of Structural Engineering ... 179

Chapter 1

Introduction

The overall aim of the research project which this PhD position has been a part of, has been to contribute to the cost reduction of solar cell modules by further developing and improving a novel type of electrically conductive adhesive (ECA), developed at Conpart AS and their daughter-company Mosaic Solutions AS [1].

As much of the focus on ECAs has been towards their applications as interconnects for the electronics industry, several book chapters and review articles can be found on this topic [2-12]. The following background chapter will instead introduce ECAs as interconnects for solar modules, although many of the advantages and challenges of using these composite materials, as well as the findings presented in the articles included in this thesis [13-18], are not limited to this application. Section 2.1.1 gives a brief introduction to the manufacturing of a conventional solar module, with emphasis on factors relevant for the interconnections. The advantages and challenges of both lead-based and lead-free metallic solders are described in Section 2.1.2. A general introduction to ECAs is given in Section 2.1.3, with emphasis on isotropic conductive adhesives (ICAs). Section 2.1.4 reviews ICAs as solar module interconnects, with the aim of giving readers insight on parameters that are important for the development of new ICAs for the purpose. Section 2.1.1 introduces metallized polymer spheres (MPS) as filler particles in ECAs, and Section 2.2.2 reviews the literature on ICAs with spheres plated with silver thin films (AgPS).

Chapter 3 discusses the aims of the thesis (Section 3.1), and summarizes the main findings and novel characterization methods of the included articles (Section 3.2).

Chapter 4 contains a discussion of the results, with focus on the outlook and further research that should be conducted for AgPS-based ECAs to be viable interconnect alternatives in solar modules.

Chapter 2

Background

2.1 Conductive Adhesives for Solar Module Manufacturing

2.1.1 Conventional solar module design

If inquired to imagine a solar module, the first thing that comes into one's mind is perhaps the excitation of electrons by incoming photons in the semiconductor that is the heart of the technology. There are three main categories of photovoltaic (PV) technologies, based on crystalline, thin film, and organic semiconductors [19]. Of these, crystalline silicon (Si) is still the most common technology, accounting for about 93 % of the worldwide PV wattage production in 2015 [20]. The voltage produced by a single crystalline Si wafer, ~0.5 V, is too low for a standard energy supply, and the wafers are therefore connected in series to increase the total voltage [19]. To extract the electric current and connect the wafers in series, metallic ribbons are attached onto the surface of the solar cells [21]. The interconnects between the solar cell and the ribbons provide electrical, mechanical and thermal contacts, and are thus crucial to the performance of the solar module. The two most common crystalline module designs are the traditional H-pattern and back-contact solar cells. As most investigations on conductive adhesive interconnects have been done on the traditional H-pattern designs, these will be introduced in the following paragraph. However, conductive adhesives are also used in back-contact designs [22]. For a good review specifically on back-contact solar cells, see Kerschaver and Beaucarne [22]. A summary of other alternative crystalline solar module designs can be found in Zarmai et al. [21].

A typical conventional solar module H-pattern design can be seen in Fig. 1**.** A thin poly- or monocrystalline silicon wafer is covered on one side with an antireflective coating (ARC) to increase the absorption of incoming photons. The ARC is typically a single-layer of silicon nitride, which is also responsible for the characteristic deep blue color of most commercially

available solar cells [23]. A layer, typically of aluminum (Al), is printed on the rear side of the cell and heated to create a rear contact field [21]. If the solder and rear contact metal are not compatible, another contact structure is printed on top or in holes in the rear contact field, as seen in Fig. 1 a). To create Ohmic contacts to the front of the silicon wafer, a silver-based (Ag-based) thick film paste is screen printed into lead structures (fingers and busbars) and fired through the ARC. Metallic ribbons, typically copper (Cu), coated with metallic solder, are then placed along the length of the busbars and extended onto the backside of the next cell. The ribbons are further interconnected to the contacts on the wafers by heating the solder above its melting or reflow temperature, so that it wets the busbars and backside contacts before being cooled down to a solid state. After soldering, the solar cell assembly (wafers, interconnect structures, and wires) is encapsulated in a material that provides structural support, physical

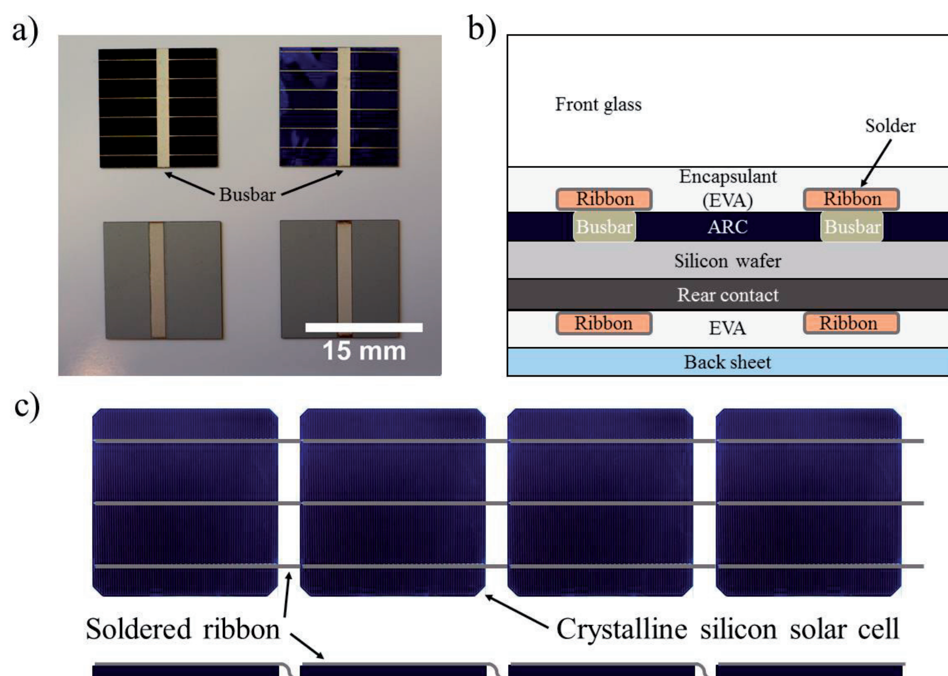

Fig. 1. a) Laser cut pieces of monocrystalline (left) and polycrystalline (right) silicon wafers, showing front side busbar and fingers, as well as the rear contact field with solderable contact strips. b) Schematic cross-section of a typical conventional laminated crystalline solar cell. c) Solar cell assembly of crystalline silicon wafers interconnected in series with ribbons. (Thicknesses are exaggerated for illustrative purposes.)

and chemical protection, and electrical isolation, while still being transparent to photons of the relevant wavelengths and thermally conductive [24]. The most commonly used encapsulation material is a statistical copolymer, poly(ethylene-covinyl-acetate) (EVA), which is pressed onto the solar cell and cured into an elastomer at temperatures usually ranging from 140 – 160 °C [25], although other lamination materials based on e.g. polyurethane or new EVAs can be cured at temperatures around 80 °C [26]. The encapsulation layers also serve as an adhesion layer to the front glass plate and protective back sheet of typically glass or polymer. For more details on the lamination process, see Li et al [25].

2.1.2 Lead-based and lead-free metallic solders

Reports on failure of field installed solar modules have identified that up to 40 % of the failures are caused by interconnect and cell breakage, and although this number have decreased somewhat with improved materials and automated processing, interconnect reliability is still an important concern in solar module manufacturing [21, 27]. Lead-based metallic solders have long been the mainstay of the solar module industry, as they also were in the electronics industry. Lead (Pb) decreases the melting temperature and increases the thermo-mechanical reliability by increasing the ductility of the alloy [11]. However, over the last 10-15 years, both the European Union and Japan have imposed legislature that inhibits the use of lead in electronics due to its toxicity both to humans and to the environment [6, 11, 28, 29]. This has directed the electronics industry to shift its focus towards lead-free alternatives, which primarily are lead-free solders or ECAs [11, 28]. Although the latest version of the European legislature (Restriction of Hazardous Substances (RoHS) in Electrical and Electronic Equipment) makes an exemption for the solar module industry to assist with the transition to renewable energy sources [29, 30], developments in lead-free alternatives for the electronics industry are beginning to make these viable alternatives also in solar modules [21].

The most common lead-free solder alternative is an alloy of tin/silver/copper (SnAgCu) [21, 28]. In addition to the obvious cost increase of replacing cheap lead with more expensive Ag, Cu, and Sn, the melting temperature increases from 183 °C for the eutectic SnPb alloy to 217 °C for the most commonly used SnAgCu alloy [28]. Like most other lead-free solder alloys, this means that the processing temperature must be increased with at least 30 – 40 °C to achieve sufficient wetting of the contacting surfaces, compared to a lead-based solder. This increase in temperature is detrimental to the solar cells, as it can induce or increase the size of already present microcracks in the wafer [31, 32] as well as put stresses on the interconnects that can

Fig. 2. Bending induced in a silicon wafer through mismatch in thermal expansion coefficients of the Cu-ribbon and wafer upon cooling. (Adapted from [33].)

accelerate fatigue related damage [21]. Microcracks can be behind 5-10 % of the losses in a typical manufacturing facility, and especially cracks that occur parallel to the busbars can lead to significant reductions in module output power [31, 32]. The main cause behind these thermally related effects is the difference in coefficients of thermal expansion (CTEs) between the metallic ribbon (CTE ~ 17×10^{-6} K^{-1} for Cu) and silicon wafer (~ 3×10^{-6} K^{-1}), leading to a larger shrinkage of the metallic ribbon than in the wafer during cooling [21, 32, 33]. This causes tensional stress in the ribbon and shear stress in the wafer, which can induce bending or warpage of the wafer, as illustrated in Fig. 2. In addition to higher stresses induced by higher temperatures, lead-free solders have higher Young's modulus and lower creep rates than eutectic SnPb, and thus contribute less to stress relaxation [19]. Although the soldering of ribbons to the backside will compensate for the thermally induced bending and flatten the wafer, the process still leads to tensional stress in the ribbons and stress-buildup in the wafers, which can ultimately lead to microcracks and/or failure [33]. These effects restrict the lower thickness limits of the brittle crystalline wafers, which again affect the series resistance of the solar cell assembly, in addition to having economic implications by setting a lower boundary for material consumption. Due to these thickness limitations, the typical wafer thickness of conventional solar cells is in the range of 150 – 200 μm [34].

2.1.3 Electrically conductive adhesive (ECAs)

The foremost alternative to solders is ECAs, as the electronics industry already has decades of experience with these materials for electronic packaging and a large range of commercial alternatives is already available. ECAs have been used as die-attach materials since the 1960s, but are today mainly used in advanced electronic packaging technologies such as chip-on-glass, chip-on-flex, and flip-chip attachments on printed circuit boards [11]. ECAs are composite materials composed of a continuous organic matrix that provides most of the structural integrity and adhesion, containing dispersed filler particles that bestow electrical and thermal

conductivity. The adhesive can be thermoplastic, meaning that it becomes a viscous liquid and can be reshaped at temperatures higher than the glass transition temperature (T_g). However, thermosetting polymers, especially based on epoxy resins, are more common due to properties such as high heat resistance and excellent adhesion to a large range of surfaces. When thermosetting polymers are heated, they go through a curing reaction that involves the formation of covalent cross-links between the polymers. An interconnection process using thermosetting polymer-based adhesives is thus non-reversible. In addition to the adhesive matrix and curing conditions, the type, shape, size, and content of filler particles will also have an impact on the final properties of the ECA. Still, some general properties apply to most all ECAs [4, 6, 10, 11]:

- Lower processing temperatures than solders. Most ECAs are cured at 120 – 150 °C, although epoxies exist that will cure even at room temperature or by ultraviolet (UV) or other wavelength radiation [35, 36].
- Flux-less application. With solders, flux is generally required to deoxidize and improve wetting of the contacting surfaces. In addition to adding to the number of processing steps, conventional fluxes are removed by cleaning with environmentally polluting chlorofluorocarbons (CFCs), although water-soluble and no-clean fluxes can be used instead (i.e. low-residue fluxes that can be left on the solar cell after soldering) [6, 37].
- Compatibility with a large range of surfaces, such as glass, ceramics and other non-solderable substrates.
- When used in electronics; no solder masks required, and potential for finer pitch-application than solders.

ECAs are generally divided into three classes, depending on the amount of filler particles [4, 8, 11], as illustrated in Fig. 3. Non-conductive adhesives (NCAs) are simply adhesives without conductive particles. An NCA forms an electrical joint by holding surface asperities on the contact surfaces in electrical contact. Anisotropic conductive adhesives (ACA) are ECAs where the volume fraction of filler particles is too small for the particles to connect and form conductive pathways (typically 5 – 10 vol%). ACAs are also available as flexible films with particles embedded, in which case they are known as anisotropic conductive films (ACFs). Generally, both NCAs and ACAs require the application of pressure during curing to form conductive bridges between the contacting surfaces. As the adhesive cures and hardens, the

external pressure is removed and the conductive bridges are sustained by contracting stresses from the polymer matrix.

If the volume fraction of filler particles is increased, the particles will at a certain point from a continuous conductive pathway, at which the resistivity of the ECA drops by many orders of magnitude. After this percolation threshold is reached, the resistivity decreases more slowly as more particles come into contact, forming an isotropic conductive network that percolates the adhesive in all directions. This class of ECAs is named isotropic conductive adhesives (ICAs). The formation of the percolating network by randomly distributed filler particles is a statistical phenomenon [4]. At a given volume fraction of fillers, the probability of forming a conductive pathway increases with increasing surface-to-volume ratio of the fillers particles. For this reason, flakes are the conventional filler geometry in ICAs, although often with a bimodal size distribution where the smaller particles can be either flakes or powders. Contrarily, spheres are the geometry with the lowest surface-to-volume ratio, and have thus generally been regarded as unsuitable as filler particles in ICAs. Even with flakes as the primary filler geometry, most ICAs contain at minimum 25 – 30 vol% filler particles to achieve reasonable conductivity.

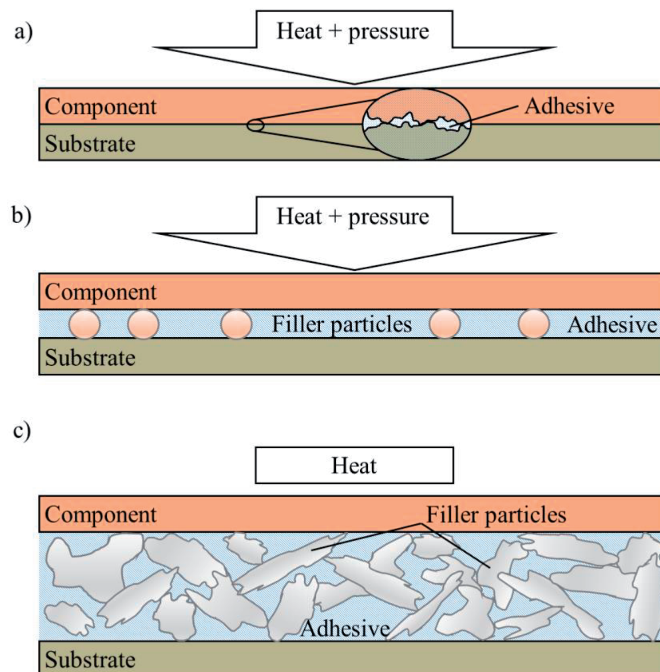

Fig. 3. The three categories of electrically conductive adhesives (ECAs). a) Non-conductive adhesive (NCA), b) anisotropic conductive adhesive (ACA), and c) isotropic conductive adhesive (ICA).

Resistivity is the reciprocal of conductivity, and commercial Ag-flake-based ICAs normally exhibit resistivities in the range of 10^{-3} – 10^{-4} Ω·cm [38]. This is one to two orders of magnitude higher than that of eutectic solders, which typically have room temperature resistivities around 1– 3×10^{-5} Ω·cm, depending on the alloy composition [39, 40]. Higher resistivity results in a higher electrical resistance, which increases effect losses and resistive heating when current is conducted through the interconnect. These higher resistivities is one of the major obstacles with ICAs compared to solders.

The resistivity of the ICA is dependent on the resistivity of the filler particles, and as the metal with lowest electrical resistivity and highest thermal conductivity, 1.62×10^{-6} Ω·cm and 429 W/m·K at 25 °C [41] respectively, silver is the most commonly used filler material. Although pure copper is almost as good a conductor (1.72×10^{-6} Ω·cm and 401 W/m·K at 25 °C [41]), copper has a lower standard electrode potential than silver, +0.52 V against +0.80 V [41], and is thus more readily oxidized. While copper oxide is an insulator, most articles on ICAs state that silver oxide is conductive. However, the literature values on the resistivity of silver oxides are somewhat ambiguous, although there is agreement that the most thermodynamically stable form (Ag_2O) is a p-type semiconductor. Abe et al. reported that AgO thin films made by RF sputtering yielded a resistivity of 59.3 Ω·cm, whereas the resistivity of Ag_2O was 7×10^{8} Ω·cm [42]. Reddy et al. reported much lower values, 5.2×10^{-3} Ω·cm for Ag_2O films prepared by RF sputtering onto substrates with a temperature of 303 K [43]. It is generally found that silver-based ICAs show stable or even improved conductivity upon aging tests with high temperature and high humidity [9, 44], whereas the resistivity of copper-based ICAs usually increase at such conditions, even when reagents are included to decrease oxidation [9]. However, some reports on Cu-filled ICAs suggest that these can be prepared to be resilient against aging [45, 46], questioning the generality of this claim.

2.1.4 ICAs as solar module interconnects

The potential of using ICAs as interconnects in solar cell assemblies have been known since before the turn of the millennium, but the incorporation into commercial production lines have until recently been limited, especially for crystalline cell technology with its high demands for cost-efficiency, due to the relatively high-price of ICAs with ≥ 25 vol% silver [26, 47-49]. However, the cost of using an ICA interconnect with relative high silver-content is partly balanced by the potential for cost-reductions in other parts of the production line. ICAs can also be used in other cell designs than the traditional front-side metallized structure described in

Section 2.1.1 [22, 50]. The most obvious advantage with ICAs is lowered processing temperatures compared to solders, as this decreases thermo-mechanical stress in the wafers, which reduces warpage, microcracks and breakage. Lowered processing temperatures also make it possible to decrease the wafer thickness, decreasing material costs as well as reducing the electrical resistance contribution from the wafers to the series resistance of the solar cell assembly. In addition to decreasing wafer thickness, it is desirable to increase wafer size, as this increases the current produced by the cell [51]. However, higher current also demands thicker ribbons to decrease ribbon resistance, which again is possible only with lower processing temperatures if increased warpage is to be avoided [32, 51]. Eikelboom et al. compared soldered interconnects with ICA interconnects cured at either 160 °C or 80 °C [26]. The soldered interconnects yielded more bending in the silicon wafers than the ICA interconnects, although bending was only completely avoided with curing at 80 °C [26]. With curing at 80 °C, 80 μm thin wafers could be interconnected, which was not possible with soldering without causing cell breakage. Beaucarne et al. compared soldering with an ICA cured at 150 °C, and found that both interconnection methods induced bending [33]. Zemen et al. compared solar cell assemblies interconnected with solder processed at 220 °C to assemblies made with ICA cured at 130 °C, and found that although the bending was much larger in the soldered assemblies, it also occurred in the glued assemblies [52]. It is clear that although the decrease in processing temperature by switching from a solder interconnect, especially a lead-free alloy, to an ICA comes with several benefits, the most common curing temperatures are still too high if the goal is to completely eliminate thermally induced bending.

An important factor when determining the quality of a solar cell interconnect is electrical performance, which can be investigated directly by measuring the conductivity and contact resistance towards the contacting surfaces [53]. However, it is also common to measure cell to module (CTM) power loss, i.e. the percentage difference between the initial output power of the single cell and the final power output of the module, or fill factor, which is the ratio of the maximum output power of the contacted solar cell to the product of the open circuit voltage and the short circuit current. As the interconnects need to be reliable over the whole lifetime of the module and normal module warranty is 20 years or higher, these factors are often investigated before, during, and after accelerated stress tests to imitate the influence of environmental factors [27]. The most usual tests are thermal cycling between -40 °C and +85 °C for at least 200 cycles, and long-term storage (> 1000 h) at +85 °C and 85 % relative humidity (RH). Eikelboom et al. showed that ICA interconnects yielded stable contact resistance over 2500 h at 85 °C/85 %RH,

and only a 2% decrease in fill factor after more than 900 cycles, well within the allowed limit of 5 % decrease [26]. These results were obtained with Ag-coated Cu-ribbons. When plain Cu-ribbons were used, the initial results were very good, but the contact resistance increased quickly when exposed to rapid aging tests. Zemen et al. obtained very stable values (< 2 % CTM after 400 thermal cycles) with ICA interconnects when the ribbons were coated with a SnPbAg alloy [52]. When using ICAs specifically developed for solar module interconnects, Schneider et al. also found that Ag-coated Cu ribbons were very stable at high temperature and high humidity conditions, for more than 1500 h [48]. However, in this investigation pure Cu-ribbons were almost as stable, while Sn-coated Cu-ribbons were very unstable. The differences were attributed to different levels of electrochemical corrosion due varying differences in standard electrode potentials between the silver and the various ribbon coatings.

Incorporation of adhesive curing into the assembly process is also a concern, as normal curing times for ICAs are ≥ 15 min, much longer than the time it takes to reflow and cool a solder. Although more reactive adhesive systems can be used, this decreases the pot-life and also the processing window of the ICA. Several groups have showed the possibility of curing the adhesives simultaneously with the EVA during the lamination process [51, 54, 55], although Geipel and Eitner revealed that the curing process of both the ICA and EVA is delayed by the extended non-isothermal heating phase of the laminator before it reaches the maximum temperature [56, 57]. As mentioned in Section 2.1.1, the lamination temperature normally peaks around 150 °C, and is thus similar to standard curing temperatures for ICAs. In addition, some pressure is applied during lamination [25], which can be positive for the electrical properties of the ICAs. Modules where the ICA interconnects were cured during lamination yielded higher fill factors and higher maximum output power than modules prepared with eutectic SnPb solders, in addition to being more stable during thermal cycling, showing that ICA interconnects may actually be superior to lead-based solders as well as the lead-free solders [54]. When ICAs were cured without lamination, ICA-based assemblies yielded equal power outputs as solder-based [53].

Another large advantage of ICAs is the potential of interconnecting the ribbons directly to the solar cell, omitting the busbar altogether and thereby saving up to 40 % of the front side silver paste [33, 47, 58]. Schwertheim and colleagues showed that ICAs can be printed directly onto an ARC layer of indium-tin oxide (ITO) without the need for busbars, and that these assemblies were more stable than cells with busbars during thermal cycling [58]. Schneider et al. tested a

range of conductive adhesives against various ribbon metallizations, and wafers with and without busbars, and compared these to conventional interconnects with solders [47]. Busbar-less solar cells showed no additional mechanical or electrical losses compared to cells with busbars. CTM effect losses ranged from about 10 – 75 % higher than the soldered reference, which was attributed to the higher specific resistance of the conductive adhesives as well as contact resistance between the adhesive and the ribbon, solar cell, and backside contacts. During thermal cycling and damp heat tests, the performance was generally better for adhesives than solder, although with large variations between the different adhesives. This shows the importance of understanding the conduction mechanisms of the ICAs as well as the material behavior during accelerated aging tests.

Together with a growing understanding of the benefits of using conductive adhesives as solar module interconnects, ICAs have gotten cheaper, as products with lower silver content have been specifically developed for the cost-demanding PV market [33, 47, 48, 59]. This is achievable by e.g. replacing much of the silver with copper powder, which is the case for the commercially available Dow Corning® PV-5802 [59]. According the safety data sheet per 2016/01/07, the product contain 70 – 80 wt% Cu and 10 wt% Ag. The developers state a resistivity of 2×10^{-4} Ω·cm and a very low shear storage modulus of less than 2×10^{7} Pa in the temperature range between -20 – +80 °C, and relative power losses well below the 5 % guidelines for thermal cycling and damp heat tests. This ICA can thus be regarded as the commercial state of the art, and is a standard to measure the novel ICAs investigated in this thesis up against. Several research papers have been published with various versions of silver coated filler particles. As already mentioned, Cu-powder or flakes is the most commonly investigated filler core material [60-62], although carbon materials such as graphite [63], graphene [64], or carbon nanotubes [65] have also been investigated. In general these yield resistivities in the range of 10^{-3} – 10^{-4} Ω·cm, although Cui et al reported values as low as 4.5×10^{-5} Ω·cm for Ag-coated Cu-powders. This is still higher than what is achievable with surface modified silver-flakes [38], but in line with most commercial silver flake-based ICAs. Although the Cu-based fillers can decrease the silver content significantly, they still contain a large amount (> 80 wt%) of metal, which generally has a negative effect on the ductility of the ICA joints [10]. To decrease metal-content, Krupka et al. coated polyamide powder particles with Ag at a metal-to-polymer ratio of 35 vol% [66]. The fillers were incorporated in a thermoplastic polyethylene matrix, and yielded a very low percolation threshold and a minimum resistivity of 1.5×10^{-3} Ω·cm at 33 vol%. However, to our knowledge, no follow-up studies were conducted.

2.2 Metal-coated polymer spheres (MPS) as ECA filler particles

2.2.1 Metal-coated polymer spheres

An alternative approach is to use metal-coated polymer spheres (MPS) as filler particles, and although the idea of using MPS in ICAs is relatively new, their application in other electronic interconnects is not. Polymer core solder balls (PCSBs) are already used in ball grid arrays (BGAs), a surface mount technology, as the plastic cores have been shown to increase the compliance and thereby the reliability of the interconnects compared to conventional BGA packaging with all-metal solder balls [67-69]. The diameter of the PCSBs are usually in the range from 100 – 800 μm, and the metal coating is normally comprised of an inner layer of Cu with a thicker outer layer (~20 μm) of solder alloy [67, 68, 70]. Recently, a new type of fine-pitch BGA interconnect have been proposed, where the PCSB are replaced by smaller (30 μm) polymer spheres coated with 200 – 250 nm Ag [70, 71]. Instead of an outer layer of solder alloy, the MPS are dispersed on a substrate with a thin layer of conductive ink with Ag nanoparticles (Ag-NPs). The ink is drawn up the surface of the MPS, forming necks that are dried at 80 °C and sintered at 200 °C. By a flip-chip process, these can further be contacted to another substrate with a thin layer of ink, followed by a new round of drying and sintering, resulting in fine-pitch BGA arrays.

MPS have also been used as fillers in ACAs/ACFs for decades, and are of special importance in chip-on-glass technology for flat panel display applications [12, 72]. With higher resolution displays in addition to the miniaturization of screens for e.g. smartphones and tablets, the demand for fine-pitch contacts have been steadily increasing, and present day technology often requires MPS with diameters in the range of 2 – 10 μm [73, 74]. Being more easily deformed than solid metal particles, MPS offer larger bonding surfaces in addition to the obviously lowered metal consumption. The most typical ACA plating is a cost-efficient inner layer of Ni (~ 30 – 120 nm thick) with a thinner outer layer of gold for enhanced conductivity and corrosion resistance [74].

There are several methods to produce micron-sized polymer spheres, as described by He in her PhD thesis, but most of these have drawbacks such as broad size distribution (suspension polymerization), low-crosslinking density or irregularly shaped particles (dispersion polymerization), or difficulties with process-control and limited particle size (emulsion polymerization) [75]. Contrarily, the patented two-step swelling process is capable of producing micron-sized polymer spheres with narrow size distribution, homogeneous mechanical

properties, controllable particle size and high cross-linking density [76-79]. The method is also known as the Ugelstad method after its discoverer, the late John Ugelstad, a professor at NTH (now NTNU). The process is illustrated in Fig. 4. It comprises two swelling steps, and starts with the preparation of seed particles by emulsion polymerization in water, typically yielding highly mono-sized spheres with sizes < 500 nm [78]. In the first swelling step, a low-molecular weight and low-water solubility organic compound, which can be the polymerization initiator, is added to the emulsion where it diffuses into the seeds and causes slight swelling [77]. The main role of this organic compound is to increase the swelling capacity of the seeds from about 5x to between 30x to 1000x their original volume in a following swelling step. The increased swelling capacity is an entropic effect, and the process can thus be done with a range of organic compounds [77]. In the second swelling step, another component, which may be a single monomer, a mixture of monomers, or a mixture of monomers and other ingredients, is added to the dispersion containing the activated seeds, where it diffuses into the seeds and causes significant swelling [78]. Generally, polymerization initiators that are activated by heat are preferred, as this allows for all of the second swelling compound to diffuse into the particles before polymerization is started by elevating the temperature. The process can be used to create spheres from a large range of monomers, such as vinyl (e.g. styrene), acrylic, methacrylate, and other monomers co-polymerizable with these [77]. The final size and size distribution of the spheres is determined by those of the initial seeds as well as the stoichiometry between the first and second compound [78]. The resultant homogeneously sized polymer spheres are known as Ugelstad beads and have since their discovery been used in a still expanding range of applications, primarily in biotechnological or pharmaceutical applications under the brand name Dynabeads® [80], as functional additives in coatings and paints (Spheromers® [81]), as calibration standards (Calibre® [81]), or as rheology and texture modifiers in cosmetics (Caché® [81]).

To deposit continuous and compact metallic coatings on particulate substrates, the preferred method is electroless plating, as illustrated in Fig. 5. In this process, metallic ions are deposited onto a surface in an autocatalytic redox process without application of an external current, thereby the name [82]. The surfaces, in this case polymer spheres, to be plated are immersed in an aqueous solution, which contains a reducing agent as well as metal cations, complexing agents and other chemicals to control the process. The process starts by the donation of electrons from a reducing agent to the substrate (if the surface is inherently conductive), or to catalyst seeds deposited on the substrate. This is followed by absorption of the cations, which bind the

electrons and are reduced to their metallic form, attached to the initiation sites. The reducing agent continues to deliver electrons to the reduction process, and metal grains grow from the initial catalyst sites until a continuous, polycrystalline film covers the surface. The final structure and thickness of the film is thus dependent on the initial density of the nucleation sites, as well as controllable process parameters such as pH, temperature and the composition of the bath [74, 82]. An example of polymer spheres plated by an electroless process can be observed in Fig. 6.

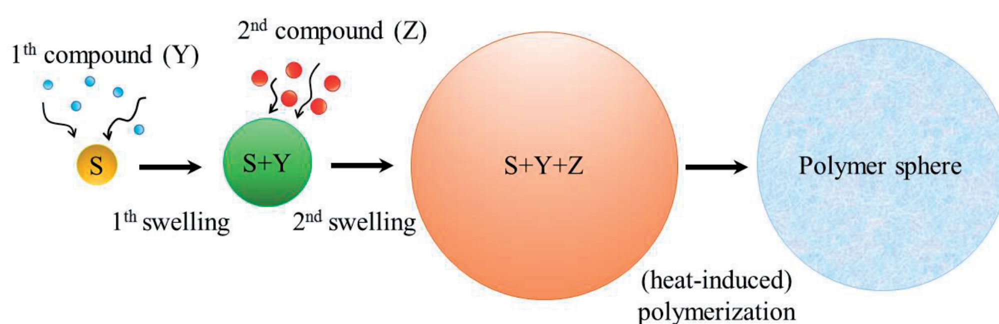

Fig. 4. Preparation of micron-sized polymer spheres by the Ugelstad method; two-step swelling from a seed particle (S), followed by (preferentially) heat-induced polymerization.

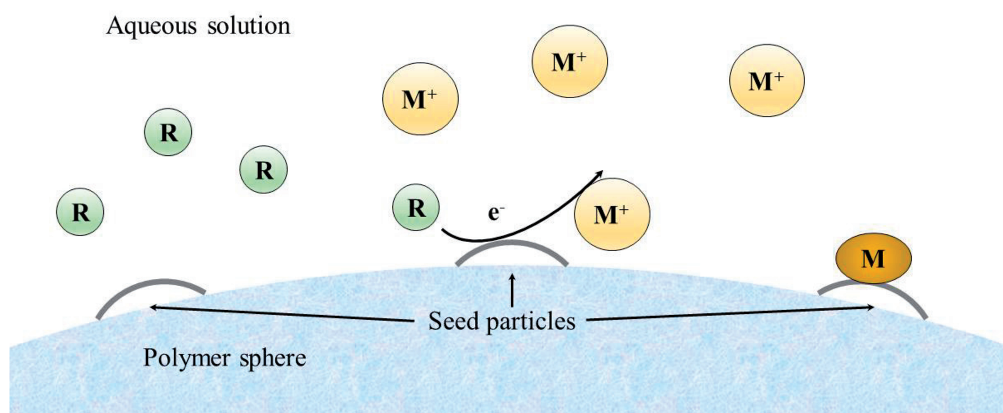

Fig. 5. Electroless plating of a metal onto a polymer surface. A reducing agent (R) donates an electron (e^-) to seed particles on the surface, being oxidized in the process. A metal cation absorbs onto the surface, binds the electron, and is reduced to its metallic form, attached to the nucleation site.

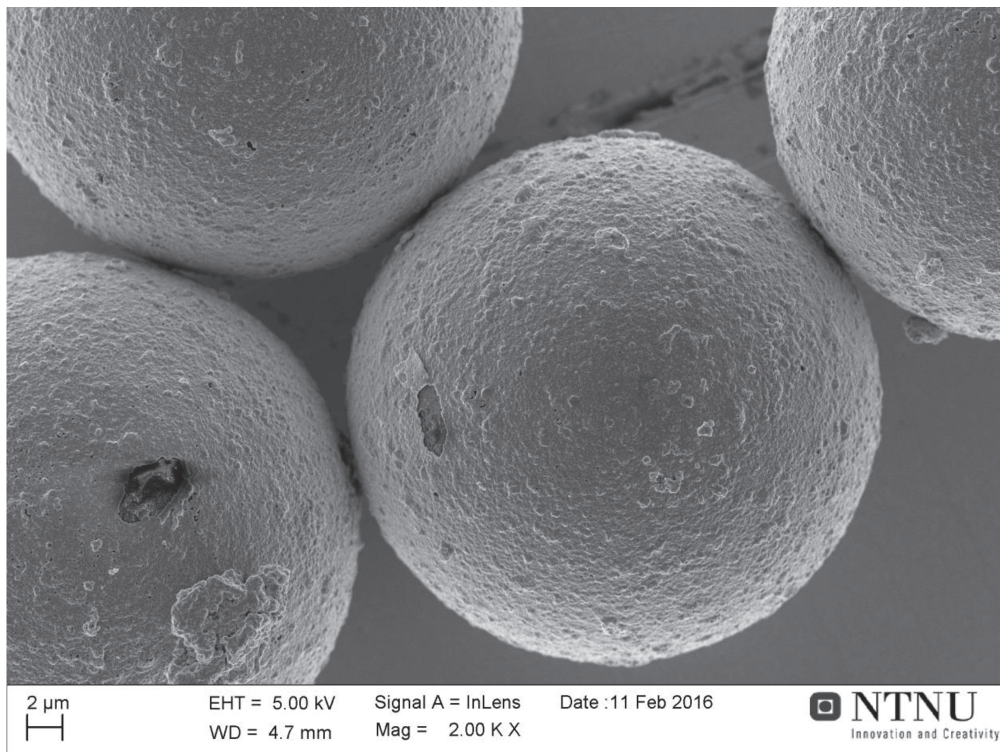

Fig. 6. 30 µm spheres of poly(methyl methacrylate) (PMMA) prepared by the Ugelstad method, coated with 100 nm thick silver films by electroless plating.

2.2.2 ICAs with silver-coated polymer spheres (AgPS)

Conpart AS is a Norwegian company specializing in the manufacturing, application and development of Ugelstad beads for electronic interconnects, mainly plated with NiAu in ACAs/ACFs and as spacer particles for LCD technology, as well as in BGAs [79, 83]. Based on Conpart's expertise from ACA technology, the daughter-company Mosaic Solutions AS was established in 2009 to develop a novel type of ICAs with silver-coated polymer spheres (AgPS) especially for the solar module market [83, 84]. As described in the patent filed by Kristiansen, Redford, and Helland, the main advantages by using AgPS as filler particles is a significantly decreased silver content compared to conventional ICAs, as well as less mismatch in material properties such as coefficients of thermal expansion (CTE), density, etc. between the adhesive matrix and the filler particles [1]. A comparison between a flake-based and AgPS-based ICA can be seen in Fig. 7.

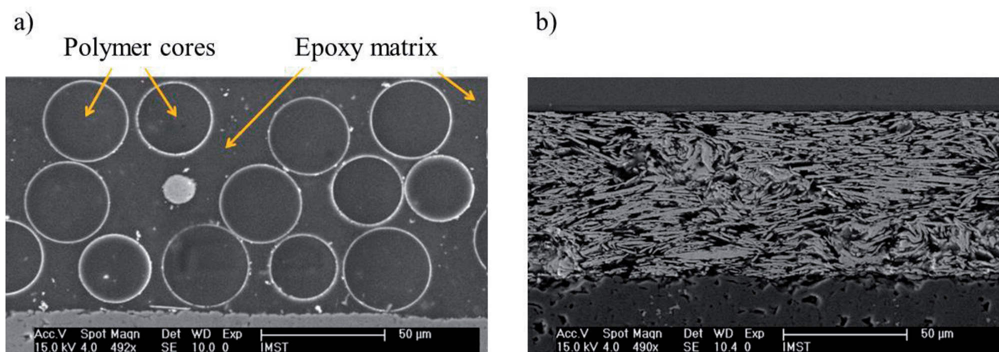

Fig. 7. Cross-sections of an ICA containing 45 vol% AgPS (a), and a commercial ICA with 31 vol% Ag flakes. (Adapted from [85].)

The first scientific investigation of MPS-based ICAs were presented by Kristiansen et al., in which adhesives containing more than 50 vol% gold-plated particles (AuPS) were prepared and shown to be suitable for stencil printing despite the high filler content [86]. The ICA bonds exhibited shear strengths more than 100 % higher than the ~ 6 MPa requirement of a military standard (MIL-STD-833), but the measured bulk resistances of the ICAs were > 1 × 10^7 Ω. This was attributed to the presence of a surfactant added to the surfaces of the gold plated spheres, to aid the uniform dispersion of the particles in the adhesive matrix in their originally intended ACF application. When AgPS without any surfactants were used instead, the resistance dropped to ~ 3 Ω. Several research groups have been involved in the further research and development of the ICA, but most of the published work on these ICAs have been conducted during two PhD projects. In the first, Nguyen focused mainly on the rheological effect of replacing silver flakes with AgPS as well as investigation of the mechanical properties of the ICA through shear-strength tests [87]. In the second project, Jain focused on establishing an understanding of the basic electrical properties of the ICA, by investigating the effects of varying AgPS content, size, and film thickness [88]. Nguyen's thesis is paper-based, pertaining six papers related to AgPS-based ICAs [85, 89-93]. Jain's thesis is a monograph, but mostly based on the work presented in [93-96]. A review article by Nguyen. et al gives a nice summary of this work [97], although new investigations have been published after this. A recap of the main previous findings on AgPS-based ICAs therefore will be given in the following paragraphs.

Shear strength tests give important information on the bonding strength and thus the mechanical reliability of the interconnects [11]. Nguyen et al. found that there was no clear difference

between the shear-strengths for adhesive samples with uncoated small (6 µm) or large (30 µm) polymer spheres [89]. The shear strengths decreased with increasing filler contents, but the lowest value was still ~29 MPa, more than twice the strength of a flake-based ICA and within the lower range of literature values for solders. ICAs with AgPS yielded equal shear strengths as epoxies with uncoated spheres [90, 91]. When compared to a commercial flake-based ICA, an ICA with AgPS yielded higher shear strengths, and similar trends with decreasing strengths at elevated temperatures, although even at 120 °C the shear strength was ~19 MPa [90]. In another investigation, an ICA with 45 vol% AgPS was found to yield shear strengths 140 % higher than an in-house prepared flake-based ICA with 25 vol% flakes and the same epoxy matrix, and 23% higher than a commercial ICA [85]. Gakkestad et al. performed a set of very harsh reliability tests on MPS-based ICAs where the samples were first run through rapid 100 cycles between -55 and + 125 °C, or 10 thermal cycles followed by a rapid firing test where the test structures were exposed to a setback acceleration of more than 60,000 g [98]. An ICA with 30 µm AgPS yielded relatively low initial shear strengths. Surprisingly, the values increased with thermal cycling, but no shear test structures survived the rapid firing test. Another ICA with 4 µm NiAuPS showed higher initial shear strengths, only a small decrease during thermal cycling, and a unexpected increase in strength after the firing test. These variations in behavior and strength was partially credited to varying quality in the printed structures and a limited amount of samples, but it is clear that the thermal cycling behavior of the AgPS-based ICAs requires further investigation. Recently, a finite element (FE) investigation was performed to define the optimal adhesive volume and geometry for mounting a 3D system-on-chip on a ceramic package [99]. Experimental shear relaxation data was obtained on an ICA containing 5 µm cores with 250 nm thick silver films, and used to estimate the necessary material properties for running FE simulations at extreme operating temperatures equal to 120 °C and -40 °C. Such an approach shows the value of combining experimental data with computer modelling to gain insight and understanding of the material.

The rheological, i.e. flow, properties of the ICAs are crucial for their processing performance. Oscillatory strain measurements showed that an epoxy resin filled with 45 vol% 30 µm AgPS has a viscoelastic regime at small strains, where it behaved as a viscoelastic gel [92]. As the strain increased, the storage modulus decreased more than the loss modulus, until at one point, the storage modulus became smaller than the loss modulus and the mixture became a viscous liquid. When the strain was decreased, the dispersion regained its elastic properties. The dispersion also showed shear thinning behavior, i.e. decreasing viscosity with increasing shear

rate, in steady-state measurements. These material properties where attributed mainly to particle-particle and particle-matrix interactions through e.g. the surface roughness of the silver films, and makes the AgPS-based ICAs very suitable for dispensing and printing processes.

Jain et al. presented investigations on the basic electrical properties of the AgPS-based ICAs in three papers [94-96]. As explained in Section 2.1.3, the volume fraction of filler particles where the particles will form an interconnected conducting pathway is a crucial parameter for an ICA, as the volume fraction should be elevated enough above this percolation threshold for a stable

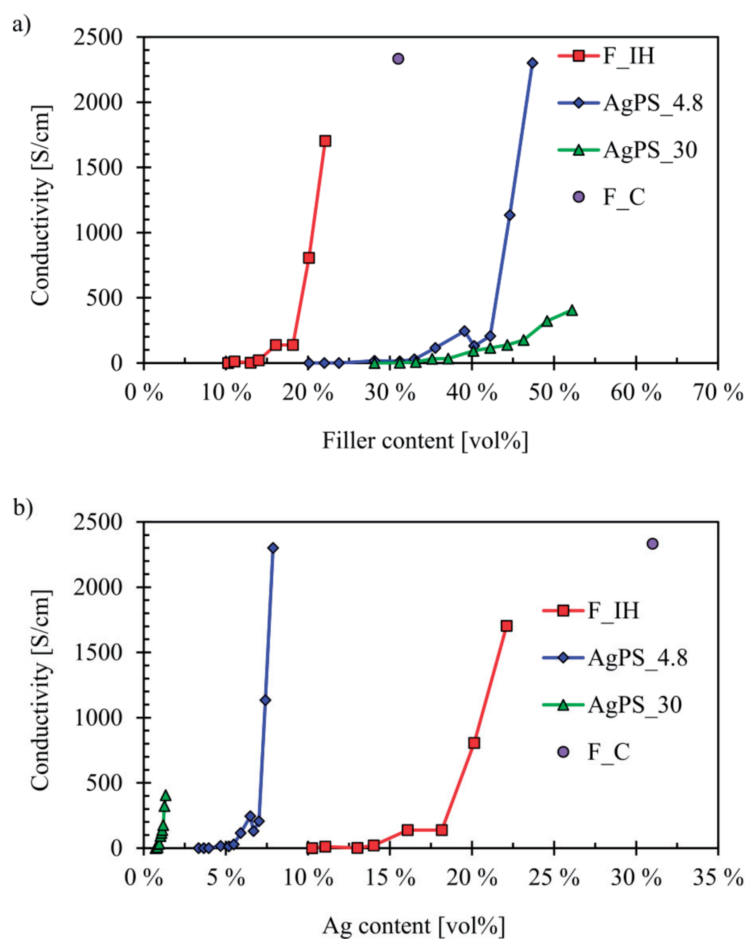

Fig. 8. Conductivity as a function of filler content (a) and Ag content (b) for ICAs containing 4.8 µm spheres with 150 nm thick silver films (AgPS_4.8), 30 µm spheres with 130 nm thick silver films (AgPS_30), silver flakes about 1 µm thick and with a size distribution between 1.4 – 11.0 µm, prepared in-house (F_IH), and a commercial flake-based ICA (F_C). (Data taken from [94].)

conductive network to be present. ICAs were therefore prepared using a two-component epoxy matrix containing increasing volume fractions of 30 µm spheres with 130 nm Ag films, 4.8 µm spheres with 150 nm Ag films, and commercial silver flakes about 1 µm thick and with a size distribution between 1.4 – 11.0 µm [94]. A commercial ICA was also prepared for comparison. The results can be seen in Fig. 8 a). For the silver flakes, the percolation threshold is ~15 vol%, for the small AgPS it is ~24 vol%, while for the large AgPS it is ~33 vol%. This trend is expected, due to the decreasing total surface-to-volume ratio of the fillers as the spheres become larger. For the same volume fraction, smaller spheres will have a larger total surface area, increasing the probability of inter-particle contacts and thus increasing the number of parallel conducting pathways. However, when plotted against volume fraction of Ag as done in Fig. 8 b), it is clear that the silver is used more efficiently by the larger AgPS, as these yield the lowest resistivities per volume of Ag. In another investigation, the effect of silver film thickness was researched by comparing ICAs containing 30 µm cores with 100, 150, 200, and 250 nm nominal film thicknesses [95]. The percolation threshold increased with decreasing film thickness, but all thicknesses were conductive at > 40 vol%. Above this limit, the resistivity at any given volume fraction generally increased with thinner silver films, although there was some overlap between the two thickest films. Several possible mechanisms were discussed, such as differences in contact resistance and different intrinsic resistivities caused by more severe electron scattering in the thinner films, but no conclusions could be drawn from the data. In a third study, the effect of particle size and film thickness was reinvestigated, and the finding from the first paper that smaller AgPS yielded lower resistivities was confirmed [96]. The silver film thicknesses were all ≥ 200 nm, and it was found that the resistivity of the ICA correlated well with the total silver content for such relatively thick films when the films were prepared with the same plating process. ICAs with AgPS plated in different processes, but with equal size and film thickness were also compared, but the results were ambiguous and no clear conclusions could be drawn. In addition, ICAs with the same AgPS but two different epoxy systems, one with relatively high reactivity and viscosity and one with lower reactivity and viscosity, were compared. It was found that the epoxy with lower viscosity yielded lower resistivities, and allowed for a higher filler content. The impact of curing temperature was checked for one of the epoxies, and it was found that a higher curing temperature (150 °C) generally yielded slightly lower resistivities than the lower (120 °C), although the difference between the two were within the scatter in the data. Jain also measured the volume change of a range of flake-based and AgPS-based ICAs after cure and found that, while the flake-based

ICAs showed relative shrinkage ranging from a few percent to about 20 %, the AgPS-based ICAs generally expanded by a few percent [88]. As the same epoxies decreased in volume when flakes where used, it was deduced that the volume expansion in the AgPS-based ICAs had to be caused by air trapped in the adhesive, outgassing from the polymer cores, polymer core expansion, or a combination of these. From these investigations, it can be concluded that the electrical resistivity of the ICA obviously is a complex phenomenon, depending on a range of factors such as AgPS content, AgPS size, silver film thickness, inter-particle contact resistance, the resistivity and quality of the silver films, in addition to the properties of the polymer adhesive.

Even though ICA bulk resistivity is a complex phenomenon, the basic impact of factors such as AgPS size and silver film thickness can be understood by a very simple model, conceived by Jain in her thesis and illustrated in Fig. 9 [88]. The model assumes simple cubic packing of equally sized MPS, i.e. an AgPS content of 52 vol %, with each MPS being in electrical contact only with two other particles, with contact radii normal to the direction of the current. Each particle contributes with three resistances in series; the resistance of the spherical thin film (R_{MPS}), constriction resistance from one contact, and tunneling resistance from one contact, where the two last contributions are the two parts of the contact resistance (R_C) from classical

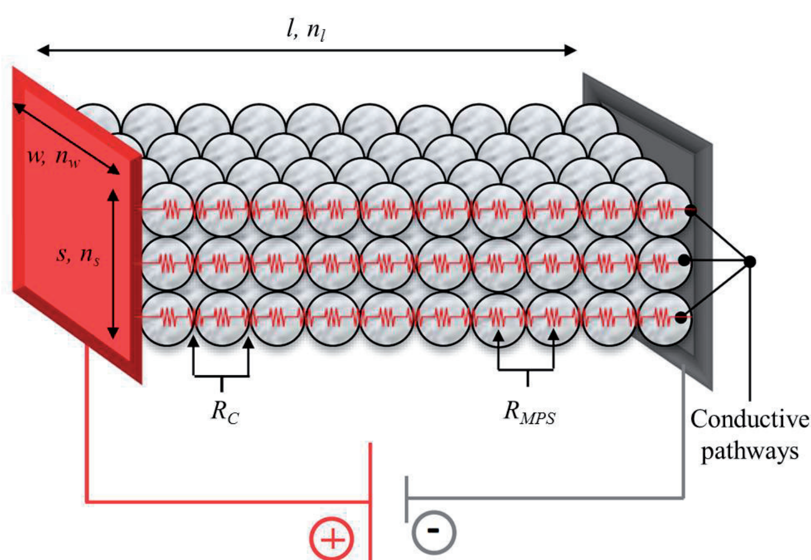

Fig. 9. Schematic illustration of Jain's model for ICA bulk resistivity, for an ICA with AgPS stacked in a simple cubic packing structure (i.e. 52 vol% AgPS). (Adapted from [88].)

Holm's contact theory [100, 101]. There are n_l MPS along the length l, n_w along the width w, and n_s along the side length s, respectively. Ignoring edge effects, the total resistance of the ICA (R_{tot}) then comprises $n_w \cdot n_s$ series resistances, $n_l \cdot (R_{MPS}+R_C)$, in parallel. As $l = n_l \cdot Ø$, $w = n_w \cdot Ø$, and $s = n_s \cdot Ø$, where $Ø$ is the diameter of the MPS, the bulk ICA resistivity (ρ_{ICA}) can be calculated by

$$\rho_{ICA} = Ø \cdot \left(\left(\frac{\rho_m}{\pi \cdot t_m} \right) \cdot \left(-\ln \left(\tan \frac{r_c}{Ø} \right) \right) + \frac{\rho_m}{2 \cdot r_c} + \frac{\rho_t}{\pi \cdot r_c^2} \right). \quad (1)$$

In Eq. 1, ρ_m is the resistivity of the metal films [Ω·cm], t_m is the thickness of the metal films, r_c is the contact radius, and ρ_t is the tunneling resistivity [Ω·cm^2]. For a full derivation of the model, see [88]. From the model, one can immediately see that smaller MPS, lower metal resistivity, lower tunneling resistivity, thicker metal films, and larger contacts will decrease the ICA resistivity.

The bulk conductivity/resistivity of the ICA is only one of the factors influencing the final resistance of the interconnect; contact resistance between the ICA and the contacting surfaces is also crucial for the electrical performance. Gakkestad et al. tested the contact resistance of ICAs with both NiAuPS and AgPS against contacts coated with about 100 nm Au [98]. The NiAuPS-based ICA yielded approximately three times lower contact resistance than the ICA with AgPS, and both increased by about 90 % after 100 thermal cycles between -55 and + 125 °C. Importantly, the contact resistances did not change much after the previously described rapid firing tests. In her thesis, Jain measured a large range of AgPS-based ICAs towards test leads of Cu/Ni with an Au-finish [88]. Generally, the contact resistance decreased with increasing AgPS content, and smaller AgPS yielded lower contact resistance at the same volume fraction. This was attributed to larger contact areas and more contact spots. ICAs containing AgPS with the same core size but different film thicknesses yielded no significant differences. The largest impact came from varying the epoxy type; a less viscous epoxy yielded significant improvement in contact resistance, similar to that obtained with commercial flake-based ICAs.

The interconnects of both electronic devices and PV modules conduct heat as well as electricity. The thermal conductivity of AgPS-based ICAs containing 30 µm or 15 µm cores with 150 nm silver films has been investigated as a function of filler content, and compared with flake-based ICAs [102]. Generally, the same behavior is seen in the thermal conductivity as in the electrical

conductivity, with increasing conductivity at higher filler content and smaller AgPS. However, there is no percolation threshold, as the epoxy matrix also has the capability to conduct heat, although inferiorly to the silver films. Importantly, a thermal conductivity of 1 W/(m·K) was achieved with only 1.4 vol% silver using AgPS, whereas the flake-based ICA required 16 vol% to reach the same value. The thermal expansion of the ICAs was also measured, and found to be dividable into three regimes; below the glass transition temperature (T_g) of the epoxy, over the T_g of the epoxy but below that of the polymer cores, and above the T_g of the cores.

The aims of the previous work summarized in this section have to a large extent been proof-of-concept, to establish the basic characteristics of AgPS-based ICAs and show that AgPS is a feasible alternative to all-metal particles and silver flakes. With some exceptions, the focus has been on the macroscopic properties and bulk behavior of the material, with less attention to the nanomaterial characteristics of the silver thin films. Jain discussed the impact of inter-particle contact resistance on the bulk resistivity of the ICAs, as well as how the resistivity of the silver films could deviate from that of bulk silver, and even constructed the simple analytical model shown in Eq. 1 [88, 95]. However, as the structure of the contacts was not investigated, the impact of the different factors could not be separated, making it challenging to gain any further understanding of the conduction mechanisms. In addition, the long-term reliability of the ICA, one of the uttermost important characteristics of an electronic interconnect, has only been investigated in one study by Gakkestad et al., and this yielded ambiguous results [98].

Chapter 3

Objectives and main results

3.1 Aim of thesis

The main goal of this thesis has been to enhance the understanding of the factors controlling conduction in AgPS-based ICAs, motivated primarily by;

i) A need to decrease the bulk electrical resistivity of the material. Although AgPS-based ICAs can use silver relatively efficiently compared to most commercial ICAs, the bulk resistivity is still lower for the latter. The most effective use of silver reported in the earlier work on AgPS-based ICAs was a resistivity of 6.2×10^{-4} Ω·cm at a silver content of 2.9 vol% [102]. This is higher than the bulk resistivity normally reported for commercial Ag-flake-based ICAs (in the lower end of the 10^{-4} Ω·cm range), and also higher than the reported value for the commercial Cu- and Ag-based ICA developed especially for the PV industry, as was described in Section 2.1.4 [59]. By understanding the mechanisms controlling the bulk resistivity, strategies for decreasing this can be developed.

ii) An aspiration to optimize the long-term reliability of the ICA. It is important that conductivity of the electronic interconnects do not degrade significantly over time. E.g. in a PV module, increased resistivity in the interconnects will reduce the output effect. For an installed, stationary PV module, the main degradation factors will be oscillations in temperature and humidity. It is thus important to understand how the conductivity of the ICA develops at such conditions.

iii) An interest in reducing the processing temperatures. As discussed in Section 2.1.4, a curing temperature of 150 °C is still high enough to induce bending and thermomechanical stresses in the silicon wafers and metallic ribbons of solar cell assemblies. In addition, flexible, low-cost electronic devices are often very

temperature-sensitive [103]. The development of ICAs that acquire conductivity at lower curing temperatures would be beneficial for both these applications. However, optimization of the system to achieve conductivity at lower temperatures requires an understanding of how the system acquires conductivity in the first place.

iv) An interest in enhancing the thermal conductivity of the ICAs. The ability of the ICAs to transport heat is important for a range of applications, although more so in electronics than in PV modules. As electrons are responsible for virtually 100% of the heat conduction in metals, the thermal and electrical conductivity are closely related.

Jain, Nguyen, Gakkestad, et al. established the important basics of the conduction mechanisms by investigating the effects of AgPS volume fraction, AgPS size, and silver film thickness [88, 93-96, 102]. However, potential implications of the silver thin films being nanomaterials were only briefly discussed, and not investigated experimentally. A goal in this thesis has thus been to understand how size-related properties such as increased electron scattering and increased reactivity influences the properties of both individual AgPS and the bulk ICA. As electrical characterization of individual AgPS requires advanced characterization methods, the first goal of the thesis has been to develop suitable methods for single-particle characterization. However, the bulk resistivity of the ICA is not only dependent on the resistivity of the silver thin films, but also on the inter-particle contact resistance. It has thus been an objective in this work to gain better understanding on how the AgPS contact each other in the ICA, and how these contacts can be improved.

As no reliability testing with high humidity had been published on the AgPS-based ICAs, this was deemed an important topic for investigation. Normally such tests are performed on bonded components, and the impact is investigated through performance tests that compares component properties from before and after, and sometimes during, the environmental exposure. Examples of such properties can be shear or impact strength, contact resistance, or in the case of PV assemblies, effect losses or ribbon peel strengths. However, such properties can be quite complex, as they are dependent not only on the adhesive, but also on the interconnected components and the interfaces between the component and the adhesive. To gain an understanding on what happens with the structure and conductive properties of the ICA during long-term heat and humidity testing (85 °C/85 %RH), it was therefore decided to first conduct such an investigation on detached samples of ICA. The results from this first study were so

surprising and interesting that it was decided to do follow-up studies, also focusing on the bulk ICA. These studies were combined with an investigation of curing temperature, as combinations of these different parameters were expected to yield a better understanding of the results.

Only one study had previously been conducted on thermal transport in AgPS-based ICAs, and this investigated the impact of filler volume fraction [102], as discussed in Section 2.2.2. As the impact of silver film thickness had not been investigated, this was deemed an important parameter to explore. To interpret the results, it is vital to understand how the methods can affect the outcome. As the flash diffusivity method has become one of the most common methods for estimating thermal conductivity, each parameter of the method was analyzed methodically.

3.2 Main findings and novelty of methods

3.2.1 Paper I

In this work, two methods have been developed to characterize the electrical properties of individual MPS. The first method is a further development of a flat punch nanoindentation-based setup previously developed at NTNU Nanomechanical Lab, capable of performing uniaxial load-deformation measurements of individual polymer spheres and MPS [104-111]. An early version had already been developed, capable of doing current-voltage (*IV*) measurements between a conductive tip and conductive substrate during particle compressions. This setup had been used to measure resistance as a function of deformation for a set of AgPS with 30 µm methacrylate cores and different silver film thicknesses. This data was used successfully by both Nguyen and Jain in their respective theses [87, 88], and was recently published in a journal paper [93]. However, this setup had several shortcomings, and had to be completely redesigned to acquire the data presented in Paper I [13]. In addition to producing data of publishable quality, the new setup is of great value to our industrial partners Conpart AS and Mosaic Solutions AS as a rapid and reliable method for doing quality tests of production batches of MPS. With the new setup, it was found that smaller AgPS (10 µm) must be deformed to a much higher nominal strain than larger AgPS (30 µm) before the contact resistance converges to a semi-constant, negligible value. We also confirmed the results first presented by Nguyen and Jain that thicker films yield lower resistances and less spread in data, but that this improvement levels out at a certain thickness. The results are valuable input for designing both ACA and ICA assemblies. However, as explained in [13], the measured resistance is the sum

of a series of resistances, from the flat-punch tip, tip-to-MPS and MPS-to-substrate contacts, substrate, and the thin metal film of the MPS. To estimate the thin film resistivity from these measurements would be a cumbersome task, where one have to separate each single contribution to the total resistance, including the contact resistance. Thus, although the method is valuable, it is not suited to find the resistivities of the thin films.

3.2.2 Paper II

For this task, a novel method was conceived and developed, in which four-point measurements were conducted directly on individual AgPS, using four individually controlled micromanipulators under real-time observation in a scanning electron microscope (SEM), as described in Paper II [14]. By combining the IV-measurements with probe positions on the particle acquired from the SEM images, a simple FE model could be constructed that allowed for the estimation of the thin film resistivities of AgPS with four different film thicknesses. This was further combined with x-ray diffraction (XRD) to estimate the grain sizes of the films. It was found that when the films became very thin (~ 60 nm) in combination with small grain sizes, the resistivity increased significantly. The method thus gives valuable input for the electroless plating process. Although the method is easiest to implement on symmetrical geometries, it is by no means limited to spherical shell structures, and could thus be used to investigate the resistivity of other microstructures.

3.2.3 Paper III

In Paper III, we prepared ICAs with a high content of AgPS (~ 56 vol%) with 30 μm cores, but with four different film thicknesses (60 nm, 100 nm, 150 nm, and 270 nm). In accordance with the results by Jain [88, 95], we found that the bulk ICA resistivity increased with thinner films, especially noticeable for the 60 nm films, which yielded ICA resistivities an order of magnitude higher than the three thicker films as well as much higher scatter in data [15]. For the first time on AgPS-based ICAs, we investigated the effect of long-term exposure to elevated heat and humidity (85 °C/85 %RH), and found that the resistivities decreased for all samples, but much more for the samples with 60 nm films. By combining the investigations with cross-sectioning of the ICA samples by high quality ion milling, and further imaging these with high resolution field emission scanning electron microscopy (FE-SEM), we were for the first time able to identify and study inter-particle contacts within the ICAs. In the ICAs with 100, 150, and 270 nm films, the AgPS had formed metallurgical contacts, but no such contacts were identified in the ICA with 60 nm films. After elevated heat and humidity exposure, metallurgical contacts

were observed also in the ICAs with 60 nm films, correlating well with the larger decrease in resistivities for these samples. The discovery of metallurgical inter-particle contacts in the AgPS ICAs have been a large contribution towards understanding the conduction mechanisms of these ICAs. Metallurgical contacts means that the bulk resistance and thus the bulk resistivity of the material is controlled by geometrical resistance factors and the resistivity of the silver, and not the tunneling resistance that is dominating in conventional flake-based ICAs [112]. We also conceived an equation, a Figure of Merit (FoM), to compare how efficiently different ICAs use the incorporated silver [15]. The FoM have been very useful for further understanding the conduction mechanisms of the ICAs, and is given by

$$FoM_{ICA} = \frac{\rho_{Ag}}{\rho_{ICA} \cdot \Phi_{Ag}}, \quad (2)$$

where Φ_{Ag} is the volume fraction of silver [15]. A FoM of 1.0 or 100% means that the incorporated amount of silver conducts electrons as well as bulk silver, i.e. that there is no geometrically induced resistance or contact resistance in the silver network.

3.2.4 Paper IV

To better understand the formation of the metallurgical contacts, we designed a large follow-up study, where we prepared one AgPS-based ICA, containing 30 μm cores with 100 nm thick silver films, and split the samples in three series, which were cured at room temperature, 85 °C, and 150 °C, respectively. Further, each curing series was split into three parallels, and stored at either 85 °C/85 %RH, 85 °C, or immersed in water at room temperature, to separate the effects of heat and humidity. The resistivity was measured before, during, and after the environmental exposures, samples from before and after environmental exposure were cross-sectioned and imaged with SEM, and the grain sizes were estimated with XRD. The initial results were presented at the 2016 IEEE 66th Electronic Components and Technology Conference (ECTC) and in the conference proceedings presented in Paper IV [16]. It was found that the conductivity increased significantly with elevated curing temperatures, and the mechanisms behind this was discussed. SEM-images suggested that the metallic contacts formed at room temperature were mechanically held together by the epoxy matrix, while the AgPS formed metallurgical contacts when cured at 150 °C. It was confirmed that the conductivity increased during storage at 85 °C/85 %RH, and that this increase was much higher than during storage at only elevated temperature. A methodic study of the inter-particle contacts was presented, and it was found that the number of metallic contacts was much higher in the samples stored at 85 °C/85 %RH,

than in the as-prepared samples and samples stored at 85 °C. The higher number of contacts is directly related to the contacts being wider, which increases the probability for the random two-dimensional cross-section to cut through a contact. This was the first experimental evidence that wider contacts were related with higher bulk conductivity in the ICAs.

3.2.5 Paper V

The bulk of the results were presented in Paper V [17]. Although Paper IV also presented results from the series cured at room temperature, these were emphasized in this paper. With this study, we showed that conductivity can be achieved not only with curing at 85 °C, but even with curing at room temperature and with an only partially cured epoxy matrix. This is a significant contribution to the field, as this means that lower processing temperatures with AgPS-based ICAs are not limited by the AgPS, but rather by the choice of adhesive matrix. The grain size of the as-cured samples increased with increasing curing temperature, supporting sintering and/or grain growth as important mechanisms behind the lower resistivities and the metallurgical contacts observed the ICAs cured at 150 °C. Just as important, the grain size increased much more in the samples stored at 85 °C/85 %RH than in the samples exposed only to elevated heat or immersion in water, and the grain growth was more significant for the samples cured at lower temperatures, especially at room temperature. This means that the silver films to a large extent can be stabilized by a more densely cross-linked adhesive matrix, and that these require simultaneously elevated temperature and humidity for large structural changes to occur, which is important knowledge for optimizing the processing conditions. We also found that the lowest resistivities were not achieved in the samples that showed largest grain growth, meaning that although the grain size has an effect of the bulk resistivity, it is not the most important factor. Finally, we presented an explanation on the grain growth at elevated humidity based on an electrochemical Ostwald ripening process. This had been suggested also in Papers III and IV, but the separation of heat and humidity coupled with the XRD measurements of grain size yielded very compelling evidence for this mechanism. This mechanism is a size-effect, unique to systems with a heterogeneous size distribution of silver grains or particles in the nanometer-regime, and to our best knowledge, this is the first time this mechanism has been found in a composite system.

3.2.6 Paper VI

In Paper VI, we investigated the thermal properties of the same AgPS that was described in Paper III [15, 18]. This was the first investigation of thermal properties as a function of silver

film thickness, and also the first investigation of thermal conductivity at temperatures higher than room temperature. It was found that the thermal conductivity increased until reaching the glass transition temperature of the epoxy, after which it decreased with further elevated temperatures. The most important finding of this investigation was that the thermal conductivity, when estimated by the commonly used flash diffusivity method as a product of the thermal diffusivity, density, and specific heat capacity of the samples, showed large variation dependent on the method used to estimate the specific heat capacity. This finding is important not only for the AgPS-based ICAs, but for all polymer composites with dispersed conductive filler particles.

Chapter 4

Discussion and outlook

4.1 Decreasing ICA bulk resistivity

The ICAs yield FoM values around 10%, which is better than for most commercial ICAs, but the bulk resistivity is still around 5 – 10 times larger than that of commercial ICAs. For AgPS to be an alternative to other low-Ag fillers such as silver-coated Cu-flakes, the resistivity should be at most in the lower range of 10^{-4} Ω·cm.

4.1.1 Metallic contacts

The combined results in Papers III – V gives a compelling argument for the presence of mechanical metallic and even metallurgical contacts in the AgPS-based ICAs [15-17]. However, we do not conclude on whether these are the norm of the inter-particle contacts, or if there still is a large tunneling contribution to the ICA conductivity. Comparing ρ_{ICA} calculated by Jain's model (Eq. 1) with the experimental values found for the ICA cured at 150 °C in Papers IV and V shed more light on this subject. At a AgPS content of 51 vol%, corresponding to 1.0 vol% Ag, this ICA has an AgPS content very close to the 52 vol% of the model, although in the real ICA the AgPS are randomly dispersed and not in the simple cubic packing of the model [16, 17]. The tunneling resistivity is a function of the work function of the metal, the gap width between the metal surfaces, and the relative permittivity of the gap material, and is thus not dependent on the resistivity of the gap material [100]. A very conservative estimate for a potential tunneling resistivity is 1×10^{-8} Ω·cm^2, and most tunneling barriers can be expected to be higher than this [100, 101]. Jain's model was used to estimate ρ_{ICA} for AgPS with $Ø$ = 30 μm and t_m = 100 nm, equivalent to the AgPS used in Papers IV and V, as a function of contact radius, and with ρ_t either equal to 1×10^{-8} Ω·cm^2 or zero (i.e. no tunneling barrier/metallic contacts). In addition, the FoM in Eq. 2 was used to estimate the minimum achievable ρ_{ICA} for

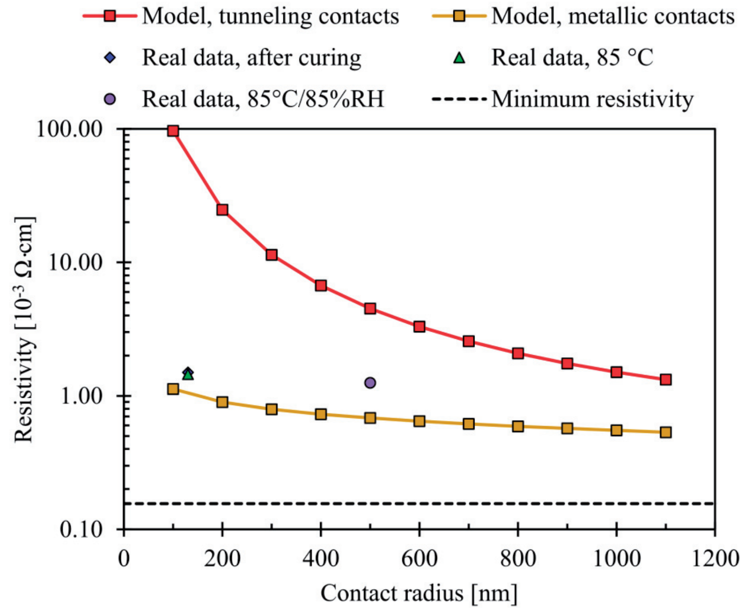

Fig. 10. ρ_{ICA} estimated by Jain's model (Eq. 1) with $\varnothing$ = 30 µm and t_m = 100 nm, with and without a tunneling barrier of 1×10^{-8} Ω·cm^2. Also shown is experimental data from Papers IV and V, for the ICA cured at 150 °C with AgPS of the same parameters as in the model, at 51 vol% [16, 17]. The stippled line shows the resistivity if there were no geometric or contact resistances in the material, calculated from Eq. 2 with FoM = 1.0.

the volume fraction of silver in the model (1.03 vol%) by setting FoM equal to 1.0 and solving for ρ_{ICA}. The results can be seen in Fig. 10, and it is clear that the model supports the domination of metallic contacts. At a contact radius of 100 nm, ρ_{ICA} becomes 9.66×10^{-2} Ω·cm when the tunneling barrier is included (omitted from the figure for illustrative purposes). The contact radius has to be in the order of 1000 nm before the model values including tunneling start approaching the experimental values, and it is clear from the cross-sectioned samples that the contacts are definitely metallurgical in this range, as this is only achievable after the large grain growth during 85 °C/85 %RH. The reasons why the experimental values are higher than those of the model is likely a combination of increased resistivity of the silver films compared to bulk silver, the randomly meandering pathways of AgPS being longer than l in the model, and cul-de-sacs, i.e. AgPS that do not contribute to the conductive network but instead form dead-ends. Even though the work presented in this thesis strongly supports the presence of metallic and metallurgical contacts, the role of silver oxide is still an open question, and would be an

interesting topic for further investigation. The AgPS are not coated with any protective barriers to prevent oxidation, and as they are stored as dry powder in air before being incorporated into the polymer adhesive, silver oxide is almost certainly present on the surface of the particles. The role of silver oxide, e.g. as an energy barrier against sintering may be worth pursuing to gain further understanding of the inter-particle contact mechanisms.

4.1.2 AgPS size and film thickness

Combining the FoM (Eq. 2) with Jain's model (Eq. 1) can be used gain further understanding of the limits of the resistivity achievable with the AgPS-based ICAs. As expected, both lowering the AgPS size and increasing silver film thickness contribute to decreasing the resistivity, as can be observed in Fig. 11 a). According to Paper II, the film thicknesses should preferentially be > ~ 100 nm to avoid large increases in the resistivity of the silver films [14]. Decreasing the AgPS size will therefore necessarily lead to increased silver content, as the film thickness cannot be decreased correspondingly. One of the major advantages of the AgPS-based ICAs is the low silver consumption, and lowering the resistivity should be accomplished without increasing the silver content to a point where the AgPS-based ICAs loose this advantage. If one sets a maximum limit of the silver content at e.g. 5 vol%, it is seen from Fig. 11 b) that the AgPS cannot be smaller than ~ 10 µm and the films cannot be thicker than ~ 150 nm. According to the model, 20 µm AgPS with 300 nm films can achieve approximately the same resistivities as 10 µm AgPS with 100 nm films, but the silver content is lower and the FoM is higher in the latter. However, in the real ICA, other factors will also contribute, such as the ability of asperities on the film surfaces to penetrate the adhesive and form metallic contacts. In Paper III we found that the thinnest film (60 nm) formed no observable metallic contacts during curing at 150 °C, which also correlated with the much higher resistivity and standard deviation, $1.7 \pm 1.3 \times 10^{-2}$ Ω·cm, observed for this series compared to the ICAs containing AgPS with thicker films [15]. Even though Fig. 10 shows that the real ICAs can achieve resistivities close to the model values, Fig. 11 a) reveals that the lower limit is in the range of $2.4 – 3.2 \times 10^{-4}$ Ω·cm for a monodisperse size distribution, and real ICAs will likely achieve somewhat higher values. As there does not seem to be much more to gain from using homogeneous size distributions, future investigations should study multimodal size distributions, as are already successfully used in conventional ICAs [4].

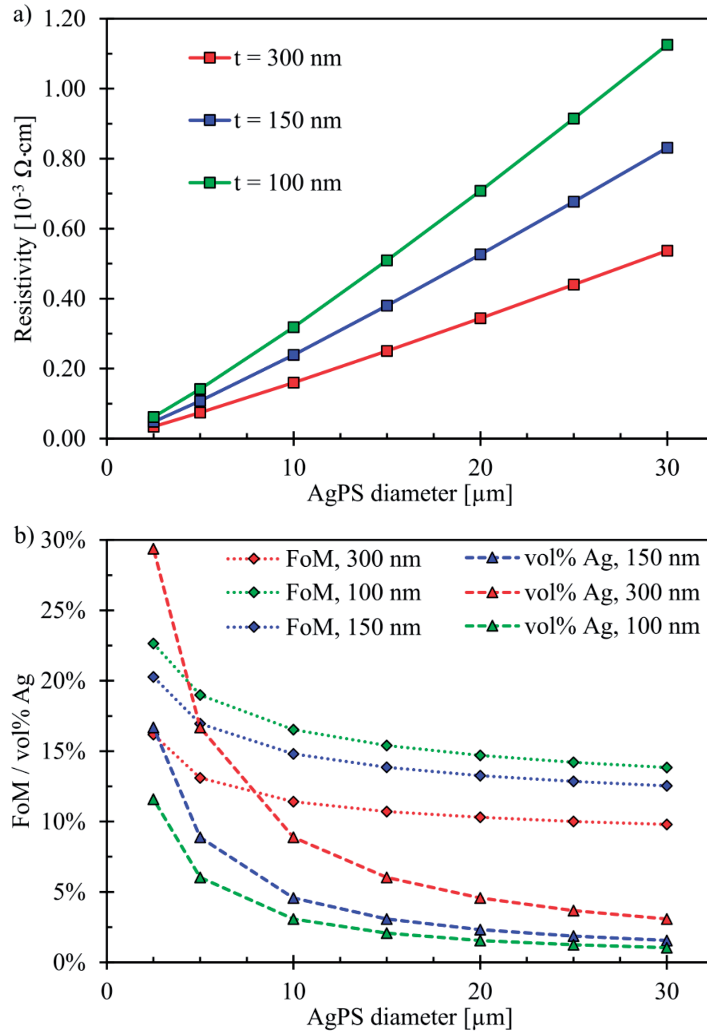

Fig. 11. a) ρ_{ICA} estimated by Jain's model and b) vol% Ag and FoM as a function of AgPS diameter, *Ø*, for three silver film thicknesses (t_m = 300 nm, 150 nm, and 100 nm), with no tunneling barrier, r_c = 100 nm, and $\rho_m = 1.6 \times 10^{-6}$ Ω·cm.

4.2 Reliability investigations

Next to the lowering of the bulk resistivity, the reliability of the AgPS-based ICAs require further studies before these can compete with conventional ICAs. As discussed in Section 2.1.4 and mentioned in Section 3.1, the main degradation factors for the interconnects of an installed, stationary PV module will be oscillations in temperature and humidity.

4.2.1 Grain growth at elevated temperature and humidity

We have shown in Papers III – V that significant grain growth occurs in the ICAs when exposed to elevated temperatures and humidity [15-17]. This grain growth has a positive impact on the conductivity, as it decreases grain boundary scattering and increases the sizes of the inter-particle contacts. However, the investigations were all conducted with no applied bias voltage across the ICAs. In e.g. a PV interconnect there will be a direct current conducted through the interconnect when the solar cell produces electricity, and further studies should be done to investigate the impact of bias voltage on the bulk resistivity during high temperature and humidity storage. If the application of a voltage has a degrading effect on the electrical conductivity, methods to stabilize the silver films against grain growth has to be conceived. Some measures are already evident from the investigations in Papers III – V. Paper III suggest that the grain growth is more significant in the thinner films [15]. This was not measured by XRD, but the larger decrease in resistivity for the thinnest film, as well as the post-ET appearance of the 100Ag series in the imaged cross-sections support more grain growth in these. The electrochemical Ostwald ripening is a size-effect, and thicker films (~ 150 nm) with larger grains should work against the grain growth, as well as improve the intrinsic electrical conductivity. Papers IV – V reveal that the grain growth is less prominent in the ICAs cured at elevated temperatures [16, 17]. As discussed in Paper V, this may be due to a higher water uptake and more free amine groups in the less cross-linked epoxies cured at lower temperatures. The more densely crosslinked epoxy of the ICA cured at elevated temperatures likely stabilize the silver films.

4.2.2 Thermal cycling

As discussed in Section 2.2.2, only one investigation have been done on the effect of thermal cycling on the AgPS-based ICAs, and the results from this study were ambiguous [98]. Although the similar CTE of the polymer cores and adhesive matrix is expected to have a positive effect on the thermal cycling properties of the material, it is unclear what effects different glass transition temperatures will have at different temperature regimes. It is also unclear how the metallurgical contacts discovered in Papers III – V will be affected by repeated thermal cycles [15-17]. The structure of the contacts in the room temperature cured ICA investigated in Papers IV – V suggest that the contacts do not have to be metallurgical for the ICA to achieve conductivity, but the ICAs where metallurgical contacts are found do yield lower resistivities [16, 17].

4.2.3 Contact resistance

The few investigations that have been conducted on the contact resistance between the ICA and contact pads suggest that the AgPS-based ICAs can achieve contact resistances similar to flake-based ICAs with a low-viscosity epoxy system [88]. Both previous investigations were performed against contacts with an Au-finish [88, 98]. In cost-demanding PV modules, stabilizing the contacts with Au is not an option. Contact resistance tests before and after thermal cycling and elevated temperature and humidity storage should therefore be conducted, primarily against Cu-ribbons and Ag-coated Cu-ribbons, and against the silver busbars of solar cells or an equivalent test structure. The contacts formed against silver would be of special interest, as the potential of the AgPS to form sintered metallurgical connections is not necessarily restricted to between the silver films [70, 71].

4.3 Optimization of lower curing temperature adhesive systems

The adhesive used for all the investigations in this thesis is a standard structural epoxy adhesive, not specialized for electronic applications. It is therefore clear that much of the potential improvement of the AgPS-based ICAs will come from optimization of the adhesive system. In Papers IV – V we showed that the AgPS are capable of forming metallic contacts even when the ICAs are cured at room temperature, although the sintering into metallurgical contacts seem to require elevated temperatures [16, 17]. However, the room-temperature epoxy was not fully cross-linked, with the already discussed impacts this had on grain growth and resistivity development. Adhesive systems that yield a larger degree of conversion at temperatures lower than 150 °C are of interest both for developing lower temperature interconnection processes for PV module manufacturing, and for interconnecting other temperature-sensitive electronic components. Much of the advantage of ICA vs. solders as solar module interconnects is that the lowered processing temperatures in theory allows for thinner wafers, which can lead to significant cost-reductions. It would also be interesting to investigate how adhesive systems with higher degree of shrinkage affect the bulk ICA resistivity. More reactive adhesives have the downside of shorter pot-life and processing windows. Adhesives with other curing mechanisms such as UV-curing could therefore also be of interest. Newer processes, such as the photonic curing used with great success by Cui et al. [35], would be very interesting to try with AgPS-fillers.

4.4 Further thermal transport investigations

Although the study by Gakkestad et al. in combination with the study in Paper VI have revealed much about the basic mechanisms of thermal transport in the AgPS-based ICAs, there are still open questions [18, 102]. Both investigations were conducted using the flash diffusivity / laser flash analysis (LFA) approach. This is a transient method, and the percolating network of silver films thus dominates the thermal transport, as these have a much higher thermal diffusivity than the epoxy matrix and polymer cores. Further studies should include comparison with steady-state thermal conductivity measurements. In addition, the rate and mechanisms of heat transfer across the metal-polymer interfaces are suitable areas for future investigations, both experimental and modelling-based.

Bibliography

1. H. Kristiansen, K. Redford, and T. Helland, *Isotropic conductive adhesive*, Patent number: US 2013/0323501 A1, 2013.
2. J.E. Morris, L. Jeahuck, and J. Liu, *Isotropic Conductive Adhesive Interconnect Technology in Electronics Packaging Applications,* 5th International Conference on Polymers and Adhesives in Microelectronics and Photonics, (Wroclaw, Poland, 2005), doi: 10.1109/POLYTR.2005.1596485
3. Y. Li and C.P. Wong, *Recent advances of conductive adhesives as a lead-free alternative in electronic packaging: Materials, processing, reliability and applications,* Materials Science and Engineering: R: Reports, 2006, **51**(1–3): p. 1-35.
4. J. E. Morris and J. Liu, *Electrically Conductive Adhesives: A Research Status Review*, in *Micro- and Opto-Electronic Materials and Structures: Physics, Mechanics, Design, Reliability, Packaging*, edited by: E. Suhir, Y.C. Lee, and C.P. Wong, 2007, Springer Science+Business Media LLC, New York. p. 527-570.
5. J.E. Morris, *Isotropic conductive adhesives: Future trends, possibilities and risks,* Microelectronics Reliability, 2007, **47**(2–3): p. 328-330.
6. I. Mir and D. Kumar, *Recent advances in isotropic conductive adhesives for electronics packaging applications,* International Journal of Adhesion and Adhesives, 2008, **28**(7): p. 362-371.
7. D. Daniel Lu, Y. Grace Li, and C.P. Wong, *Recent Advances in Nano-conductive Adhesives,* Journal of Adhesion Science and Technology, 2008, **22**(8-9): p. 815-834.
8. M.J. Yim, Y. Li, K.-s. Moon, K.W. Paik, and C.P. Wong, *Review of Recent Advances in Electrically Conductive Adhesive Materials and Technologies in Electronic Packaging,* Journal of Adhesion Science and Technology, 2008, **22**(14): p. 1593-1630.
9. Y. Li, D. Lu, and C.P. Wong, *Isotropically Conductive Adhesives (ICAs)*, in *Electrical Conductive Adhesives with Nanotechnologies*, edited by: Y. Li, D. Lu, and C.P. Wong, 2010, Springer Science+Business Media LLC, New York. p. 121-225.
10. J. Liu, O. Salmela, J. Särkkä, J.E. Morris, P.-E. Tegehall, and C. Andersson, *Conductive Adhesive Joint Reliability*, in *Reliability of Microtechnology: Interconnects, Devices and Systems*, edited by: J. Liu, O. Salmela, J. Särkkä, J.E. Morris, P.-E. Tegehall, and C. Andersson, 2011, Springer Science+Business Media LLC, New York. p. 71-98.
11. S.-B. Jung and J.-W. Kim, *Electrical Industry*, in *Handbook of Adhesion Technology*, edited by: L.M. da Silva, A. Öchsner, and R. Adams, 2011, Springer Berlin Heidelberg, 1289-1313.

12. Y.C. Lin and J. Zhong, *A review of the influencing factors on anisotropic conductive adhesives joining technology in electrical applications,* Journal of Materials Science, 2008, **43**(9): p. 3072-3093.
13. M. Bazilchuk, S.R. Pettersen, H. Kristiansen, Z. Zhang, and J. He, *Electromechanical characterization of individual micron-sized metal coated polymer particles,* Journal of Applied Physics, 2016, **119**(24): p. 245102.
14. S.R. Pettersen, A.E. Stokkeland, H. Kristiansen, J. Njagi, K. Redford, D.V. Goia, Z. Zhang, and J. He, *Electrical four-point probing of spherical metallic thin films coated onto micron sized polymer particles,* Applied Physics Letters, 2016, **109**(4): p. 043103.
15. S.R. Pettersen, H. Kristiansen, S. Nagao, S. Helland, J. Njagi, K. Suganuma, Z. Zhang, and J. He, *Contact Resistance and Metallurgical Connections Between Silver Coated Polymer Particles in Isotropic Conductive Adhesives,* Journal of Electronic Materials, 2016, **45**(7): p. 3734–3743.
16. S.R. Pettersen, H. Kristiansen, K. Redford, S. Helland, E. Kalland, Z. Zhang, and J. He, *Controlling the Conduction Mechanisms in Isotropic Conductive Adhesives with Silver-Coated Polymer Spheres,* IEEE 66th Electronic Components and Technology Conference (ECTC), 2016), doi: 10.1109/ECTC.2016.53
17. S.R. Pettersen, K. Redford, J. Njagi, H. Kristiansen, S. Helland, E. Kalland, D.V. Goia, Z. Zhang, and J. He, *Room-temperature curing and grain growth at high humidity in conductive adhesives with ultra-low silver content,* Journal of Electronic Materials, submitted, 2016.
18. S.R. Pettersen, S. Nagao, H. Kristiansen, S. Helland, J. Njagi, K. Suganuma, Z. Zhang, and J. He, *Investigation of thermal transport in polymer composites with percolating networks of silver thin films by the flash diffusivity method,* In process, 2016.
19. S. Wiese, F. Kraemer, N. Betzl, and D. Wald, *Interconnection technologies for photovoltaic modules - analysis of technological and mechanical problems,* 11th International Conference on Thermal, Mechanical & Multi-Physics Simulation, and Experiments in Microelectronics and Microsystems (EuroSimE), (Bordeaux, France, 2010), doi: 10.1109/ESIME.2010.5464518
20. S. Philipps and W. Warmuth, *Photovoltaic Report*, Fraunhofer Institute for Solar Energy Systems, ISE, Freiburg, Germany, 2016, https://www.ise.fraunhofer.de/de/downloads/pdf-files/aktuelles/photovoltaics-report-in-englischer-sprache.pdf.
21. M.T. Zarmai, N.N. Ekere, C.F. Oduoza, and E.H. Amalu, *A review of interconnection technologies for improved crystalline silicon solar cell photovoltaic module assembly,* Applied Energy, 2015, **154**: p. 173-182.
22. E.V. Kerschaver and G. Beaucarne, *Back-contact solar cells: a review,* Progress in Photovoltaics: Research and Applications, 2006, **14**(2): p. 107-123.

23. J.H. Selj, T.T. Mongstad, R. Søndenå, and E.S. Marstein, *Reduction of optical losses in colored solar cells with multilayer antireflection coatings,* Solar Energy Materials and Solar Cells, 2011, **95**(9): p. 2576-2582.
24. A.W. Czanderna and F.J. Pern, *Encapsulation of PV modules using ethylene vinyl acetate copolymer as a pottant: A critical review,* Solar Energy Materials and Solar Cells, 1996, **43**(2): p. 101-181.
25. H.-Y. Li, L.-E. Perret-Aebi, V. Chapuis, C. Ballif, and Y. Luo, *The effect of cooling press on the encapsulation properties of crystalline photovoltaic modules: residual stress and adhesion,* Progress in Photovoltaics: Research and Applications, 2015, **23**(2): p. 160-169.
26. D.W.K. Eikelboom, J.H. Bultman, A. Schonecker, M.H.H. Meuwissen, M.A.J.C.v.d. Nieuwenhof, and D.L. Meier, *Conductive adhesives for low-stress interconnection of thin back-contact solar cells,* 29th IEEE Photovoltaic Specialists Conference, (New Orleans, United States, 2002), doi: 10.1109/PVSC.2002.1190544
27. J.H. Wohlgemuth, *Reliability of PV systems,* Proc. of SPIE, 2008, **7048**: p. 704802-704802-13.
28. Y. Li, K.-s. Moon, and C. Wong, *Electronics without lead,* Science, 2005, **308**(5727): p. 1419-1420.
29. M.M. Aman, K.H. Solangi, M.S. Hossain, A. Badarudin, G.B. Jasmon, H. Mokhlis, A.H.A. Bakar, and S.N. Kazi, *A review of Safety, Health and Environmental (SHE) issues of solar energy system,* Renewable and Sustainable Energy Reviews, 2015, **41**: p. 1190-1204.
30. *Restriction of Hazardous Substances (RoHS) II Directive: Directive 2011/65/EU*,2011, The European Parliament and the Council of the European Union: http://eur-lex.europa.eu/LexUriServ/LexUriServ.do?uri=OJ:L:2011:174:0088:0110:EN:PDF.
31. M. Abdelhamid, R. Singh, and M. Omar, *Review of Microcrack Detection Techniques for Silicon Solar Cells,* IEEE Journal of Photovoltaics, 2014, **4**(1): p. 514-524.
32. J. Wendt, M. Träger, M. Mette, A. Pfennig, and B. Jäckel, *The link between mechanical stress induced by soldering and micro damages in silicon solar cells,* 24th European Photovoltaic Solar Energy Conference, (Hamburg, Germany, 2009), doi: 10.4229/24thEUPVSEC2009-4AV.3.40
33. G. Beaucarne, I. Kuzma-Filipek, F. Campeol, X. Young, J. Wei, Y. Yu, R. Russell, and F. Duerinckx, *Innovative Cell Interconnection Based on Ribbon Bonding of Busbar-less Cells Using Silicone-based Electrically Conductive Adhesives,* Energy Procedia, 2015, **67**: p. 185-193.
34. H. Wirth, *Lasers in Wafer-based PV Module Production,* Laser Technik Journal, 2010, **7**(4): p. 36-38.

35. H.-W. Cui, J.-T. Jiu, S. Nagao, T. Sugahara, K. Suganuma, H. Uchida, and K.A. Schroder, *Ultra-fast photonic curing of electrically conductive adhesives fabricated from vinyl ester resin and silver micro-flakes for printed electronics,* RSC Advances, 2014, **4**(31): p. 15914-15922.
36. E.M. Petrie, *Epoxy Adhesive Formulations*. 2006, United States: McGraw-Hill.
37. Y. Tsuo, J. Gee, P. Menna, D. Strebkov, A. Pinov, and V. Zadde, *Environmentally benign silicon solar cell manufacturing*, 2nd World Conference and Exhibition on Photovoltaic Solar Energy Conversion, (Vienna, Austria, 1998), p. 2-7
38. C. Yang, C.P. Wong, and M.M. Yuen, *Printed electrically conductive composites: conductive filler designs and surface engineering,* Journal of Materials Chemistry C, 2013, **1**(26): p. 4052-4069.
39. M. Abtew and G. Selvaduray, *Lead-free Solders in Microelectronics,* Materials Science and Engineering: R: Reports, 2000, **27**(5–6): p. 95-141.
40. T. Siewert, S. Liu, D.R. Smith, and J.C. Madeni, *Properties of Lead-Free Solders*, National Institute of Standards and Technology, Colorado, USA, 2002, http://www.msed.nist.gov/solder/NIST_LeadfreeSolder_v4.pdf.
41. D.R. Lide, *CRC Handbook of Chemistry and Physics, 84th Edition*. 2003: Taylor & Francis.
42. Y. Abe, T. Hasegawa, M. Kawamura, and K. Sasaki, *Characterization of Ag oxide thin films prepared by reactive RF sputtering,* Vacuum, 2004, **76**(1): p. 1-6.
43. P.N. Reddy, M.H.P. Reddy, J.F. Pierson, and S. Uthanna, *Characterization of Silver Oxide Films Formed by Reactive RF Sputtering at Different Substrate Temperatures,* ISRN Optics, 2014, **2014**: p. 7.
44. D. Klosterman, L. Li, and J.E. Morris, *Materials characterization, conduction development, and curing effects on reliability of isotropically conductive adhesives,* Components, Packaging, and Manufacturing Technology, Part A, IEEE Transactions on, 1998, **21**(1): p. 23-31.
45. L.-N. Ho, H. Nishikawa, and T. Takemoto, *Effect of different copper fillers on the electrical resistivity of conductive adhesives,* Journal of Materials Science: Materials in Electronics, 2011, **22**(5): p. 538-544.
46. Z.-M. Dang, B. Zhang, J. Li, J.-W. Zha, and G.-H. Hu, *Copper particles/epoxy resin thermosetting conductive adhesive using polyamide resin as curing agent,* Journal of Applied Polymer Science, 2012, **126**(3): p. 815-821.
47. A. Schneider, R. Harney, S. Aulehla, E. Lemp, and S. Koch, *Progress in Interconnection of Busbar-less Solar Cells by Means of Conductive Gluing,* Energy Procedia, 2013, **38**: p. 387-394.
48. A. Schneider, R. Harney, S. Aulehla, F. Demiralp, S. Koch, J. Scheurer, and C. Seeger, *Comprehensive Study of Material Dependency for Silver based Conductive Glues,* Energy Procedia, 2014, **55**: p. 509-518.

49. J.M. Gee, S.E. Garrett, and W.P. Morgan, *Simplified module assembly using back-contact crystalline-silicon solar cells,* 26th IEEE Photovoltaic Specialists Conference, (Anaheim, CA, United States, 1997), doi: 10.1109/PVSC.1997.654276
50. M.W.P.E. Lamers, C. Tjengdrawira, M. Koppes, I.J. Bennett, E.E. Bende, T.P. Visser, E. Kossen, B. Brockholz, A.A. Mewe, I.G. Romijn, E. Sauar, L. Carnel, S. Julsrud, T. Naas, P.C. de Jong, and A.W. Weeber, *17.9% Metal-wrap-through mc-Si cells resulting in module efficiency of 17.0%,* Progress in Photovoltaics: Research and Applications, 2012, **20**(1): p. 62-73.
51. P. De Jong, D. Eikelboom, R. Kinderman, A. Tip, J. Bultman, M. Meuwissen, and M. Van den Nieuwenhof, *Single-step laminated full-size PV modules made with back-contacted mc-Si cells and conductive adhesives*, 19th EPVSEC, (Paris, France, 2004), p. 2145
52. Y. Zemen, T. Prewitz, T. Geipel, S. Pingel, and J. Berghold, *The impact of yield strength of the interconnector on the internal stress of the solar cell within a module*, 5th World Conference on Photovoltaic Energy Conversion, (Valencia, Spain, 2010), p. 4073-4078
53. Y. Zemen, S.C. Schulz, H. Trommler, S.T. Buschhorn, W. Bauhofer, and K. Schulte, *Comparison of new conductive adhesives based on silver and carbon nanotubes for solar cells interconnection,* Solar Energy Materials and Solar Cells, 2013, **109**: p. 155-159.
54. H.H. Hsieh, W.K. Lee, T.C. Chang, and C.S. Hsi, *Photovoltaic modules of crystalline solar cells using a new type assembly structure,* 5th International Microsystems Packaging Assembly and Circuits Technology Conference (IMPACT), (Taipei, Taiwan, 2010), doi: 10.1109/IMPACT.2010.5699598
55. J.H. Bultman, D.W.K. Eikelboom, R. Kinderman, A.C. Tip, C.J.J. Tool, M.A.C.J.v.d. Nieuwenhof, C. Schoofs, F.M. Schuurmans, and A.W. Weeber, *Fast and easy single step module assembly for back-contacted c-Si solar cells with conductive adhesives*, 3rd World Conference on Photovoltaic Energy Conversion, (Osaka, Japan, 2003), p. 979-982
56. T. Geipel and U. Eitner, *Cure Kinetics of Electrically Conductive Adhesives,* Energy Procedia, 2013, **38**: p. 340-347.
57. T. Geipel and U. Eitner, *Cure Kinetics of Electrically Conductive Adhesives for Solar Cell Interconnection,* IEEE Journal of Photovoltaics, 2013, **3**(4): p. 1208-1214.
58. S. Schwertheim, M. Scherff, T. Mueller, W. Fahrner, and H. Neitzert, *Lead-free electrical conductive adhesives for solar cell interconnectors,* 33rd IEEE Photovolatic Specialists Conference (PVSC), (San Diego, CA, United States, 2008), doi: 10.1109/PVSC.2008.4922588
59. G. Beaucarne, K. Broek, B. Chislea, Y. Yu, J. Wei, A. Zambova, and I. Bennett, *Study of Compatibility of Silicone-based Electrically Conductive Adhesives and Conductive Backsheets for MWT Modules,* Energy Procedia, 2014, **55**: p. 444-450.

60. R. Zhang, W. Lin, K. Lawrence, and C.P. Wong, *Highly reliable, low cost, isotropically conductive adhesives filled with Ag-coated Cu flakes for electronic packaging applications,* International Journal of Adhesion and Adhesives, 2010, **30**(6): p. 403-407.
61. R. Zhang, W. Lin, K.-S. Moon, Q. Liang, and C.P. Wong, *Highly Reliable Copper-Based Conductive Adhesives Using an Amine Curing Agent for in Situ Oxidation/Corrosion Prevention,* Components, Packaging and Manufacturing Technology, IEEE Transactions on, 2011, **1**(1): p. 25-32.
62. H.-W. Cui, J.-T. Jiu, T. Sugahara, S. Nagao, K. Suganuma, and H. Uchida, *High performance heat curing copper-silver powders filled electrically conductive adhesives,* Electronic Materials Letters, 2015, **11**(2): p. 315-322.
63. Y. Zhang, S. Qi, X. Wu, and G. Duan, *Electrically conductive adhesive based on acrylate resin filled with silver plating graphite nanosheet,* Synthetic Metals, 2011, **161**(5–6): p. 516-522.
64. X. Peng, F. Tan, W. Wang, X. Qiu, F. Sun, X. Qiao, and J. Chen, *Conductivity improvement of silver flakes filled electrical conductive adhesives via introducing silver–graphene nanocomposites,* Journal of Materials Science: Materials in Electronics, 2014, **25**(3): p. 1149-1155.
65. H.P. Wu, X.J. Wu, M.Y. Ge, G.Q. Zhang, Y.W. Wang, and J. Jiang, *Properties investigation on isotropical conductive adhesives filled with silver coated carbon nanotubes,* Composites Science and Technology, 2007, **67**(6): p. 1182-1186.
66. I. Krupa, G. Miková, I. Novák, I. Janigová, Z. Nógellová, F. Lednický, and J. Prokeš, *Electrically conductive composites of polyethylene filled with polyamide particles coated with silver,* European Polymer Journal, 2007, **43**(6): p. 2401-2413.
67. N. Okinaga, H. Kuroda, and Y. Nagai, *Excellent reliability of solder ball made of a compliant plastic core,* 51st Electronic Components and Technology Conference, (Orlando, FL, United States, 2001), doi: 10.1109/ECTC.2001.928006
68. R. Johannessen, F. Oldervoll, H. Kristiansen, H. Tyldum, H.V. Nguyen, and K. Aasmundtveit, *Investigation of compliant interconnect for ball grid array (BGA)*, European Microelectronics and Packaging Conference (EMPC), (Rimini, Italy, 2009), p. 1-6
69. M.M.V. Taklo, A. Larsson, A.S.B. Vardøy, H. Kristiansen, L. Hoff, and K. Waaler, *Compliant interconnects for reduced cost of a ceramic ball grid array carrier,* IEEE 62nd Electronic Components and Technology Conference (ECTC), (San Diego, CA, United States, 2012), doi: 10.1109/ECTC.2012.6249099
70. D.N. Wright, M.M.V. Taklo, A.S.B. Vardøy, and H. Kristiansen, *Metal coated polymer spheres for compliant fine pitch ball grid arrays,* International 3D Systems Integration Conference (3DIC), (Kinsdale Ireland, 2014), doi: 10.1109/3DIC.2014.7152177

71. R.F. Hamou, D.N. Wright, A.S.B. Vardøy, M. Haupt, S. Helland, H. Kristiansen, and M.M.V. Taklo, *Analyzing thermo-mechanical reliability of an interconnect based on metal coated polymer spheres (MPS),* 16th International Conference on Thermal, Mechanical and Multi-Physics Simulation and Experiments in Microelectronics and Microsystems (EuroSimE), (Budapest, Hungary, 2015), doi: 10.1109/EuroSimE.2015.7103164
72. H. Kristiansen and J. Liu, *Overview of conductive adhesive interconnection technologies for LCDs,* IEEE Transactions on Components, Packaging, and Manufacturing Technology: Part A, 1998, **21**(2): p. 208-214.
73. L. Jia, X. Sheng, Z. Xiong, Z. Wang, and H. Ding, *Particle on Bump (POB) technique for ultra-fine pitch chip on glass (COG) applications by conductive particles and adhesives,* Microelectronics Reliability, 2014, **54**(4): p. 825-832.
74. I. Halaciuga, J.I. Njagi, K. Redford, and D.V. Goia, *Deposition of continuous nickel shells on polymer microspheres,* Journal of Colloid and Interface Science, 2012, **383**(1): p. 215-221.
75. J. He, *Nanomechanics of polymer and composite particles*, Ph.D. thesis, Norwegian University of Science and Technology (NTNU), Trondheim, Norway, 2009.
76. J. Ugelstad, K.H. Kaggerud, F.K. Hansen, and A. Berge, *Absorption of low molecular weight compounds in aqueous dispersions of polymer-oligomer particles, 2. A two step swelling process of polymer particles giving an enormous increase in absorption capacity,* Die Makromolekulare Chemie, 1979, **180**(3): p. 737-744.
77. A. Jørgedal, E.M. Aksnes, G. Fonnum, A. Molteberg, R. Nordal, H. Pettersen, T. Tårneby, S. Staale, E. Weng, and F. Hansen, *Process for the preparation of monodisperse polymer particles*, Patent number: US 9,309,368 B2, 2016.
78. J. Ugelstad, A. Berge, T. Ellingsen, R. Schmid, T.N. Nilsen, P.C. Mørk, P. Stenstad, E. Hornes, and Ø. Olsvik, *Preparation and application of new monosized polymer particles,* Progress in Polymer Science, 1992, **17**(1): p. 87-161.
79. H. Kristiansen, K. Redford, Z. Zhang, J. Hee, M. Fleissner, and P.I. Dahl, *Development and characterisation of micrometer sized polymer particles with extremely narrow size distribution,* 12th International Symposium on Advanced Packaging Materials: Processes, Properties, and Interfaces, (San Jose, CA, United States, 2007), doi: 10.1109/ISAPM.2007.4419931
80. Dynabeads, https://www.thermofisher.com/no/en/home/brands/product-brand/dynal.html, cited: 24.09.2016.
81. Micro-beads, http://www.micro-beads.com/Company.aspx, cited: 24.09.2016.
82. J. Sudagar, J. Lian, and W. Sha, *Electroless nickel, alloy, composite and nano coatings – A critical review,* Journal of Alloys and Compounds, 2013, **571**: p. 183-204.
83. Conpart AS, http://conpart.no/#productsservices, cited: 24.09.2016.

84. Mosaic Solutions AS, http://www.mosaicsolutions.no/?page=conductiveadhesive, cited: 24.09.2016.
85. H.-V. Nguyen, E. Andreassen, H. Kristiansen, and K.E. Aasmundtveit, *Die shear testing of a novel isotropic conductive adhesive-Epoxy filled with metal-coated polymer spheres,* IEEE Transactions on Components, Packaging and Manufacturing Technology, 2013, **3**(7): p. 1084-1093.
86. H. Kristiansen, M.M.V. Taklo, T. Bakke, J. Gakkestad, P. Dalsjø, R. Johannessen, F. Oldervoll, and H.V. Nguyen, *Development of low modulus conductive adhesive for MEMS interconnects*, 14th Pan Pacific Microelectronics Symposium and Tabletop Exhibition, (Kamuela, HI, United States, 2009), p. 306-310
87. H.-V. Nguyen, *Interconnection technologies based on metal-coated polymer spheres*, Ph.D. thesis, University of Oslo, Oslo, Norway, 2012.
88. S. Jain, *Isotropically conductive adhesive filled with silver metalised polymer spheres*, Ph.D. thesis, Loughborough University, Loughborough, UK, 2016.
89. H.-V. Nguyen, H. Kristiansen, J. Gakkestad, R. Johannessen, N. Hoivik, and K.E. Aasmundtveit, *Spherical polymer particles in isotropic conductive adhesives a study on rheology and mechanical aspects,* 3rd Electronic System Integration Technology Conference (ESTC), (Berlin, Germany, 2010), doi: 10.1109/ESTC.2010.5643022
90. H.-V. Nguyen, H. Kristiansen, R. Johannessen, E. Andreassen, A. Larsson, N. Hoivik, and K.E. Aasmundtveit, *Temperature Dependence of Mechanical Properties of Isotropic Conductive Adhesive Filled with Metal Coated Polymer Spheres,* IEEE 61th Electronic Components and Technology Conference (ECTC), (Lake Buena Vista, FL, United States, 2011), doi: 10.1109/ECTC.2011.5898580
91. H.-V. Nguyen, H. Kristiansen, R. Johannessen, E. Andreassen, N. Hoivik, and K.E. Aasmundtveit, *Isotropic conductive adhesive filled with metal-coated polymer spheres - Effects of metal coating on rheological and mechanical properties,* 4th Electronic System Integration Technology Conference (ESTC), (Amsterdam, Netherlands, 2012), doi: 10.1109/ESTC.2012.6542147
92. H.-V. Nguyen, E. Andreassen, H. Kristiansen, R. Johannessen, N. Hoivik, and K.E. Aasmundtveit, *Rheological characterization of a novel isotropic conductive adhesive – Epoxy filled with metal-coated polymer spheres,* Materials & Design, 2013, **46**(0): p. 784-793.
93. H.-V. Nguyen, J. He, T. Helland, H. Kristiansen, and K.E. Aasmundtveit, *Electrical characterization of individual metal-coated polymer spheres used in isotropic conductive adhesives,* Journal of Applied Polymer Science, 2016, **133**(31): p. 43764.
94. S. Jain, D.C. Whalley, M. Cottrill, H. Kristiansen, K. Redford, C.B. Nilsen, T. Helland, and C. Liu, *Electrical properties of an Isotropic Conductive Adhesive filled with silver coated polymer*

spheres, 18th European Microelectronics and Packaging Conference (EMPC), (Brighton, UK, 2011), p. 1-7

95. S. Jain, D.C. Whalley, M. Cottrill, T. Helland, H. Kristiansen, K. Redford, and C. Liu, *The effect of coating thickness on the electrical performance of novel isotropic conductive adhesives prepared using metallised polymer micro-spheres,* IEEE 63rd Electronic Components and Technology Conference (ECTC), (Las Vegas, NV, United States, 2013), doi: 10.1109/ECTC.2013.6575664

96. S. Jain, D.C. Whalley, M. Cottrill, H. Kristiansen, K. Redford, S. Helland, T. Helland, E. Kalland, and C. Liu, *Factors affecting conduction in novel isotropic conductive adhesives filled with silver coated polymer spheres*, 19th European Microelectronics Packaging Conference (EMPC), (Grenoble, France, 2013), p. 1-7

97. H.-V. Nguyen, K.E. Aasmundtveit, H. Kristiansen, and T. Helland, *An Overview of Isotropic Conductive Adhesives Filled with Metal-coated Polymer Spheres,* International Symposium on Microelectronics, 2013, **2013**(1): p. 000200-000207.

98. J. Gakkestad, P. Dalsjo, H. Kristiansen, R. Johannessen, and M.M.V. Taklo, *Use of conductive adhesive for MEMS interconnection in ammunition fuze applications,* Journal of Micro/Nanolithography, MEMS, and MOEMS, 2010, **9**(4): p. 041108-041108-10.

99. R.F. Hamou, P. Dalsjø, C. Dorum, S. Helland, H. Kristiansen, M.M.V. Taklo, and J. Gakkestad, *Numerical investigation of ceramic package/ interposer interconnects using isotropic conductive adhesive,* 16th International Conference on Thermal, Mechanical and Multi-Physics Simulation and Experiments in Microelectronics and Microsystems (EuroSimE), (Budapest, Hungary, 2015), doi: 10.1109/EuroSimE.2015.7103144

100. R. Holm, *Electric contacts: Theory and Application*. 4th ed. 1967, Berlin/Heidelberg/New York: Springer-Verlag.

101. G.R. Ruschau, S. Yoshikawa, and R.E. Newnham, *Resistivities of conductive composites,* Journal of Applied Physics, 1992, **72**(3): p. 953-959.

102. J. Gakkestad, L. Zhuo, T. Helland, and C.P. Wong, *Thermo-mechanical properties of Isotropic Conductive Adhesive filled with Metallized Polymer Spheres,* IEEE 15th Electronics Packaging Technology Conference (EPTC), (Singapore, 2013), doi: 10.1109/EPTC.2013.6745715

103. R. Zhang, K.-s. Moon, W. Lin, J.C. Agar, and C.-P. Wong, *A simple, low-cost approach to prepare flexible highly conductive polymer composites by in situ reduction of silver carboxylate for flexible electronic applications,* Composites Science and Technology, 2011, **71**(4): p. 528-534.

104. J.Y. He, Z.L. Zhang, and H. Kristiansen, *Mechanical properties of nanostructured polymer particles for anisotropic conductive adhesives,* International Journal of Materials Research, 2007, **98**(5): p. 389-392.

105. J.Y. He, Z.L. Zhang, M. Midttun, G. Fonnum, G.I. Modahl, H. Kristiansen, and K. Redford, *Size effect on mechanical properties of micron-sized PS-DVB polymer particles,* Polymer, 2008, **49**(18): p. 3993-3999.

106. J.Y. He, T. Helland, Z.L. Zhang, and H. Kristiansen, *Fracture of micrometre-sized Ni/Au coated polymer particles,* Journal of Physics D: Applied Physics, 2009, **42**(8): p. 085405.

107. J.Y. He, Z.L. Zhang, and H. Kristiansen, *Nanomechanical Characterization of Single Micron-Sized Polymer Particles,* Journal of Applied Polymer Science, 2009, **113**(3): p. 1398-1405.

108. J.Y. He, Z.L. Zhang, and H. Kristiansen, *Compression properties of individual micron-sized acrylic particles,* Materials Letters, 2009, **63**(20): p. 1696-1698.

109. J. He, T. Helland, Z. Zhang, and H. Kristiansen, *Cracking and delamination of nanoscale metal coating on composite polymer particles*, 18th European Conference on Fracture (ECF18), (Dresden, Germany, 2010), p. 1-8

110. J. He, Z. Zhang, and H. Kristiansen, *Deformation and Fracture of Crosslinked Polystyrene particles*, 19th European Conference on Fracture (ECF19), (Kazan, Russia, 2013), p. 1-9

111. J. He, Z. Zhang, H. Kristiansen, K. Redford, G. Fonnum, and G. Modahl, *Crosslinking effect on the deformation and fracture of monodisperse polystyrene-co-divinylbenzene particles,* Express Polymer Letters, 2013, **7**(4): p. 365-374.

112. J.C. Agar, K.J. Lin, R. Zhang, J. Durden, K. Lawrence, K.S. Moon, and C.P. Wong, *Deconstructing the myth of percolation in electrically conductive adhesives and its implications,* 60th Electronic Components and Technology Conference (ECTC), (Las Vegas, NV, United States, 2010), doi: 10.1109/ECTC.2010.5490742

Paper I

Electromechanical characterization of individual micron-sized metal coated sized polymer particles

Molly Bazilchuk, Sigurd R. Pettersen, Helge Kristiansen, Zhiliang Zhang, and Jianying He.

Journal of Applied Physics, 2016, **119**(24), 245

JOURNAL OF APPLIED PHYSICS **119**, 245102 (2016)

Electromechanical characterization of individual micron-sized metal coated polymer particles

Molly Bazilchuk,[1,2] Sigurd Rolland Pettersen,[1] Helge Kristiansen,[1,2] Zhiliang Zhang,[1] and Jianying He[1,a)]
[1]*Department of Structural Engineering, Norwegian University of Science and Technology, Trondheim 7491, Norway*
[2]*Conpart AS, Skjetten 2013, Norway*

(Received 15 March 2016; accepted 4 June 2016; published online 22 June 2016)

Micron-sized polymer particles with nanoscale metal coatings are essential in conductive adhesives for electronics assembly. The particles function in a compressed state in the adhesives. The link between mechanical properties and electrical conductivity is thus of the utmost importance in the formation of good electrical contact. A custom flat punch set-up based on nanoindentation has been developed to simultaneously deform and electrically probe individual particles. The set-up has a sufficiently low internal resistance to allow the measurement of sub-Ohm contact resistances. Additionally, the set-up can capture mechanical failure of the particles. Combining this data yields a fundamental understanding of contact behavior. We demonstrate that this method can clearly distinguish between particles of different sizes, with different thicknesses of metal coating, and different metallization schemes. The technique provides good repeatability and physical insight into the behavior of these particles that can guide adhesive design and the optimization of bonding processes. *Published by AIP Publishing.*
[http://dx.doi.org/10.1063/1.4954218]

I. INTRODUCTION

In electronic assembly, conductive adhesives are used in applications that require properties such as low assembly temperature, minimal mechanical stress, and fine pitch.[1] Conductive adhesives compete with lead-free solders as a non-toxic alternative to traditional solder.[2] Micron-sized polymer spheres (MPS) with nanoscale metal coatings are applied as the conductive component in conductive adhesives due to their low cost and superior mechanical characteristics.[1] Conductive adhesives may be either anisotropic or isotropic, and specific applications require different particle sizes, concentrations, and metallization schemes.[2]

In an anisotropic conductive adhesive (ACA), an adhesive film containing conductive particles is compressed between two electrical components. The MPS are deformed under compression, forming contact surfaces against the electrical components. The size and nature of these contact surfaces have a significant effect on the resulting contact resistance. At higher compressive strains, the metal coating, and eventually the particle core, will fracture. Fracture can interrupt the contact and cause increased resistance and decreased long-term performance.[3] The conductive characteristics of the adhesive are therefore strongly linked to the mechanical behavior of MPS under compression, and it is of great interest to find the optimal deformation range where the electrical contact resistance reaches a minimum while still being stable under fatigue.

As a spherical particle is compressed between two rigid plates, the particle expands laterally and the contact area between the particle and the plates increases nonlinearly. Both theoretical and experimental studies of the mechanical properties of individual polymer particles and MPS have been performed. Several models have been proposed to explain the deformation and fracture of particles, incorporating finite element analysis,[4] molecular dynamics simulation,[5] and analytical modeling.[6] Mechanical characterization of individual polymer particles and MPS have been performed by He *et al.* using a custom nanoindentation set-up with a flat punch.[7] The influence of factors such as particle size,[8] polymer cross-linking density,[9] loading rate,[10] and chemical composition on the mechanical behavior has been quantified. Furthermore, the fracture behavior of MPS has been studied.[11] The present work therefore emphasizes the correlation between mechanical behavior and electrical resistance in MPS rather than a detailed analysis of mechanical characteristics.

We shall consider the electrical resistance of the MPS under compression as being the sum of a shell resistance and a contact resistance, as illustrated in Fig. 1. The contact resistance is the resistance experienced by current passing through the area of the particle that is in contact with the object compressing the body. The shell resistance is the resistance due to current passing through the unconstricted areas of metal coating

The contact resistance may be seen as the sum of a constriction term and an interface resistance term. Constriction resistance stems from the geometrical constriction of the current at the interface, essentially a bottleneck of the current. Interface resistance comes from higher resistivity layers that form barriers at the interface, such as oxides.[12] As a rule, contact resistance decreases with increasing contact area.

[a)]Author to whom correspondence should be addressed. Electronic mail: jianying.he@ntnu.no

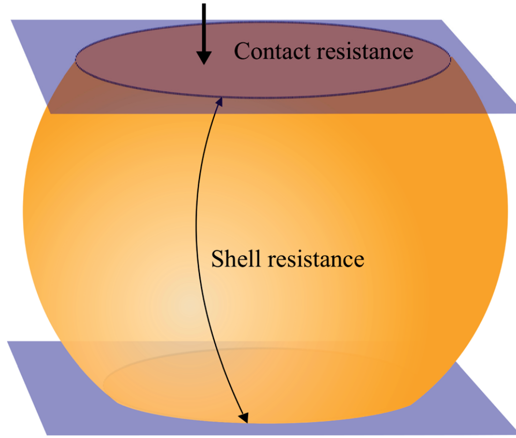

FIG. 1. The resistance of an MPS is the sum of the shell resistance and the contact resistances at either interface.

At the early stages of particle compression, the contact area between the particle and the compressive body is very small, which causes constriction resistance.[13] Furthermore, the true contact area is made up of spots where nanoscale asperities in the contacting bodies meet. Since the true contact is formed in these asperities, the constriction resistance is always larger than the apparent contact area suggests. The shape and distribution of asperities on the surface of the metal coating are unknown, as is their mechanical behavior during the compression of the particle. Additionally, although constriction resistance at semi-infinite (i.e., bulk) metal interfaces has been described analytically,[14] thin metal films will deviate considerably from this theory.[15]

The shell resistance of a single particle depends on the coating thickness t and resistivity ρ, as well as the nominal strain $\varepsilon = \frac{\delta}{D}$, where δ is the deformation and D is the undeformed particle diameter. Määttanen developed an expression for the shell resistance by integrating over the metallic cross-section area of the deformed sphere.[16] The principle assumptions made in this model are that $t \ll D$, where the metal coating is uniform and homogeneous, and the area of the metal coating is constant, i.e., the coating does not crack during compression. It is nonetheless a good first approximation of the shell resistance. Using this model, the expression for the shell resistance is as follows:

$$R_{shell} = \frac{\rho}{\pi t} \ln \tan \frac{\pi}{4}(2 - \varepsilon). \quad (1)$$

Although the current-carrying length through the metal coating increases with particle size, so does the cross-sectional area of the coating. For a given thickness, the increase in resistive length and cross-sectional area cancel each other out and the shell resistance is found to be independent of particle size.

Other attempts to calculate the shell resistance take into account more complex deformation mechanisms, often using a finite element approach.[1] However, none of the previous work has compared the results with the measurements on individual particles, and all predict much lower resistance values than those measured in bulk conductive adhesives.[17] Analyzing the resistance of individual MPS under compression can yield a fundamental understanding that will facilitate the tailoring of particles and the bonding process for electronics assembly.

The body of literature on anisotropic conductive adhesives (ACA) pertaining to electrical resistance focuses on the resistance of bonded ACA joints. This implies many particles in parallel, as in Refs. 17–21. Few attempts have been made to measure the deformation resistance characteristics of single particles. Both Dou *et al.*[22] and Shih *et al.*[23] have reported electromechanical measurements on the ACA particles, but the magnitude of the resistance measurements is such that we may infer a large parasitic resistance skewing the results. Additionally, large particle-to-particle variations lead us to question the accuracy and repeatability of the measurement procedure. In this work, the electromechanical behavior of several MPS is explored by a custom flat punch nanoindentation technique.

II. EXPERIMENTAL

Ten and thirty micron Spherica™ MPS with silver coatings in a variety of thicknesses as well as a gold/nickel bilayer coating were provided by Conpart AS (Skjetten, Norway). The polymer cores are fabricated using the Ugelstad method,[24] and coated using electroless plating. The 10 μm cores (CV = 1.1%, where CV is the coefficient of variation) are made of styrene with a moderate cross-linking density of 20%, and exhibit viscoelastic behavior.[9] The 30 μm cores (CV < 5%) are made of PMMA, with a low cross-linking density of 1%, giving them an elastic-plastic mechanical behavior. Each type of particle will be referred to as follows: 10–100Ag, where the first number is the polymer core diameter in micrometers, the second the coating thickness in nanometers, and the final letters indicate the metallization of the coating. Table I summarizes the particles examined in this work.

During sample preparation, dry particles were suspended in micro-filtered ethanol and dispersed using an ultrasonic bath. Samples consisting of several hundred individual particles of a given type were created by placing a drop of the ethanol-particle solution onto substrates consisting of a silicon wafer sputter-coated with 1 μm of gold and cut into 1.5 × 1.5 cm squares. Two copper wires were glued to the opposing sides of the gold-coated silicon square using isotropic conductive adhesive (ICA). Short-circuit resistance

TABLE I. The different particle types measured in this work.

Particle diameter (μm)	Core chemistry	Coating thickness(es) (nm)	Coating metallization
10	Styrene, cross-linking density 20%	35, 50, 70, 100, 140, 200	Ag
10	Styrene, cross-linking density 20%	120 Ni + 30 Au	Ni/Au
30	PMMA, cross-linking density 1%	60, 100, 150, 270	Ag

measurements between the copper wires confirmed good contact between the gold film and ICA.

The Hysitron Triboindenter 950 (Minneapolis, USA) is a commercially available nanoindentation system that operates in load-controlled mode with a force resolution <2 nN. The nanoscale electrical contact resistance tool, abbreviated nanoECR, is an additional module that allows precise, correlated electrical and mechanical indentation measurements. Current or voltage can be sourced and measured across a conductive nanoindentation tip, sample, and conductive stage during selected segments of the indentation cycle. The nanoECR module has been previously used in a high-resolution application to investigate an electrical current spike associated with nanoscale plasticity in gallium arsenide.[25]

The commercial nanoECR set-up was designed to measure relatively high resistances in semiconductor samples, and has been modified to facilitate the measurement of sub-Ohm resistances occurring in individual MPS. The aforementioned custom conductive substrates were connected directly to the current and voltage leads in the Triboindenter, bypassing the nanoECR stage. Fig. 2 shows a schematic of the electromechanical measurements performed.

In the work of He *et al.*,[6–10] a diamond flat punch was used to indent single particles. In this work, the indenter was required to be highly conductive in addition to hard, and thus a tungsten carbide flat punch with a diameter of 50 μm fabricated by Synton-MDP (Nidau, Switzerland) was employed.

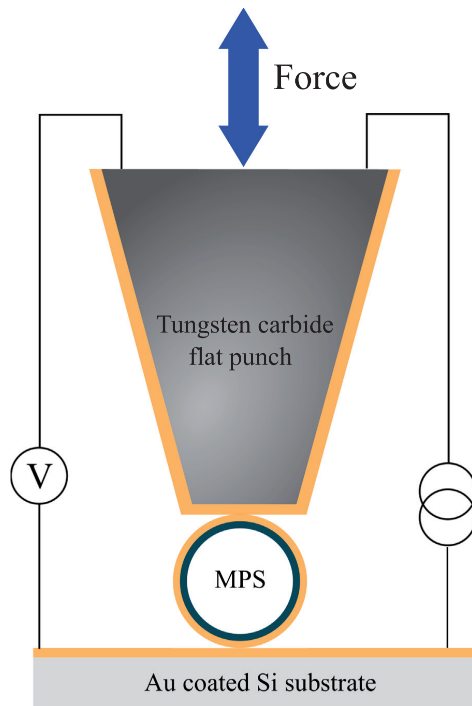

FIG. 2. A schematic showing the principle of the electromechanical measurements conducted in this study.

The tip was dry etched in argon plasma and subsequently sputter-coated with 150 nm of gold in order to maintain a highly conductive surface. Before performing measurements, tip planarity was verified by indenting on a planar indium sample, and low resistance confirmed by performing test indents directly on the gold-coated silicon substrate.

Isolated single particles, at least 50 μm from any neighboring particles, were identified using the optical microscope in the Triboindenter. To remove the influence of the lead resistance, measurements were conducted in 4-wire mode, with the wires connected as shown in Fig. 2. Resistance was obtained by dividing the measured voltage by the sourced current value. To test for Ohmic behavior, measurements including current sweeps were performed on several occasions. These measurements confirmed the linearity of the resistance characteristics within the relevant, albeit small, voltage range.

Due to the placement of the current and voltage wires on the substrate as shown in Fig. 2, the measurement encompassed the indentation tip, the MPS, and part of the substrate. The measured resistance was thus comprised of a series of resistances,

$$R_{measured} = R_{tip} + R_{contact\,tip-MPS} + R_{shell} + R_{contact\,MPS-substrate} + R_{substrate}. \qquad (2)$$

The true resistance of the MPS, or the shell and contact resistances, will be always smaller than the measured resistance, although the highly conductive probe and substrate reduce parasitic resistances. The resistance contributions from the probe R_{tip} and substrate $R_{substrate}$ have been considered to be independent of particle deformation, although in reality there is a contact resistance at their interfaces for which this is not entirely the case.

All electrical measurements were conducted with a sourced current of 1 mA, selected because it was large enough to give a good signal but small enough to avoid sufficient heating to alter the mechanical behavior of the particles. The current was switched on 0.2 s after the initial contact was achieved, as shown in Fig. 3, in order to ensure sufficient thermal contact before the electrical measurement was initiated. The mechanical indentation data of several types of particles with and without applied current were compared, and it was confirmed that any Joule heating did not visibly alter the mechanical results.

In all measurements, force was applied at a constant rate of 2 mN/s, up to a maximum of 12 mN, as shown in Fig. 3. This maximum force value was limited by the Triboindenter equipment. The maximum force was then held for 2 s before being released at the same rate. The resulting mechanical deformation of the particles was monitored continuously throughout the loading cycle.

III. RESULTS AND DISCUSSION

A. Representative electromechanical behavior

Fig. 4 shows the result of a typical electromechanical measurement for a 10–100Ag particle. The measured

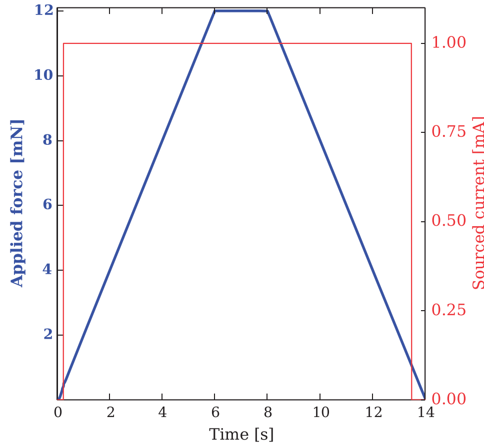

FIG. 3. The representative load and current function for the electromechanical measurements performed on MPS.

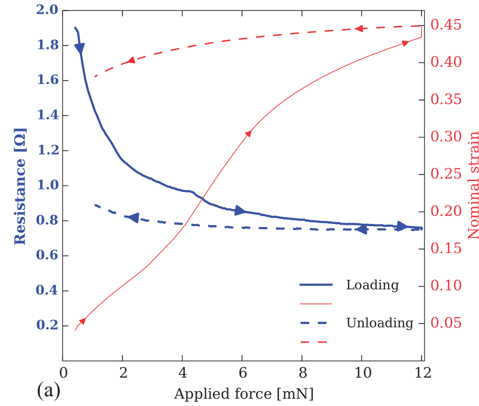

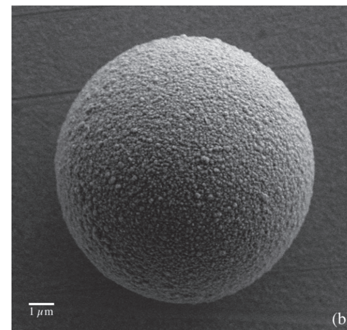

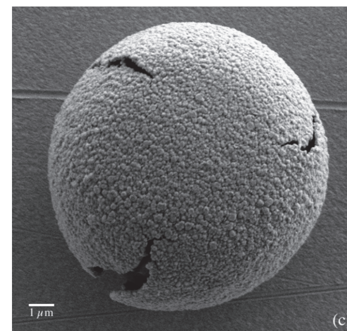

FIG. 4. Representative electromechanical results for particle type 10-100Ag (a), where the deformation and resistance have been monitored as a function of the applied force. Arrows denote the direction of the measurement in time. Micrographs showing a particle before (b) and after (c) compression.

resistance depends strongly on the applied force, indicating that the resistance of the MPS is significant in the measurement. Excluding Fig. 4, all the results presented in this work reflect statistical averages of 8–10 particles where the error bars represent the standard deviation. This contributes to verifying the uniformity and repeatability of the results.

In Fig. 4, the measured resistance can be seen to decrease rapidly during the initial stages of loading, and level off for large applied forces. As the particle is compressed, the contact area at the particle interfaces increases while the current-carrying length through the coating decreases. The decrease in resistance can be attributed to a combination of these changes.

At the rate the particle is unloaded, the core does not have sufficient time for viscoelastic recovery, so the measurement ends at a high strain of 40%. However, the measured resistance increases gradually during unloading. This indicates an elastic rebound, causing the tip to remain in contact during unloading, rather than an abrupt loss of contact as would be expected if the particle were permanently deformed.

B. Effect of particle size

Fig. 5 shows a comparison of the resistance-strain behavior of 30–100Ag and 10–100Ag. The MPS differ both in size and core material, but the coatings are the same thickness and material. The measurements for 30–100Ag stop at a much lower strain than 10–100Ag because the same force produces a lower strain in the larger particles, and the largest available force is only enough to produce around 5% strain.

The Määttanen model for the shell resistance as described by Eq. (1) predicts that the resistance of metal coating is independent of the particle size, depending only on the strain, coating thickness, and resistivity. We therefore consider the R_{shell} contribution in Eq. (2) to be equal for 30–100Ag and 10–100Ag at a given strain. The discrepancies between the two curves can therefore be attributed to the contact resistance contributions in Eq. (2), $R_{contact\,tip-MPS}$ and $R_{contact\,MPS-substrate}$ both of which depend on the contact area. Since the contact area increases radially and thus scales with the square of the particle size, it increases more rapidly in 30–100Ag, yielding the lower resistances observed at small strains.

The standard deviation of the resistance at a given strain is indicated by the error bars in Fig. 4, and represents the particle-to-particle variability of the measurement. Uniform resistance characteristics in MPS are desirable because they

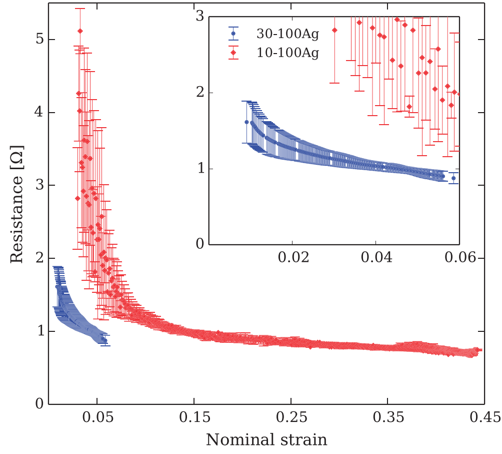

FIG. 5. The resistance-strain characteristics of 30-100Ag and 10-100Ag. The inset is a close-up of the 30-100 Ag curve.

give an adhesive with predictable behavior. The low particle-to-particle variability at high strain confirms the stability and repeatability of the measurements. At 40% strain, the particle-to-particle variability of 10–100Ag is 6%. By comparison, particle-to-particle variability measured by Dou *et al.* was 35% at 40% strain.[22]

As indicated by the error bars in Fig. 5, the particle-to-particle variability in the resistance is largest during the initial stages of deformation. This can be attributed to the nanoscopic asperities in the coating, the distribution of which varies from particle to particle. At higher strains, the behavior becomes more uniform. At this point, the contact area has grown large enough for the contact resistance to have a negligible contribution to the measured resistance. The measured resistance is then governed by coating resistivity and thickness, which are relatively uniform for particles from the same batch.

C. Effect of coating thickness

The effect of coating thickness on the resistance characteristics has been analyzed for the 10-XXAg and 30-XXAg series by comparing the particles at the highest available applied strain, in order to minimize the contribution of contact resistance, which is largest at low strains. Ten micron particles with different coating thicknesses have been compared at 40% strain and 30 μm particles at 5% strain, again limited by the maximum available force.

As shown in Eq. (1), the coating thickness is expected to be inversely proportional to the shell resistance. To evaluate the effect of the coating thickness, R_{tip}, $R_{contact\,tip-MPS}$, $R_{contact\,MPS-substrate}$, and $R_{substrate}$ are all assumed to be independent of thickness and constant for a given strain. These contributions are lumped into a constant resistance R_{cst}. According to Eq. (2), the remaining resistance contribution is the shell resistance. The measured resistance may be expressed by the following equation:

$$R = \frac{c}{t} + R_{cst}, \qquad (3)$$

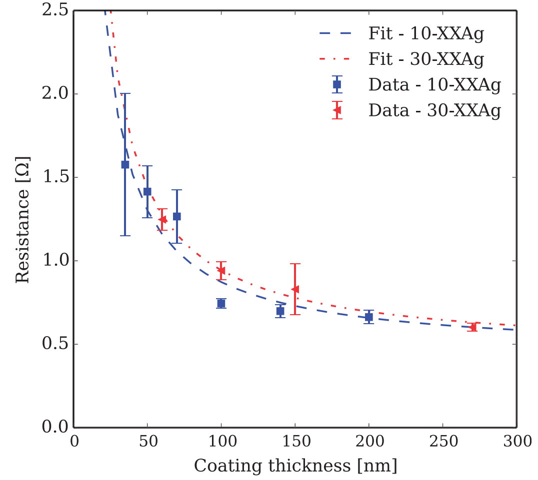

FIG. 6. The average resistance at 10 mN applied force for 10 and 30 μm particles with different coating thicknesses. The resistances are taken at 40% and 5% strain, respectively. The curves have been fit to Eq. (3).

where t is the coating thickness and c is the fitting constant. Fig. 6 shows 10-AgXX and 30-AgXX fit to Eq. (3).

In order to equate the fit parameter to a meaningful value, we will assume that the shell resistance follows Eq. (1). The strain ε is well-known due to the high resolution of the nanoindenter system. The conductivity ρ, however, may deviate from the bulk value $\rho_{Ag} = 1.59 \times 10^{-8}\,\Omega\,\mathrm{m}$[26] and the coating thickness t is a nominal, not measured, value. We thus multiply Eq. (1) with an ideality factor m which describes how the ratio between ρ and t deviates from the ideal case. By equating Eq. (1) to the thickness-dependent term in Eq. (3) and rearranging, we find an expression for the ideality factor

$$m = \frac{c\,\pi}{\rho_{Ag} \ln \tan \frac{\pi}{4}(2-\varepsilon)}. \qquad (4)$$

Table II summarizes the fitting parameters and calculates the ideality factors for each case.

The ideality factor m is larger than unity for both sets of particles. This could indicate either that the coatings are thinner than their nominal value or that the resistivity is higher than that of bulk silver. The resistivity of thin metal films is known to deviate from the bulk resistivity values.[27] This effect is significant when the film thickness or grain size approaches the electron mean free path (EMFP), which is 52 nm for bulk silver.[26] However, surface and grain boundary scattering limited resistivity can only account for a

TABLE II. The fitting parameters used to fit Eq. (3) to the curves in Fig. 6, and the ideality factor m as expressed by Eq. (4).

Particle group	R_{cst} (Ω)	c (Ω nm)	m
10-XXAg	0.44	43.0	7.6
30-XXAg	0.45	49.6	3.0

twofold increase of the resistivity at room temperature.[26] Therefore, other non-idealities must also be considered.

Larger than ideal resistivity could also stem from impurities in the coating due to chemicals used in the coating process or coating roughness which would cause "bottlenecks" in the current flow. It is likely that the non-ideal behavior of the coatings is due to a combination of impurities in the coating, unevenness and surface and grain boundary scattering limited resistivity. The decoupling of these contributions requires further investigation.

Figs. 7(a) and 7(b) show the effect of the coating thickness on the particle-to-particle variability of the resistance characteristics, which can be observed to decrease with increasing coating thickness. The thinner the coating, the more impact uneven areas in the coating will have on the shell resistance, through the creation of bottlenecks in thin areas of the coating. The most uniform behavior is consistently observed in the thickest metal coatings. The variability is largest during the early stages of the deformation (most clearly illustrated by 10–35Ag in Fig. 7), as has previously been discussed for Fig. 4.

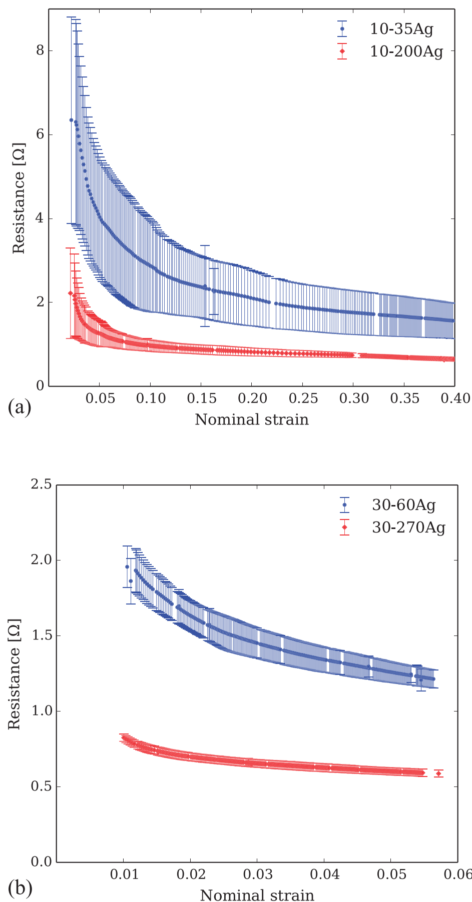

FIG. 7. A comparison of the average resistance-strain characteristics of (a) 10-35Ag and 10-200Ag; and (b) 30-60Ag and 30-270Ag, where the error bars represent the particle to particle variability.

D. Effect of metallization

The effect of the metallization scheme was compared using 10–140Ag and 10–120Ni/30Au, which have the same polymer core and comparable metal coating thicknesses. Figure 8 shows the mechanical behavior, while Fig. 9 compares the resistance-strain characteristics. The nominal stress is given by $\sigma = \frac{F}{\pi(0.5\times D)^2}$, where F is the applied force, while the nominal strain, as previously mentioned, is found by $\varepsilon = \frac{\delta}{D}$.

Mechanically, the nickel-gold system is more brittle than the silver system. In Fig. 8, we can clearly see that 10–120Ni/30Au is stiffer than 10–140Ag initially, due to the mechanical stiffness of nickel. At a strain of approximately 0.2, a pop-in or displacement burst occurs. Since the measurement is load controlled, a sudden movement of the sample causes a displacement burst and an apparent gap in the data. Pop-ins have previously been demonstrated to be indicative of brittle fracture of the metal coating.[10] The particle-to-particle variability is largest in the pop-in region, due to variations in exactly when the pop-in occurs. After the pop-in, the stiffness of the system is decreased, since the coating has been significantly weakened by cracking. In contrast, 10–140Ag exhibits a continuous stress-strain behavior with no pop-ins. The silver coating is ductile, and fractures gradually rather than abruptly. Although the coating is a relatively small part of the particle, it clearly contributes significantly to the mechanical strength of the particles.

Fig. 9 shows the effect of the metallization on the electromechanical behavior. Initially, the high particle-to-particle variability renders the particles virtually indistinguishable. At high strains, the resistance of 10–140Ag converges to a significantly lower value than 10–120Ni/30Au. This follows the expectation based on bulk silver, where the resistivity is lower

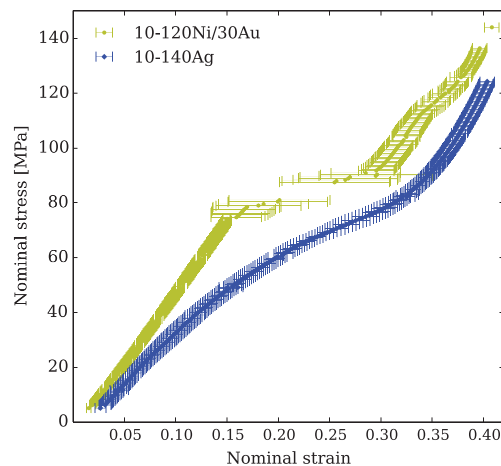

FIG. 8. A comparison of the stress-strain characteristics of 10-140Ag and 10-120Ni/30Au.

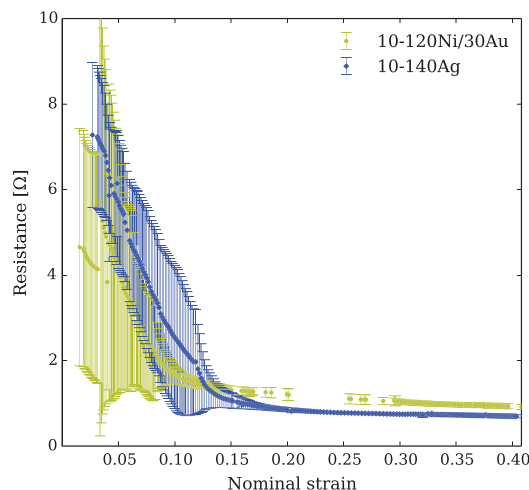

FIG. 9. A comparison of the average resistance-strain characteristics of 10-140Ag and 10-120Ni/30Au.

than that of both bulk nickel and gold. These measurements demonstrate that the set-up is sensitive enough to distinguish between coatings of different materials but similar thicknesses.

Again, a pop-in can be observed in the 10–120Ni/30Au curve, indicating brittle fracture of the metal coating. The gradient of the resistance-strain curve is not visibly affected by the pop-in, suggesting that cracking occurs parallel to the direction of applied force rather than circumferentially. Longitudinal fracture has previously been observed in the Ni/Au system,[11] and a similar fracture pattern is confirmed by SEM images of the Ag system after compression, as shown in Fig. 4(c).

IV. CONCLUSION

Our flat-punch electromechanical nanoindentation technique has been used to measure individual MPS. The measurements are repeatable and precise, and can be used to clearly distinguish different MPS. By studying resistance as a function of strain, we can easily locate the range where the contact resistance has converged to a semi-constant, negligible value, which is useful in the context of the conductive adhesive application. For 10 μm particles, it is observed that the gains in resistance are minimal once the strain passes 15%. Thirty micron particles achieve low resistance values at an earlier stage of deformation.

The measured resistance displays an inverse proportional relationship to the particle coating thickness as expected. The decrease in resistance is therefore most significant when increasing thicknesses up to 100 nm, after which the gains are much smaller. The effect of the metallization scheme on the resistance follows the trends in bulk resistivity of the metallization scheme. However, the mechanical behavior is affected significantly by the metallization of the coating. Both the mechanical behavior and the particle resistance can thus be tuned by changing the metallization and coating thickness.

The measured resistance is a sum of several contributions which cannot be decoupled using this method alone; however, it gives good indications of the relative conductivity of different MPS, and an upper limit of the resistance of single MPS, which has not previously been measured at this level of detail.

ACKNOWLEDGMENTS

The Research Council of Norway provided funding through Projects No. 228453—“Novel Particle Technology for Display Interconnect” and 225962—“Novel Conductive Adhesive Technology for Solar Industry.” Partial funding has also been obtained from the Programme FP7-NMP-2013-LARGE-7 under Grant Agreement No. 604668 (“Quantiheat”) and by funding from the European Union Seventh Framework Programme (FP7/2007-2013) under Grant Agreement No. FP7-NMP- 310420 (“HyperConnect”).

[1]Y. C. Lin and J. Zhong, “A review of the influencing factors on anisotropic conductive adhesives joining technology in electrical applications,” J. Mater. Sci. **43**(9), 3072–3093 (2008).
[2]Y. Li and C. P. Wong, “Recent advances of conductive adhesives as a lead-free alternative in electronic packaging: Materials, processing, reliability and applications,” Mater. Sci. Eng. R **51**(1–3), 1–35 (2006).
[3]Y. Chan and D. Luk, “Effects of bonding parameters on the reliability performance of anisotropic conductive adhesive interconnects for flip-chip-on-flex packages assembly II. Different bonding pressure,” Microelectron. Reliab. **42**(8), 1195–1204 (2002).
[4]Z. L. Zhang, H. Kristiansen, and J. Liu, “A method for determining elastic properties of micron-sized polymer particles by using flat punch test,” Comput. Mater. Sci. **39**(2), 305–314 (2007).
[5]J. Wu, S. Nagao, Z. Zhang, and J. He, “Deformation and fracture of nano-sized metal-coated polymer particles: A molecular dynamics study,” Eng. Fract. Mech. **150**, 209–221 (2015).
[6]J. Paul, S. Romeis, J. Tomas, and W. Peukert, “A review of models for single particle compression and their application to silica microspheres,” Adv. Powder Technol. **25**(1), 136–153 (2014).
[7]J. Y. He, Z. L. Zhang, and H. Kristiansen, “Nanomechanical characterization of single micron-size polymer particles,” J. Appl. Polym. Sci. **113**(3), 1398–1405 (2009).
[8]J. Y. He, Z. L. Zhang, M. Midttun, G. Fonnum, G. I. Modahl, H. Kristiansen, and K. Redford, “Size effect on mechanical properties of micron-sized PS–DVB polymer particles,” Polymer **49**(18), 3993–3999 (2008).
[9]J. Y. He, Z. L. Zhang, H. Kristiansen, K. Redford, G. Fonnum, and G. I. Modahl, “Crosslinking effect on the deformation and fracture of monodisperse polystyrene-co-divinylbenzene particles,” Express Polym. Lett. **7**(4), 365–374 (2013).
[10]J. Y. He, S. Nagao, H. Kristiansen, and Z. L. Zhang, “Loading rate effects on the fracture of Ni/Au nano-coated acrylic particles,” Express Polym. Lett. **6**(3), 198–203 (2012).
[11]J. Y. He, T. Helland, Z. L. Zhang, and H. Kristiansen, “Fracture of micrometre-sized Ni/Au coated polymer particles,” J. Phys. D: Appl. Phys. **42**(8), 085405 (2009).
[12]R. S. Timsit, “Electrical contact resistance: Fundamental principles,” in *Electrical Contacts: Principles and Applications*, edited by P. G. Slade (CRC Press, 2014), pp. 3–111.
[13]J. H. Constable, “Analysis of ACF contact resistance,” in *IPACK03*, 2003, pp. 1–8.
[14]J. A. Greenwood, “Constriction resistance and the real area of contact,” Br. J. Appl. Phys. **17**(12), 1621–1632 (1966).
[15]R. S. Timsit, “Constriction resistance of thin film contacts,” IEEE Trans. Compon. Packag. Technol. **33**(3), 636–642 (2010).
[16]J. Määttänen, “Contact resistance of metal-coated polymer particles used in anisotropically conductive adhesives,” Soldering Surf. MountTechnol. **15**(1), 12–15 (2003).

[17]M. Chin, K. A. Iyer, and S. J. Hu, "Prediction of electrical contact resistance for anisotropic conductive adhesive assemblies," IEEE Trans. Compon. Packag. Technol. **27**(2), 317–326 (2004).
[18]M. J. Yim and K. W. Paik, "The contact resistance and reliability of anisotropically conductive film (ACF)," IEEE Trans. Adv. Packag. **22**(2), 166–173 (1999).
[19]M. A. Uddin, M. O. Alam, Y. C. Chan, and H. P. Chan, "Adhesion strength and contact resistance of flip chip on flex packages—effect of curing degree of anisotropic conductive film," Microelectron. Reliab. **44**(3), 505–514 (2004).
[20]C. K. Chung and K. W. Paik, "Effects of the degree of cure on the electrical and mechanical behavior of anisotropic conductive films," J. Electron. Mater. **39**(4), 410–418 (2010).
[21]C. K. Chung, G. D. Sim, S. B. Lee, and K. W. Paik, "Effects of conductive particles on the electrical stability and reliability of anisotropic conductive film chip-on-board interconnections," IEEE Trans. Compon., Packag., Manuf. Technol. **2**(3), 359–366 (2012).
[22]G. Dou, D. Whalley, and C. Liu, "Mechanical and electrical characterisation of individual ACA conductor particles," in *2006 International Conference on Electronic Materials and Packaging* (2006), pp. 1–9.
[23]C. Shih, K. Chen, and H. Li, "Mechanical and electrical properties investigation of micro-size single metal-coated polymer particle," in *ICEP-IAAC 2015 Proceedings* (2015), pp. 527–531.
[24]J. Ugelstad, A. Berge, T. Ellingsen, R. Schmid, T.-N. Nilsen, P. C. Mørk, P. Stenstad, E. Hornes, and Ø. Olsvik, "Preparation and application of new monosized polymer particles," Prog. Polym. Sci. **17**(1), 87–161 (1992).
[25]R. Nowak, D. Chrobak, S. Nagao, D. Vodnick, M. Berg, A. Tukiainen, and M. Pessa, "An electric current spike linked to nanoscale plasticity," Nat. Nanotechnol. **4**(5), 287–291 (2009).
[26]W. Zhang, S. H. Brongersma, O. Richard, B. Brijs, R. Palmans, L. Froyen, and K. Maex, "Influence of the electron mean free path on the resistivity of thin metal films," Microelectron. Eng. **76**(1–4), 146–152 (2004).
[27]D. C. Larson and B. T. Boiko, "Electrical resistivity of thin epitaxially grown silver films," Appl. Phys. Lett. **5**(8), 155–156 (1964).

Paper II

Electrical four-point probing of spherical metallic thin films coated onto micron sized polymer particles

Sigurd R. Pettersen, August Emil Stokkeland, Helge Kristiansen, John Njagi, Keith Redford, Dan V. Goia, Zhiliang Zhang, and Jianying He.

Applied Physics Letters, 2016, **109**(4), 043103

Electrical four-point probing of spherical metallic thin films coated onto micron sized polymer particles

Sigurd R. Pettersen,[1,a)] August Emil Stokkeland,[1] Helge Kristiansen,[1,2] John Njagi,[3] Keith Redford,[2] Dan V. Goia,[3] Zhiliang Zhang,[1] and Jianying He[1,a)]

[1]*NTNU Nanomechanical Lab, Department of Structural Engineering, Norwegian University of Science and Technology (NTNU), NO-7491 Trondheim, Norway*
[2]*Conpart AS, Dragonveien 54, NO-2013 Skjetten, Norway*
[3]*Center for Advanced Materials Processing, Clarkson University, Potsdam, New York 13699-5814, USA*

(Received 23 May 2016; accepted 7 July 2016; published online 25 July 2016)

Micron-sized metal-coated polymer spheres are frequently used as filler particles in conductive composites for electronic interconnects. However, the intrinsic electrical resistivity of the spherical thin films has not been attainable due to deficiency in methods that eliminate the effect of contact resistance. In this work, a four-point probing method using vacuum compatible piezo-actuated micro robots was developed to directly investigate the electric properties of individual silver-coated spheres under real-time observation in a scanning electron microscope. Poly(methyl methacrylate) spheres with a diameter of 30 μm and four different film thicknesses (270 nm, 150 nm, 100 nm, and 60 nm) were investigated. By multiplying the experimental results with geometrical correction factors obtained using finite element models, the resistivities of the thin films were estimated for the four thicknesses. These were higher than the resistivity of bulk silver. *Published by AIP Publishing.* [http://dx.doi.org/10.1063/1.4959783]

Metal-coated micron-sized polymer spheres (MPS) have long been used as conductive fillers in anisotropic conductive adhesives/films (ACA/ACF) for electronic interconnects,[1] and have recently been presented as a promising alternative to silver flakes in isotropic conductive adhesives (ICAs).[2] The conductivity of these composite materials stems from electrical contacts between the metal films of the particles and the interfaces of the electronic joint. The isotropic conductivity of ICAs is due to inter-particle contacts caused by a much larger volume fraction of particles than that of ACAs.

The bulk electrical resistivity of a conductive composite with a uniform cross-sectional area is easily estimated from the measured bulk resistance, but the electrical properties of the individual filler particles are difficult to investigate. In an ACA assembly wherein individual particles are compressed between the chip and substrate, contact resistance to the contact pads contributes significantly to the measured resistance. Several models have been made to estimate the contact resistances and bulk resistivities of both ACA assemblies[1] and high filler fraction conductive composites,[3] but these all require that the intrinsic resistivity of the conductive filler material is given. The intrinsic resistivity of a flat metallic thin film may deviate from that of the bulk metal. Scattering of electrons at the film surface will become significant as the film thickness approaches the electron mean free path length (EMFP) of the bulk metal,[4] which for silver is 52 nm.[5] If the grain sizes of polycrystalline films are in the same range as the EMFP, electron scattering at the grain boundaries will occur more frequently and increase the resistivity.[6,7] Higher surface roughness in the films will increase the scattering of electrons and can increase film resistivity further.[8] Higher level of impurities[9] and increased porosity[10] may also raise the resistivity, and especially for chemically deposited films, these factors may be a concern. Although these effects occur also in spherical thin films, methods for investigating this have been lacking.

Four-point measurements is a well-known method for investigating the resistivity of flat thin films,[11] but have not been reported for measurements on spherical shell structures such as the metallic thin films of MPS. In this work, four-point measurements were performed directly on individual silver-coated polymer spheres (AgPS) using four separately controlled piezo-actuated micro robots (miBot™ BT-11-VP on a miBase BS-43-VP stage, Imina Technologies, Switzerland), equipped with sharp tungsten (W) probes and connected to an Agilent B2909A Precision Source/Measure Unit (SMU). These micro robots have recently been used to simultaneously apply bending tension and voltage across individual silicon microwires,[12] showing their versatility and positioning resolution. Current (I) was sourced between the outer pair of probes (*source* probes), and the voltage drop (U) along the surface due to resistance in the film was picked up by the inner pair of probes (*sense* probes). The measurements were conducted in a dual beam focused ion beam/scanning electron microscope (FIB/SEM) instrument (FEI Helios NanoLab DualBeam), wherein SEM was used to monitor the movement of the probes in real time. More details can be found in our previous study,[13] as well as in the supplementary material. To provide repeatable apparent contact areas for the probes and decrease the current density at the *source* contacts, the end of the probes were milled to a flat punch geometry approximately 2.5 μm in diameter using FIB. AgPS comprised of poly(methyl methacrylate) (PMMA) spheres with a nominal diameter of 30 μm and nominal silver film thicknesses of 60 nm, 100 nm, 150 nm,

a)Authors to whom correspondence should be addressed. Electronic addresses: sigurd.r.pettersen@ntnu.no and jianying.he@ntnu.no

and 270 nm were provided by Mosaic Solutions AS (Skjetten, Norway). The silver films were coated onto the polymer cores by electroless plating, and the nominal film thicknesses were estimated from the amount of silver used in the plating process. Seven consecutive bi-directional four-point voltage sweeps (0 V → −0.2 mV → 0.2 mV → 0 V) were performed on each measured particle without moving the miBots and an average linear *U*/*I* slope was calculated for each measured particle. To compare the real film thicknesses with the nominal values, cross-sections were made with FIB at an incident angle normal to the film surface. Crystallographic data of the silver films were acquired with a Bruker-AXS D8 Focus X-ray diffractometer (XRD). The crystallite sizes were estimated using Scherrer's equation.[14]

In the four-point procedure, the current density is higher closer to the *source* probes, setting up an inhomogeneous electrical field with a distribution dependent on the *source* probe positions. The voltage drop picked up by the *sense* probes is dependent on the positions of the *sense* probes in the field, and the corresponding *U*/*I* value is thus a function of all four probe positions. The electrical resistivity of the film is estimated by multiplying the measured *U*/*I* value with a correction factor that accounts for specimen shape and probe positions.[11] In this work, the positioning of the probes could be accurately controlled by the miBots with a step-size <100 nm, but there were still variations in probe positions from particle to particle, so a geometric correction factor had to be calculated separately for each measured AgPS. Analytical solutions would only be possible if the *source* probes were placed exactly 180° apart. Finite element (FE) simulations were therefore conducted using the Electric Current (ec) interface of the AC/DC module of COMSOL Multiphysics 5.0. For each measured AgPS, probe positions relative to particle size were acquired from the SEM images and translated into the model using a parameterized geometry and spherical coordinates. Each AgPS-model was built as a homogeneous, fully spherical shell with thickness equal to the nominal film thickness. The probes were simulated as the top surface areas of spherical caps, with sizes approximated from the SEM images. A static voltage field was applied by setting the *source* probes as equipotential surface terminals with different potentials, and the resulting total current I_{FE} was obtained. U_{FE} was calculated by averaging the scalar voltage values at each of the *sense* probes and taking the difference between these.

The FE model solves a current conservation equation based on Ohm's law with the scalar electric potential as the dependent variable. The calculated U/I_{FE} value is thus proportional to the input resistivity value (ρ_{FE}) of the homogeneous shell, and for any specific geometry, the ratio between these will be constant. For a given set of probe positions, U/I_{FE} is independent of the diameter of the shell. Increasing the size of the shell with a factor increases the arc lengths between the probes by the same factor as long as the areas of the probes are increased accordingly. However, this also increases the cross-sectional area of the shell by the same factor, and U/I_{FE} thus remains constant. In contrast, U/I_{FE} is dependent on t^{-1}, where t is the thickness of the shell. The ratio between ρ_{FE} and U/I_{FE} is thus dependent only on three variables: probe positions, the size of the probe areas relative to the surface area of the shell, and shell thickness. This ratio then serves as a geometric correction factor, to which the measured U/I_{miBots} can be multiplied to achieve an estimated film resistivity ρ_{film}

$$\rho_{film} = U/I_{miBots} \frac{\rho_{FE}}{U/I_{FE}}. \quad (1)$$

As can be observed in Fig. 1(a), the positioning control of the miBots is so sensitive that four probes can be placed on a single AgPS without penetrating the thin silver film. Fig. 1(b) shows the seven consecutive voltage sweeps performed on the AgPS in Fig. 1(a). The plots are linear, as expected from measurements on an Ohmic material, and deviations between the measurements are negligible. By linear regression, this particular AgPS yields an average slope (U/I_{miBots}) of 0.126 Ω. The FE model with probe positions acquired from the SEM image in Fig. 1(a) and a shell thickness of 150 nm generates a geometric correction factor of 30.79 nm. Through (1), ρ_{film} is thus estimated as 3.88 μΩ cm for this AgPS. The behavior shown for this particular AgPS is representative for all AgPS measured in this work; each individual AgPS yields linear *U*/*I* plots and ρ_{film} higher than that of bulk silver at room temperature, as can be observed in Table I.

U/I_{miBots} follows the expected trend for the 270 nm, 150 nm, and 60 nm films, but the 100 nm films yields lower

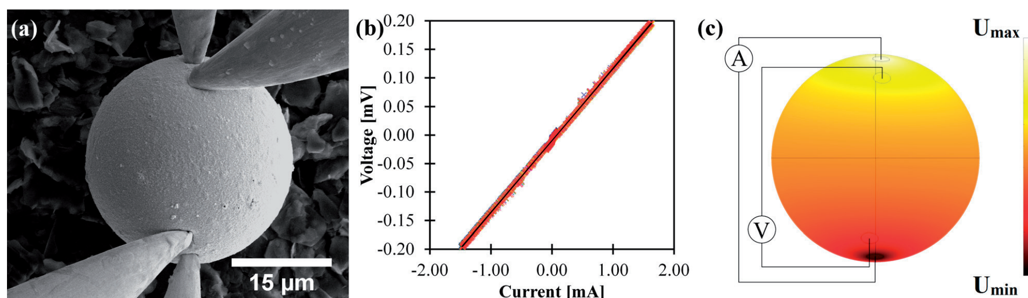

FIG. 1. (a) Four-point probing of a single 30 μm polymer sphere coated with 150 nm silver. (b) Seven consecutive voltage sweeps (0 V → −0.2 mV → 0.2 mV → 0 V) performed on the same particle. (c) The corresponding FE model, showing the voltage field on a 150 nm thick spherical shell with the same probe positions as (a). (The ampere- and volt-meter symbols are included for illustrative purposes.)

TABLE I. Averages ± one standard deviation: U/I_{miBots}, arc lengths along the AgPS surface between *source* probe centers, arc lengths between the *sense* probe centers, and estimated film resistivities. All values are calculated separately for each AgPS and then averaged. For reference, the resistivity of bulk silver at 298 K is 1.62 $\mu\Omega$ cm.[15]

Nominal film thickness (nm)[a]	U/I_{miBots} (Ω)	*Source* arc length (μm)	*Sense* arc length (μm)	ρ_{film} ($\mu\Omega$ cm)
60 ($n = 8$)	0.624 ± 0.209	36.6 ± 2.6	26.6 ± 3.1	7.27 ± 2.59
100 ($n = 17$)	0.080 ± 0.026	35.9 ± 6.1	18.4 ± 5.0	2.47 ± 0.57
150 ($n = 17$)	0.108 ± 0.017	36.6 ± 2.9	25.5 ± 2.9	3.28 ± 0.39
270 ($n = 6$)	0.085 ± 0.008	33.5 ± 4.7	24.5 ± 4.7	4.25 ± 0.44

[a]n = number of individual AgPS measured upon.

values than the 150 nm films. This is partly because some of the 100 nm films were used to test the sensitivity to the *sense* probe positions by positioning these closer together. The measured voltage U between the *sense* probes is dependent on the positions of the probes in the electric field, not just the arc length between the probes. However, the *sense* probes were purposefully placed so that the arc lengths were approximately overlapping with the *source* probe arc lengths, with similar distance between the *source* and *sense* probes at both sides. With these precautions, the ratio between the *source* probe and *sense* probe arc lengths will be the dominating influence on the U/I values of films of the same thickness, as seen in Fig. 2. This partly explains why the 100 nm films yield a lower average U/I_{miBots} value than the 150 nm films. Nevertheless, the FE model accounts for factual probe positions, and the estimated ρ_{film} values suggest that the lower U/I_{miBots} values in the 100 nm films are caused by lower resistivities in these films.

Through (1), ρ_{film} inversely correlates with U/I_{FE}. As U/I_{FE} depends on the thickness t of the homogeneous shell in the FE model by t^{-1}, ρ_{film} is linearly dependent on t. An under- or overestimation of the nominal film thickness compared to the real film thickness will thus cause an under- or overestimation of ρ_{film}. To investigate the real film thickness, cross-sections were ion milled in AgPS. These revealed that the real film thickness inclines toward higher values than the nominal, but only in the range of about 10–30 nm, and with some variations between AgPS of the same nominal thickness. The nominal values are therefore reasonable as conservative average estimates for shell thickness in the FE models, although the obtained ρ_{film} values may be slight underestimations. Deviation between the nominal and real film thicknesses is one potential cause for the scatter observed in ρ_{film} for each of the film thicknesses.

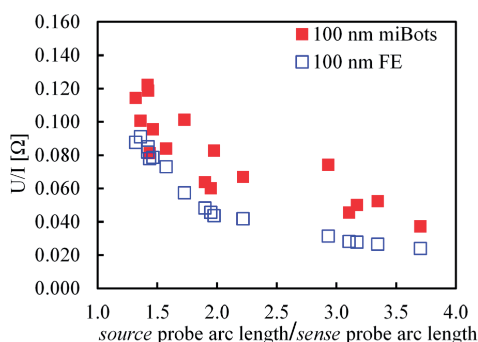

FIG. 2. U/I from miBots measurements and corresponding FE models for each AgPS with 100 nm nominal film thickness. The U/I_{FE} values are calculated with $\rho_{FE} = 1.62$ $\mu\Omega$ cm.

Measurement induced effects, such as probe damage and resistive heating, do not have any observable influence on ρ_{film} (for more details, see the supplementary material). Instead, several factors suggest intrinsic electron scattering effects caused by the structure and compositions of the films. Only the thinnest films have a nominal thickness value at which, for a flat and smooth silver film, we expect the resistivity to be significantly increased due to electron scattering at the surface.[7] However, the surfaces of all four film thicknesses are relatively rough due to the nodular grain structure, which will increase the resistivity compared to smooth films.[8] XRD measurements reveal that the average grain sizes are smaller than the EMFP of bulk silver for all four film thicknesses, as can be observed in Table II. Interestingly, the average grain size of the thickest film is smaller than those of the 150 nm and 100 nm films, almost as small as for the thinnest films. This coincides well with the estimated resistivity values in Table I and suggests that the elevation in resistivity is at least partly caused by increased electron scattering due to shorter distance between grain boundaries.[6,7] Although the four series have the same cores, they were coated separately with slight changes in process parameters to achieve the different film thicknesses, which can cause some variations in film structure. The 100 nm films yield lower resistivities than the 150 nm coatings, while being comprised of smaller grains, suggesting influence also from other scattering mechanisms. As the different film thicknesses were prepared in separate processes, it is possible that the level of impurities varies between the films. Impurities can increase the resistivity either by disrupting the lattice structure inside the grains, or by increasing the grain boundary reflection.[9] Different levels of porosity is also a potential contributing factor behind the differences in ρ_{film}.[10] It may also be that the relative underestimation of film thickness is slightly larger for the 100 nm than the 150 nm films.

TABLE II. Grain sizes calculated from peak with highest intensity in the XRD spectra obtained for the four nominal film thicknesses.

270 nm (nm)	150 nm (nm)	100 nm (nm)	60 nm (nm)
28	44	33	25

We have shown that it is possible to perform four-point measurements directly on spherical thin films coated onto micron-sized polymer particles using micromanipulators with step size resolution in the nanometer range. By multiplying the measured U/I values with geometrical correction factors obtained from simple FE models, probe positions can be accounted for, and the resistivities of the thin films estimated. Spherical electroless plated silver thin films yield higher resistivities than bulk silver at four different thicknesses, which are attributed to higher levels of electron scattering compared to bulk silver. It is evident that simply increasing the amount of silver, i.e., the film thickness, does not necessarily yield better electric properties. To gain efficient usage of the plating metal, it is desirable to control the grain size, as well as keep the porosity and level of impurities at a minimum.

See supplementary material for a more thorough description and discussion of the measurements and FE model, as well as XRD spectra for the four nominal film thicknesses.

The Research Council of Norway is acknowledged for funding through Project No. 225962/E20—"Novel conductive adhesive technology for solar industry" and for the support to the Norwegian Micro- and Nano-Fabrication Facility, NorFab. Partial funding has also been obtained from the European Union Seventh Framework Programme FP7-NMP-2013-LARGE-7 under Grant Agreement No. 604668 ("Quantiheat") and by funding from the European Union Seventh Framework Programme (FP7/2007-2013) under Grant Agreement No. FP7-NMP-310420 ("HyperConnect"). Vidar T. Fauske (Department of Physics, NTNU) is acknowledged for writing the control script for the sourcemeter.

[1]M. Chin, K. A. Iyer, and S. J. Hu, IEEE Trans. Compon. Packag. Technol. **27**, 317 (2004).
[2]J. Gakkestad, P. Dalsjo, H. Kristiansen, R. Johannessen, and M. M. Visser Taklo, J. Micro/Nanolithogr., MEMS, MOEMS **9**, 041108 (2010); S. R. Pettersen, H. Kristiansen, S. Nagao, S. Helland, J. Njagi, K. Suganuma, Z. Zhang, and J. He, J. Electron. Mater. **45**, 3734 (2016).
[3]G. R. Ruschau, S. Yoshikawa, and R. E. Newnham, J. Appl. Phys. **72**, 953 (1992).
[4]K. Fuchs, Math. Proc. Cambridge **34**, 100 (1938); E. H. Sondheimer, Adv. Phys. **1**, 1 (1952).
[5]U. Kreibig and C. v. Fragstein, Z. Phys. **224**, 307 (1969).
[6]A. F. Mayadas and M. Shatzkes, Phys. Rev. B **1**, 1382 (1970).
[7]W. Zhang, S. H. Brongersma, O. Richard, B. Brijs, R. Palmans, L. Froyen, and K. Maex, Microelectron. Eng. **76**, 146 (2004).
[8]S. M. Rossnagel and T. S. Kuan, J. Vac. Sci. Technol., B **22**, 240 (2004); V. J. Logeeswaran, N. P. Kobayashi, M. Saif Islam, W. Wu, P. Chaturvedi, N. X. Fang, S. Y. Wang, and R. S. Williams, Nano Lett. **9**, 178 (2009).
[9]E. E. Glickman, V. Bogush, A. Inberg, Y. Shacham-Diamand, and N. Croitoru, Microelectron. Eng. **70**, 495 (2003).
[10]M. S. M. Peterson and M. Deutsch, J. Appl. Phys. **106**, 063722 (2009).
[11]L. B. Valdes, Proc. IRE **42**, 420 (1954); F. M. Smits, Bell Syst. Tech. J. **37**, 711 (1958).
[12]M. M. McClarty, J. P. Bruce, M. S. Freund, and D. R. Oliver, Appl. Phys. Lett. **106**, 022107 (2015).
[13]A. E. Stokkeland, M.S. thesis, Norwegian University of Science and Technology, 2015.
[14]P. Scherrer, Göttinger Nachrichten Math. Phys. **2**, 98 (1918); available at https://eudml.org/doc/59018.
[15]R. A. Matula, J. Phys. Chem. Ref. Data **8**, 1147 (1979).

Supplementary Information to

Electrical four-point probing of spherical metallic thin films coated onto micron sized polymer particles

Sigurd R. Pettersen [1], August Emil Stokkeland [1], Helge Kristiansen [2], John Njagi [3], Keith Redford [2], Dan V. Goia [3], Zhiliang Zhang [1], and Jianying He [1,*].

[1] *NTNU Nanomechanical Lab, Department of Structural Engineering, Norwegian University of Science and Technology (NTNU), NO-7491, Trondheim, Norway.*

[2] *Conpart AS, NO-2013, Skjetten, Norway.*

[3] *Center for Advanced Materials Processing, Clarkson University, Potsdam, NY 13699-5814, USA.*

[*] Corresponding author: jianying.he@ntnu.no

miBots measurement setup

Fig. S1 shows the placement of the miBots and miBots stage in the chamber of the dualbeam FIB/SEM instrument. The miBots were easily controlled with four degrees of spatial freedom (X, Y, and R for the miBots on the stage, Z for the probe) by either a graphical user interface or a regular gaming controller. As seen in Fig. S2, the tungsten probes were many orders of magnitude larger than the micron-sized, silver coated particles (AgPS), but they could still be steered with such a spatial control that all four probes could be placed on an individual AgPS without detaching it from the substrate or breaking the thin film. SEM was used to monitor the placement of the probes on the spherical thin films in real time, and images were acquired between measurements. The electron beam was shielded during the measurements. The substrates were silicon chips coated with a thin layer of conductive carbon cement carbon cement (Leit-C, Agar Scientific, UK). The conductive layer was necessary to provide adhesion and avoid charging effects in the substrate when imaging with the SEM. Other substrates such as carbon tape and silver paint were also tried, but these either led to charging effects or provided too little adhesion. To ensure adhesion, dry AgPS were drizzled onto the substrates before the carbon cement dried. If the particles were pushed too far with one probe, they would still detach, which made it difficult to obtain good electrical contact with the probes. To avoid this, the probes were moved step-wise towards the particles while switching between the miBots. Each of the probes were connected to the SMU by individual leads, and the SMU was situated outside the dualbeam FIB/SEM. This provided the opportunity to alter which probe was connected to the Hi and Lo source and sense channels at any given time, which could be used to troubleshoot problems, e.g. like identifying bad electrical contacts.

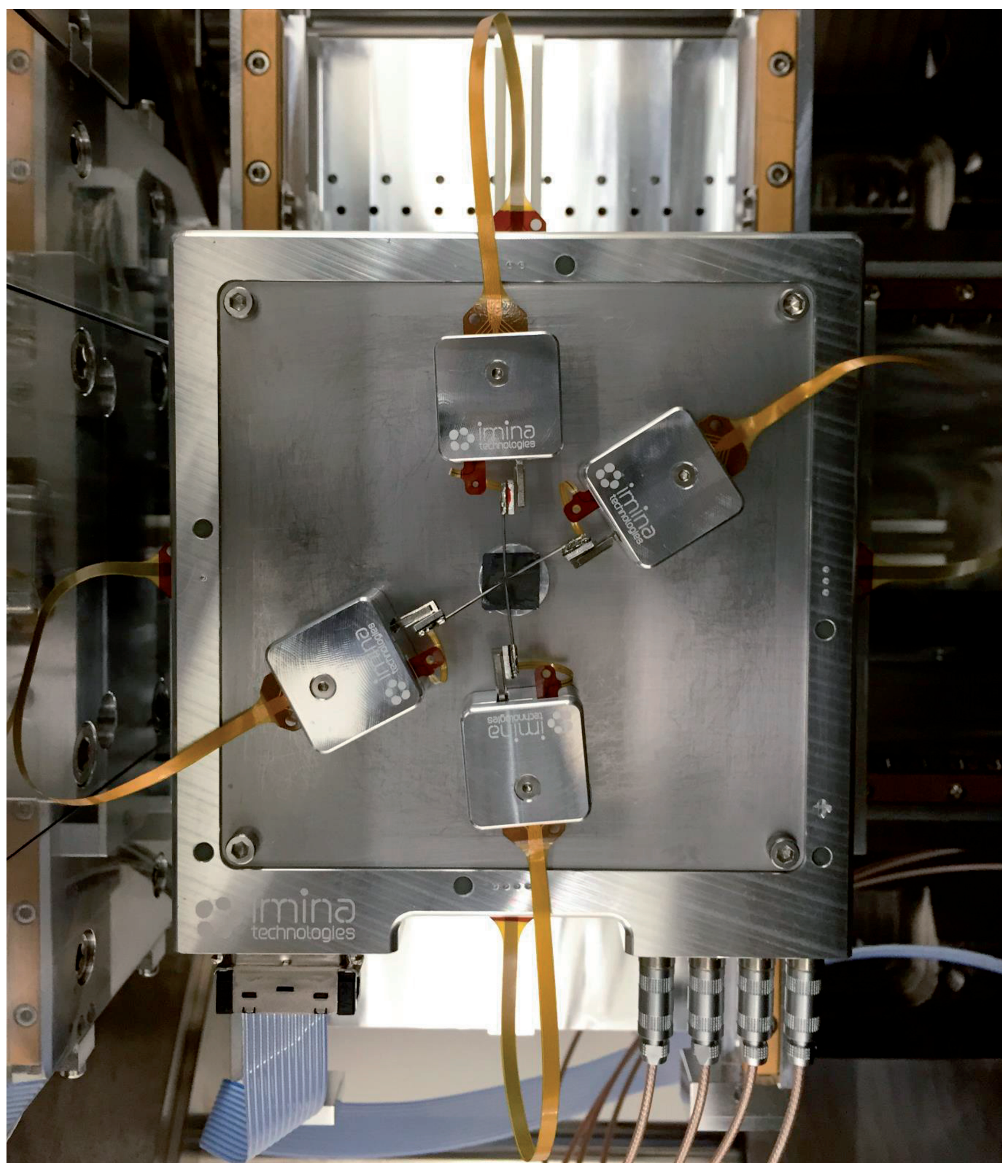

Fig. S1. Four separately controlled vacuum compatible piezo-actuated micro robots (miBot^{TM} BT-11-VP on a miBase BS-43-VP stage, Imina Technologies, Switzerland), equipped with sharp polycrystalline tungsten probes, situated inside the vacuum chamber of dualbeam FIB/SEM instrument (FEI Helios NanoLab DualBeam).

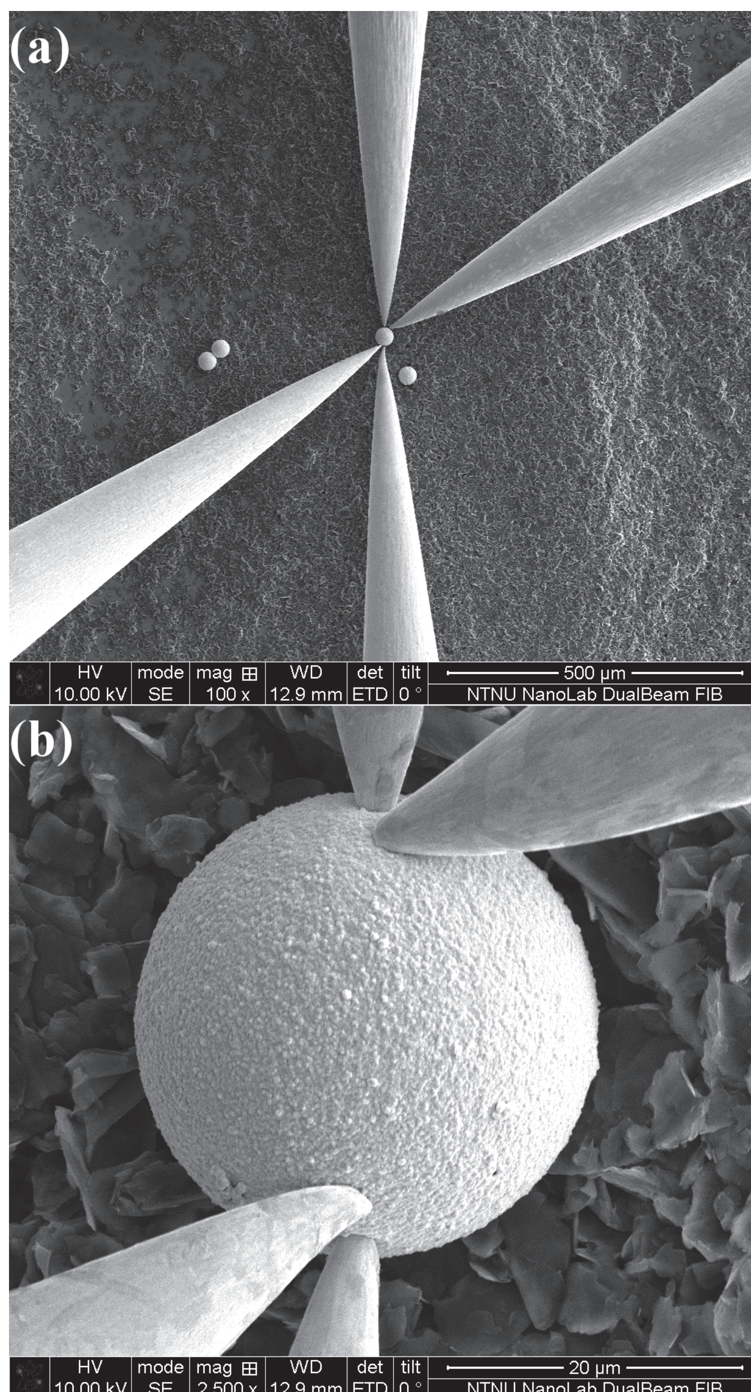

Fig. S2. The placement of four individually controlled tungsten probes on a single micron-sized PMMA sphere coated with approximately 270 nm silver, acquired at 100 x (a) and 2500 x (b) magnification.

Finite element (FE) model

The total diameter and relative 2D probe positions for each AgPS were found by cropping SEM images into a quadratic format that enclosed the AgPS at the equatorial plane parallel to the substrate, as seen in Fig. S3 (b). Using COMSOL Multiphysics 5.0, a corresponding finite element (FE) model was built as a spherical shell with total diameter equal to that of the measured AgPS and shell thickness equal to the nominal film thickness. The origin of the model coordinate system was set at the center of the shell, with the xy-plane equivalent to the equatorial plane of the imaged AgPS. The 2D coordinates of the probes acquired from the SEM image were thus equivalent to projections of the 3D probe positions onto the xy-plane. Using spherical coordinates, the probe positions on the surface of the shell were calculated. The probes were created as intersections between the shell and four cylinders with a diameter of 2.5 μm and height axis overlapping with the radial axis of the shell. The surface areas of the resulting spherical caps were used to simulate the probes, as described in the main text. As the coordinates of the centers of the probes were known, the chord lengths c between the centers of the *source* probes and between the centers of *sense* probes could be calculated as the vector lengths of the straight vectors between these. The corresponding arc lengths s were estimated from a simple geometrical relation (S1),

$$s = d\ arcsin\left(\frac{c}{d}\right), \text{(S1)}$$

where d is the total diameter of the AgPS.

The geometry was meshed automatically by the software using tetrahedral elements, but with user control of the element size and growth rate. As the probes were inherently a part of the model geometry and there was no real symmetry in the positions of the probes, the resulting mesh was asymmetrical, as seen in Fig. S3. Convergence tests were performed by varying the mesh size, and with the mesh sizes shown in Fig. S3 and used in the FE models, the models were well below the convergence limit.

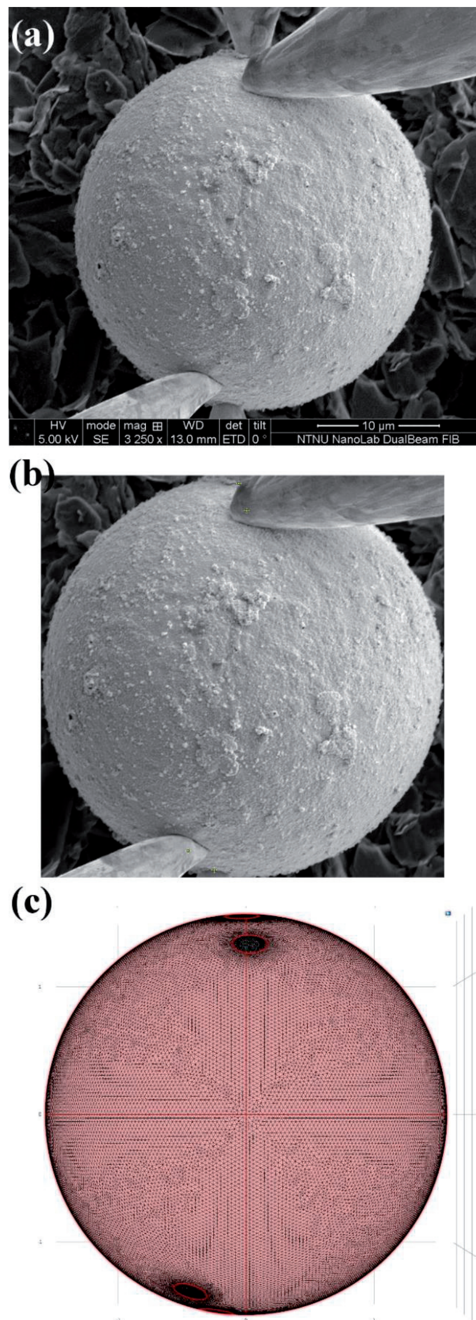

Fig. S3. (a) SEM image of on an AgPS with 60 nm nominal coating thickness. The image was cropped to a quadratic format (b), and the total diameter of the AgPS and 2D coordinates of the probes were acquired and translated into the FE model using spherical coordinates. (c) shows the corresponding meshed FE model.

Probe damage and deviations in film thickness

As explained in the main text, any deviations in the estimated ρ_{film} values from that of bulk silver are either caused by an elevated intrinsic resistivity in the silver films, or by geometric deviations from the perfectly spherical shell used in the FE model.

These deviations can inherently be part of the film structure, or induced by the measurements. The FE models assumes that the probes are in full, perfect contact across the whole spherical cap contact areas, while in reality, this is not the case due to surface roughness and plastic deformation caused by the probes. However, both the measurements and FE simulations suggest that damages induced by the probes will have very little impact on the U/I values. As seen by comparing Fig. S4 and Fig. S5, the AgPS which is most damaged yield the lowest U/I_{miBots} value. When the probe positions are translated into the FE model, the model corresponding to the particle in S4 also yield the lowest U/I_{FE} value, suggesting that probe positions have a larger effect than damages induced by the probes.

Simulating the damage done by the probes by replacing the spherical caps at the probe areas with holes of the same diameter in the geometry of the FE model as shown in Fig. S6 has negligible impact on the U/I_{FE} value. The model shown Fig. S6 yields a total current of 1.8184 mA and a voltage difference between the *sense* probes of 0.0957 mV with ρ_{FE} = 1.62 μΩ·cm, and thus a U/I_{FE} of 0.0526 Ω with the undamaged shell structure. With holes instead of spherical caps, the model yields 1.8159 mA, 0.0959 mV, and thus 0.0528 Ω, respectively, an increase of only 0.38 %. Cylindrical indents without full penetration of the shell yields values between these two extremes.

Simulating probe damages in the geometry of the shells thus have an insignificant impact on the estimated values. However, the FE model assumes equipotential surfaces on the *source* probe areas, and that the voltage at the *sense* probes can be found by averaging the voltage values at the *sense* probe areas, i.e. that all four probes are in perfect contact over the whole contact areas. In reality, surface roughness and deviations in the probe contact angles from the normal angles assumed in the FE model will lead to deviations from the perfect contacts in the model. Although the probes were not actively moved between subsequent measurements on the same particles, creep and plastic deformation in the polymer cores and silver thin films often resulted in further indentation of the probes between the measurements. The measurements were conducted in four-point mode, and variations in the contact resistance should thus be

irrelevant. Variations in contact resistance changes the voltage drop across the contact and the total current. However, as the films are made of an Ohmic material, only the magnitude and not the distribution of the electric field changes due to changed contact resistance, and the scalar changes linearly with the total current, so U/I remains constant. Changes in the contact resistance are thus irrelevant for the same reason that the magnitude of the applied voltage or current is irrelevant (as long as resistive heating is negligible, as discussed later). However, changes in the contact structure or area could lead to slight alterations in the distribution of the electrical field, at least close to the contacts, as the probes are likely not in perfect electrical contact over the whole contact area. Such alterations are a likely cause for the slight increase or decrease in U/I_{miBots} between subsequent measurements, but not for the deviations between the particles, as these were much larger, as can be observed in Fig. S7. This figure shows U/I_{miBots} and the corresponding U/I_{FE} for all measured AgPS of all four film thicknesses. Fig. S7 (c) is equivalent to Fig. 2 in the main text. As can be seen by comparing Fig. S7 (b) and (c), at the same arc length ratios the 150 nm and 100 nm films have quite similar U/I_{miBots} values, with somewhat larger scatter and some higher values in the 150 nm films. This suggest that the main reason that the 100 nm films yield lower ρ_{film} values than the 150 nm films is the film thickness of the FE models. Unless the real film thicknesses are almost equal, the similar U/I_{miBots} values have to be caused by intrinsic resistivity effects in the real films.

As discussed in the main text, the FE model assumes a shell thickness equal to the nominal film thickness. Deviations from the nominal film thickness would be a cause of deviations between the measurements and the model. Fig. S8 show the calculated U/I_{FE} and ρ_{film} for the AgPS in Fig. 1 in the main text as a function of shell thickness in the FE model. The values are calculated by keeping the total diameter and probe sizes and positions constant, while decreasing or increasing the shell thickness. As can be seen, the model yields a power law dependence of U/I_{FE} on the shell thickness, and a linear dependence of ρ_{film} on the shell thickness. This is as expected from Ohms law, and (1) in the main text.

By using the focused ion beam with an incident angle normal to the films to mill away cross sections, the real film thicknesses could be estimated. As seen in Fig. S9, such cross sections show that the nominal film thicknesses are reasonable minimum values, although deviations from these could be in the range of several tens of nanometer. Deviations were towards thicker films than the nominal values, so the elevated resistivity values cannot be explained by overestimation of the film thicknesses in the FE models. The thinner the films, the more difficult

it was to obtain clear cross-sections with the FIB, which is the reason why Fig. S9 only shows the three thickest films. However, AgPS from the same four production series used in this work were previously used as filler particles in isotropic conductive adhesives (ICAs) [ref. 2 in the main text[1]], meaning they were mixed into epoxy and cured. These ICAs were cross-sectioned using broad beam ion milling (IM4000, Hitachi High-Technologies Co., Ltd. Japan) and imaged with FEG-SEM (for more details, see ref. 2). As the AgPS are randomly distributed in the ICA and the PMMA cores have a certain, although small, size distribution, there is no way of deciding if the cross sectional plane is normal to the film thickness. Still, AgPS that yield cross-sectional diameters close to the nominal core diameter of 30 μm can still be used to gain some rough estimates of the film thickness, as seen in Fig. S10. These support that the nominal film thicknesses used in the FE models are conservative values. If there are errors in the estimated resistivities introduced by the nominal film thickness values used in the FE model, these are underestimations, and not overestimations.

[1] Pettersen, S.R., et al., Contact Resistance and Metallurgical Connections Between Silver Coated Polymer Particles in Isotropic Conductive Adhesives. Journal of Electronic Materials, 2016: p. 1-10.

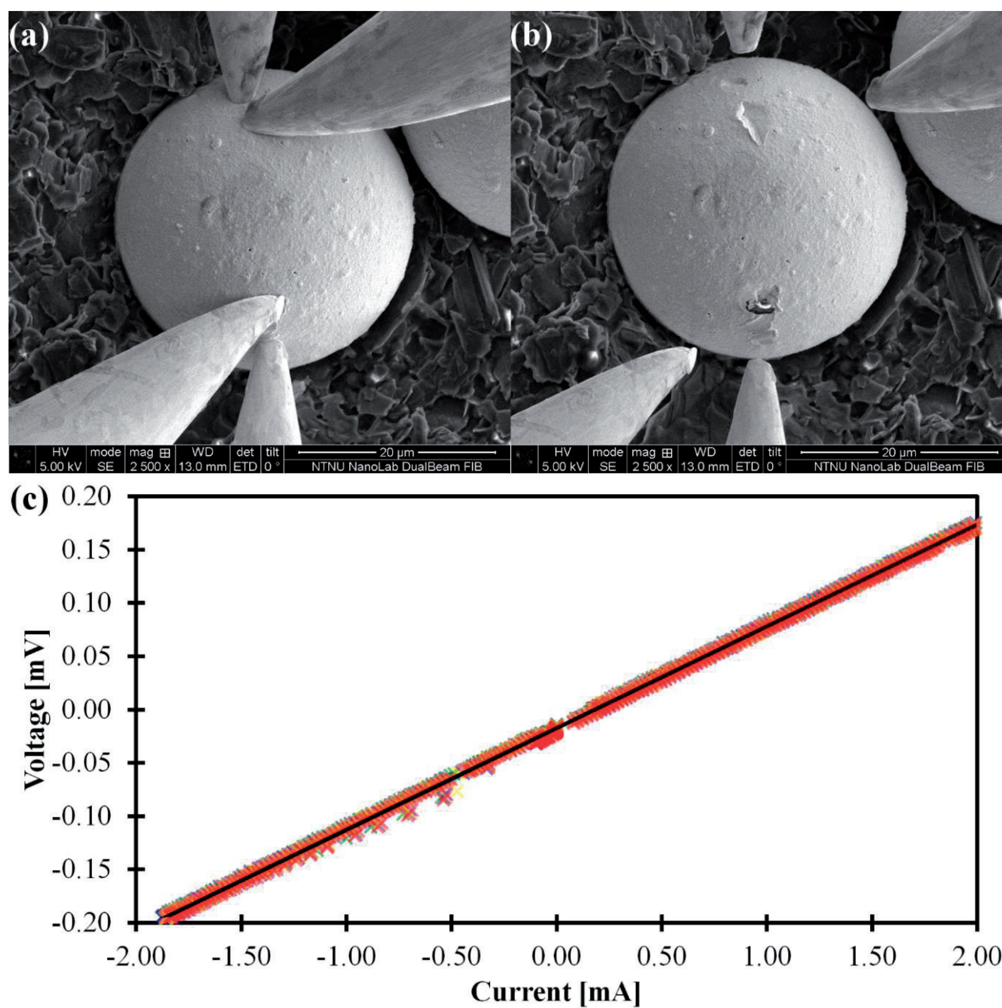

Fig. S4. SEM images acquired before (a) and after (b) measurements on an AgPS with 100 nm nominal coating thickness. The seven subsequent voltage sweeps were almost overlapping, and yielded an average U/I_{miBots} slope of 0.095 Ω. The arc lengths between the source probe centers and sense probe centers were estimated to 30.6 µm and 20.9 µm, respectively. The corresponding FE model yielded a U/I_{FE} value of 0.078 Ω, and ρ_{film} of 1.97 µΩ·cm when ρ_{FE} was 1.62 µΩ·cm.

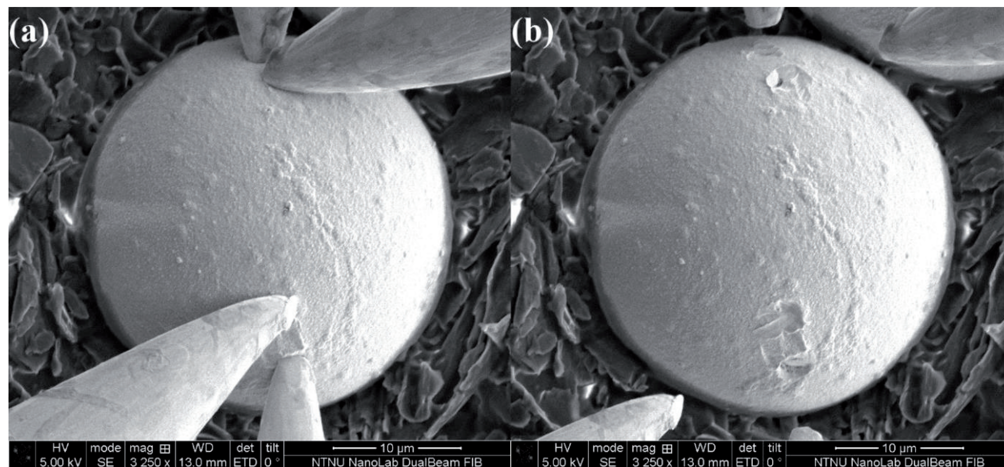

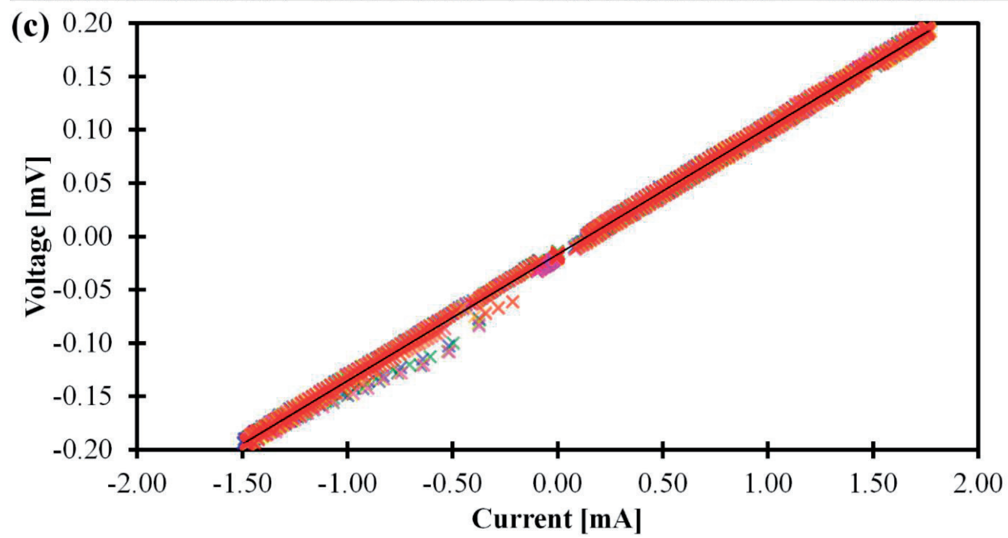

Fig. S5. SEM images acquired before (a) and after (b) measurements on an AgPS with 100 nm nominal coating thickness. The seven subsequent voltage sweeps were almost overlapping, and yielded an average U/I_{miBots} slope of 0.119 Ω. The arc lengths between the source probe centers and sense probe centers were estimated to 29.0 µm and 20.4 µm, respectively. The corresponding FE model yielded a U/I_{FE} value of 0.085 Ω, and ρ_{film} of 2.26 µΩ·cm when ρ_{FE} was 1.62 µΩ·cm.

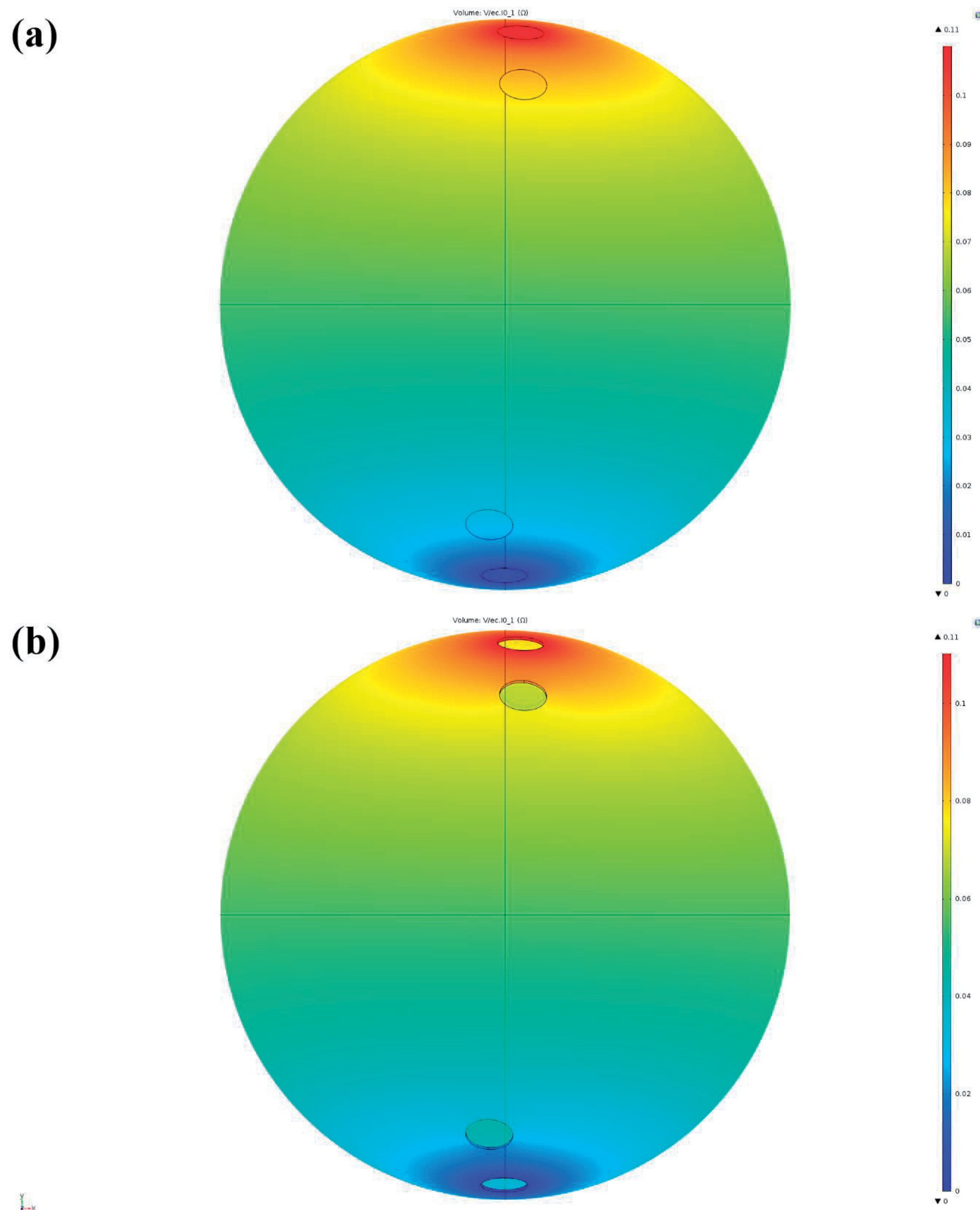

Fig. S6. The voltage field divided by the total current (U/I) from the FE model corresponding to the particle with 150 nm nominal film thickness shown in Fig. 1. in the main text. (a) shows a homogeneous shell where the probes are simulated as the surfaces of spherical caps 2.5 μm in diameter, while in (b), holes have been made through the spherical shell and the voltage is applied or measured on the ring-formed areas around the holes. The models yield U/I_{FE} of 0.0526 Ω and 0.0528 Ω, respectively.

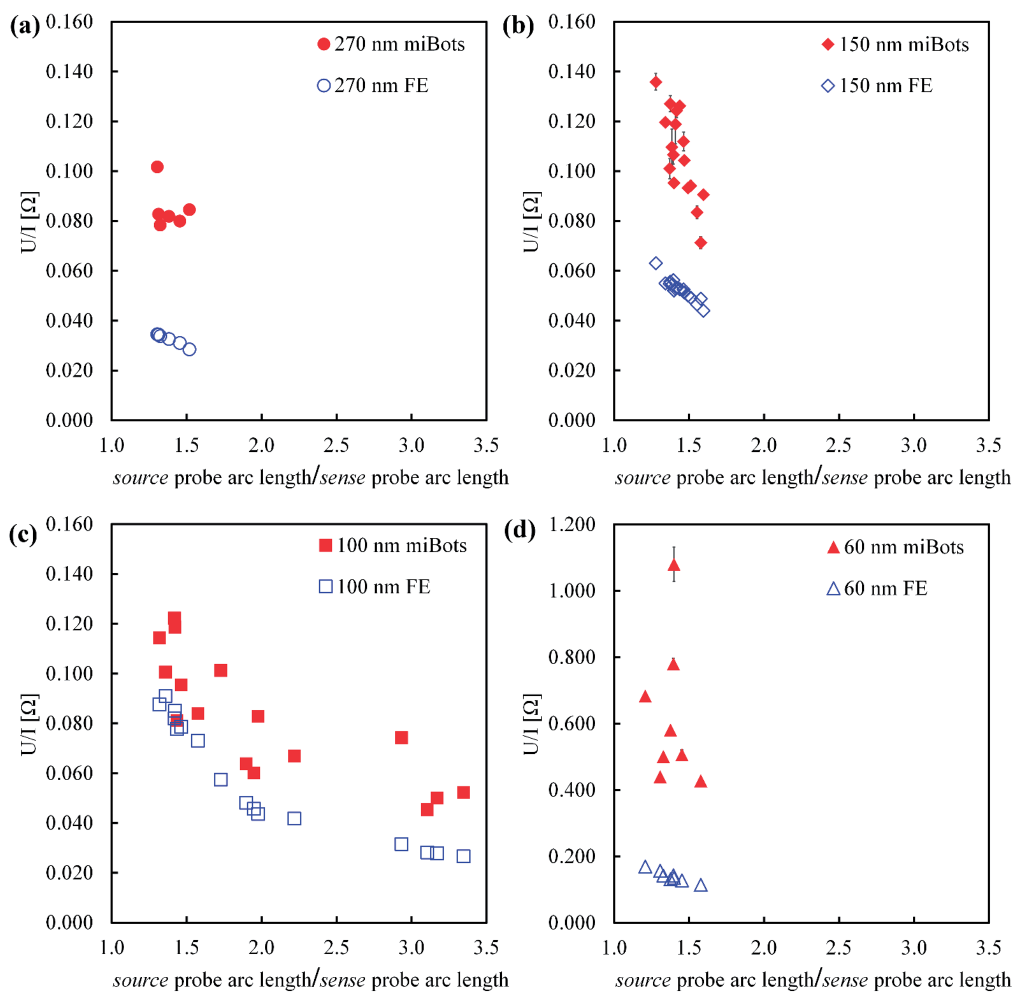

Fig. S7. *U*/*I* from miBots measurements and corresponding FE models for each AgPS for each of the four nominal film thicknesses. NB! Beware of the much larger scale on the *y*-axis of the 60 nm films. The error bars show the standard deviation caused by differences between the seven subsequent measurements on each AgPS. For most particles, this deviation was completely negligible compared to the difference between each particle.

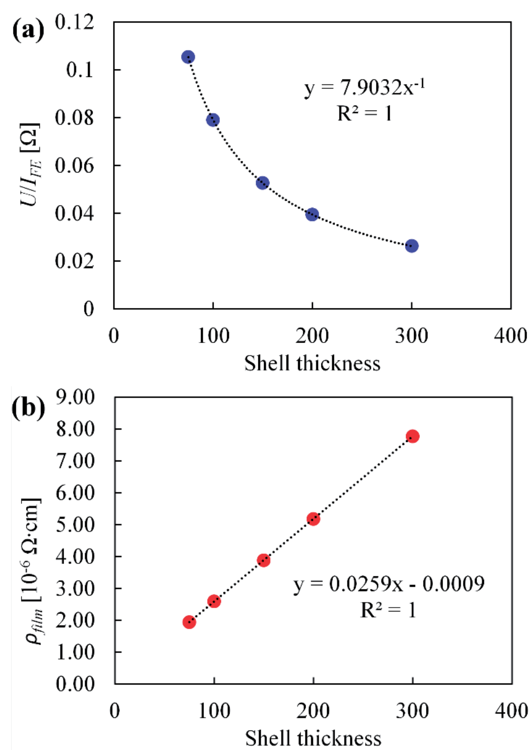

Fig. S8. U/I_{FE} (a) and the corresponding ρ_{film} (b) for the AgPS in Fig. 1 as a function of shell thickness in the FE model. The values given in the main text and used in the average values in Table I are calculated with 150 nm shell thickness, which is the nominal film thickness of the AgPS.

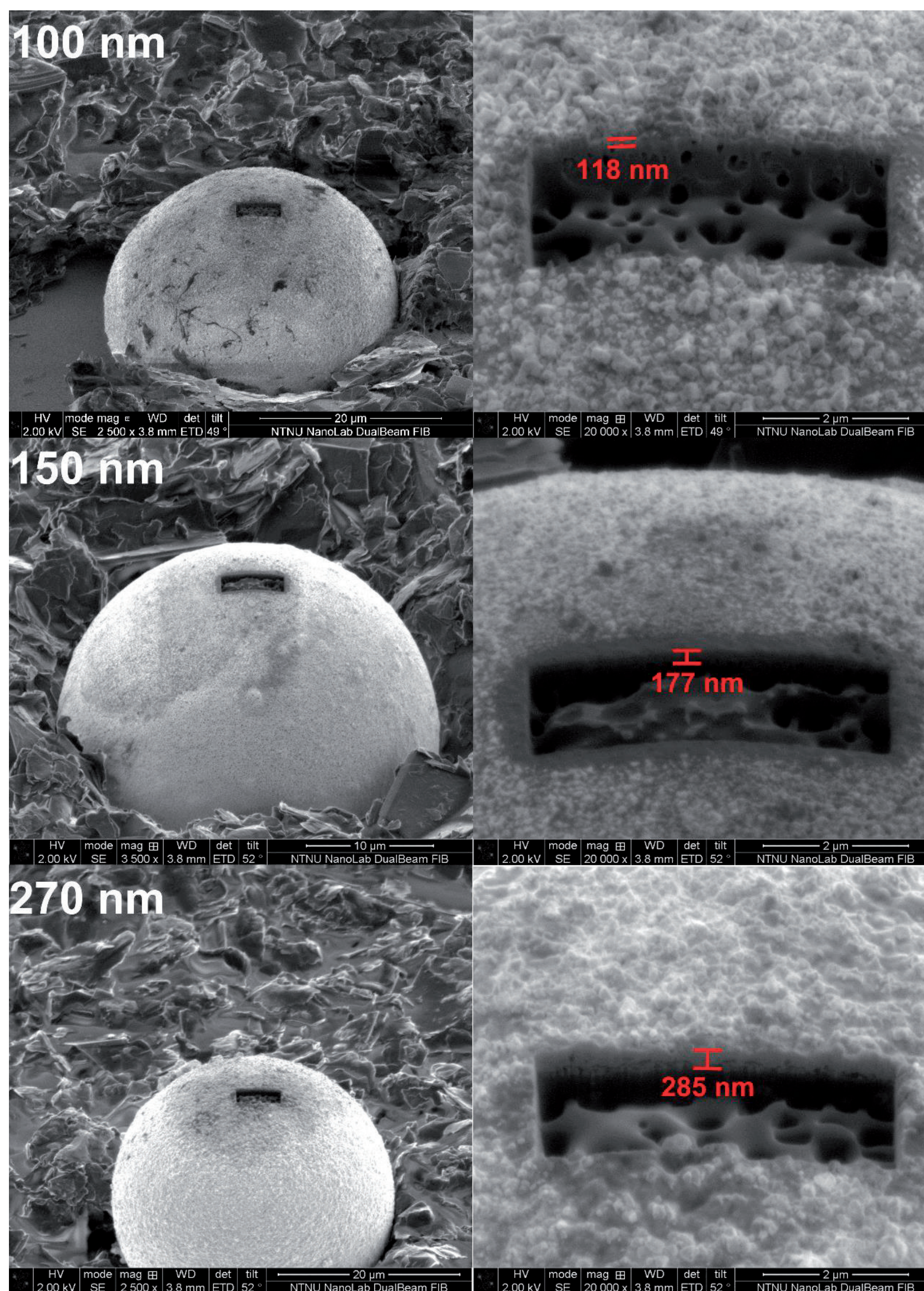

Fig. S9. SEM image of cross-sections milled in AgPS with 100 nm, 150 nm, and 270 nm silver film thickness with the FIB normal to the film surfaces. The film thicknesses have been estimated by accounting for the incident angle of the SEM on the cross-sections.

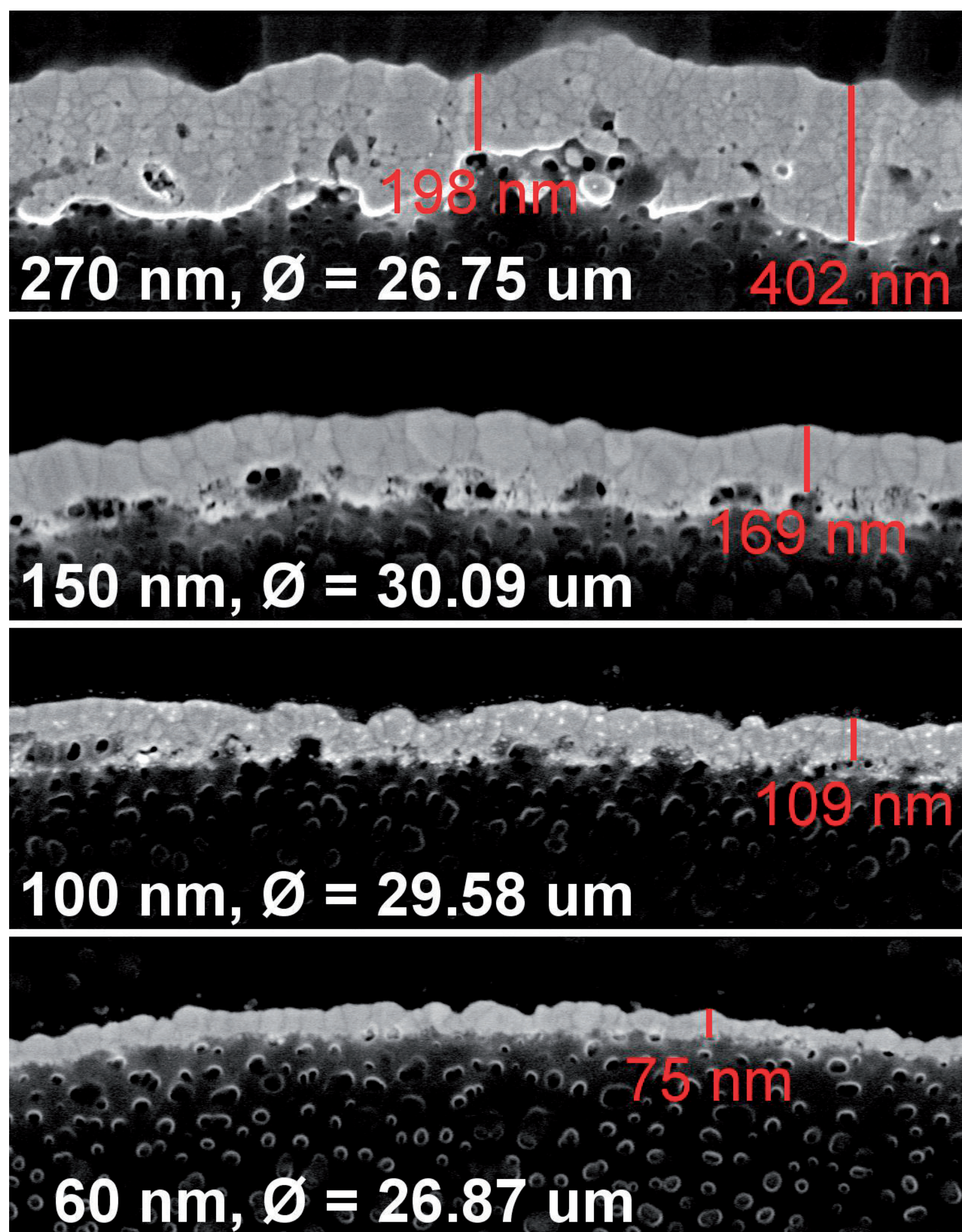

Fig. S10. FEG-SEM images of broad beam ion-milled cross-sections of isotropic conductive adhesives with the same AgPS used in this work as filler particles. Ø is the cross-sectional diameter of the PMMA cores. The cross-section is a random 2D cross-section through a matrix of randomly dispersed AgPS, thus the large difference in diameters. For more details, see ref. 3

Resistive heating

A possible effect induced by the measurements could be elevated temperatures in the metal films caused by resistive heating due to resistance in the films or at the *source* probe contacts. However, the temperatures necessary to achieve bulk silver resistivities similar to the estimated ρ_{film} values found in Table I in the main text, especially for the 60 nm and 270 nm nominal film thicknesses, are so large that we would expect the particles to start degrading. In the SEM images acquired between the measurements, no such degradation or change were evident, as seen in Fig. S11, which shows an AgPS on which one of the highest currents was measured. The silver films were in good metallic contact with four tungsten probes, and at the dimensions of the particles, any produced heat would dissipate almost instantaneously. Resistive heating, if present, should be larger at the maxima of the voltage sweeps, where the current is at its largest. This should be observable as higher U/I values, i.e. non-linear slopes, towards the maxima of the sweeps, yet no such behavior is observable for any of the measured AgPS. It is thus unlikely that the increased resistivities were caused by resistive heating.

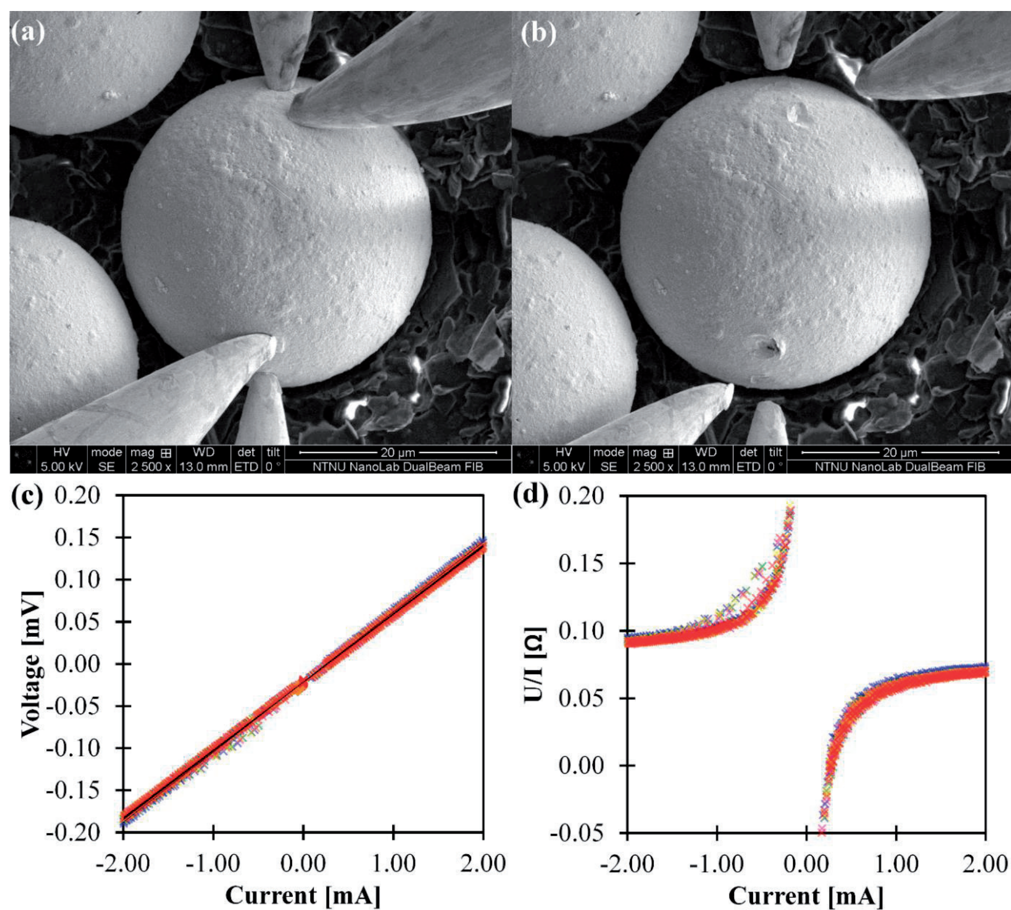

Fig. S11. SEM image captured before (a) and after (b) seven subsequent measurements on an AgPS (100 nm film thickness) that yielded a relatively high current. No degradation caused by resistive heating is evident. As seen, the *U*/*I* plot is linear (c) , and there is no increase in *U*/*I* towards the larger currents.

XRD data

Table II in the main text shows the grains sizes calculated from the peak with highest intensity in the XRD spectra for each of the film thicknesses. Fig. S12 shows the spectra for the 270 nm, 150 nm, 100 nm, and 60 nm nominal film thicknesses, respectively. The grain sizes calculated from all the peaks are shown in Table SI. The grain size trend given by the XRD results are also supported by the cross-sectional images shown in Fig. S10, which show that the average grain size of the 270 nm films are smaller than the 150 nm films.

TABLE SI. Grain sizes calculated from each peak in the XRD spectra obtained for the four nominal film thicknesses.

Position [°]	270 nm [nm]	100 nm [nm]	100 nm [nm]	60 nm [nm]
38.1	28	44	33	25
44.3	18	31	22	17
64.4	24	46	31	28
77.3	21	35	30	25
81.5	39	48	35	26

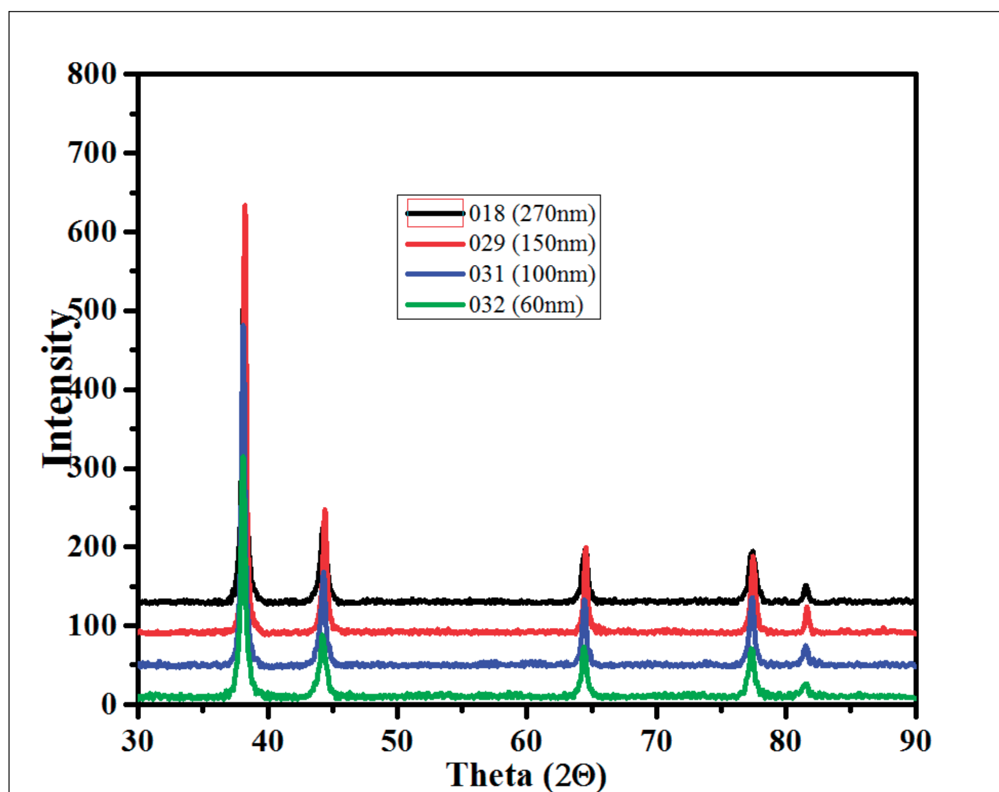

Fig. S12. XRD spectra of the four film thicknesses.

Paper III

Contact Resistance and Metallurgical Connections between Silver Coated Polymer Particles in Isotropic Conductive Adhesives

Sigurd R. Pettersen, Helge Kristiansen, Shijo Nagao, Susanne Helland, John Njagi, Katsuaki Suganuma, Zhiliang Zhang, and Jianying He.

Journal of Electronic Materials, 2016, **45**(7), 3734–3743.

Journal of ELECTRONIC MATERIALS
DOI: 10.1007/s11664-016-4498-1
© 2016 The Author(s). This article is published with open access at Springerlink.com

Contact Resistance and Metallurgical Connections Between Silver Coated Polymer Particles in Isotropic Conductive Adhesives

SIGURD R. PETTERSEN,[1] HELGE KRISTIANSEN,[1,2] SHIJO NAGAO,[3] SUSANNE HELLAND,[4] JOHN NJAGI,[5] KATSUAKI SUGANUMA,[3] ZHILIANG ZHANG,[1] and JIANYING HE[1,6]

1.—NTNU Nanomechanical Lab, Department of Structural Engineering, Norwegian University of Science and Technology (NTNU), 7491, Trondheim, Norway. 2.—Conpart AS, 2013, Skjetten, Norway. 3.—Institute of Scientific and Industrial Research (ISIR), Osaka University, Ibaraki, Osaka 567-0047, Japan. 4.—Mosaic Solutions AS, 2013, Skjetten, Norway. 5.—Center for Advanced Materials Processing, Clarkson University, Potsdam, NY 13699-5814, USA. 6.—e-mail: jianying.he@ntnu.no

Recently, there has been an increasing interest in silver thin film coated polymer spheres as conductive fillers in isotropic conductive adhesives (ICAs). Such ICAs yield resistivities similar to conventional silver flake based ICAs while requiring only a fraction of the silver content. In this work, effects of the nanostructure of silver thin films on inter-particle contact resistance were investigated. The electrical resistivity of ICAs with similar particle content was shown to decrease with increasing coating thickness. Scanning electron micrographs of ion milled cross-sections revealed that the silver coatings formed continuous metallurgical connections at the contacts between the filler particles after adhesive curing at 150°C. The electrical resistivity decreased for all samples after environmental treatment for 3 weeks at 85°C/85% relative humidity. It was concluded that after the metallurgical connections formed, the bulk resistance of these ICAs were no longer dominated by the contact resistance, but by the geometry and nanostructure of the silver coatings. A figure of merit (FoM) was defined based on the ratio between bulk silver resistivity and the ICA resistivity, and this showed that although the resistivity was lowest in the ICAs containing the most silver, the volume of silver was more effectively used in the ICAs with intermediate silver contents. This was attributed to a size effect due to smaller grains in the thickest coating.

Key words: Conductive adhesives, contact resistance, metallic contacts, silver thin films, metal-coated polymer particles, size-dependent resistivity

INTRODUCTION

As lead-based solders are banned in a growing range of products due to environmental concerns, isotropic conductive adhesives (ICAs) are emerging as a promising alternative in electronic interconnects because of advantages such as lower processing temperatures and fewer processing steps compared to lead-free solders.[1] Conventionally, ICAs comprises micron-sized silver flakes embedded in an adhesive matrix, normally a thermosetting epoxy system. An interconnecting network of silver flakes makes the ICA electrically conductive,

Sigurd R. Pettersen: Parts of this work were done during an academic stay at Institute of Scientific and Industrial Research (ISIR), Osaka University, Ibaraki, Osaka 567-0047, Japan
(Received December 14, 2015; accepted March 24, 2016)

Published online: 19 April 2016

whereas the epoxy matrix provides structural integrity and adhesion. Even with the large surface-to-volume ratio of silver flakes, the amount of silver must be relatively large to achieve sufficient electrical conductivity; typically a volume fraction of 25–30% is required, corresponding to a weight fraction of 70–80%. This large fraction of precious metal severely affects the cost-efficiency of ICAs, and increases the impact of undesirable material properties such as brittleness and thermal expansion mismatch between the components.

Replacing the silver flakes with micron-sized polymer spheres coated with tens to hundreds of nanometres silver (AgPS) can significantly reduce the amount of precious metal required to obtain satisfactory electrical conductivity. Figure 1 shows a cross-section of such an AgPS-based ICA, containing a volume fraction of about 56% AgPS but less than 3% silver. Similar ICAs have been shown to exhibit resistivities lower than 10^{-3} Ω cm; a value in the same range as that of conventional flake-based ICAs, which contain about ten times the volume fraction of silver.[1,2] By tailoring the size and composition of the polymer cores, material property mismatch between the filler particles and epoxy matrix can be reduced. Nguyen et al. investigated the die shear strength of AgPS-based ICA and found it to be larger than both in-house produced and commercial flake-based ICAs.[3] The rheological properties of these ICAs have also been investigated and deemed suitable for stencil/screen printing and dispensing processes.[4] Gakkestad et al. investigated the thermal properties of AgPS-based ICAs.[2] A thermal conductivity of 1 W/m K was obtained at approximately 1.4 vol.% silver, whereas a flake-based ICA required 16 vol.% silver to reach the same value. Jain et al. explored the effect of various AgPS sizes, volume fractions, epoxy types and curing conditions, and coating thickness on electrical properties of these ICAs.[5–7] The resistivities of ICAs containing 30 μm AgPS with 100 nm, 150 nm, 200 nm, and 250 nm silver coatings were measured over a range of particle volume fractions.[7] In general, it was found that for the same particle volume fraction, ICAs containing AgPS with thicker coatings yielded higher conductivities.

The conductivity of conventional ICAs is often explained by percolation theory, where at a critical volume fraction of filler particles, enough inter-particle contacts are formed to create at least one complete conduction path.[1] As the filler concentration increases above this percolation threshold, the number of contacts rapidly increases to form a network of parallel conductors, where each conductor can be seen as a number of resistors in series. These resistors can be divided in two categories: the bulk resistance from the conductive filler particles, which is dependent on the resistivity and geometry of the particles, and the inter-particle contact resistance. In conventional ICAs, the contact resistance is generally regarded as the dominating factor.[8,9] In addition to a concentration of conductive fillers above the percolation threshold, most ICAs require curing to lower the resistivity to an acceptable level. Curing leads to cross-linking and shrinkage in the epoxy matrix, which presses the particles together, decreasing the contact resistance.[9]

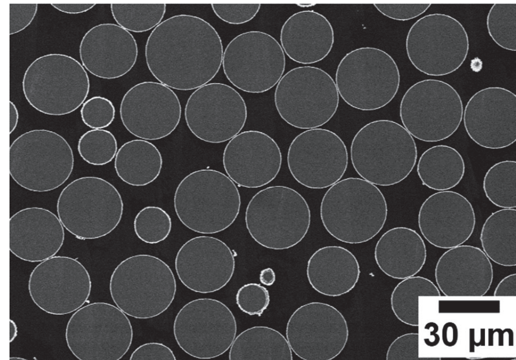

Fig. 1. FE-SEM image of a cross-sectioned ICA sample containing a volume fraction of 56% AgPS. PMMA particles (light grey) with a diameter of 30 μm are coated with 270 nm thick silver films (white) and embedded in an epoxy matrix (dark grey). The seemingly large size distribution is a result of the cross-section cutting through different planes in the randomly dispersed particles.

Constriction resistance and tunnelling resistance are the two main mechanisms behind the contact resistance, as described by Holm's classical contact theory.[10] If the contact areas are smaller than the cross-sectional areas of the particles, the flow of current will be narrowed, leading to a constriction resistance through the contacts. The resistance effect due to lattice mismatch between two metallic contact members in direct contact is similar to the resistance from the grain boundaries in a polycrystalline material. Even if there is no direct metallic contact, e.g. due to the presence of a thin polymer or oxide film, electrons may pass across the contact by quantum tunnelling. This effect is only dependent on the thickness of the insulating layer; the tunnelling decreases rapidly as the thickness increases, and at around 10 nm the tunnelling resistance is so large that tunnelling current is negligible.

In this work, we found that the resistivities of AgPS-based ICAs with similar volume fractions of particles decreased exponentially with increasing coating thickness. High resolution scanning electron microscope (SEM) imaging of cross-sectioned samples revealed that the intermediate to thickest coatings had formed metallurgical contacts. The impact of these contact structures on the conductive properties of AgPS-based ICAs are discussed, and it is concluded that the contact resistance mechanisms assumed to dominate in conventional ICAs are negligible as long as the metallurgical contacts are formed. The formation of such metallurgical

contacts thus helps explain the good conductive properties relative to the low silver content exhibited by AgPS-based ICAs.

MATERIALS AND METHODS

Sample Preparation

Poly(methyl methacrylate) (PMMA) spheres with a diameter of 30 μm (coefficient of variation ≤5%) and nominal silver coating thicknesses of 60 nm, 100 nm, 150 nm, and 270 nm were provided through Mosaic Solutions AS (Skjetten, Norway). The coating was applied by an electroless plating procedure, and the coating thicknesses were estimated from the amount of silver used in the coating process, assuming that all the silver was incorporated in the coatings. Representative particles with each coating thickness can be observed in Fig. 2. The density of the polymer cores was given by the manufacturer as 1.16 g/cm^3, and the densities of the silver coatings were assumed to be equal to that of bulk silver (10.49 g/cm^3). The epoxy matrix was prepared by mixing a low viscosity epoxy resin consisting of a mixture of bisphenol A and bisphenol F epoxy with a low viscosity polyetheramine curing agent at a ratio of 1:0.35 by weight. The uncured densities of the resin and curing agent were given by the manufacturer as 1.18 g/cm^3 and 0.95 g/cm^3, respectively. Particles were mixed into the epoxy at a volume fraction of approximately 56% using a centrifugal vacuum mixer (ARV-310, Thinky Corporation, Japan). The mixing was done in two steps: 2000 rpm for two min at atmospheric pressure, followed by 1000 rpm for four min at 0.3 kPa pressure to remove air from the samples. The ICA was screen printed into Teflon moulds with dimensions 10 mm × 10 mm × 1 mm, and cured at 150°C for 30 min. The moulds confined potential flow of the uncured ICAs, thus minimizing influence of the different coating surfaces on the rheological behaviour of the ICAs. The four ICA series are denoted 60Ag, 100Ag, 150Ag, and 270Ag, respectively. The calculated particle and silver content of the series can be found in Table I.

Electrical 4-Pin Measurements

The electrical volume resistivity was measured with a 4-pin setup (Loresta-GP MCP-T610 with a 4-pin NSCP probe, Mitsubishi Chemical Analytech, Japan) on six samples from each ICA series. The probe had a built-in spring system, ensuring equal contact pressure on the samples in each measurement. The thickness of each sample was measured with a digital calliper, and the instrument automatically calculated the resistivity for each measurement by multiplying the resistance with the thickness and a resistivity correction factor (RCF). The RCF corrected for restrictions imposed on the electrical field by the sample size and geometry, as well as the probe position. The resistivities of the ICA series were averaged from eight measurements on each of the six samples from every series.

Harsh Environmental Testing

To investigate how the sample properties would change after a harsh environment test, the samples were placed in an environmental chamber (Espec SH-240 temperature and humidity chamber, Espec Corporation, Japan) at 85°C and 85% relative humidity (RH) for 3 weeks. After the environmental test, the samples were dried in ambient conditions for at least 48 h before the electrical resistivity was measured following the same procedure. The data sets from before and after the environmental test are denoted *pre-ET* and *post-ET*, respectively.

Polishing and FE-SEM Imaging of ICA Cross-Sections

To investigate the structure of the silver coatings at the various thicknesses, both *pre-ET* and *post-ET* samples from the four ICA series were cross-sectioned and further imaged by field emission scanning electron microscopy (FE-SEM). The samples were first mechanically polished with SiC paper (#4000 from Struers; grain size 5 μm) at 150 rpm to get cross-sections a certain distance into the bulk of the samples. A segment of each cross-section was further ion milled by argon ions at 6 kV for approx. 3–5 h using an ion milling system in cross-sectional milling mode (IM4000, Hitachi High-Technologies Co., Ltd. Japan). The cross-sections were imaged by field emission SEM (SU8020, Hitachi High-Technologies Co., Ltd. Japan) at an acceleration voltage of 2 kV.

RESULTS

Electrical Resistivity

With the exception of the ICA series with the thinnest coating before the environmental chamber test (60Ag *pre-ET*), the spread in resistivity values within each series was small. There is a clear trend that the resistivity of the ICA decreased as the estimated silver content increased, as can be observed in Fig. 3. The lowest average resistivity value was found for the 270Ag *post-ET* series, at $6.7 \times 10^{-4} \pm 0.5 \times 10^{-4}$ Ω cm. The other striking feature is the decrease in resistivity for the samples after 3 weeks at 85°C and 85%RH, most obvious in the 60Ag series. As the electrical measurements were conducted on the same samples *pre-* and *post-ET*, this large decrease in both spread and average resistivity for the samples with the thinnest coatings suggest that a significant structural change occurred in these samples during the environmental treatment. Before the environmental treatment, the coefficient of variation (CV) was 77% for the 60Ag series, and this decreased to 7% *post-ET*. For the 100Ag, 150Ag, and 270Ag series, the CV decreased

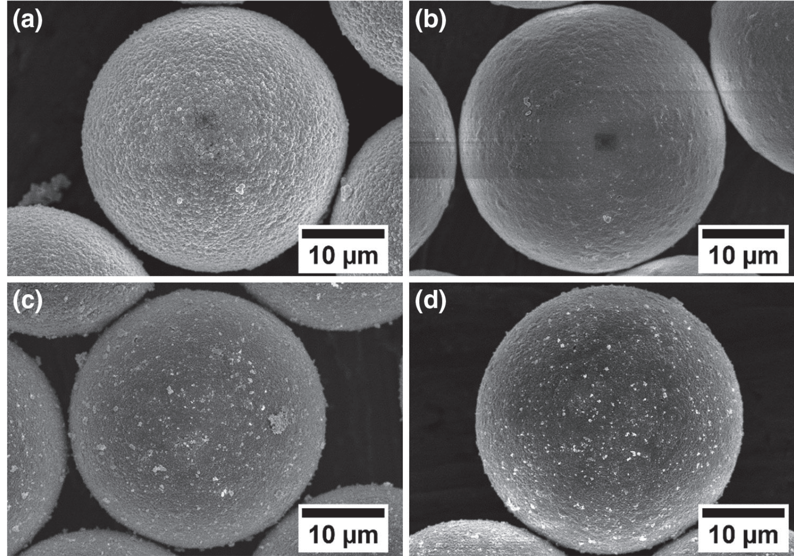

Fig. 2. Representative particles with nominal coating thicknesses of 270 nm (a), 150 nm (b), 100 nm (c), and 60 nm (d), respectively. Each particle is covered by a continuous film of silver, made up of nodular grain structures.

Table I. Particle, volume, and mass fractions of the four ICA series, calculated from the measured weights, as well as densities and dimensions given by Mosaic Solutions

Series	Nominal coating thickness (nm)	Volume fraction particles (%)	Volume fraction silver (%)	Mass fraction silver (%)
60Ag	60	56.0	0.7	5.8
100Ag	100	56.1	1.1	9.3
150Ag	150	56.5	1.7	13.4
270Ag	270	56.4	2.9	21.8

Calculations are based on uncured density values.

from 11% to 8%, 14% to 10%, and 9% to 7%, respectively.

Cross-Sectional FE-SEM Images

Contact Zones

As the AgPS are randomly dispersed in the epoxy matrix, an arbitrary cross-section may cut through all possible normal planes along the particle diameters. Even with a large estimate for the contact diameter, e.g. 1 μm, only about 3% of all possible arbitrary cross-sections along the particle diameter pass through the contact zones. The small inter-particle contact zones will, therefore, not be observable for most particles in an arbitrary cross-section through the ICA. Even though it looks like many of the particles are in contact in Fig. 1, increasing the magnification reveals that most particles in the cross-sections are separated by tens to hundreds of nanometers of epoxy. For particles where the cross-sections went through the contact zones, the polycrystalline grain structure was continuous over the contact zone, forming an uninterrupted metallurgical connection between the particles. The exception was the *pre-ET* 60Ag series, where no such metallurgical contacts were observed. In the *post-ET* 60Ag series, metallurgical contacts were present similar as in the series with thicker coatings. Representative cross-sections of the contact zones of the four ICA series can be seen for *pre-ET* samples in Fig. 4 and for *post-ET* samples in Fig. 5.

Grain Size

By directly measuring the widths of grain cross-sections, it can be observed that many grains were smaller than 50 nm for the 60 nm coatings. It should be noted that this procedure may

underestimate the grain size, as an arbitrary cross section can pass through all cut planes along a grain and not only where the grains are at their widest. The relative grain size seemed to increase for the 100 nm and 150 nm coatings. The 270 nm coatings on the other hand contained more small grains than the two coatings of intermediate thicknesses, but the thickest coatings also encompassed many abnormally large grains with cross-sectional widths of several hundred nanometres. After storage at 85°C/85% RH, these abnormally large grains were even more prominent.

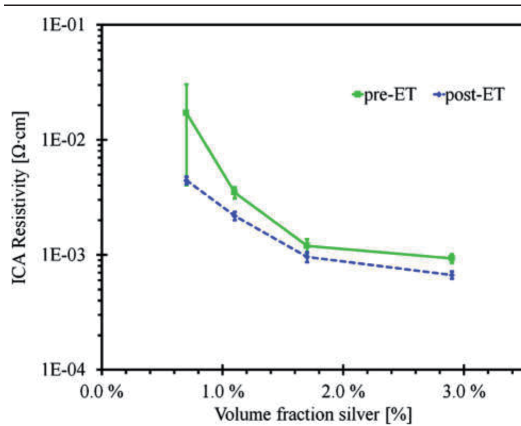

Fig. 3. Electrical resistivity of the four ICA series before (*pre-ET*) and after (*post-ET*) storage for 3 weeks 85°C and 85%RH, averaged from 48 measurements on six samples for each series. The error bars show ± one standard deviation.

DISCUSSION

Conduction and Resistance Mechanisms In AgPS-Based ICAs

Varying Coating Thickness

The electrical conduction in the AgPS-based ICAs requires a combination of conduction in the metal coatings and contacts between the particles. Both are expected to contribute to the resistivity of the ICA. The resistivities shown in Fig. 3 are calculated based on the bulk dimensions of the ICA samples. At about 56%, the volume fraction of particles was well above the percolation limit, which for 30 μm AgPS have been reported to be around 35%, with a slight dependence on coating thickness.[7] The particle volume fraction was almost identical in all four ICA series, and the number of potential parallel conducting pathways should thus be similar in all samples. As a first order estimate, it can be assumed that the conductive fraction of a cross-sectional area of the ICA will be equal to the volume fraction of silver. Increasing the silver coating thickness thus increases the total cross-sectional area of the parallel conducting pathways of the ICA samples. Effective resistivities for the different silver coating thicknesses can, therefore, be calculated by multiplying the measured resistivity of the ICAs by the volume fraction of silver. Figure 6 shows such effective resistivity values, where the ICA

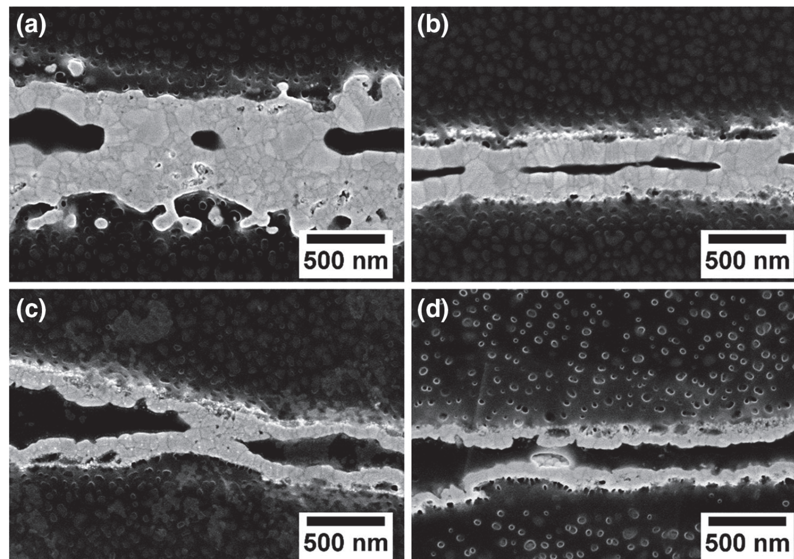

Fig. 4. Representative cross-sections of contact zones between two particles from 270Ag (a), 150Ag (b), 100Ag (c), and 60Ag (d) *pre-ET* ICA series, respectively. In the three thickest coatings, the metallurgic connections were observable in the contact zones. For the 60Ag *pre-ET* series, no such continuous contacts were observed.

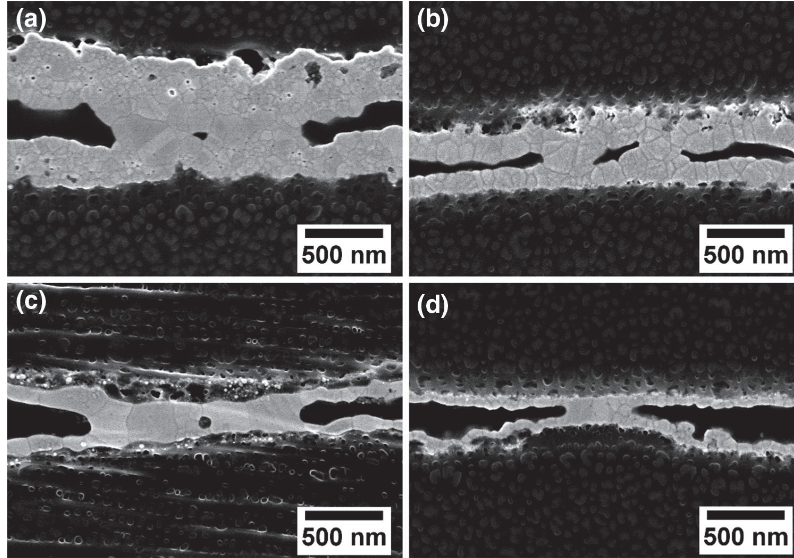

Fig. 5. Representative cross-sections of contact zones between two particles from 270Ag (a), 150Ag (b), 100Ag (c), and 60Ag (d) *post-ET* ICA series, respectively.

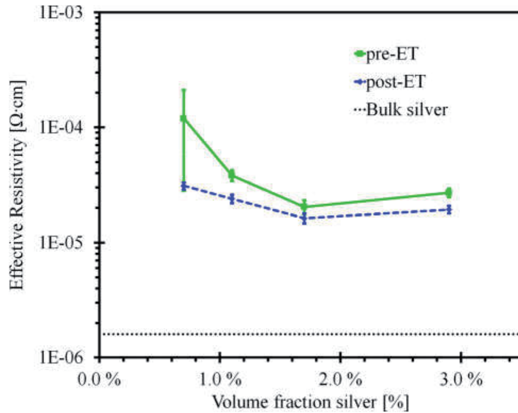

Fig. 6. Effective resistivity values for the conductive volume fraction of the four ICA series. Calculated by multiplying the measured ICA resistivity values before (*pre-ET*) and after (*post-ET*) storage for 3 weeks 85°C and 85%RH with the corresponding volume fractions of silver. The error bars show ± one standard deviation.

resistivity from each 4-pin measurement has been multiplied with the corresponding volume fraction of silver and further averaged for each ICA series.

By comparing the data in Figs. 6 to 3, it is clear that most of the differences in resistivity for the ICA series *post-ET* were due to the differing thickness of the silver coatings. However, it is obvious that also other factors influenced the ICA resistivity, especially for the *pre-ET* samples. If coating thickness was the only factor influencing the ICA resistivity, the effective values in Fig. 6 should be constant. Reasons for these deviations are discussed in the following sections. Additionally, a figure of merit (*FoM*) (1) can be defined based on the ratio between bulk silver resistivity and effective resistivity.

$$FoM_{\mathrm{ICA}} = \frac{\rho_{\mathrm{Met}}}{\rho_{\mathrm{ICA}} \times \Phi_{\mathrm{Met}}} \tag{1}$$

where ρ_{Met} is the bulk resistivity of the metal, ρ_{ICA} is the bulk resistivity of the adhesive and Φ_{Met} is the volume fraction of metal. Assessment of such values is a suitable method for characterizing and comparing the use of metal in the various ICAs, as an ICA in which the conductive volume fraction conducts current as well as bulk silver would yield a *FoM* value of 1. Calculated *FoM* values can be found in Table II, and reveal that although the lowest resistivity is achieved in the 270Ag ICAs, the volume of silver is more effectively utilized in the 150Ag series. For comparison, a good conventional flake-based ICA can be assumed to have a resistivity of about 2×10^{-4} Ω cm and a volume fraction of 25% silver. This yields a *FoM* value of 0.032, indicating that the utilization of silver is more effective in almost all the AgPS-based ICAs in the present study.

Inter-particle Contact Resistance

The values given in Figs. 3 and 6 are derived from measurements on the same samples *pre-* and *post-ET*, so the large decrease in resistivity and data spread for the ICA with the thinnest coatings

Table II. Figure of merit (*FoM*) values for the four ICA series, calculated from measured resistivities before (*pre-ET*) and after (*post-ET*) storage for 3 weeks 85°C and 85%RH

Series	*FoM* (*pre-ET*)	*FoM* (*post-ET*)
60Ag	0.01	0.05
100Ag	0.04	0.07
150Ag	0.08	0.10
270Ag	0.06	0.08

suggest that a substantial change occurred in the silver coating and/or the contacts between the particles as a consequence of the environmental exposure. This is supported by the SEM study of the ICA cross-sections, as the continuous metallurgical contacts observed in the 100Ag, 150Ag, and 270Ag series were not found in the 60Ag series before the environmental test. However, such metallurgical contacts were clearly observable in a sample from the 60Ag series after 3 weeks at 85°C/85%RH. These structures will have a large impact on the contact resistance between the particles, and it is reasonable that the absence of such contacts in the 60Ag *pre-ET* series would significantly increase the resistivity of this ICA. The classical contact resistance theory of Holm is based on two semi-infinite structures in contact through a small contact area.[10] In such structures the constriction resistance is caused by a local narrowing of the electrical field lines close to the contact. For a structure with a conductive shell and insulating core such as the AgPS, the constriction is caused by the decreasing cross-sectional area of the spherical coating as the current flows towards a contact. When the current reaches the contact zone, the electrical field lines bend and the current flows through the contact into the adjacent coating. If the contact zone has a radius larger than the coating thickness, and assuming that the whole contact area is in perfect metallic contact, the available area is actually such that the current may spread out through the contact. In addition, the effective length of the conductive path through the contact zone is in the same range as the thickness of the metal film. The radii of the observed metallurgical contacts were usually in the same range or wider than the film thicknesses. Some observed contact structures were narrower than this, but a random two-dimensional cross-section of a three-dimensional structure is not very likely to cut through the widest section of the structure, so the actual contacts may have been wider. Contrary to what expected from most other models for ICA resistance, it is clear that the resistance of these AgPS-based ICAs is not dominated by inter-particle contact resistance as long as these metallurgical contacts are formed. The main impact of further widening of the metallurgical contact areas will be a reduced constriction of the current flow and shorter conduction path in the coating, and not the lowered resistance in the actual contact zone. The appearance of these connections also suggests that any tunnelling contribution to the contact conductance is negligible.[10]

Coating Structure and Size Effects

The nature of the inter-particle contacts will have a large impact on the ICA resistivity, as discussed in the previous section, but as long as the metallurgical connections are present and have a radius larger than the coating thickness, the resistance contribution from these will be very small compared to the bulk coating resistance. As can be observed in Fig. 6, there was a decrease in effective resistivity with increasing coating thickness, even in the series where these metallurgical connections were present. The exception is the 270Ag series, where the effective resistivity increased slightly compared to the 150Ag series. Mayadas-Shatzkes theory predicts that for polycrystalline films where the grain size is close to or smaller than the bulk electron mean free path, scattering at the grain boundaries will have a significant contribution on the resistivity.[11] It could be observed directly from the SEM images that the thinnest coatings contained grains smaller than 52 nm, which is the mean free path length of electrons in bulk silver.[12] The 100Ag and 150Ag series also contained grains smaller than this threshold, although the average grain size seemed to increase with coating thickness for these. In contrast, the coatings of the 270Ag series were comprised of many grains smaller than the grains of the intermediate coating thicknesses, but at the same time this series contained the largest amount of abnormally large grains. Parts of the variation in the effective resistivity in Fig. 6 may originate from a size effect due to a decrease in the mean free path of the electrons. After the environmental test, even larger grains were observed, supporting grain growth as an explanation for the decreased resistivity in the *post*-ET samples. In previous work on AgPS-based ICAs, poor quality of the thinner coatings has been reported as a possible explanation for the higher resistivities of ICAs containing AgPS with thin coatings.[7] However, SEM observation of both individual particles and ICA cross-sections revealed that in this work, even the 60Ag particles are completely coated with silver, as can be observed in Fig. 2.

Mechanisms for Grain Growth and Metallurgical Contacts

Sintering of Nano-sized Grains

Sintering of nano-sized silver particles in conductive adhesives at 150°C, which also is the curing temperature used to prepare the ICA samples in this study, have been reported by several

authors.[13–15] However, the grain sizes observed in the SEM images were much larger than the particle sizes for which sintering at such low temperatures have been observed (below 20 nm), and thus the lowered sintering temperature of nanoparticles is not by itself a fully satisfactory explanation for the structural changes observed in the ICA samples in this study. Still, it should be noted that the grain sizes observed in the SEM images were those of already cured samples, and so the initial grain size of the silver coatings before curing may have been smaller.

Artefact Investigation

Images were acquired in the larger cross-sections only polished mechanically with SiC paper, and metallurgical contacts were observable also in these rougher areas. It cannot be ruled out that the metallurgical contacts in these regions were a result of plastic deformation due to the shear force from the mechanical polishing. However, as the average roughness of the SiC paper was 5 μm and the ion beam milled approximately 100 μm further down in the cross-sections, it is unlikely that the metallurgical contacts in the ion milled sections were caused by the mechanical polishing. To check if the metallurgical contacts could be a result of heating from the ion milling, a sample was ion milled with a metallic protective mask directly connecting the surface of the ICA with a continuously refilled reservoir of liquid nitrogen. The metallurgical contacts were present also in this sample cross-sectioned with cooling, supporting the assumption that these were not artefacts. However, these results still cannot completely rule out localized heating introduced by the ion beam, so this should be a subject for further investigations. It is also unlikely that these metallurgical contacts are artefacts from the coating procedure. The contacts seemed to occur between two fully formed coatings, where each coating displayed a thickness equal to the coating outside of the contacts. If the metallurgical connections were formed during the coating procedure, the film thickness through the metallurgical contacts should be significantly thinner and not the observed thickness of at least twice that of the coatings.

Thermal Expansion and Epoxy Shrinkage

Inter-particle pressures are expected to impact the formation of metallic contacts. Gakkestad and co-workers reported a linear coefficient of thermal expansion (CTE) of 203 ppm/K at 150°C for an ICA comprised of the same epoxy matrix, cured at the same conditions, and containing AgPS with the same PMMA cores as used in this work.[2] The authors found that ICAs with a volume fraction of 40% AgPS yielded similar CTE values as at 46%, which was identical as the CTE value of the epoxy matrix without particles. This suggests that the addition of AgPS have very little impact on the thermal expansion of the ICA. The reference linear CTE value for bulk PMMA above the glass transition temperature is 190 ppm/K, very close to that of the ICA at 150°C.[16] At approximately 19 ppm/K, the CTE of silver is just a fraction of the CTE of the polymers.[17] Moreover, the volume fraction of silver as well as the thickness of the coatings are small compared to that of the polymers, hence it is reasonable that the silver has a negligible impact on the thermal expansion of the ICA. If the thermal expansion of the epoxy matrix was much larger than that of the filler particles, this would be expected to draw the particles apart at elevated temperatures. As the thermal expansion of the PMMA cores is similar to that of the surrounding epoxy, such an effect should be negligible in these ICAs. Gakkestad and co-workers performed their measurements on already cured ICAs. During curing, we expect shrinkage of the ICA due to cross-linking of the epoxy matrix.[18] Shrinkage of the epoxy matrix in addition to thermal expansion of the PMMA cores will press the silver coatings into contact, and this inter-particle pressure should advance the formation of metallic contacts. As the ICAs cool down after curing, the PMMA cores and cured epoxy go through approximately the same degree of thermal retraction due to similar CTEs, and the inter-particle pressure is maintained. In addition, a compressive stress field will occur in the silver coatings that will press the grains together as long as the external pressure from the epoxy matrix is larger than the internal pressure from the PMMA cores. Oh et al. have done extensive research on the hillock or abnormal grain growth dynamics in sputtered Ag thin films due to stress migration.[19–22] When compressive stresses are induced in silver thin films, stress relaxation will lead to increased diffusion of silver atoms along the grain boundaries, which can cause grain growth on the film surfaces. A similar process may occur in the AgPS-based ICAs. As can be observed in Fig. 2, the particles were covered in small agglomerations of silver particles not incorporated in the coatings. It may be that these free silver nanoparticles helped create the initial inter-particle contacts, if they were present in between the particles in the contact zones when the particles were pressed together during curing. Asperities due to the inherent surface roughness of the coatings may have had the same effect. Post-curing and thus further shrinkage of the epoxy matrix have been used to explain further decrease in resistivity of already cured flake-based ICAs during storage at elevated temperatures.[1] For most of the samples in this study, there was a slight decrease in measured *post-ET* thickness, on average between 1% and 3% for all the ICA series, suggesting that there may have been some shrinkage due to post-curing of the epoxy matrix. However, this is in the smallest range measurable by the digital callipers, so this shrinkage is not certain.

Effect of Varying Stiffness Behaviour

The mechanical behaviour of the AgPS should be more influenced by the properties of the polymer cores as the coating thickness decreases. The 60Ag particles were thus softer than the particles with thicker coatings, and it may be that this affected the stresses in the silver films as well as inter-particle pressure in a way that inhibited the formation of the metallurgical contacts. Gakkestad et al. reported the glass transition temperature ($T_{g,epoxy}$) of a cured epoxy system equal to the one used in these ICA samples to be around 78°C.[2] The glass transition ($T_{g,PMMA}$) of similar PMMA cores as the ones used in this study was reported as about 122°C. This is higher than the glass transition temperature normally reported for PMMA, which is around 105°C, although some authors have reported $T_{g,PMMA}$ around this temperature.[16] During the environmental test in this study, the chamber temperature was 85°C; above that of $T_{g,epoxy}$, but lower than $T_{g,PMMA}$. Below the glass transition temperature, the polymer cores will behave stiffer and the thermal expansion coefficient will be smaller. In addition, there is a balance in the epoxy matrix between thermal expansion and possible shrinkage due to post-curing. These are all factors that will affect the type and magnitude of stress in the silver coatings, as well as the inter-particle pressure. The complex interplay between the temperature-dependent properties of the polymer components and the formation and growth of the metallurgical connections during harsh environmental testing are not clear from the present data, and should be a topic for further investigation.

Electrochemical Ostwald Ripening at High Humidity

The mechanisms suggested in the previous sections do not take into account possible effects from the high moisture content during environmental testing. A possible explanation for the decreased resistivity *post-ET* could be at least partly electrochemical in nature. Redmond et al. described how larger silver nanoparticles grow on the detriment of smaller particles when the particles are immersed in water and in electrical contact through a conductive substrate.[23] Because of size-dependent shifts in the standard electrode potentials of nanoparticles, smaller particles are more easily oxidized than larger, setting up a larger concentration of silver ions (Ag^{+}) around the smaller particles at equilibrium. A similar size-dependent shift in the work function means that electrons can escape more easily from smaller particles. At equilibrium, this creates partial positive charges in the smaller particles and partial negative charges in the larger particles, drawing Ag^{+} towards the larger particles. The ions are absorbed onto the larger particles, which re-establish electrical equilibrium by accepting electrons from the smaller particles through a conductive substrate, and the growth cycle continues. For AgPS-based ICAs the silver films could by themselves act as the conductive substrates. As long as Ag^{+} can diffuse through the water-saturated polymer network, the electrochemical Ostwald ripening proposed by Redmond et al. is a possible mechanism for grain growth during the environmental test, which would help explain the decreasing resistivity values.

CONCLUSIONS

When the silver flakes of conventional isotropic conductive adhesive are replaced by micron-sized polymer spheres coated with tens to hundreds of nanometers of silver, the result is a complex composite system with a large range of factors influencing the material properties. Such ICAs yield resistivities similar to conventional ICAs while using only a fraction of the silver content, but the conduction mechanisms responsible for this effective use of silver have not yet been properly understood. In this work, we showed that for ICAs prepared with approximately the same volume fraction of particles, but different estimated coating thicknesses (60 nm, 100 nm, 150 nm, and 270 nm), the electrical resistivity decreased with increasing coating thickness. The resistivity also decreased for all four ICA series after storage for 3 weeks at 85°C/85% RH. FE-SEM imaging of ion milled ICA cross-sections revealed the nano-grained structure of the silver coatings and that metallurgical connections wider than the thicknesses of the films were formed at the inter-particle contacts. When such contacts are formed, the ICA bulk resistance will not be dominated by the contact resistance, but instead by the conductivity and thickness of the silver coatings. Possible mechanisms for the formation of metallurgical connections during adhesive curing and environmental testing were suggested. Increased inter-particle pressures due to curing of the epoxy and thermal expansion of the polymer cores is a likely mechanism. Grain growth owed to elevated temperatures and electrochemical Ostwald ripening at high moisture contents are also likely contributing factors. Further work to understand these mechanisms should thus include investigating the impact of various curing conditions, as well as de-coupling the influence of temperature and humidity on this composite system.

ACKNOWLEDGEMENTS

The Research Council of Norway is acknowledged for funding through Project Number 225962/E20—“Novel conductive adhesive technology for solar industry”. Partial funding for this work was obtained from the Norwegian Ph.D. Network on Nanotechnology for Microsystems, which is sponsored by the Research Council of Norway, Division for Science, under Contract No. 221860/F40. Partial funding has also been obtained from the European Union Seventh Framework Programme FP7-NMP-

2013-LARGE-7 under Grant Agreement No 604668 ("Quantiheat") and by funding from the European Union Seventh Framework Programme (FP7/2007-2013) under Grant Agreement No FP7-NMP-310420 ("HyperConnect"). This work was supported by JSPS Core-to-Core Program, A. Advanced Research Networks. Hao Zhang and Jun Wang, both at The Institute of Scientific and Industrial Research, Osaka University, are gratefully acknowledged for their help with instrument training and sample preparation for SEM imaging. Lindberg & Lund AS (Vestby, Norway) are acknowledged for making available their adhesive lab for sample preparation. The authors of Ref. 2 are thankfully recognized for sharing their Thermal Mechanical Analyzer data on the epoxy matrix.

OPEN ACCESS

This article is distributed under the terms of the Creative Commons Attribution 4.0 International License (http://creativecommons.org/licenses/by/4.0/), which permits unrestricted use, distribution, and reproduction in any medium, provided you give appropriate credit to the original author(s) and the source, provide a link to the Creative Commons license, and indicate if changes were made.

REFERENCES

1. Y. Li, D. Lu, and C.P. Wong, *Electrical Conductive Adhesives with Nanotechnologies* (New York: Springer, 2010), pp. 121–225.
2. J. Gakkestad, Z. Li, T. Helland, and C.P. Wong, *IEEE Electron. Packag. Technol. Conf., 15th* (2013) doi:10.1109/EPTC.2013.6745715.
3. H.V. Nguyen, E. Andreassen, H. Kristiansen, and K.E. Aasmundtveit, *IEEE Trans. Comp. Packag. Manuf. Technol.* (2013). doi:10.1109/TCPMT.2013.2259166.
4. H.V. Nguyen, E. Andreassen, H. Kristiansen, R. Johannessen, N. Hoivik, and K.E. Aasmundtveit, *Mater. Des.* 46, 784 (2013).
5. S. Jain, D.C. Whalley, M. Cottrill, H. Kristiansen, K. Redford, C.B. Nilsen, T. Helland, and C. Liu, *Microelectronics and Packaging Conference (EMPC), 2011 18th European* (Brighton, UK 2011).
6. S. Jain, D.C. Whalley, M. Cottrill, H. Kristiansen, K. Redford, S. Helland, T. Helland, E. Kalland, and C. Liu, *Microelectronics Packaging Conference (EMPC), 2013 European* (Grenoble, France 2013).
7. S. Jain, D.C. Whalley, M. Cottrill, T. Helland, H. Kristiansen, K. Redford, and C. Liu, *IEEE Electron. Compon. Technol. Conf.* (2013). doi:10.1109/ECTC.2013.6575664.
8. G.R. Ruschau, S. Yoshikawa, and R.E. Newnham, *J. Appl. Phys.* 72, 953 (1992).
9. D. Lu, Q.K. Tong, and C.P. Wong, *Proc. Int. Symp. Adv. Packag. Mater.: Processes, Prop. Interfaces* (1999) doi: 10.1109/ISAPM.1999.757278.
10. R. Holm, *Electric Contacts: Theory and Application*, 4th ed. (Berlin: Springer, 2000), pp. 1–16, 118–134.
11. A.F. Mayadas and M. Shatzkes, *Phys. Rev. B* 1, 1382 (1970).
12. U. Kreibig and C.V. Fragstein, *Z. Phys.* 224, 307 (1969).
13. H. Jiang, K.S. Moon, J. Lu, and C.P. Wong, *J. Electron. Mater.* 34, 1432 (2005).
14. H. Jiang, K.S. Moon, Y. Li, and C.P. Wong, *Chem. Mater.* 18, 2969 (2006).
15. Y. Li, K.S. Moon, and C.P. Wong, *J. Appl. Polym. Sci.* 99, 1665 (2006).
16. J. Brandrup, E.H. Immergut, E.A. Grulke, A. Abe, and D.R. Bloch, *Polymer Handbook*, 4th edn. vol. 1. (Wiley, New York, 1999), pp. V/87, VI/203–VI/204.
17. D.R. Lide, *CRC Handbook of Chemistry and Physics*, 84th ed. (Boca Raton: CRC Press, 2003), pp. 12–220.
18. E.M. Petrie, *Epoxy Adhesive Formulations*, 1st ed. (New York: McGraw-Hill Education, 2006), pp. 57–58.
19. C. Oh, S. Nagao, T. Kunimune, and K. Suganuma, *Appl. Phys. Lett.* 104, 161603 (2014).
20. C. Oh, S. Nagao, and K. Suganuma, *J. Electron. Mater.* 43, 4406 (2014).
21. C. Oh, S. Nagao, T. Sugahara, and K. Suganuma, *Mater. Lett.* 137, 170 (2014).
22. C. Oh, S. Nagao, and K. Suganuma, *J. Mater. Sci.: Mater. Electron.* 26, 2525 (2015).
23. P.L. Redmond, A.J. Hallock, and L.E. Brus, *Nano Lett.* 5, 131 (2005).

Paper IV

Controlling the Conduction Mechanisms in Isotropic Conductive Adhesives with Silver-Coated Polymer Spheres

Sigurd R. Pettersen, Helge Kristiansen, Keith Redford, Susanne Helland, Erik Kalland, Zhiliang Zhang, and Jianying He.

IEEE 66th Electronic Components and Technology Conference (ECTC), Las Vegas, NV, USA, 31 May-3 June 2016. **DOI**: 10.1109/ECTC.2016.53

Is not included due to copyright

Paper V

Room-temperature curing and grain growth at high humidity in conductive adhesives with ultra-low silver content

Sigurd R. Pettersen, Keith Redford, John Njagi, Helge Kristiansen, Susanne Helland, Erik Kalland, Dan V. Goia , Zhiliang Zhang, and Jianying He.

Journal of Electronic Materials, submitted.

Room-temperature curing and grain growth at high humidity in conductive adhesives with ultra-low silver content

Sigurd R. Pettersen [1], Keith Redford [2], John Njagi [3], Helge Kristiansen [1, 2], Susanne Helland [4], Erik Kalland [4], Dan V. Goia [3], Zhiliang Zhang [1], and Jianying He [1,a)].

[1] NTNU Nanomechanical Lab, Department of Structural Engineering, Norwegian University of Science and Technology (NTNU), NO-7491, Trondheim, Norway.

[2] Conpart AS, Dragonveien 54, NO-2013, Skjetten, Norway.

[3] Center for Advanced Materials Processing, Clarkson University, Potsdam, NY 13699-5814, USA.

[4] Mosaic Solutions AS, Dragonveien 54, NO-2013, Skjetten, Norway.

Isotropic conductive adhesives (ICAs) are alternatives to metallic solders as interconnects in solar modules and electronic devices, but normally require silver contents > 25 vol% and elevated curing temperatures to achieve reasonable conductivity. In this work, ICAs are prepared with a silver content of 1.0 vol% by using polymer spheres coated with nanograined silver thin films as filler particles. In contrast to conventional ICAs, there are no organic lubricants on the film surfaces to obstruct the formation of metallic contacts, and conductivity is achieved even when the adhesive is cured at room temperature. When exposed to long-term storage at 85 °C and 85 % relative humidity, the silver films undergo significant grain growth, evidenced by FEG-SEM observation of ion-milled cross-sections and x-ray diffraction (XRD). This has a positive effect on the electrical conductivity of the ICA through the widening of metallic contacts and decreased scattering of electrons at grain boundaries, and is explained by an electrochemical Ostwald ripening process. The effects of decoupling heat and humidity is investigated by storage at either 85 °C or immersion in water. It is shown that the level of grain growth during the various post-curing treatments is dependent on the initial curing temperature.

[a)] Author to whom correspondence should be addressed. Electronic mail: jianying.he@ntnu.no.

Keywords: conductive adhesives; silver thin films; grain growth; electrochemical Ostwald ripening; electrical conductivity; curing.

1. Introduction

Electrically conductive adhesives (ECAs) have been available as alternatives to metal solder interconnects in electronic devices for decades, and have more recently been shown as very promising materials for interconnecting metallic ribbons to crystalline solar cells [1-6]. Isotropic conductive adhesives (ICAs) are ECAs containing filler particles, conventionally silver flakes, at a large enough volume fraction (vol%) that a percolating conductive network is formed throughout the polymer adhesive, normally a thermoset epoxy [7, 8]. Commercial flake-based ICAs typically reach bulk resistivity values around $1 \cdot 10^{-4}$ Ω·cm, but they require a high silver content, usually in the range of 25 – 40 vol% [8-10]. Despite the name, flake-based ICAs can exhibit large anisotropies in the conductive properties, due to the tendency of silver flakes to align with the shear flow direction during processing [10]. ICAs require curing (i.e. cross-linking) of the epoxy matrix to become electrically conductive, as curing induces shrinkage or compressive stress which leads to the formation of electrical contacts between the fillers [9, 11]. To increase the curing rate and epoxy conversion (i.e. percentage of cross-linked epoxide groups), ICAs are cured at elevated temperatures, usually in the range of 120 – 150 °C, although the optimal curing temperature depends on both the epoxy system and curing method [12]. Many substrates for flexible electronics require processing temperatures of 150 °C or below to avoid thermal deformation or degradation [13-15], while silicon solar cells have been shown to fully avoid bending induced by thermal mismatch between the silicon and metallic ribbons only at temperatures below 100 °C [4, 5, 16], making ICAs very suitable interconnection alternatives for these applications. The main reasons why ICAs are still only niche products in electronic devices and have not yet been fully adopted by the solar module industry are reliability concerns and high material costs. The first point is most often investigated by accelerated aging tests such as thermal cycling or long-term storage at high temperature and high humidity conditions. To reduce silver content, several groups have suggested coating silver onto cheaper materials, most commonly copper powder [17-19]. These still contain large amounts of metal (> 80 wt%), yielding low resistivity but generally at the expense of high brittleness [20].

In later years, micron-sized polymer spheres coated with silver thin films (AgPS) have been introduced as alternative fillers in ICAs [21-24]. Such AgPS-based ICAs yield bulk resistivities as low as $6 – 7 \cdot 10^{-4}$ Ω·cm while containing less than 3 vol% silver, and due to the spherical geometry and densities close to the epoxy matrix, the ICAs are truly isotropic [22, 23]. High-

resolution field-emission scanning electron microscopy (FEG-SEM) investigation of broad beam ion milled cross sections has revealed that the silver films of AgPS in ICAs cured at 150 °C for 30 min are sintered together and form continuous metallurgical contacts [23]. The same method has shown that metallic contacts are formed between AgPS even when the epoxy is cured at room temperature, although these appear to be mechanically connected by compressional stresses from the epoxy matrix, and not the continuous structures observable when the ICAs are cured at 150 °C [24]. This is supported by electrical measurements, as the conductivity is several times higher when the ICA is cured at 150 °C than at room temperature.

AgPS-based ICAs also show a substantial decrease in resistivity when the ICAs are stored over time at 85 °C/85 % relative humidity (RH) [23, 24]. This is connected to a significant grain growth observed in the cross-sections of the silver films after these storage conditions, which lead to even wider and more intimate metallic contacts. It has been hypothesized that this grain growth is caused by electrochemical Ostwald ripening, at which larger grains grow by consuming smaller grains if these are in electrical contact and in contact with water [23-25]. A newly developed four-point method for probing individual AgPS have revealed that the resistivity of the spherical silver thin films is higher than that of bulk silver [26]. The silver thin films are coated onto the polymer cores by electroless plating, which yields granular thin film structures with thicknesses and grain sizes in the same range or smaller than the electron mean free path length (EMFP) of bulk silver [23, 26]. At such dimensions, electron scattering at the film surface and grain boundaries will occur more frequently than in bulk silver, which increases the resistivity [27-30]. A natural inference from these results is that larger grains should yield lower resistivities in AgPS and thus also in ICAs. However, the changes in grain size during high humidity storage have previously only been observed in FEG-SEM images of cross-sections [23, 24], and the effects of moisture and temperature have not yet been fully separated.

In this work, an AgPS-based ICA was cured at different temperatures and further exposed to long-term storage at either 85 °C, 85 °C/85 % RH, or immersion in de-ionized (DI) water at room temperature (RT). Silver grain size was estimated by x-ray diffraction (XRD), and the structure of the contacts were investigated by broad ion beam cross-sectioning and FEG-SEM imaging. The resistivity was measured by a four-wire procedure. To ensure equal starting conditions, all ICA samples were prepared together from the same mix of epoxy and AgPS. It is found that the electrical resistivity decreases and the grain size increases with increasing

curing temperature. The evolution of the resistivity as well as the grain size development during the various environmental exposures is found to depend heavily on the initial curing temperature.

2. Methods and materials

Poly(methyl methacrylate) (PMMA) spheres with a nominal diameter of 30 µm (coefficient of variation ≤ 5 %), coated with silver to a nominal silver film thickness of 100 nm in an electroless plating procedure, were provided by Mosaic Solutions AS (Skjetten, Norway). The plating process yielded a continuous, granular thin film structure, as can be observed in Fig. 5 a). A low viscosity epoxy resin consisting of a mixture of bisphenol A and bisphenol F epoxy (Araldite PY-302-2, Huntsman Corporation, USA) was blended with a low viscosity polyetheramine curing agent (Jeffamine D-230, Huntsman Corporation, USA) at a ratio of 1:0.35 by weight. The density of the uncured resin and curing agent were given as 1.18 g/cm^3 and 0.95 g/cm^3 by the manufacturer, while the PMMA cores had a nominal density of 1.16 g/cm^3. AgPS were stirred into the epoxy mix at a weight fraction (wt%) of 55 %, corresponding to 51 vol% AgPS, and mixed two times at 2000 rpm for 2.5 min using a centrifugal mixer (SpeedMixer DAC 150.1 FVZ-K). The content of silver was estimated to 1.0 vol%, or 8.5 wt%. ICA was stencil printed as strips onto PCB boards for electrical measurements as described by Jain et al. [21] or into polytetrafluoroethylene (PTFE) molds to prepare pure, detached ICA bricks with dimensions 1 mm x 1mm x 0.1 mm for cross-sectioning and imaging (see Pettersen et al. [23] for details), as well as for XRD. The samples were divided into three series and cured at ambient lab conditions (approx. 20 °C and 20 %RH) for > 240 h, at 85 °C for 420 min, or at 150 °C for 30 min. The curing times were taken from the manufacturer data sheets. The curing series are named RT, 85 °C, and 150 °C, respectively.

Both ICA strips and bricks from each curing series were split into three parallels and stored at: i) 85 °C / 85 %RH in an environmental chamber (VCL 7006, Vötsch Industrietechnik, Germany) for 480 h, ii) 85 °C in a convection oven (art. no. 9010-0082, Binder, Germany) for 480 h, or iii) long-term storage (> three months) at ambient lab conditions followed by full immersion in DI water at ambient lab temperature for 260 h. The parallels are named 85 °C /85 %RH, 85 °C, or WI, respectively. See Fig. 1 for an overview of the sample preparation and environmental exposure.

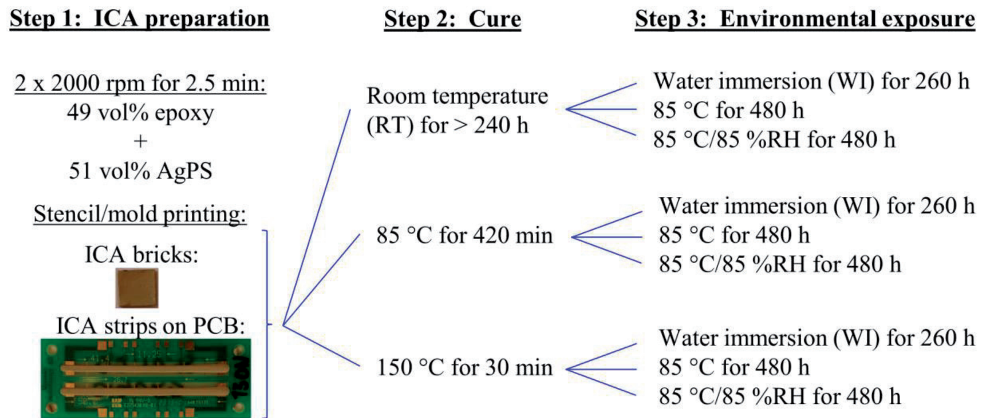

Fig. 1. Overview over ICA sample preparation, curing temperature series, and environmental exposure parallels.

Four-wire resistance measurements were conducted on the stencil printed ICA strips using a Keithley 3706 System Switch/Multimeter, as described by Jain et al. [21]. Resistivity (ρ) was calculated by $\rho = R \cdot w \cdot t / l$, where R is the measured resistance, w and t are the width and thickness of the metal stencil used for printing the strips, 2 mm and 0.2 mm, respectively, and l is the length between the voltage contacts on the strips.

Crystallographic data on the silver films of the ICA was acquired with a Bruker-AXS D8 Focus X-ray diffractometer. The scanning step width was 0.03 degree, the step period 2 sec, while the source, sample, and detector slits were 2.0, 0.6, and 0.1 mm, respectively. The data were processed through Rietveld refinement with TOPAZ Academic software, and the grain sizes were determined using the Scherrer equation [31, 32].

An IM4000 argon ion milling system (Hitachi, Japan) was used to cut cross-sections approximately 0.1 mm into the edge of the detached ICA pieces. The instrument was run in cross-sectioning mode, with an acceleration voltage of 4 kV and a milling time of 6 hours per sample. The cross-sectioned surfaces were imaged with FEG-SEM (Ultra 55 limited edition, Zeiss, Germany) at an acceleration voltage of 2 kV, using an in-lens secondary electron detector.

3 Results

3.1 Evolution of resistivity

29 h after preparation, the average resistivity of the RT series was 7.7×10^{-3} Ω·cm, with a standard deviation of 1.7×10^{-3} Ω·cm for 30 ICA strips (n = 30). At this point, the epoxy had gelled, but not fully cured. After 264 h, the RT series had surpassed the curing time given in the datasheet and the resistivity decreased to $7.0 \times 10^{-3} \pm 1.5 \times 10^{-3}$ Ω·cm. The 85 °C and 150 °C series were cured immediately after preparation, and yielded resistivities $3.0 \times 10^{-3} \pm 0.4 \times 10^{-3}$ Ω·cm (n = 28) and $1.5 \times 10^{-3} \pm 0.1 \times 10^{-3}$ Ω·cm (n = 28), respectively, after curing. The WI parallels were stored for > three months at ambient lab conditions before being immersed in water and showed no change in resistivity during that period. It should be emphasized that the standard deviations are due to scatter between the individual ICA strip resistances, and that this scatter decreased in both absolute and relative values as the curing temperature increased. The average resistivity of each parallel was thus different from the total series average, even before the long-term environmental exposures. Every individual ICA strip followed the resistivity development of its parallel, shown in Fig. 2 and Fig. 3.

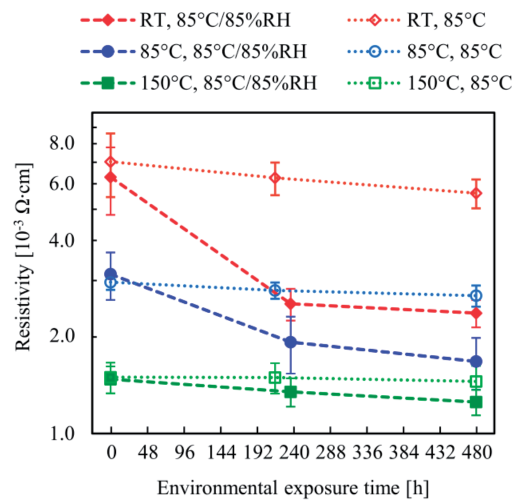

Fig. 2. Resistivity development of the series cured at room temperature (RT), 85 °C or 150 °C as a function of time stored at either 85 °C or at 85 °C / 85 % RH. The error bars show ± 1 standard deviation.

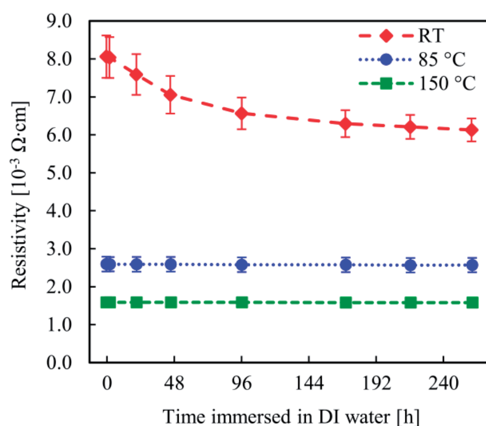

Fig. 3. Resistivity development of the series cured at room temperature (RT), 85 °C or 150 °C as a function of time immersed in DI water. The error bars show ± 1 standard deviation.

3.2 Grain sizes

As shown in Fig. 4, the ICA yielded XRD spectra with five distinct peaks at around 38, 44, 64, 77, and 81 °. The peak at 38 ° was the most intensive for all samples. The grain sizes estimated from this peak before and after the three post-treatment parallels for all three curing series can be found in Table I. XRD spectra for the 85 °C and 150 °C curing series as well as estimated grain sizes from all diffraction peaks can be found in the supplementary material.

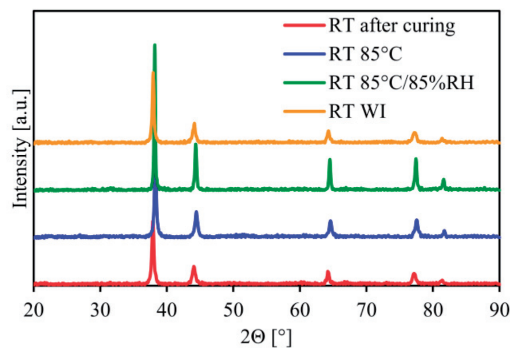

Fig. 4. XRD spectra for the ICA series cured at room temperature before and after the three parallel environmental exposures.

Table I. Grain sizes calculated from the peaks with highest intensity (≈ 38 °) for all three curing series before and after environmental exposure.

Series/Parallel	After curing [nm]	85 °C [nm]	85 °C /85 %RH [nm]	WI [nm]
RT	28.9	36.3	65.4	35.4
85°C	32.0	33.1	48.3	32.7
150°C	34.3	33.6	38.3	34.1

3.3 FEG-SEM cross-section investigation

Fig. 5 a) shows that the AgPS are monodisperse in size, with diameters around 30 μm. When mixed in epoxy to form an ICA, the AgPS are randomly dispersed, and a two-dimensional cross section can thus reveal cut planes along the whole diameter of the AgPS, as seen in Fig. 5 b). Fig. 6 shows contact structures in cured samples before as well as after the three environmental exposure parallels of the RT series. As seen in Fig. 6 a), a metallic contact have formed between two AgPS, with the original film surfaces still clearly traceable along the contact interface. However, many of the films in close vicinity observable in the two-dimensional cross-sections were not in metallic contact, as illustrated in Fig. 6 b). This can be either because the cross-sectional plane does not cut through the area in the three-dimensional contact structure where the films are in metallic contact, or because there is no metallic contact between the films of these specific particles. The presence of such contact structures where the silver films are separated by only a few nm of epoxy supports the assumption that the metallic contacts observed between other films in the cross-section are not artefacts from the ion milling process, as discussed in more detail in [23]. No large changes in the structure of the films and contacts are observed after storage at 85 °C without elevated humidity, as shown in Fig. 6 c), nor after immersion in water, as can be observed in Fig. 6 d). After storage at 85 °C/85 %RH, significant grain growth is observed along the whole circumference of the silver thin films. As can be seen in Fig. 6 e), this leads to wide, continuous metallurgical contacts. ICAs cured at elevated temperatures show the same behavior, although with a tendency toward metallurgical contacts before post-curing treatments, and significant grain growth after storage at 85 °C/85 %RH, as can be observed in the supplementary material as well as in [23, 24].

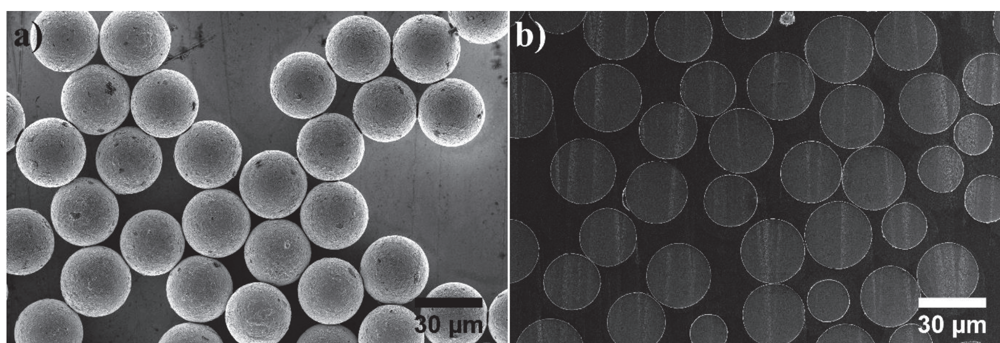

Fig. 5. (a) 30 μm PMMA spheres coated with 100 nm silver (AgPS). (b) Ion-milled cross-section of 51 vol% AgPS embedded in epoxy, i.e. an ICA with 1.0 vol% silver.

4 Discussion

4.1 Conductivity after room-temperature curing

The resistivity of this ICA decreases with increasing curing temperature, which is consistent with previous reports on both conventional [33-35] and AgPS-based [21, 24] ICAs. This is caused by a more densely cross-linked epoxy matrix, leading to higher inter-particle pressures and thus larger and more intimate contacts, as well as likely sintering of the silver films [23, 24]. However, relatively low resistivities are achieved in AgPS-based ICAs even when the samples are cured at room temperature. Furthermore, the ICA is conductive already after 29 h at room temperature, at which the epoxy matrix have gelled, but not fully cured. The resistivity does not decrease much during the next 211 h, which is approximately the period required for the epoxy to reach its full cross-linking potential at room temperature. The epoxy system used in this investigation thus provides enough compressional stress for electrical contacts to be formed between the AgPS already in its gelled state, i.e. before it is fully cured and hardened. Further long-term storage (> 3 months) at the same, ambient conditions does not lead to additional decrease in resistivity.

As seen in Fig. 6 a), metallic contacts are formed between the surfaces of the silver films, although the original film surfaces are clearly observable along the contact interface, suggesting pressure-induced contacts in the ICAs cured at room-temperature. In conventional ICAs, a thin layer of lubricant in the form of carboxylate salts is present on the surface of the silver flakes [15, 36]. This lubricant layer is a leftover from the silver flake production process, and prevents the flakes from agglomerating. It is also detrimental to the conductivity of the ICA, although

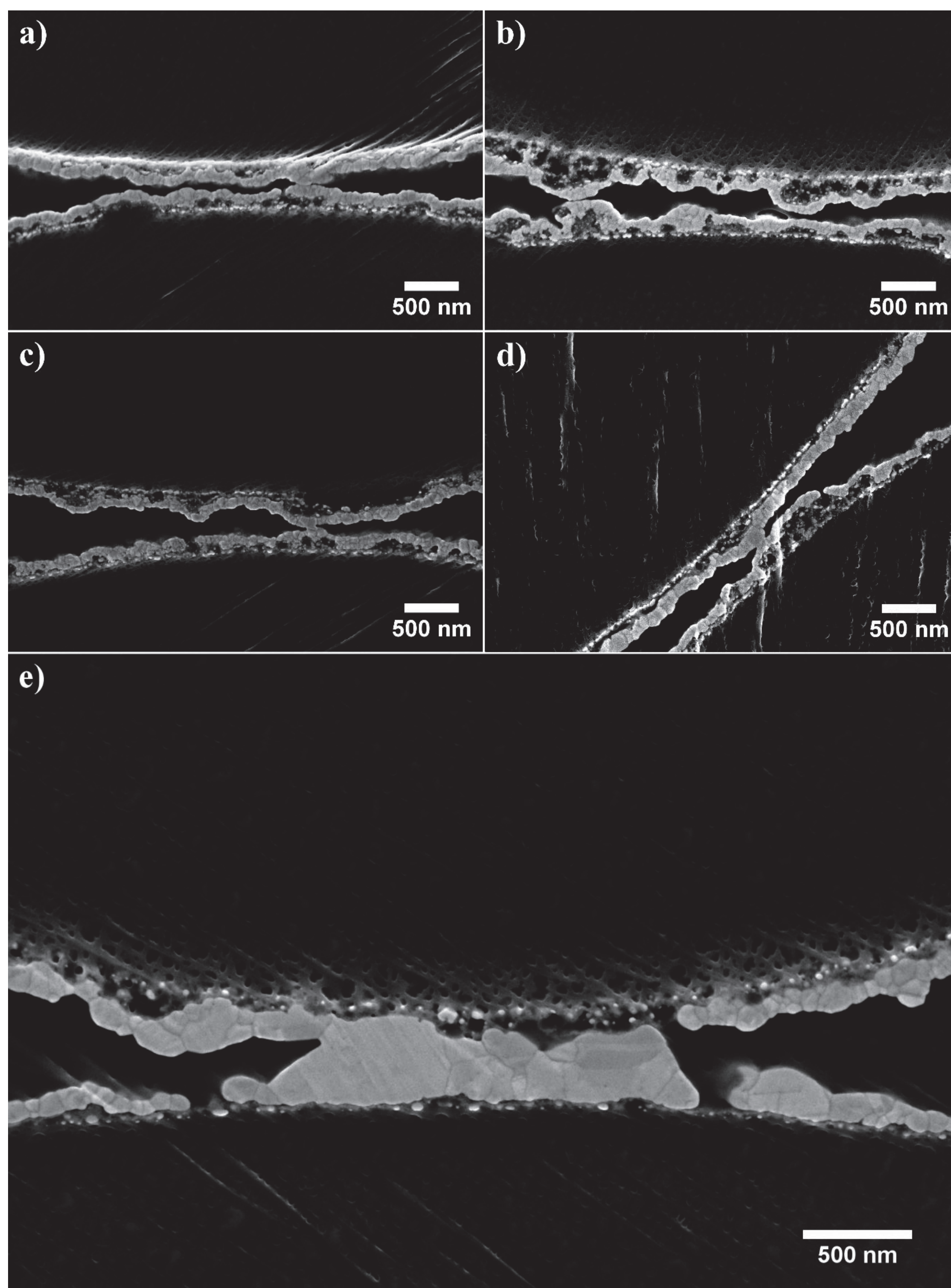

Fig. 6. Contact structures of the various parallels of the RT series. Metallic (a) and non-metallic (b) contacts before environmental storage, and metallic contacts after storage at 85 °C (c), immersion in water (d), and at 85 °C/ 85 %RH (e).

lubricant removal is not a prerequisite for achieving conductivity [36]. This is because electrical contacts also can be non-metallic, as electrons can cross a thin (< about 10 nm) non-conductive layer by quantum tunnelling [37]. However, the resistance contribution from a non-metallic contact will be much higher than that of a metallic contact of the same size. Zhang et al. showed that by using epoxies with mild reducing capacities, the silver carboxylate salts could be reduced and removed, allowing metallurgical joints to form between the silver flakes when cured at 150 °C [15]. This yielded resistivities as low at 2.5×10^{-5} Ω·cm with 80 wt% silver flakes, an order of magnitude lower than conventional ICAs. The reduction was only reported for elevated temperatures, so such a method might not be usable for room-temperature curing. Still, from this and other investigations, it is clear that a reduction or removal of the lubricant layer and/or oxide layer on silver flakes allows for ICA with low resistivities due to the formation of mechanical metallic contacts and even sintered metallurgical contacts [38]. These contacts can be formed either directly between the silver flakes, by sintering of nanoparticles, or reduction of silver salts. Contrarily, the AgPS do not have any lubricants on the surface of the silver films, and should theoretically be able to form metallic contacts if the silver films can penetrate the intermediate epoxy. It can be observed from the cross-sections that asperities on the silver films are pressed into contact with adjacent films even with curing at room temperature. Such contacts are likely initial spots for the sintering of metallurgical contacts at elevated temperatures. A certain amount of surface roughness and asperities on the silver film surfaces may thus be beneficial for the conductivity of the ICAs.

4.2 Grain size and growth effect on resistivity

The grain sizes increase for all curing series during most of the environmental exposures, and here is an obvious correlation between the level of grain growth and the resistivity. The resistivity of the RT series decreases from an average value of 7.0×10^{-3} Ω·cm to 5.6×10^{-3} Ω·cm and 6.1×10^{-3} Ω·cm at the last measurements of the 85 °C and WI parallels, respectively. The corresponding grain sizes estimated from the peak at 38 ° increase from 28.9 nm to 36.3 nm and 35.4 nm, respectively. For the 85 °C/85 %RH parallel of the RT series, the final resistivity is 2.4×10^{-3} Ω·cm and the grain size 65.4 nm. For the 85 °C and 150 °C series, grain growth also occurs during curing, with higher curing temperatures yielding larger grains, which also correlates with the decreasing resistivity at elevated curing temperatures.

When the grain size of metal thin films becomes smaller than the EMFP of the bulk metal, electron scattering at the grain boundaries will occur more frequently and the resistivity

increases above that of the bulk metal [29, 30]. The EMFP of bulk silver is 52 nm [39], and individually measured single AgPS with grain sizes below this limit have indeed been shown to have higher resistivities than bulk silver [26]. However, although the trends in the grain growth correlate with the development in resistivity, the absolute values do not. The 150 °C series yield lower resistivities than the 85 °C/85 %RH parallel of the RT series even before any environmental exposure, although the latter yields the largest grain size and is the only parallel where the grain size is larger than the EMFP of bulk silver. This suggests that an effect of grain size on the intrinsic resistivity of the silver films is only one of several contributions to the bulk resistivity of the ICA, and not the most important.

During storage at 85 °C/85 %RH, the number of observed metallic contacts in the cross-sections increases, as does the average width of the contacts [24]. When the cross-sectional area of a conductor decreases, this will cause a constriction resistance [37]. Wider contacts decrease this constriction resistance, as well as decreasing the length between the contacts, which will reduce the overall resistance [23]. The widening of the contacts is connected to the significant grain growth occurring at these conditions. For the 150 °C series, this widening and change in the contact structures only leads to a small decrease in bulk resistivity, from $1.5 \cdot 10^{-5}$ to $1.3 \cdot 10^{-5}$ Ω·cm. This suggests that the contacts of the 150 °C series after curing are so intimate and wide that there is not much more to gain in reduced contact and constriction resistance by further widening. For the 85 °C series and even more for the RT series, the gains in reduced resistivity from the increased contact areas are larger, supporting the assumption that these were not as wide and intimate as the 150 °C series after curing.

4.3 Grain growth mechanisms

Theoretically, two perfectly flat and clean metallic surfaces will spontaneously form bonds through inter-atomic forces when brought into contact [40]. Contaminations are obstacles against such bonding, but these can be overcome by adding energy through heat or pressure [38]. For nanoscale contacts, the probability to encounter defects are much smaller due to the small contact areas, and these require less energy to achieve metallic bonding via interdiffusion compared to macroscale bonding. Due to a large surface-to-volume ratio, the grains of the silver thin films will also be more reactive and sensitive to heat than the larger grains of bulk silver. From the XRD results it is evident that there is a certain amount of grain growth due to the additional heat induced by the elevated curing temperatures.

It is also clear that any further grain growth after the primary curing is influenced by the initial curing temperature. Although the measured resistivities and FEG-SEM images suggest that compressive stresses from the epoxy matrix are larger for the ICAs cured at elevated temperatures, the grain growth during the environmental exposures is largest in the RT series, implying that the compressive stresses are not the main factor influencing the grain size. The number of non-reacted amine groups on the polyetheramine crosslinker molecules is higher in the ICAs cured at lower temperatures. If these function as coordinating ligands for the silver ions, more ions can be mobile at a given time, which will change the equilibrium concentration of ions and thus increase the reaction rate of the silver grain growth. Alkylamines can form complexes with silver ions, and have been used to stabilize and disperse silver nanoparticles [41-43], supporting the feasibility of this mechanism. A certain amount of the decrease in resistivity at elevated temperatures may be ascribed to further cross-linking by post-curing, as this process naturally will be higher for the epoxies with more non-reacted groups. However, post-curing does not explain the differences in grain growth, nor the large difference between the 85 °C and 85 °C/85 %RH environmental exposure parallels.

The most prominent result in the grain size development, supported by both cross-sections and XRD, is that there is significant grain growth when the ICAs are saturated with water. The grain size increases more when the samples are stored at 85 °C/85 %RH than when the samples are fully immersed in water at room temperature, suggesting that although water is a driving factor for grain growth, the process is accelerated by higher temperatures. According to Gakkestad et al., the glass transition temperature (T_g) of the same epoxy system as used in this work is 78 °C when the ICA is cured at 150 °C for 30 min [22]. T_g is a function of conversion of the epoxy [44, 45], and the thermal expansion of the ICAs increases above the glass transition [22]. Thus, the thermal expansion at 85 °C should be higher for the ICAs cured at lower temperatures. This yields less compressive stresses, but will also increase the volume available for water absorption.

The grain growth process observed here can be explained by an electrochemical Ostwald ripening process, as introduced by Redmond et al [25]. There is a negative shift in the standard electrode potential of small metal particles, especially prominent for particles with diameters < 20 – 30 nm, causing smaller particles to oxidize more easily and more readily release ions than larger particles of the same material. The equilibrium concentration of silver ions will therefore be larger around smaller particles. For small particles in water, there will also be a depression

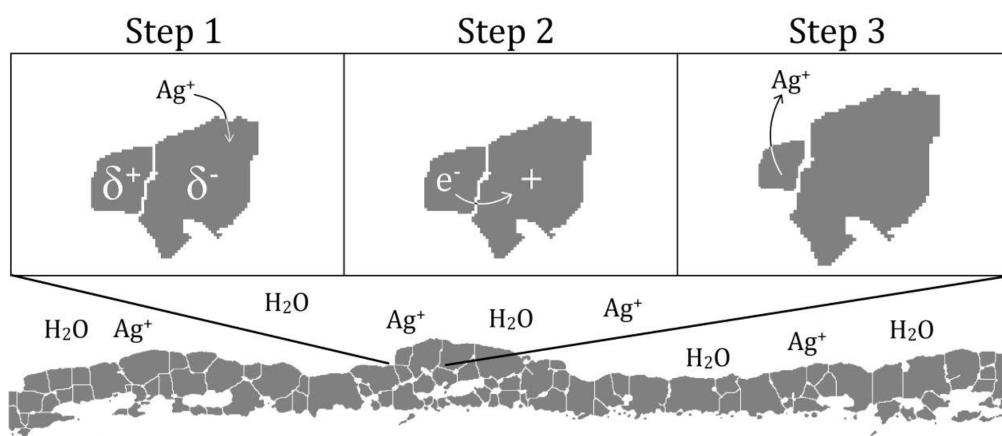

Fig. 7. Illustration of the electrochemical Ostwald ripening process in silver thin films.

of the work function, and smaller particles will release electrons more easily than larger particles. At electrical equilibrium there will thus be a partial positive charge on smaller particles and a partial negative charge on larger particles, setting up an electrical field that will draw silver ions towards the larger particles. The grain growth process is illustrated in Fig. 7. The silver ion accepts an electron and is incorporated onto a larger grain (step 1). The larger grain accepts an electron from the smaller grain to re-establish electrical equilibrium (step 2). The process thus demands that the reacting grains are in electrically conductive contact, either directly or through intermediary grains or a conductive substrate. For electrical equilibrium to be re-established also in the smaller, now even more positively charged grain, it releases a silver ion (step 3) and the growth cycle can continue. Although Redmond et al. investigate the process for individual silver particles on conductive substrates [25], they find several examples of thin films in literature that can be explained by the same process. A controlling factor is the diffusion of silver ions from the smaller to the larger grains, which means that the rate of the process increases with elevated temperature. The process will also be dependent on the amount of dissolved silver ions, and is thus in line with the previous hypothesis of non-reacted amine groups functioning as coordinating ligands.

4.3 Long-term stability

The grain structure of the silver films is not energetically stable, as evident from the grain growth first during elevated curing temperatures and further during the various environmental conditions. However, it is also evident that the ICAs are partially stabilized after the initial grain

growth during curing at elevated temperatures. Both the 85 °C and 150 °C series require simultaneous exposure to both elevated temperature and moisture (85 °C/85 %RH) before any substantial changes in the structural and electrical properties occur. The RT series is more vulnerable, as this shows grain growth both after storage at 85 °C and after immersion in water. Over the periods of time investigated in this work, the net effect of grain growth on the electrical properties of the ICAs is positive. However, in a real application where the ICA is used as an electrical interconnect, this may not be the case if there is silver migration towards only one side of the contact due to an electrical field. Further studies should thus investigate the electrical properties of ICAs under influence of a bias voltage, as well as means for controlling the grain growth process. According to Redmond et al., the electrochemical Ostwald ripening process is accelerated by silver nitrate and slowed down by sodium nitrate, and also sensitive to pH [25], whereas this work implies that the role of amines is worth further investigation.

5 Conclusion

This investigation show that both the stability and electrical conductivity of ICAs with ultra-low silver content increase with increasing isothermal curing temperature. However, reasonable conductivity is achieved already after gelling, when the curing temperature is not elevated above room temperature. This is attributed to the absence of the organic lubricant layer that is ordinarily present on conventional silver flake fillers, as the lack of such a layer eases the formation of inter-particle contacts. The combination of very low silver content and the ability to achieve conductivity at room temperature should make AgPS-based ICAs attractive options for interconnects with high demands for cost-efficiency and low-temperature requirements, such as solar modules and flexible electronics. The curing time at room temperature is too long for most practical applications, but this can be circumvented by the use of more reactive epoxy systems and by increasing the curing temperature within the processing window of the contacting components. When the ICAs are exposed to heat and moisture after curing, there is an increase in the grain size of the silver films of the filler particles, which correlates inversely with the initial curing temperature. This grain growth has a net positive effect on the electrical conductivity of the ICAs, lowering the resistivity of samples cured at room temperature towards the resistivity of the samples cured at elevated temperatures. The grain growth is explained by an electrochemical process, and further studies could reveal how and to what extent the process can be accelerated or decelerated at various environmental and chemical conditions. However, the lowest resistivity and best long-term stability are still obtained for ICAs initially cured at

elevated temperatures, so these qualities have to be weighed against the need for lower processing temperatures.

Acknowledgements

The Research Council of Norway is acknowledged for funding through project number 225962/E20 – "Novel conductive adhesive technology for solar industry". We thank Lindberg & Lund AS (Vestby, Norway) for making available their climate chambers. PFI (Paper and Fibre Research Institute, Trondheim, Norway) is acknowledged for giving us access to their ion milling instrument. IMT EMLab is recognised for providing access to their FEG-SEM instruments. Stian Johansen at Conpart AS is gratefully acknowledged for help with the four-wire measurements.

Supplementary Data

Supplementary data to this article can be found at [insert link here].

References

1. Y. Li, K.-s. Moon, and C. Wong, *Electronics without lead,* Science, 2005, **308**(5727): p. 1419-1420.
2. M.T. Zarmai, N.N. Ekere, C.F. Oduoza, and E.H. Amalu, *A review of interconnection technologies for improved crystalline silicon solar cell photovoltaic module assembly,* Applied Energy, 2015, **154**: p. 173-182.
3. A. Schneider, R. Harney, S. Aulehla, E. Lemp, and S. Koch, *Progress in Interconnection of Busbar-less Solar Cells by Means of Conductive Gluing,* Energy Procedia, 2013, **38**: p. 387-394.
4. G. Beaucarne, I. Kuzma-Filipek, F. Campeol, X. Young, J. Wei, Y. Yu, R. Russell, and F. Duerinckx, *Innovative Cell Interconnection Based on Ribbon Bonding of Busbar-less Cells Using Silicone-based Electrically Conductive Adhesives,* Energy Procedia, 2015, **67**: p. 185-193.
5. D.W.K. Eikelboom, J.H. Bultman, A. Schonecker, M.H.H. Meuwissen, M.A.J.C.v.d. Nieuwenhof, and D.L. Meier, *Conductive adhesives for low-stress interconnection of thin back-contact solar cells,* 29th IEEE Photovoltaic Specialists Conference, (New Orleans, United States, 2002), doi: 10.1109/PVSC.2002.1190544

6. H.H. Hsieh, W.K. Lee, T.C. Chang, and C.S. Hsi, *Photovoltaic modules of crystalline solar cells using a new type assembly structure,* 5th International Microsystems Packaging Assembly and Circuits Technology Conference (IMPACT), (Taipei, Taiwan, 2010), doi: 10.1109/IMPACT.2010.5699598
7. Y. Li and C.P. Wong, *Recent advances of conductive adhesives as a lead-free alternative in electronic packaging: Materials, processing, reliability and applications,* Materials Science and Engineering: R: Reports, 2006, **51**(1–3): p. 1-35.
8. J. E. Morris and J. Liu, *Electrically Conductive Adhesives: A Research Status Review*, in *Micro- and Opto-Electronic Materials and Structures: Physics, Mechanics, Design, Reliability, Packaging*, edited by: E. Suhir, Y.C. Lee, and C.P. Wong, 2007, Springer Science+Business Media LLC, New York. p. 527-570.
9. D. Lu and C.P. Wong, *Effects of shrinkage on conductivity of isotropic conductive adhesives,* International Journal of Adhesion and Adhesives, 2000, **20**(3): p. 189-193.
10. M. Inoue, H. Muta, T. Maekawa, S. Yamanaka, and K. Suganuma, *Physical Factors Determining Thermal Conductivities of Isotropic Conductive Adhesives,* Journal of Electronic Materials, 2009, **38**(3): p. 430-437.
11. D. Lu, Q.K. Tong, and C.P. Wong, *Conductivity mechanisms of isotropic conductive adhesives (ICAs),* International Symposium on Advanced Packaging Materials: Processes, Properties and Interfaces, 1999), doi: 10.1109/ISAPM.1999.757278
12. H.-W. Cui, J.-T. Jiu, S. Nagao, T. Sugahara, K. Suganuma, H. Uchida, and K.A. Schroder, *Ultra-fast photonic curing of electrically conductive adhesives fabricated from vinyl ester resin and silver micro-flakes for printed electronics,* RSC Advances, 2014, **4**(31): p. 15914-15922.
13. V. Zardetto, T.M. Brown, A. Reale, and A. Di Carlo, *Substrates for flexible electronics: A practical investigation on the electrical, film flexibility, optical, temperature, and solvent resistance properties,* Journal of Polymer Science Part B: Polymer Physics, 2011, **49**(9): p. 638-648.
14. A.C. Siegel, S.T. Phillips, M.D. Dickey, N. Lu, Z. Suo, and G.M. Whitesides, *Foldable Printed Circuit Boards on Paper Substrates,* Advanced Functional Materials, 2010, **20**(1): p. 28-35.
15. R. Zhang, K.-s. Moon, W. Lin, J.C. Agar, and C.-P. Wong, *A simple, low-cost approach to prepare flexible highly conductive polymer composites by in situ reduction of silver*

carboxylate for flexible electronic applications, Composites Science and Technology, 2011, **71**(4): p. 528-534.

16. Y. Zemen, T. Prewitz, T. Geipel, S. Pingel, and J. Berghold, *The impact of yield strength of the interconnector on the internal stress of the solar cell within a module*, 5th World Conference on Photovoltaic Energy Conversion, (Valencia, Spain, 2010), p. 4073-4078
17. H.-W. Cui, J.-T. Jiu, T. Sugahara, S. Nagao, K. Suganuma, and H. Uchida, *High performance heat curing copper-silver powders filled electrically conductive adhesives,* Electronic Materials Letters, 2015, **11**(2): p. 315-322.
18. R. Zhang, W. Lin, K.-S. Moon, Q. Liang, and C.P. Wong, *Highly Reliable Copper-Based Conductive Adhesives Using an Amine Curing Agent for in Situ Oxidation/Corrosion Prevention,* Components, Packaging and Manufacturing Technology, IEEE Transactions on, 2011, **1**(1): p. 25-32.
19. R. Zhang, W. Lin, K. Lawrence, and C.P. Wong, *Highly reliable, low cost, isotropically conductive adhesives filled with Ag-coated Cu flakes for electronic packaging applications,* International Journal of Adhesion and Adhesives, 2010, **30**(6): p. 403-407.
20. J. Liu, O. Salmela, J. Särkkä, J.E. Morris, P.-E. Tegehall, and C. Andersson, *Conductive Adhesive Joint Reliability*, in *Reliability of Microtechnology: Interconnects, Devices and Systems*, edited by: J. Liu, O. Salmela, J. Särkkä, J.E. Morris, P.-E. Tegehall, and C. Andersson, 2011, Springer Science+Business Media LLC, New York. p. 71-98.
21. S. Jain, D.C. Whalley, M. Cottrill, H. Kristiansen, K. Redford, S. Helland, T. Helland, E. Kalland, and C. Liu, *Factors affecting conduction in novel isotropic conductive adhesives filled with silver coated polymer spheres*, 19th European Microelectronics Packaging Conference (EMPC), (Grenoble, France, 2013), p. 1-7
22. J. Gakkestad, L. Zhuo, T. Helland, and C.P. Wong, *Thermo-mechanical properties of Isotropic Conductive Adhesive filled with Metallized Polymer Spheres,* IEEE 15th Electronics Packaging Technology Conference (EPTC), (Singapore, 2013), doi: 10.1109/EPTC.2013.6745715
23. S.R. Pettersen, H. Kristiansen, S. Nagao, S. Helland, J. Njagi, K. Suganuma, Z. Zhang, and J. He, *Contact Resistance and Metallurgical Connections Between Silver Coated Polymer Particles in Isotropic Conductive Adhesives,* Journal of Electronic Materials, 2016, **45**(7): p. 3734–3743.
24. S.R. Pettersen, H. Kristiansen, K. Redford, S. Helland, E. Kalland, Z. Zhang, and J. He, *Controlling the Conduction Mechanisms in Isotropic Conductive Adhesives with Silver-*

Coated Polymer Spheres, IEEE 66th Electronic Components and Technology Conference (ECTC), 2016), doi: 10.1109/ECTC.2016.53

25. P.L. Redmond, A.J. Hallock, and L.E. Brus, *Electrochemical Ostwald Ripening of Colloidal Ag Particles on Conductive Substrates,* Nano Letters, 2005, **5**(1): p. 131-135.
26. S.R. Pettersen, A.E. Stokkeland, H. Kristiansen, J. Njagi, K. Redford, D.V. Goia, Z. Zhang, and J. He, *Electrical four-point probing of spherical metallic thin films coated onto micron sized polymer particles,* Applied Physics Letters, 2016, **109**(4): p. 043103.
27. K. Fuchs, *The conductivity of thin metallic films according to the electron theory of metals,* Mathematical Proceedings of the Cambridge Philosophical Society, 1938, **34**(01): p. 100-108.
28. E.H. Sondheimer, *The mean free path of electrons in metals,* Advances in Physics, 1952, **1**(1): p. 1-42.
29. A.F. Mayadas and M. Shatzkes, *Electrical-Resistivity Model for Polycrystalline Films: the Case of Arbitrary Reflection at External Surfaces,* Physical Review B, 1970, **1**(4): p. 1382-1389.
30. W. Zhang, S.H. Brongersma, O. Richard, B. Brijs, R. Palmans, L. Froyen, and K. Maex, *Influence of the electron mean free path on the resistivity of thin metal films,* Microelectronic Engineering, 2004, **76**(1–4): p. 146-152.
31. P. Scherrer, *Bestimmung der Größe und der inneren Struktur von Kolloidteilchen mittels Röntgenstrahlen,* Nachrichten von der Gesellschaft der Wissenschaften zu Göttingen, Mathematisch-Physikalische Klasse, 1918, **2**: p. 98-100.
32. U. Holzwarth and N. Gibson, *The Scherrer equation versus the 'Debye-Scherrer equation',* Nature Nanotechnology, 2011, **6**(9): p. 534-534.
33. M. Inoue and K. Suganuma, *The Dependence on Thermal History of the Electrical Properties of an Epoxy-Based Isotropic Conductive Adhesive,* Journal of Electronic Materials, 2007, **36**(6): p. 669-675.
34. M. Inoue and K. Suganuma, *Effect of curing conditions on the electrical properties of isotropic conductive adhesives composed of an epoxy-based binder,* Soldering & Surface Mount Technology, 2006, **18**(2): p. 40-45.
35. D. Klosterman, L. Li, and J.E. Morris, *Materials characterization, conduction development, and curing effects on reliability of isotropically conductive adhesives,* IEEE Transactions on Components, Packaging, and Manufacturing Technology: Part A, 1998, **21**(1): p. 23-31.

36. Y. Li, D. Lu, and C.P. Wong, *Isotropically Conductive Adhesives (ICAs)*, in *Electrical Conductive Adhesives with Nanotechnologies*, edited by: Y. Li, D. Lu, and C.P. Wong, 2010, Springer Science+Business Media LLC, New York. p. 121-225.
37. R. Holm, *Electric contacts: Theory and Application*. 4th ed. 1967, Berlin/Heidelberg/New York: Springer-Verlag.
38. C. Yang, C.P. Wong, and M.M. Yuen, *Printed electrically conductive composites: conductive filler designs and surface engineering,* Journal of Materials Chemistry C, 2013, **1**(26): p. 4052-4069.
39. U. Kreibig and C.v. Fragstein, *The limitation of electron mean free path in small silver particles,* Zeitschrift für Physik, 1969, **224**(4): p. 307-323.
40. P. Peng, A. Hu, A.P. Gerlich, G. Zou, L. Liu, and Y.N. Zhou, *Joining of Silver Nanomaterials at Low Temperatures: Processes, Properties, and Applications,* ACS Applied Materials & Interfaces, 2015, **7**(23): p. 12597-12618.
41. D. Wakuda, M. Hatamura, and K. Suganuma, *Novel method for room temperature sintering of Ag nanoparticle paste in air,* Chemical Physics Letters, 2007, **441**(4–6): p. 305-308.
42. D. Wakuda, K.S. Kim, and K. Suganuma, *Room-Temperature Sintering Process of Ag Nanoparticle Paste,* IEEE Transactions on Components and Packaging Technologies, 2009, **32**(3): p. 627-632.
43. D. Wakuda, K.S. Kim, and K. Suganuma, *Ag Nanoparticle Paste Synthesis for Room Temperature Bonding,* IEEE Transactions on Components and Packaging Technologies, 2010, **33**(2): p. 437-442.
44. J.P. Pascault and R.J.J. Williams, *Glass transition temperature versus conversion relationships for thermosetting polymers,* Journal of Polymer Science Part B: Polymer Physics, 1990, **28**(1): p. 85-95.
45. A. Hale, C.W. Macosko, and H.E. Bair, *Glass transition temperature as a function of conversion in thermosetting polymers,* Macromolecules, 1991, **24**(9): p. 2610-2621.

Supplementary Information to

Room-temperature curing and grain growth at high humidity in conductive adhesives with ultra-low silver content

Sigurd R. Pettersen [1], Keith Redford [2], John Njagi [3], Helge Kristiansen [1, 2], Susanne Helland [4], Erik Kalland [4], Dan V. Goia [3], Zhiliang Zhang [1], and Jianying He [1].

[1] *NTNU Nanomechanical Lab, Department of Structural Engineering, Norwegian University of Science and Technology (NTNU), NO-7491, Trondheim, Norway.*

[2] *Conpart AS, Dragonveien 54, NO-2013, Skjetten, Norway.*

[3] *Center for Advanced Materials Processing, Clarkson University, Potsdam, NY 13699-5814, USA.*

[4] *Mosaic Solutions AS, Dragonveien 54, NO-2013, Skjetten, Norway.*

Corresponding authors: jianying.he@ntnu.no, sigurd.r.pettersen@ntnu.no

XRD spectra and grain size data

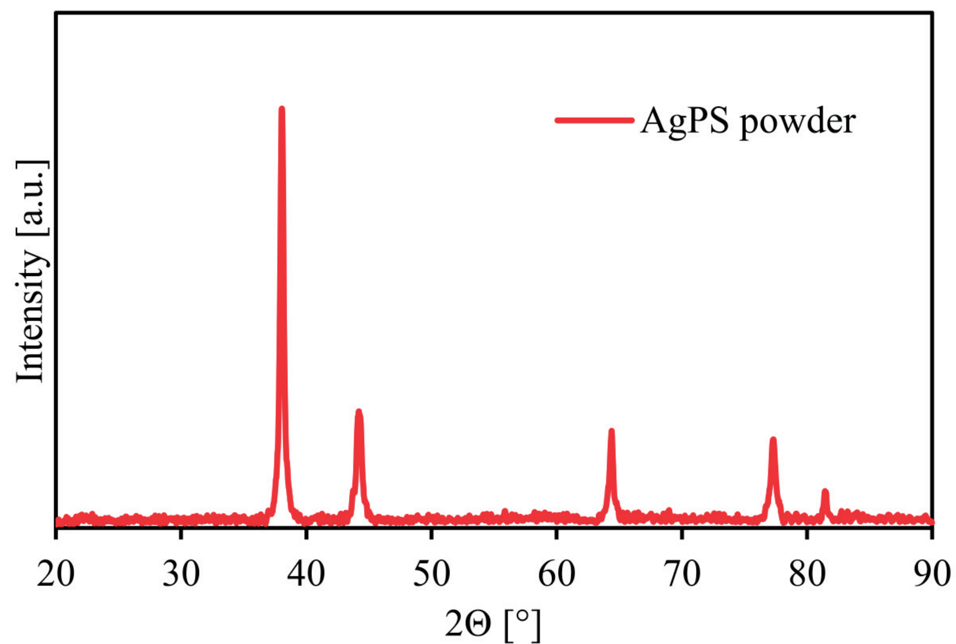

Fig. S1. XRD spectra for the AgPS powder (30 µm PMMA spheres coated with 100 nm silver). Powder has been stored at ambient conditions.

Table S1. Grain sizes calculated from the five peaks in the XRD spectra for the pure AgPS powder.

2Θ [°]	**Grain size [nm]**
38.0	**31.0**
44.2	**21.4**
64.3	**33.1**
77.2	**25.2**
81.4	**44.4**

The mean grain size of AgPS powder is larger than in the RT samples before these are subjected to the environmental conditions. The peak broadening used to estimate the grain size through Scherrer's equation is not dependent solely on grain size, but also on other factors such as lattice strains and grain shape [1, 2]. The technique is thus best suited for comparing similar samples with the same initial conditions, such as the ICAs in this investigation. The AgPS powder was measured some months after the preparation and XRD measurements of the ICAs, so this difference in grain size could also be caused by slight grain growth in the silver films of the AgPS powder during that period.

Table S2. Grain sizes calculated from the five peaks in the XRD spectra for the RT series, seen in Fig. 4 in the main article.

After curing		85°C		85°C/85%RH		WI	
2Θ [°]	**Grain size [nm]**	2Θ [°]	**Grain size [nm]**	2Θ [°]	**Grain size [nm]**	2Θ [°]	**Grain size [nm]**
37.9	**28.9**	38.3	**36.3**	38.2	**65.4**	37.9	**35.4**
44.0	**19.6**	44.4	**21.6**	44.3	**42.0**	44.1	**20.9**
64.2	**37.4**	64.5	**31.5**	64.4	**46.1**	64.2	**26.1**
77.1	**23.8**	77.5	**23.1**	77.4	**36.9**	77.2	**21.0**
81.3	**27.4**	81.6	**44.8**	81.5	**50.9**	81.3	**35.2**

[1] U. Holzwarth, N. Gibson, The Scherrer equation versus the 'Debye-Scherrer equation', Nat Nano 6(9) (2011) 534-534.

[2] P. Scherrer, Bestimmung der Größe und der inneren Struktur von Kolloidteilchen mittels Röntgenstrahlen, Nachrichten von der Gesellschaft der Wissenschaften zu Göttingen, Mathematisch-Physikalische Klasse 2 (1918) 98-100.

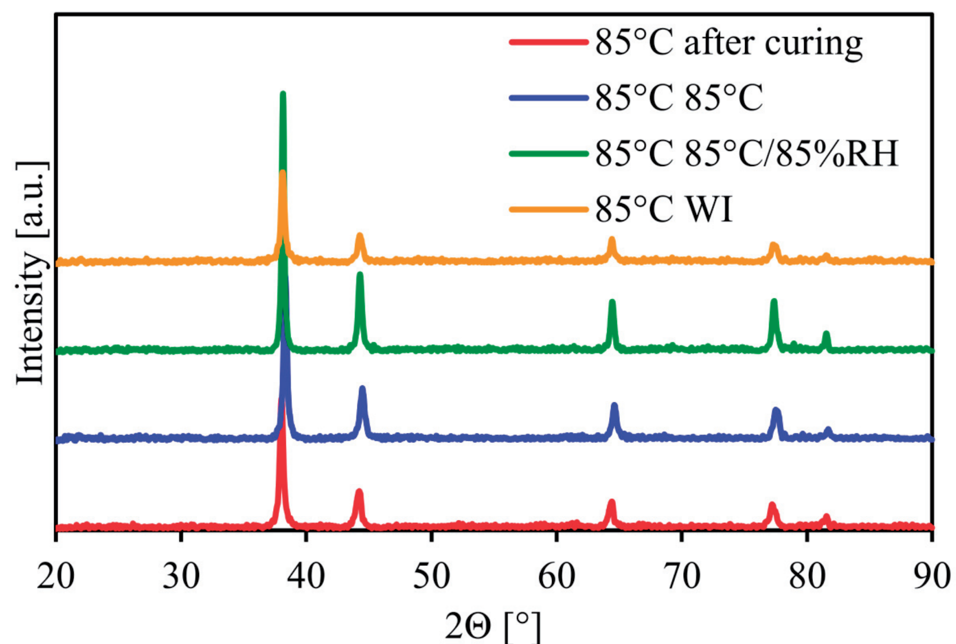

Fig. S2. XRD spectra for the ICA series cured at 85 °C before any post-curing treatment, as well as long term storage at 85 °C and 85 °C/85 %RH.

Table S3. Grain sizes calculated from the five peaks in the XRD spectra for the 85 °C series, seen in Fig. S2.

After curing		85°C		85°C/85%RH		WI	
2Θ [°]	**Grain size [nm]**	2Θ [°]	**Grain size [nm]**	2Θ [°]	**Grain size [nm]**	2Θ [°]	**Grain size [nm]**
38.0	**32.0**	38.3	**33.1**	38.1	**48.3**	38.1	**32.7**
44.1	**21.1**	44.4	**26.8**	44.3	**31.6**	44.3	**23.8**
64.3	**28.0**	64.6	**35.3**	64.4	**42.5**	64.4	**45.6**
77.2	**23.1**	77.5	**28.3**	77.3	**39.2**	77.3	**27.5**
81.4	**27.1**	81.6	**35.2**	81.5	**40.4**	81.4	**29.8**

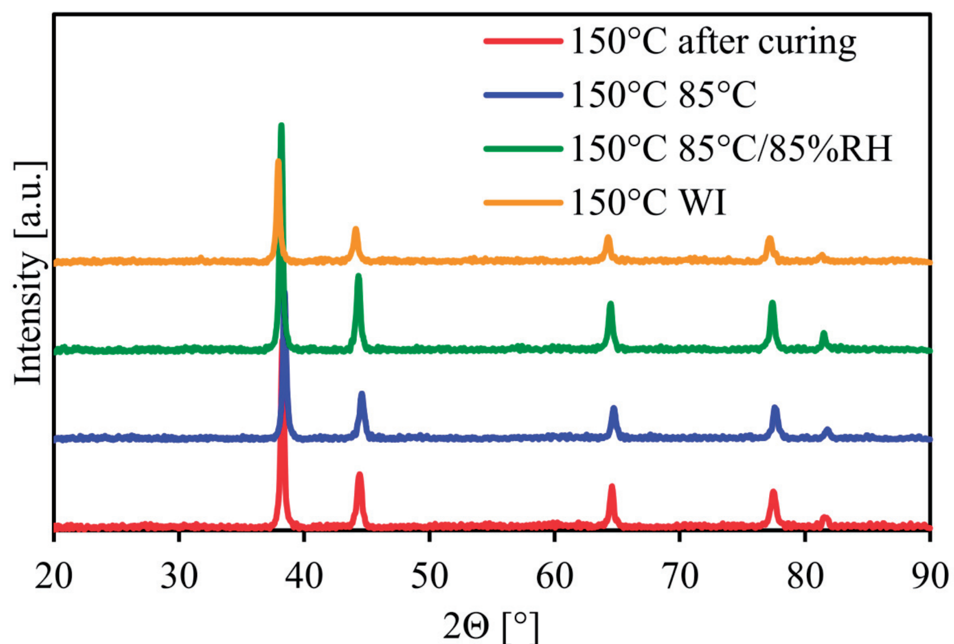

Fig. S3. XRD spectra for the ICA series cured at 150 °C before any post-curing treatment, as well as long term storage at 85 °C and 85 °C/85 %RH.

Table S4. Grain sizes calculated from the five peaks in the XRD spectra for the 150 °C series, seen in Fig. S3.

After curing		85°C		85°C/85%RH		WI	
2Θ [°]	**Grain size [nm]**	2Θ [°]	**Grain size [nm]**	2Θ [°]	**Grain size [nm]**	2Θ [°]	**Grain size [nm]**
38.4	**34.3**	38.4	**33.6**	38.1	**38.3**	37.9	**34.1**
44.6	**22.4**	44.6	**23.7**	44.3	**27.3**	44.1	**27.4**
64.7	**40.7**	64.7	**31.0**	64.4	**37.1**	64.2	**43.4**
77.6	**25.4**	77.6	**29.8**	77.3	**37.5**	77.1	**27.5**
81.7	**30.4**	81.7	**31.5**	81.5	**46.9**	81.2	**27.8**

FEG-SEM images

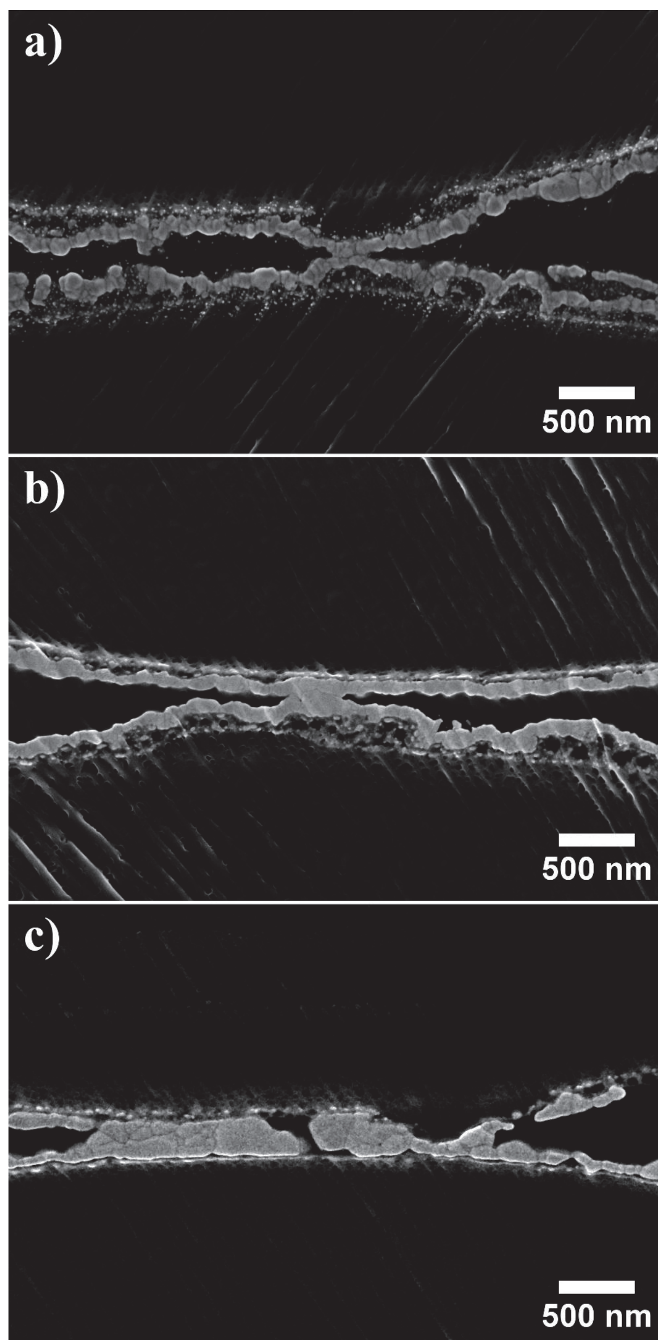

Fig. S4. Contact structures before environmental storage (a), after storage at 85 °C (b), and after storage at 85 °C/85 %RH for ICA cured at 85 °C.

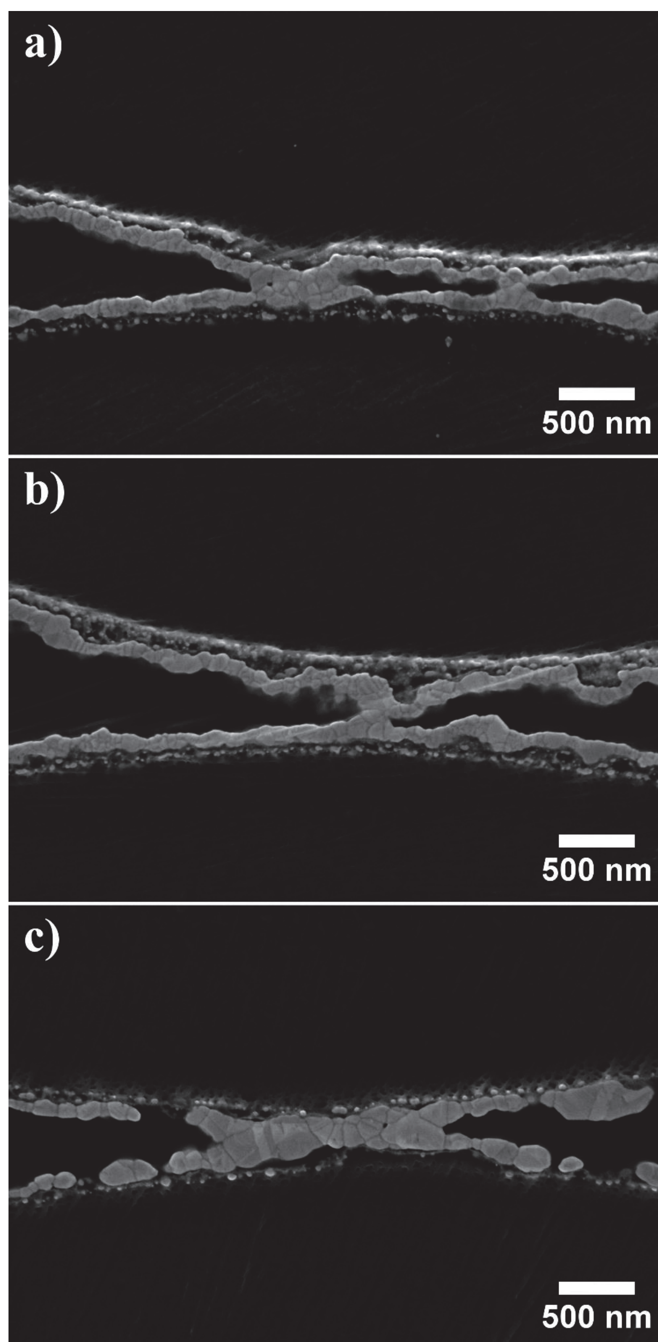

Fig. S5. Contact structures before environmental storage (a), after storage at 85 °C (b), and after storage at 85 °C/85 %RH for ICA cured at 150 °C.

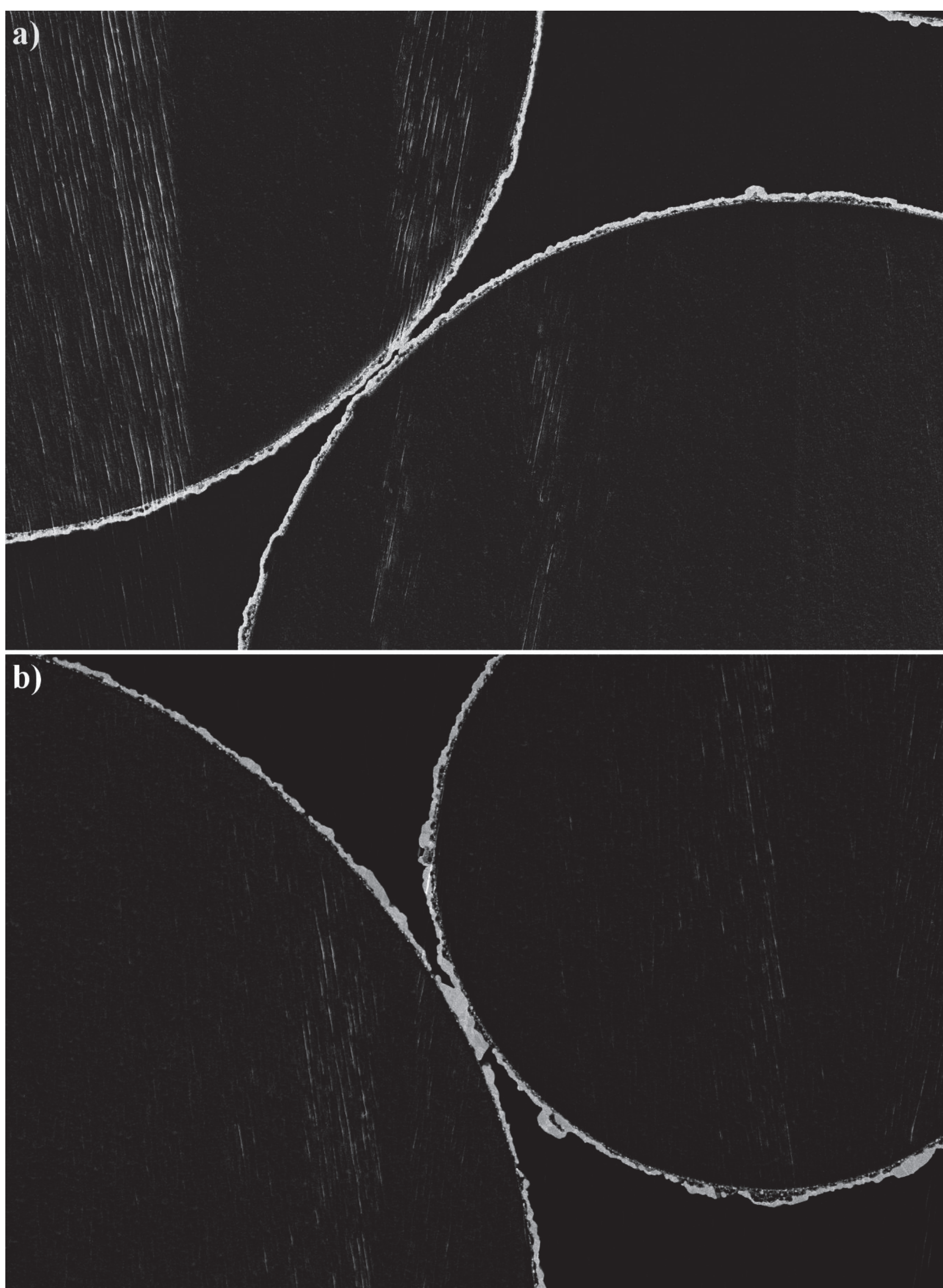

Fig. S6. Lower magnification of two of the contact structures from the RT series seen in Fig. 6 in the main text. The contact structure before environmental storage (a) is clearly narrower than the structure after storage at 85 ° C/85 %RH (b). Also notice in (b) that the massive grain growth occurs along the whole circumference of the film, not only in the contact zones.

Paper VI

Investigation of thermal transport in polymer composites with percolating networks of silver thin films by the flash diffusivity method

Sigurd R. Pettersen, Shijo Nagao, Helge Kristiansen, Susanne Helland, John Njagi, Katsuaki Suganuma, Zhiliang Zhang, and Jianying He.

Journal of Applied Physics, submitted.

Investigation of thermal transport in polymer composites with percolating networks of silver thin films by the flash diffusivity method

Sigurd R. Pettersen [1, †], Shijo Nagao [2], Helge Kristiansen [1, 3], Susanne Helland [4], John Njagi [5], Katsuaki Suganuma [2], Zhiliang Zhang [1], and Jianying He [1, *].

[1] NTNU Nanomechanical Lab, Department of Structural Engineering, Norwegian University of Science and Technology (NTNU), NO-7491, Trondheim, Norway.

[2] Institute of Scientific and Industrial Research (ISIR), Osaka University, Ibaraki, Osaka 567-0047, Japan.

[3] Conpart AS, NO-2013, Skjetten, Norway.

[4] Mosaic Solutions AS, NO-2013, Skjetten, Norway.

[5] Center for Advanced Materials Processing, Clarkson University, Potsdam, NY 13699-5814, USA.

The flash diffusivity method, also known as laser flash analysis (LFA), is commonly used to obtain the thermal diffusivity (α) and thermal conductivity (κ) of materials, due to its relative simplicity, rapid measurements, small sample size requirement, and commercially available instruments. In this work, an epoxy adhesive was filled with a large fraction of homogeneous micron-sized PMMA spheres coated with thin silver films, such that a percolating metallic network that dominated the electric and thermal transport formed through the polymer at < 3 vol% silver. Specific heat capacity (C_p) was measured from the LFA measurements by a comparative method, and from the total and reversible heat flow signals of modulated differential scanning calorimetry (MDSC). κ was estimated as the product of α, C_p, and density (ρ), and is found to vary significantly with the method to find C_p. The electron contribution is found from the electrical conductivity by Wiedemann-Franz law, and is used to elucidate the thermal transport mechanisms in the composite. A theoretical background for the various methods is also included.

† Parts of this work were done during an academic stay at [2].

* Corresponding author: jianying.he@ntnu.no

Keywords: Flash diffusivity method (LFA), thermal conductivity, thermal diffusivity, specific heat capacity, heterogeneous composites, modulated differential scanning calorimetry (MDSC), Wiedemann-Franz law, silver thin films, isotropic conductive adhesive (ICA).

1. Introduction

Thermal management becomes ever more important in electronic packaging, and increasing the thermal conductivity of packaging materials such as polymers is thus a high priority for the academic community and industry [1, 2]. To increase the thermal conductivity of polymer interconnect materials, thermally conductive fillers are typically added to the polymer matrix at high filler loadings (> 30 vol%) [2]. Such fillers can be carbon-based (e.g. graphite, graphene, carbon black, carbon nanotubes, carbon fibers, or diamond), or ceramic or metal particles [1, 2]. Isotropic conductive adhesives (ICAs), is a special class of polymer-based interconnect materials, where electrically conductive filler particles form a percolating, isotropic network through a polymer adhesive [3, 4]. ICAs are alternatives to metallic solders, and are especially suitable for interconnects that require low processing temperatures or are difficult to wet with solders. Silver is the metal with lowest electrical resistivity and highest thermal conductivity, 1.62×10^{-6} Ω·cm and 429 W/m·K at 25 °C [5], respectively. Although copper is cheaper and almost as good a conductor, it is more easily oxidized, and while copper oxide is an insulator, silver oxide is conductive [3, 4]. Due to its superior electrical properties, silver is therefore the preferred filler material in ICAs. Typical commercial ICAs are composed of a thermoset epoxy binder with silver flakes embedded for electrical and thermal conductivity, sometimes in combination with solid silver particles. Commercial ICAs attain electrical conductivities (σ) around 10^4 S/cm and thermal conductivities (κ) around 3 W/(m·K) at normal curing conditions, but require a high content of silver, around 85 weight percent (wt%) or up to 40 volume percent (vol%) [6]. In addition, the silver flakes tend to align with the shear flow direction during processing, which can lead to large anisotropies in the conductive properties [6]. In recent years, homogeneously sized polymer spheres coated with thin films of silver (AgPS) have been shown as a viable alternative to silver flakes and solid silver particles in ICAs [7, 8]. AgPS-based ICAs are truly isotropic, and as the spherical silver films are much thinner than the diameter of the polymer cores, most of the AgPS will be polymer, and percolating networks can be formed at much lower silver contents than in conventional ICAs. AgPS-based ICAs have been shown to yield σ > 1500 S/cm at less than 3 vol% silver [7, 8], and the mechanisms controlling the electrical properties of these conductive composites are starting to be clarified [8-10]. However, investigation of the thermal properties of AgPS-based ICAs have been sparse, and to our best knowledge, only one paper has been published on the subject to date [7]. The mechanisms controlling the thermal transport of these ICAs are still largely unexplored.

Thermal conductivity is typically measured indirectly through the flash diffusivity method, also known as laser flash analysis (LFA), due to its relative simplicity, rapid measurements, small sample size requirements, as well as the availability of standardized, commercial instruments [11]. In the method, thermal diffusivity (α), specific heat capacity (C_p), and volume density (ρ) are measured separately, and κ is calculated through [11-14]

$$\kappa = \alpha \cdot C_p \cdot \rho, \quad (1)$$

where all factors, including the thermal conductivity, are functions of the temperature of the material. LFA is commonly used to estimate κ for polymer composites with percolating networks of fillers, but often without revealing and discussing the intermediate factors α, C_p, and ρ [6, 7, 15-18]. C_p is commonly measured either by a comparative method directly from the LFA results [12], or separately by differential scanning calorimetry (DSC) [19, 20], while the potential deviations between the two methods are overlooked.

In this work, we investigate an epoxy matrix with AgPS at equal filler content but varying silver film thicknesses, yielding composites with silver content ranging from 0.7 – 2.9 vol%. Thermal diffusivity is measured by LFA, while specific heat capacity is estimated by both LFA and modulated DSC, where the latter can separate the reversible and non-reversible contributions to the specific heat capacity. Specific heat capacity, and further thermal conductivity, is found to be very dependent on the measurement procedure. We show that the thermal properties of the composites is dominated by the silver thin films, as these have much higher thermal conductivity than the polymer matrix and form a percolating network. In addition, the electron contribution to the thermal conductivity is estimated from electric 4-point measurements using Wiedemann-Franz law [21, 22]. By comparing the results from electronic and thermal measurements, we reveal more about the thermal transport in the composites than what would be possible by thermal measurement alone. A brief theory and methodology section is included to summarize the mechanisms behind thermal transport as well as give readers basic insight on the methods.

2. Theory and methodology

2.1 Thermal transport and Wiedemann-Franz law

Heat is conducted through a material by heat carriers, which in solids will be charge carriers (electrons and holes), and atomic lattice vibrations, the energy quanta known as phonons [1]. Polymers are generally electrical insulators, thus there are no free charge carriers, and heat is transported by phonons. As phonons are scattered by defects and non-crystalline sections, the thermal conductivity of polymers is strongly affected by their crystallinity, and can vary from around 0.2 W/(m·K) for amorphous polymers such as polymethylmethacrylate (PMMA) to around 0.5 W/(m·K) for highly crystalline polymers. Contrarily, κ in metals is generally assumed to be dominated by electron transport, and there is thus a close relationship between σ and κ, as described by the Wiedemann-Franz law [21, 22]

$$\kappa/\sigma = L \cdot T. \quad (2)$$

Here, T is the absolute temperature in Kelvins, and L is the Lorenz factor. The theoretical value of $L = (\pi^2/3)(k_B/e)^2 = 2.44\times10^{-8}\ V^2/K^2$, where k_B is Boltzmann's constant and e is the elementary charge [22]. The electrical conductivity is normally obtained from the 4-point method, where electrical current is passed through the sample between two points and the voltage is measured by two intermediate probes [11]. σ is then obtained by multiplying the resultant resistance (R) with an analytically or numerically established factor that accounts for the finite geometry of the sample. If the phonon contribution is unneglectable, κ can be expressed as [18, 22]

$$\kappa = \kappa_e + \kappa_{ph} = \sigma \cdot L \cdot T + \kappa_{ph}, \quad (3)$$

where κ_e and κ_{ph} are the electron and phonon contributions to the thermal conductivity, respectively.

2.2 Laser Flash Analysis (LFA)

Thermal conductivity, κ, is typically obtained indirectly by first finding thermal diffusivity, α, through the LFA method, where α is the speed at which a heat pulse diffuses through the material. As can be seen from Eq. (1), α is the ratio between κ and C_p times ρ. The definition of α in Eq. (1) is derived on the assumption of a homogeneous, isotropic material [23-26]. Using the procedure to measure α and further to obtain κ for composites therefore requires the implicit approximation of the composite as a hypothetical homogeneous material, where κ, α, C_p, and ρ

are effective properties of this material [23-26]. The LFA method is named after the procedure first proposed by Parker et al., where a short pulse or flash of thermal energy is released by a laser or flash lamp towards a thin material specimen, where it is absorbed on the surface [12]. Parts of the thermal energy is conducted through the material to the backside of the sample, where the surface temperature (T) rise is measured as a function of time (t), typically by an infrared (IR) detector, yielding transient curves ($T(t)$). By preparing samples with much larger width or diameter than thickness, non-axial heat flow is assumed to be negligible. With this assumption and adiabatic conditions, i.e. no heat-loss from the sample surfaces, the time (t_x) required for the backside temperature (T_x) to rise from a baseline to a fraction (x) of the maximum temperature (T_m) can be used to calculate α through

$$\alpha = k_x \cdot l^2 / t_x, \quad (4)$$

where l is the sample thickness and $k_x = 1.38/\pi^2$ at $x = 0.5$, i.e. at the half-rise time [12-14]. Perfect adiabatic transients are rarely achieved, and several models exist to correct for heat losses, such as the methods proposed by Cowan [27, 28] and Clark and Taylor [29]. In these methods, α at the half rise time as estimated from Eq. (4) is corrected by multiplication with $K_c/k_{0.5}$, where K_c is a correction factor dependent on the ratios of the rise times at certain points in the transients [13]. In modern commercial LFA instruments, the methods are implemented by fitting the whole transients to the models by least-squares methods [30].

The unknown C_p can be estimated from the same transients as α by comparison to a reference sample with known C_p values [12-14]. The specific heat capacity (heat capacity per unit mass) is a measure for the amount of thermal energy (Q) required to increase the temperature per unit mass of a material by ΔT (in K or °C),

$$C_p = \frac{Q}{m \cdot \Delta T}. \quad (5)$$

If the heat source releases the same amount of thermal energy in each flash and the heat absorption of the reference and unknown sample is equal, Eq. (5) can be rewritten as $Q = (C_p \cdot m \cdot \Delta T)_{ref} = (C_p \cdot m \cdot \Delta T)_{sample}$, where ΔT is the temperature difference from the baseline to the maximum temperature ($T_m - T_b$). As $m = \rho \cdot V = \rho \cdot l \cdot A$, where l is the thickness of the sample and A is the surface area, this becomes $(C_p \cdot \rho \cdot l \cdot A \cdot \Delta T)_{ref} = (C_p \cdot \rho \cdot l \cdot A \cdot \Delta T)_{sample}$. If $A_{ref} = A_{sample}$, which

can be solved by placing an aperture with a fixed opening between the flash lamp and samples, the unknown C_p of the sample can be found by

$$C_{p,sample} = \frac{(C_p \cdot \rho \cdot l \cdot \Delta T)_{ref}}{(\rho \cdot l \cdot \Delta T)_{sample}} \text{ . (6)}$$

When C_p is derived from LFA by the comparative method, the density of the unknown sample is a factor that must be measured and taken into account. However, it is easily seen by combining Eq. (6) with Eq. (1) that κ is independent of ρ_{sample}, i.e. that any arbitrary value can be used for the density of the sample if one is only interested in κ. Still, for Eq. (6) to be valid, in addition to the requirement of identical heat absorption, heat loss must be negligible or known in both the reference and unknown sample, which is all but impossible to achieve. The method is thus still prone to experimental errors, and is often found to be unreliable and lead to underestimation of κ [11].

2.3 Modulated Differential Scanning Calorimetry (MDSC)

The most frequently used method for obtaining C_p is differential scanning calorimetry (DSC) [11], in which the difference in heat flow required to heat or cool the sample and an inert reference sample (often an empty crucible) at the same, controlled heating or cooling rate is measured [31]. The differential heat flow signal can be used to identify phase changes such as melting of crystalline polymers (endothermic), kinetic processes such as epoxy curing (exothermic) and stress relaxation (endothermic), and material transitions such as the glass transition of amorphous polymers (endothermic) [19, 32]. However, the signal will be a superposition of all individual contributions, and overlapping contributions can be difficult to separate and identify [32]. The total differential heat flow (dQ/dt) [W] can be described by the general equation [32]

$$\frac{dQ}{dt} = C \cdot \frac{dT}{dt} + f(T,t) \text{ , (7)}$$

where C is the heat capacity of the material [J/°C], dT/dt is the heating rate [°C/s], and $f(T, t)$ [W] is the heat flow from kinetic processes, only dependent on time at an absolute temperature. In regular DSC, an (apparent) C_p can be calculated by comparing the total heat flow per unit mass of the sample to the heat flow per unit mass of a reference with known C_p [31]. However, when the heating rate is constant, the heat capacity and kinetic components cannot be separated,

and the calculated apparent C_p will contain both reversible (heat-capacity) and non-reversible (kinetic) components. Modulated DSC (MDSC) solves this by overlaying a modulated (most commonly sinusoidal) low-frequency perturbation onto the standard linear temperature ramp of a regular DSC scan [19, 20, 32]. The reversible component of the apparent total heat capacity, $C_{p,rev}$ is then acquired directly from the ratio of the modulated heat flow amplitude to the modulated heating rate amplitude times the sample mass [20]. The apparent, or total, $C_{p,tot}$ is calculated from the ratio of the normalized average heat flow to the underlying heating rate times the sample mass, and should upon the fulfillment of certain experimental conditions equal the apparent C_p obtained from regular DSC. A more detailed review of the theory behind MDSC, can be found in [20]. According to ASTM standard E2716 – 09, the estimated C_p values should be calibrated by multiplication with a specific heat capacity constant K_{Cp}, which is obtained by performing the same measurement on a sapphire control sample and taking the ratio between the known reference and measured C_p values of the sapphire sample [33]. The last value, that of the non-reversible components, is then obtained by [20]

$$C_{p,non\text{-}rev} = C_{p,tot} - C_{p,rev}. \quad (8)$$

3. Experimental

3.1 Sample preparation

AgPS comprised of monodisperse PMMA spheres with a nominal diameter of 30 μm and four different nominal silver film thicknesses (60 nm, 100 nm, 150 nm, and 270 nm) were provided by Mosaic Solutions AS (Skjetten, Norway) and mixed into epoxy to create four ICA series. ICAs and epoxy control samples were molded as detached bricks with dimensions 10 mm × 10 mm × 1 mm and cured at 150 °C for 30 min. A summary of the pre-cure densities, AgPS content, and silver content of the five sample series can be observed in Table I. For more details on sample preparation, see [8].

To create clean and planar surfaces, six samples from each series were polished on both sides at 150 rpm using SiC paper from Struers (#4000; grain size 5 μm). Typical sample surfaces before and after polishing can be observed in Fig. 1.

Table I. Calculated pre-cure densities, volume fractions [vol%], and weight fractions [wt%] of the epoxy and four ICA series. Calculations are based on the weight fractions (measured) and nominal densities (given by the manufactures) of the constituents, as well as nominal diameter and film thicknesses of the AgPS.

Series	Nominal film thickness [nm]	Density [g/cm3]	AgPS [vol%]	AgPS [wt%]	Silver [vol%]	Silver [wt%]
Epoxy	na	1.11	0.0 %	0.0 %	0.0 %	0.0 %
60Ag	60	1.20	55.7 %	59.0 %	0.7 %	5.8 %
100Ag	100	1.24	55.9 %	60.5 %	1.1 %	9.3 %
150Ag	150	1.29	56.3 %	62.4 %	1.7 %	13.4 %
270Ag	270	1.41	56.1 %	65.5 %	2.9 %	21.7 %

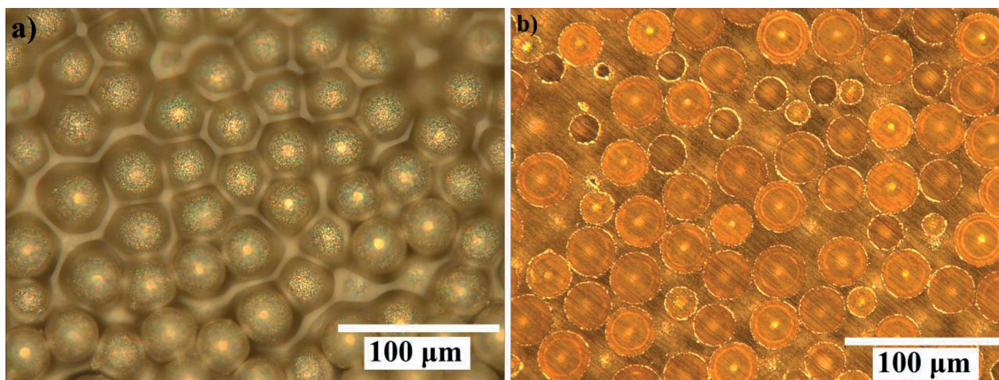

Fig. 1. Optical micrographs of the surface of a sample from the 270Ag series as-prepared (a) and after (b) mechanical polishing.

3.2 Thickness measurements and density calculations

The dimensions of each sample after polishing were measured at room temperature using a digital caliper with 1 µm resolution. The thickness of each sample was averaged from four measurements. The side lengths were measured, and the volume was calculated by assuming rectangular cuboid samples. Each sample was weighed using a balance with 0.1 mg resolution. The density at room temperature was calculated for each sample, and further averaged for each series.

3.3 Electrical conductivity measurements

The electrical volume conductivity was measured directly on the polished surfaces of six samples from each ICA series using a 4-pin setup (Loresta-GP MCP-T610 with a 4-pin NSCP probe, Mitsubishi Chemical Analytech, Japan). Each sample was measured eight times. For more details, see [8]. The conductivity was calculated by

$$\sigma = \frac{1}{R \cdot l \cdot RCF}, \quad (9)$$

where R is the measured resistance, l is the thickness of the sample, and RCF is a resistivity correction factor calculated by the instrument to account for the positioning and pin spacing of the probe and the geometry of the samples. Wiedemann-Franz law (Eq. (2)) was used to calculate the corresponding thermal conductivity, using the theoretical Lorenz factor (2.44×10^{-8} V^2/K^2) and $T = 298$ K.

3.4 Laserflash Analysis

3.4.1 Thermal diffusivity

α of the ICA and epoxy control series were determined by LFA at 25 °C, 50 °C, 75 °C, 100 °C, and 125 °C using a laserflash analysis instrument (LFA 447, Netzsch GmbH, Germany). The epoxy samples were coated with approximately 120 nm gold on both sides using an ion sputter (E-1045, Hitachi, Japan) to eliminate transmission of light through the samples. All samples, including epoxy and reference samples, were further spray coated with a thin layer of carbon on both sides to reduce reflectivity and maximize heat absorption. The LFA and 4-pin measurements were performed on the same samples. Each sample was measured three times at each temperature, and α from each measurement was calculated with the instrument software (LFA Analysis, v. 4.8.3) using the Cowan model [28] with pulse correction.

3.4.2 Specific heat capacity

An alumina reference sample with known C_p was measured under the same conditions as the ICA and epoxy samples. Each measurement on the ICA and epoxy samples was compared to the reference measurement using the instrument software (LFA Analysis, v. 4.8.3) to estimate the unknown C_p values.

3.4 Modulated Differential Scanning Calorimetry

3.4.1 Specific heat capacity

Samples were prepared by cutting small pellets from the detached ICA and epoxy bricks. To avoid influence from the LFA heating on the thermal history of the samples, MDSC was not done on the same samples as the LFA and 4-pin measurements. The samples were polished to achieve a smooth surface and good thermal contact to the crucibles. The measurements were conducted with a differential scanning calorimeter (Q2000, TA Instruments, USA), starting with temperature equilibration at 0.00 °C for 10 min, followed by an average temperature increase of 2.00 °C/min with a modulation of ± 0.50 °C per 100 s. Baseline measurements were performed with empty crucibles, and a sapphire reference sample was measured with the same parameters. An instrument calibration factor $K_{Cp}(T)$ was calculated as $Cp_{,\ ref.\ table}(T)/Cp_{,\ ref.\ measured}(T)$, where $Cp_{,\ ref.\ table}(T)$ was taken from ASTM standard E1269 – 11 [31]. The C_p from each measurement on the ICA and epoxy samples was corrected by multiplication with $K_{Cp}(T)$.

3.4.2 Glass transition temperatures

The glass transition temperatures (T_g) of the epoxy and PMMA cores were estimated from the reversible $Cp(T)$ curves as the temperatures at half height of the transitions, using the software TA Instruments Universal Analysis 2000 (version 4.5A build 4.5.0.5).

4. Results

4.1 Electrical conductivity

As seen in Fig. 2, the conductivity increases with increasing silver content, i.e. with thicker films. The variation from sample to sample is larger than variations between different measurements on the same sample, and is the main cause behind the observed scatter.

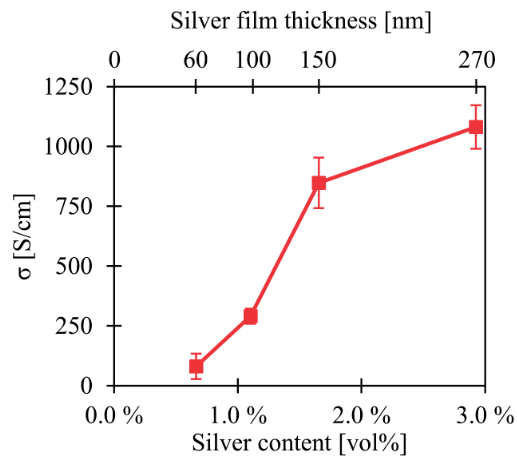

Fig. 2. Electrical conductivity of the four ICA series as a function of silver content. Error bars = ± standard deviation.

4.2 Thermal diffusivity

Fig. 3 shows the thermal diffusivity of the epoxy and ICA series as a function of temperature. The diffusivity is highly dependent on the silver content. As seen in Table I, the silver content of the 60Ag series is estimated to only 0.7 vol%, but already with this small amount of silver, the diffusivity shows a relative increase of 183% at 25 °C compared to pure epoxy. As with the 4-pin measurements, the deviations are caused by sample variation. The three measurements on each sample at each temperature always yielded close to equal values.

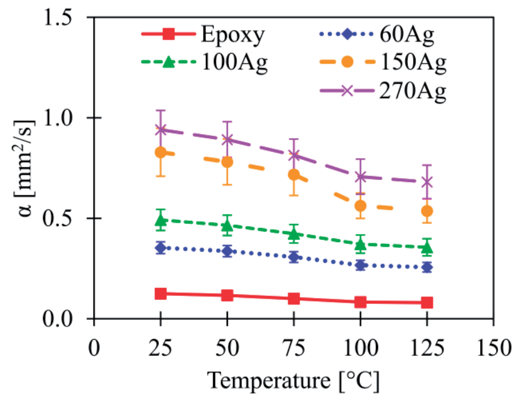

Fig. 3. Thermal diffusivity of the four ICA and epoxy control series. Error bars = ± standard deviation.

4.3 Glass transitions and specific heat capacity

Fig. 4 a) shows that the reversible C_p values of the epoxy and ICA series decreases with increasing silver content. The ICAs reveal two clear glass transitions, one at around 65 °C and another at approx. 122.5 °C. The epoxy sample only goes through the first transition, suggesting that the second transition in the ICAs is that of the PMMA cores. T_g for each series can be found in Table II. While the reversible C_p increases with temperature, with steps at the glass transitions, the non-reversible C_p (Fig. 4 b)) shows the opposite behavior, decreasing with temperature, crossing from endothermic to exothermic in the interval between 100 – 125 °C. The non-reversible C_p curves also reveal an endothermic process that peaks approximately where the glass transition starts to occur. During a second measurement on the 150Ag sample, this peak is no longer present (see supplementary material), suggesting that this peak may be caused by release of residual stress from e.g. the sample polishing or curing process as the epoxy goes from a rigid to flexible structure during the first MDSC heating.

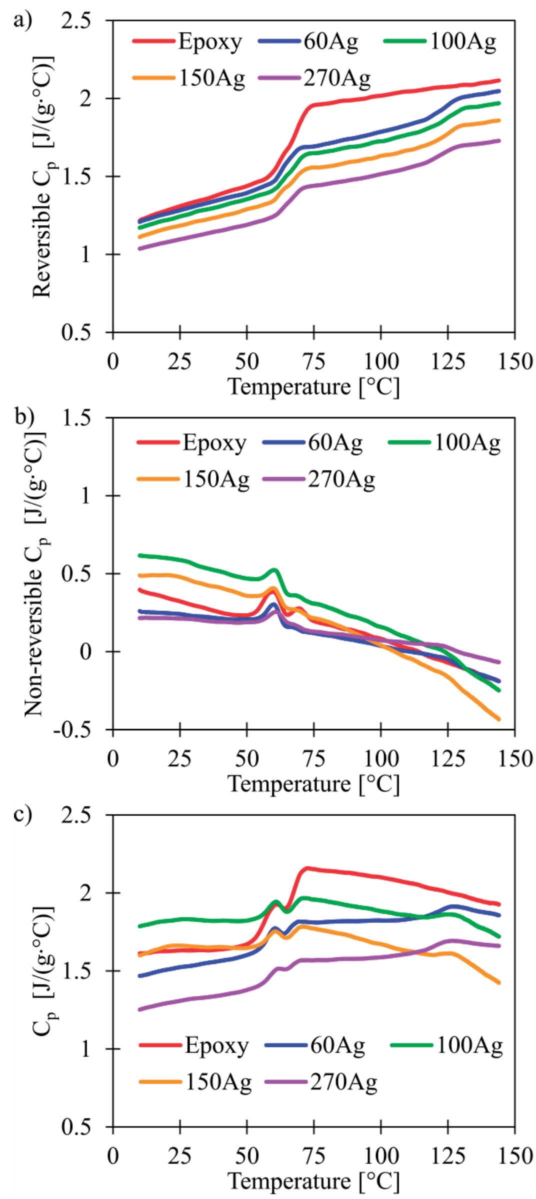

Fig. 4. Reversible (a), non-reversible (b), and total (c) specific heat capacity of the four ICA and epoxy control series.

Table II. Glass transition temperatures (T_g) of the epoxy of the four ICA and epoxy control series, as well as for the PMMA cores in the ICAs.

Series	$T_{g,\ epoxy}$ [°C]	$T_{g,\ PMMA}$ [°C]
Epoxy	66.8	na
60Ag	63.5	122.9
100Ag	66.5	122.9
150Ag	64.4	122.9
270Ag	64.9	121.2
Average	65.2	122.5
Standard deviation	1.4	0.8

These endothermic relaxation peaks are also present in the total C_p signal (Fig. 4 c)). However, as they occur in the range between 50 – 75 °C, they do not affect the values at the relevant temperatures (25, 50, 75, 100, and 125 °C). Still, there is an increase in the total C_p from 50 to 75 °C in all the samples, caused by the glass transition of the epoxy. Total C_p decreases for the epoxy, 100Ag, and 150Ag series after 75 °C, as the non-reversible C_p dominates the reversible C_p for these samples at elevated temperatures. In addition, the non-reversible C_p signals do not show the same dependence on silver content as the reversible signals, a result that is reflected in the total C_p signal from the MDSC measurement. On the other hand, the C_p from LFA correlates much better with the silver content, and the similarity with the reversible C_p signal from the MDSC measurements is conspicuous. As seen in Fig. 5, the LFA method captures the glass transition of the epoxy, although the second transition, presumably that of the PMMA cores, is not visible. LFA also yields somewhat lower C_p values than MDSC.

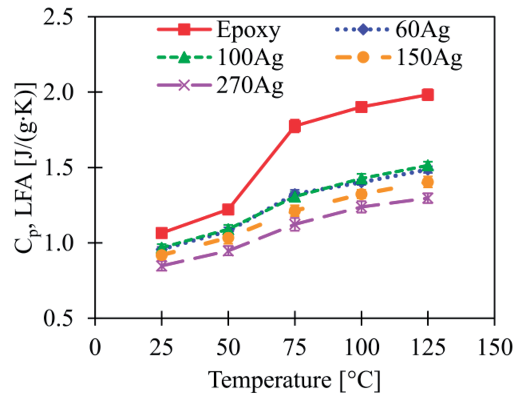

Fig. 5. Specific heat capacity from LFA. Error bars = ± standard deviation.

4.4 Density

Fig. 6 compares the densities of the epoxy and ICA series before and after cure. The estimated density increases after cure, which is expected due to shrinkage of the epoxy matrix caused by cross-linking during the curing process. The estimated density also increases with increasing silver content, which is also natural, as silver (10.5 g/cm^3 at 25 °C [5]) is about nine times more dense than the pre-cure epoxy, based on the data sheet values form the manufacturer. However, the density increases much more for the ICA than the epoxy, suggesting that the nominal densities of the AgPS may be too low. The values at 125 °C are calculated based on linear coefficients of thermal expansion (*CTE*) reported by Gakkestad et al. [7] for an ICA with the same epoxy system and PMMA cores, although slightly lower AgPS content (46 vol%). With these values, thermal expansion only leads to a relative increase of 0.89 % in height and width of the samples from 25 °C to 125 °C. The density dependence on *CTE* is three times larger, but the relative change is thus still only -2.62 %, which is smaller than the standard deviations caused by sample variation at 25 °C, as can be observed in Fig. 6. As there is some uncertainty in the transferability of the *CTE* values from [7] due to a higher AgPS-content in the ICAs in this work, thermal diffusivities and conductivities at elevated temperatures are estimated with the thickness and density values at 25 °C.

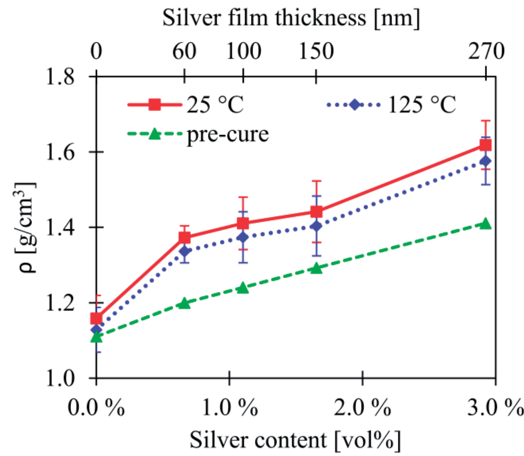

Fig. 6. Densities of the four ICA and epoxy control series as a function of silver content. Error bars = ± standard deviation.

4.5 Thermal conductivity

Thermal conductivity increases with silver content, as evident from Fig. 7 and Fig. 8. MDSC yields higher C_p than LFA, and with the same ρ and α, Eq. (1) thus yields the highest thermal conductivity with C_p from MDSC. $\kappa_{(Cp,\ LFA)}$ increases slightly to a peak at 75 °C, which is caused by the glass transition of the epoxy in the interval between 50 °C and 75 °C. At 100 °C and 125 °C, the further increase in C_p is canceled by the decrease in α. For $\kappa_{(rev.\ Cp,\ MDSC)}$, the behavior is similar to that of $\kappa_{(Cp,\ LFA)}$, but with a slight increase at 125 °C caused by the glass transition of the PMMA cores, not observable in the LFA results. $\kappa_{(tot.\ Cp,\ MDSC)}$ is affected by the more chaotic total C_p values, caused by the non-reversible part of the MDSC signal. This leads to $\kappa_{(tot.\ Cp,\ MDSC)}$ being identical, 1.99 W/(m·K) for both the 150Ag and 270 Ag series at 25 °C. $\kappa_{(tot.\ Cp,\ MDSC)}$ thus increases drastically with silver content, before leveling out before the series with thickest silver films on the AgPS, as observable in Fig. 8. This behavior is different from $\kappa_{(rev.\ Cp,\ MDSC)}$, $\kappa_{(Cp,\ LFA)}$, and $\kappa_{(WF)}$, found from the electrical conductivity through the Wiedemann-Franz law (Eq. (2)). The trends from these methods are very similar, with κ increasing with silver content up to the 270Ag series, although with a lower gradient from the 150Ag and 270Ag series than from the epoxy/60Ag series to the 150Ag series.

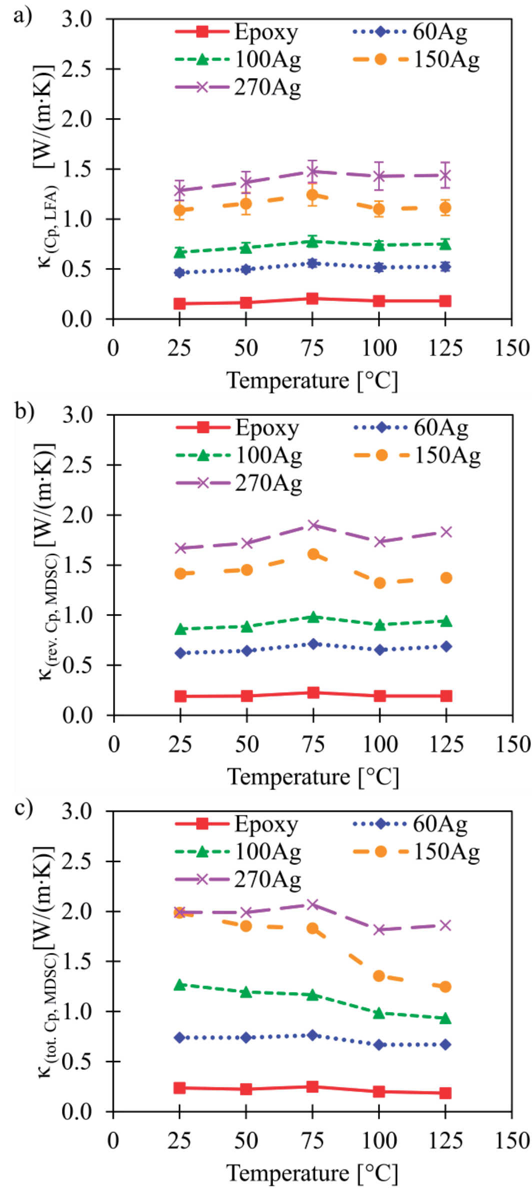

Fig. 7. Thermal conductivities of the four ICA and epoxy control series calculated using Eq. 1, with specific heat capacity (C_p) from LFA (a), reversible C_p from MDSC (b), and total C_p from MDSC (c).

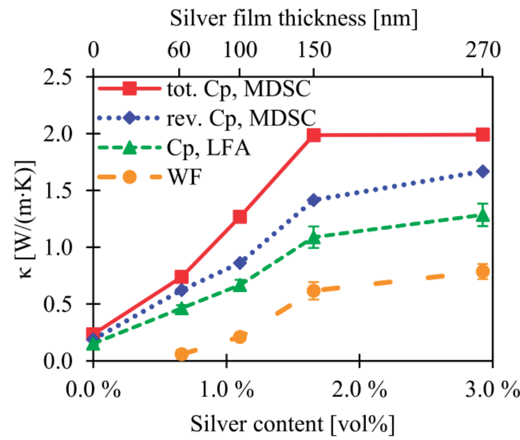

Fig. 8. Thermal conductivities of the four ICA and epoxy control series at 25 °C, calculated using Eq. (1), with total C_p from MDSC, reversible C_p from MDSC, C_p from LFA, or from the electrical conductivity using the Wiedemann-Franz law (Eq. (2)).

5. Discussion

5.1 Percolating silver network

It has previously been shown that the silver films of AgPS form continuous metallic inter-particle contacts after curing of the epoxy [8], and that the contacts become larger and more intimate at higher curing temperatures [9]. This formation of metallic contacts helps explain why AgPS-based ICAs yield lower electrical resistivities relative to their silver content when compared to conventional ICAs [8]. Although electrons in theory can pass across very thin (< 10 nm) non-conductive barriers by quantum tunneling, this current will be negligible compared to a metallic contact of the same size [34]. Therefore, electrons are mostly conducted across such metallic contacts in the AgPS-based ICAs. The corresponding κ_e is dependent on this electron transport. Conversely, in the epoxy matrix and the PMMA cores, heat is conducted by phonons. It is evident that the electrical conductivity (Fig. 2), thermal diffusivity (Fig. 3), and thermal conductivity (Fig. 7 and Fig. 8) are dominated by the network of silver films, as these parameters all increase by several hundred percent upon the addition of only a few percent silver. However, when the electron contribution to the thermal conductivity is calculated from the Wiedemann-Franz law (2), the values are lower than κ from LFA and MDSC, as shown in Fig. 8. There is a upwards shift of 0.40, 0.46, 0.47, and 0.50 W/(m·K) between $\kappa_{(WF)}$ and $\kappa_{(Cp,\ LFA)}$ for the 60Ag, 100Ag, 150Ag, and 270Ag series, respectively. From $\kappa_{(WF)}$ to $\kappa_{(rev.\ Cp,\ MDSC)}$,

the upwards shift is 0.56, 0.65, 0.80, and 0.88 W/(m·K), respectively. According to Eq. (3), these are the phonon contributions to the thermal conductivity. However, these values are all larger than κ of the epoxy, which is 0.15, 0.19, and 0.24 W/(m·K) for $\kappa_{(Cp,\ LFA)}$, $\kappa_{(rev.\ Cp,\ MDSC)}$, and $\kappa_{(tot.\ Cp,\ MDSC)}$, respectively. I.e. the sum of the electron contribution and the contribution from pure epoxy is smaller than $\kappa_{(Cp,\ LFA)}$, $\kappa_{(rev.\ Cp,\ MDSC)}$, and $\kappa_{(tot.\ Cp,\ MDSC)}$ for the ICAs. Although the silver films comprise < 3 vol% of the ICAs, their electrons conduct a large fraction of the heat from the transient heat pulse of the laser flash according to the Wiedemann-Franz law (2). Further, as the electrons of silver are much better conductors of heat than the phonons of epoxy, it is a reasonable assumption that heat is conducted mostly through metallic contacts where these are present, although some heat is possibly still transported across the epoxy in parallel with the metallic contacts. In addition, when adjacent AgPS are not in metallic contact and too far away for electron transport to be significant, heat can still be transported across the epoxy by phonons. α of bulk silver is 161 mm^2/s at 22 °C, while for the ICAs, α ranges from 0.353 – 0.940 mm^2/s at 25 °C, much closer to that of epoxy (0.125 mm^2/s). Although the meandering pathways of the interconnected silver films are longer than the thickness of the samples, it is clear that the bulk of the heat does not diffuse through the material at the same rate as it would in bulk silver. The mechanism and rate of heat transfer from the silver to the intermediate epoxy and back again to silver should be of vital importance to further the understanding of these phenomena, and would be an interesting topic for further investigations.

5.2 Deviations in results between different methods

It is obvious from Fig. 7 and Fig. 8 that both the absolute values and temperature-dependence of κ are highly dependent on the method chosen to obtain C_p. LFA is able to capture the T_g of the epoxy, but not the later T_g of the PMMA cores, and this method also yields the lowest C_p. As given by Eq. (7), reversible C_p is the true heat capacity of the composite, and as can be seen in Fig. 4 a) it is dependent on the relative amounts of the individual components. Silver has lower C_p (0.235 J/(g·°C) at 25 °C [5]) than epoxy, and it is expected that the C_p of the ICA decrease as the silver content increases, as observed in Fig. 4 a). The total C_p is a superposition of the reversible C_p and non-reversible C_p (kinetic processes), and as long as the sum of the kinetic processes are endothermic, the total C_p will be larger than the reversible C_p. As observed in Fig. 4 b), the non-reversible C_p becomes exothermic for the measured samples in the interval between 100 – 125 °C. As a result, the total C_p, and further κ calculated from these values, is approximately equal or lower than the reversible C_p and the corresponding κ at 125 °C, although

these are lower at lower temperatures. The C_p found by regular DSC is, with some exceptions, the same as the total C_p found by MDSC [20], and as shown here, these values will be significantly affected by the thermal history of the samples. Great care and consideration should thus be taken when choosing the method for finding C_p.

An advantage in using MDSC is that the glass transitions of the composite can be identified from the reversible signal. It is obvious from Fig. 4 c) that identifying T_g from the chaotic signals for the total C_p is difficult. LFA yields similar curves as the reversible MDSC signal, but can only give values at discrete temperatures, contrary to the continuous monitoring of the differential scanning method. The thermal conductivity of amorphous polymers increases with increasing temperature until T_g is reached [2], upon which the polymer transitions from a hard and brittle glassy state to a soft and flexible rubbery state. Above the T_g, the thermal conductivity decreases with increasing temperature [2]. However, κ is a function of C_p, and as evident from both Fig. 4 a) and Fig. 5, C_p increases with a smooth step as the temperature exceeds the T_g of the polymer. According to Eq. (1), κ would only decrease above T_g if the increase in C_p is balanced and outweighed by a decrease in α and ρ. In Fig. 7, it is seen that κ generally increases up to 75 °C, and then decreases as the temperature is elevated further. The T_g of the epoxy is estimated to around 65 °C, and from Fig. 4 a) it is clear that the transition is finished at 75 °C. However, as κ is not measured at 65 °C, it is possible that κ peaks at a slightly lower temperature than what is suggested by Fig. 7. As the reversible C_p from MDSC are the only values that increase with an extra step at the glass transition of the PMMA cores, κ only increases at 125 °C when these values are used. In the total C_p from MDSC, the increase in reversible C_p above the T_g of the PMMA cores is outweighed by the decrease in non-reversible C_p. The reason why the second T_g is not observable in the LFA results is possibly an outcome of the transiency of the method. Before each laser flash measurement, the temperature in the measurement chamber is equilibrated at the value of interest, and at 125 °C the PMMA cores should have passed the half-way point of their glass transition. However, the T_g of ~122.5 °C is obtained from MDSC, with much slower perturbations (tens of seconds) than the transient laser flash (milliseconds). It is well known that the glass transition temperature is dependent on the heating rate of the measurement, with increasing heating rates yielding higher values of T_g [35]. Thus, we expect that increasing the chamber temperature above 125 °C would have revealed the glass transition of the PMMA cores also for the LFA measurements.

5.3 Thickness measurements

As seen in this work, uncertainties in the specific heat capacity can cause significant scatter in the thermal conductivity. The largest source of errors in the LFA procedure except for the specific heat capacity is variations in the measured thickness (l) [11]. According to the equation for propagation of errors in expressions with a power law dependence, e.g. $\alpha = l^n$, the relative error $\Delta l/l$ will lead to a relative error $\Delta\alpha/\alpha$ by the relation [36]

$$\frac{\Delta\alpha}{|\alpha|} = |n| \cdot \frac{\Delta l}{|l|} . \quad (10)$$

From the Parker expression (Eq. (4)), we get $\alpha \propto l^2$ [12]. The correction factors from the Cowan model [27, 28] and the Clark and Taylor model [29] are not dependent on l, so thermal diffusivity is still dependent only on the square of the thickness even if these commonly used heat loss corrections are employed. A relative error in the thickness measurements will thus lead to twice the relative error in the thermal diffusivity. In (M)DSC, the input factor is the mass of the samples, and measurement errors in thickness will not affect C_p. For C_p estimated from LFA (Eq. (6)), we have that $C_p \propto (\rho \cdot l)^{-1}$. For a cylindrical or cuboid sample, $\rho \propto l^{-1}$, and C_p is thus independent of l when estimated from LFA. However, as discussed section 2.2, if C_p is measured by LFA, the ρ^{-1} dependence of C_p cancels against the ρ dependence of κ, when κ is estimated by Eq. (1). Thus, regardless of whether C_p is measured by (M)DSC or LFA, the thickness dependence of $\rho \cdot C_p \propto l^{-1}$. When κ is estimated by Eq. (1), there is a thickness dependence of $\kappa = \alpha \cdot \rho \cdot C_p \propto l^2 \cdot l^{-1} \propto l$. A relative error in the thickness measurements will directly lead to an equivalent relative error in the thermal conductivity.

6. Conclusions

By filling a polymer matrix of epoxy adhesive with a high fraction of homogeneous micron-sized PMMA spheres coated with thin silver films, a percolating metallic network that dominated the electric and thermal transport was formed through the polymer with < 3 vol% silver. The thermal transport of these composites was investigated by the commonly used flash diffusivity method, in which thermal diffusivity is estimated directly from the transient surface temperature development on the backside of the sample, caused by absorption of a heat pulse flashed onto the frontside of the sample. The thermal diffusivity increased by several hundred percent upon the addition of the filler particles, but was still closer to that of the epoxy matrix

than that of bulk silver. Thermal conductivity was calculated by multiplying thermal diffusivity with density and specific heat capacity. The specific heat capacity was estimated by comparing the LFA signal with that of a reference sample with known C_p, and from the total and reversible heat flow signals of MDSC. The LFA method provided the simplest measurements, but yielded the lowest C_p and did not capture the glass transition of the polymer cores. The reversible signal from MDSC showed strong correlation with silver content and the glass transitions of both the epoxy and polymer cores were easily distinguished. The total MDSC signal was more dependent on the thermal history of the samples, and provided chaotic signals that did not necessarily correlate with silver content. Users of the flash diffusivity method should therefore be aware that the thermal conductivity is very sensitive to the method chosen to obtain C_p. In addition, the potential impact of errors in thickness measurements were discussed, and it was concluded that thermal conductivity is linearly dependent on the thickness, regardless of the method chosen to find C_p. Finally, the electron contribution to the thermal conductivity at 25 °C was estimated from the electric conductivity by Wiedemann-Franz law, and was found to be smaller than those from the LFA method, although with similar dependence on silver content as the thermal conductivity with C_p from LFA or reversible C_p from MDSC. It was concluded that both electrons and heat are transported mainly by the percolating network of silver films, but with an additional phonon contribution from the epoxy across non-metallic contacts between neighboring filler particles.

Acknowledgments

The Research Council of Norway provided funding through project 225962 – “Novel Conductive Adhesive Technology for Solar Industry” and through project 251068 – “HEFACE”. Partial funding has also been obtained from the European Commision programme FP7- NMP-2013-LARGE-7 under grant agreement n°604668 - “Quantiheat”. S. R. Pettersen appreciates financial support given by Osaka University through the Frontier Mini Program. The authors are grateful to Ignat Tolstorebrov (Department of Energy and Process Engineering, NTNU) for his skillful conductance of the MDSC measurements.

References

1. A.L. Moore and L. Shi, *Emerging challenges and materials for thermal management of electronics,* Materials Today, 2014, **17**(4): p. 163-174.

2. Z. Han and A. Fina, *Thermal conductivity of carbon nanotubes and their polymer nanocomposites: A review,* Progress in Polymer Science, 2011, **36**(7): p. 914-944.

3. M.J. Yim, Y. Li, K.-s. Moon, K.W. Paik, and C.P. Wong, *Review of Recent Advances in Electrically Conductive Adhesive Materials and Technologies in Electronic Packaging,* Journal of Adhesion Science and Technology, 2008, **22**(14): p. 1593-1630.

4. J. E. Morris and J. Liu, *Electrically Conductive Adhesives: A Research Status Review*, in *Micro- and Opto-Electronic Materials and Structures: Physics, Mechanics, Design, Reliability, Packaging*, edited by: E. Suhir, Y.C. Lee, and C.P. Wong, 2007, Springer Science+Business Media LLC, New York. p. 527-570.

5. D.R. Lide, *CRC Handbook of Chemistry and Physics, 84th Edition*. 2003: Taylor & Francis.

6. M. Inoue, H. Muta, T. Maekawa, S. Yamanaka, and K. Suganuma, *Physical Factors Determining Thermal Conductivities of Isotropic Conductive Adhesives,* Journal of Electronic Materials, 2009, **38**(3): p. 430-437.

7. J. Gakkestad, L. Zhuo, T. Helland, and C.P. Wong, *Thermo-mechanical properties of Isotropic Conductive Adhesive filled with Metallized Polymer Spheres,* IEEE 15th Electronics Packaging Technology Conference (EPTC), (Singapore, 2013), doi: 10.1109/EPTC.2013.6745715

8. S.R. Pettersen, H. Kristiansen, S. Nagao, S. Helland, J. Njagi, K. Suganuma, Z. Zhang, and J. He, *Contact Resistance and Metallurgical Connections Between Silver Coated Polymer Particles in Isotropic Conductive Adhesives,* Journal of Electronic Materials, 2016, **45**(7): p. 3734–3743.

9. S.R. Pettersen, H. Kristiansen, K. Redford, S. Helland, E. Kalland, Z. Zhang, and J. He, *Controlling the conduction mechanisms in isotropic conductive adhesives with silver-coated polymer spheres,* 2016 IEEE 66th Electronic Components and Technology Conference (ECTC) (Las Vegas, NV, USA, 2016), doi:

10. S.R. Pettersen, A.E. Stokkeland, H. Kristiansen, J. Njagi, K. Redford, D.V. Goia, Z. Zhang, and J. He, *Electrical four-point probing of spherical metallic thin films coated onto micron sized polymer particles,* Applied Physics Letters, 2016, **109**(4): p. 043103.

11. K.A. Borup, J. De Boor, H. Wang, F. Drymiotis, F. Gascoin, X. Shi, L. Chen, M.I. Fedorov, E. Müller, and B.B. Iversen, *Measuring thermoelectric transport properties of materials,* Energy & Environmental Science, 2015, **8**(2): p. 423-435.

12. W.J. Parker, R.J. Jenkins, C.P. Butler, and G.L. Abbott, *Flash Method of Determining Thermal Diffusivity, Heat Capacity, and Thermal Conductivity,* Journal of Applied Physics, 1961, **32**(9): p. 1679-1684.

13. E. 13, *Standard Test Method for Thermal Diffusivity by the Flash Method*, in *E1461 − 13*,2013, ASTM International: West Conshohocken, PA , United States.

14. W. Nunes dos Santos, P. Mummery, and A. Wallwork, *Thermal diffusivity of polymers by the laser flash technique,* Polymer Testing, 2005, **24**(5): p. 628-634.

15. S. Ganguli, A.K. Roy, and D.P. Anderson, *Improved thermal conductivity for chemically functionalized exfoliated graphite/epoxy composites,* Carbon, 2008, **46**(5): p. 806-817.

16. W. Sun Lee and J. Yu, *Comparative study of thermally conductive fillers in underfill for the electronic components,* Diamond and Related Materials, 2005, **14**(10): p. 1647-1653.

17. S. Yu, J.-W. Lee, T.H. Han, C. Park, Y. Kwon, S.M. Hong, and C.M. Koo, *Copper Shell Networks in Polymer Composites for Efficient Thermal Conduction,* ACS Applied Materials & Interfaces, 2013, **5**(22): p. 11618-11622.

18. K. Zhang, Y. Zhang, and S. Wang, *Effectively decoupling electrical and thermal conductivity of polymer composites,* Carbon, 2013, **65**: p. 105-111.

19. P.S. Gill, S.R. Sauerbrunn, and M. Reading, *Modulated differential scanning calorimetry,* Journal of Thermal Analysis, 1993, **40**(3): p. 931-939.

20. S.L. Simon, *Temperature-modulated differential scanning calorimetry: theory and application,* Thermochimica Acta, 2001, **374**(1): p. 55-71.

21. G.V. Chester and A. Thellung, *The Law of Wiedemann and Franz,* Proceedings of the Physical Society, 1961, **77**(5): p. 1005.

22. N. Stojanovic, D. Maithripala, J. Berg, and M. Holtz, *Thermal conductivity in metallic nanostructures at high temperature: Electrons, phonons, and the Wiedemann-Franz law,* Physical Review B, 2010, **82**(7): p. 075418.

23. J.F. Kerrisk, *Thermal Diffusivity of Heterogeneous Materials,* Journal of Applied Physics, 1971, **42**(1): p. 267-271.

24. J.F. Kerrisk, *Thermal Diffusivity of Heterogeneous Materials. II. Limits of the Steady - State Approximation,* Journal of Applied Physics, 1972, **43**(1): p. 112-117.

25. H.J. Lee and R.E. Taylor, *Thermal diffusivity of dispersed composites,* Journal of Applied Physics, 1976, **47**(1): p. 148-151.

26. T.Y.R. Lee and R.E. Taylor, *Thermal Diffusivity of Dispersed Materials,* Journal of Heat Transfer, 1978, **100**(4): p. 720-724.

27. R.D. Cowan, *Proposed Method of Measuring Thermal Diffusivity at High Temperatures,* Journal of Applied Physics, 1961, **32**(7): p. 1363-1370.

28. R.D. Cowan, *Pulse Method of Measuring Thermal Diffusivity at High Temperatures,* Journal of Applied Physics, 1963, **34**(4): p. 926-927.

29. L.M. Clark III and R.E. Taylor, *Radiation loss in the flash method for thermal diffusivity,* Journal of Applied Physics, 1975, **46**(2): p. 714-719.

30. H. Wang, W.D. Porter, H. Böttner, J. König, L. Chen, S. Bai, T.M. Tritt, A. Mayolet, J. Senawiratne, C. Smith, F. Harris, P. Gilbert, J. Sharp, J. Lo, H. Kleinke, and L. Kiss, *Transport Properties of Bulk Thermoelectrics: An International Round-Robin Study, Part II: Thermal Diffusivity, Specific Heat, and Thermal Conductivity,* Journal of Electronic Materials, 2013, **42**(6): p. 1073-1084.

31. E. 11, *Standard Test Method for Determining Specific Heat Capacity by Differential Scanning Calorimetry*, in *E1269 − 11*,2011, ASTM International: ASTM International, West Conshohocken, PA, USA.

32. E. Verdonck, K. Schaap, and L.C. Thomas, *A discussion of the principles and applications of Modulated Temperature DSC (MTDSC),* International Journal of Pharmaceutics, 1999, **192**(1): p. 3-20.

33. *Standard Test Method for Determining Specific Heat Capacity by Sinusoidal Modulated Temperature Differential Scanning Calorimetry*,2014, ASTM International.

34. R. Holm, *Electric contacts: Theory and Application*. 4th ed. 1967, Berlin/Heidelberg/New York: Springer-Verlag.

35. C.T. Moynihan, A.J. Easteal, J. Wilder, and J. Tucker, *Dependence of the glass transition temperature on heating and cooling rate,* The Journal of Physical Chemistry, 1974, **78**(26): p. 2673-2677.

36. J.R. Taylor, *An introduction to error analysis: The study of uncertainty in physical measurements,* Mill Valley, CA: Anonymous University Science Books, 1982: p. 71ep.

Supplementary Information to

Investigation of thermal transport in polymer composites with percolating networks of silver thin films by the flash diffusivity method

Sigurd R. Pettersen [1, †], Shijo Nagao [2], Helge Kristiansen [1, 3], Susanne Helland [4], John Njagi [5], Katsuaki Suganuma [2], Zhiliang Zhang [1], and Jianying He [1, *].

[1] *NTNU Nanomechanical Lab, Department of Structural Engineering, Norwegian University of Science and Technology (NTNU), NO-7491, Trondheim, Norway.*

[2] *Institute of Scientific and Industrial Research (ISIR), Osaka University, Ibaraki, Osaka 567-0047, Japan.*

[3] *Conpart AS, NO-2013, Skjetten, Norway.*

[4] *Mosaic Solutions AS, NO-2013, Skjetten, Norway.*

[5] *Center for Advanced Materials Processing, Clarkson University, Potsdam, NY 13699-5814, USA.*

[†] Parts of this work were done during an academic stay at [2].

[*] Corresponding author: jianying.he@ntnu.no

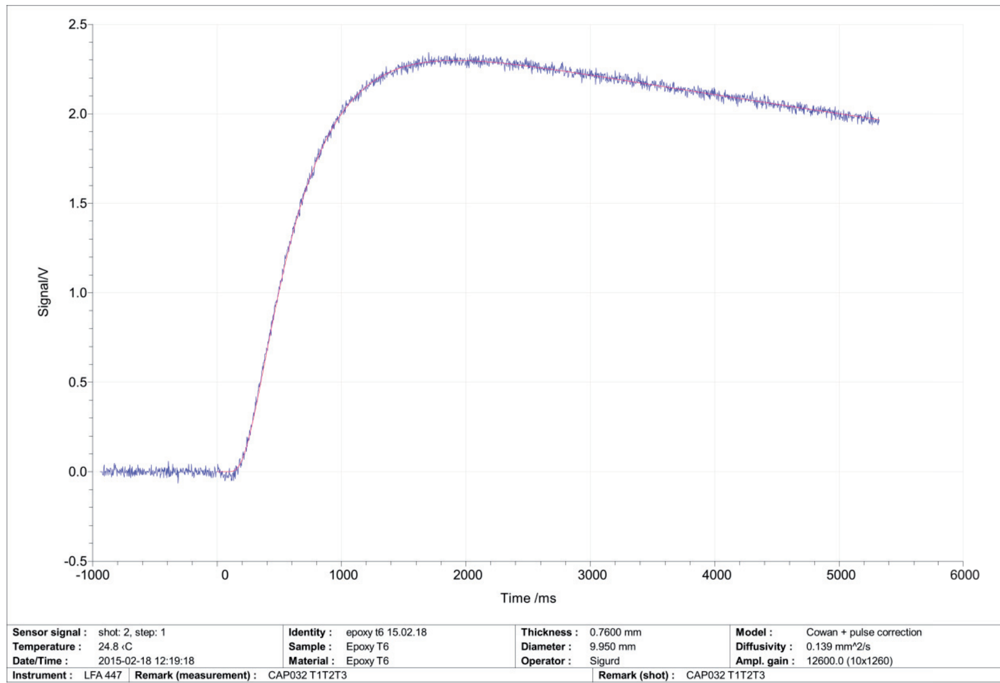

Fig. S1. Representative example of a transient LFA measurement on the pure epoxy samples.

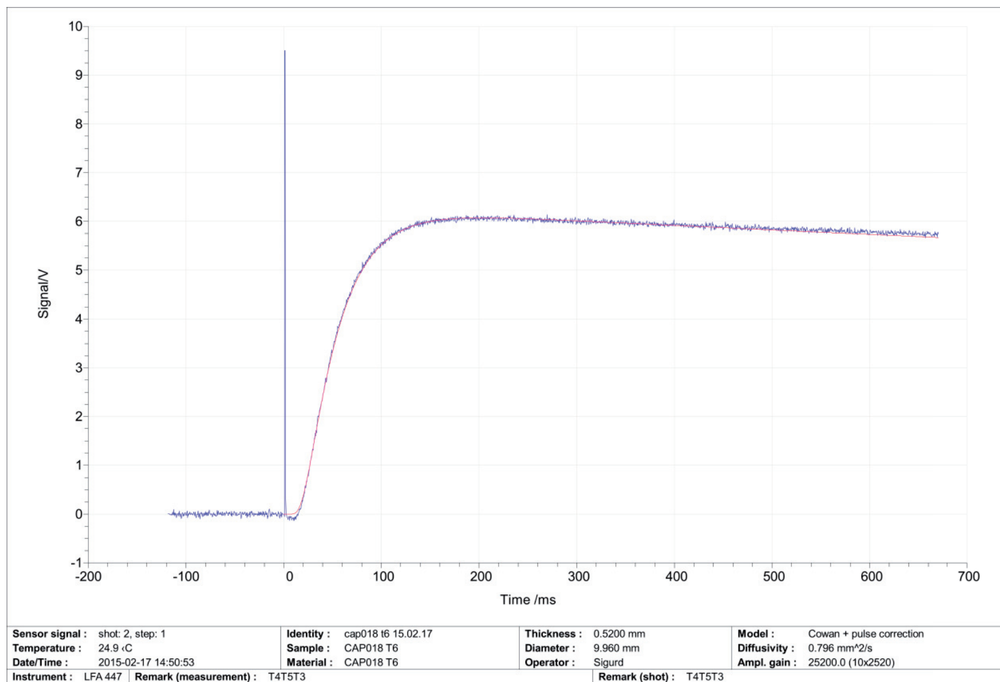

Fig. S2. Representative example of a transient LFA measurement on the 270Ag samples. The whole measurement is finished in a shorter time than it takes the epoxy sample in Fig. S1 to reach its maximum temperature. The peak at 0 ms is caused by reflections of the heat pulse and does not affect the estimated diffusivity.

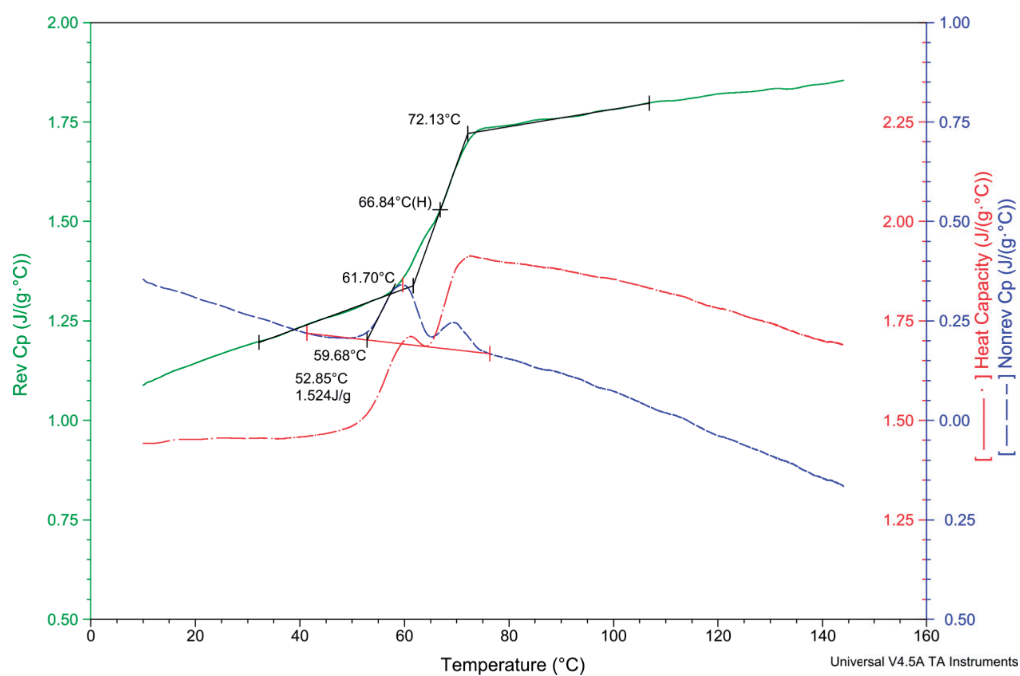

Fig. S3. MDSC signals showing the reversible C_p (green, solid line), total C_p (red, stapled and dotted line), and non-reversible C_p (blue, stapled line), as well as the glass transition of the epoxy (in reversible signal) and endothermic relaxation peaks (in non-reversible signal) of an epoxy sample.

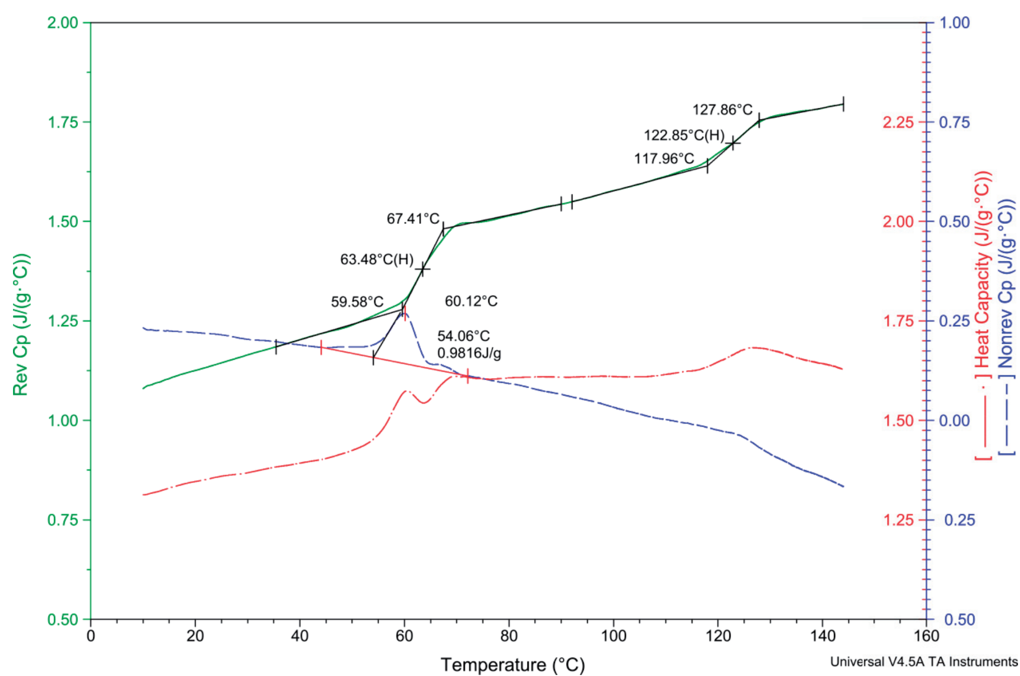

Fig. S4. MDSC signals showing the reversible C_p (green, solid line), total C_p (red, stapled and dotted line), and non-reversible C_p (blue, stapled line), as well as the glass transitions of the epoxy and PMMA cores (in reversible signal) and endothermic relaxation peaks (in non-reversible signal) of a 60Ag sample.

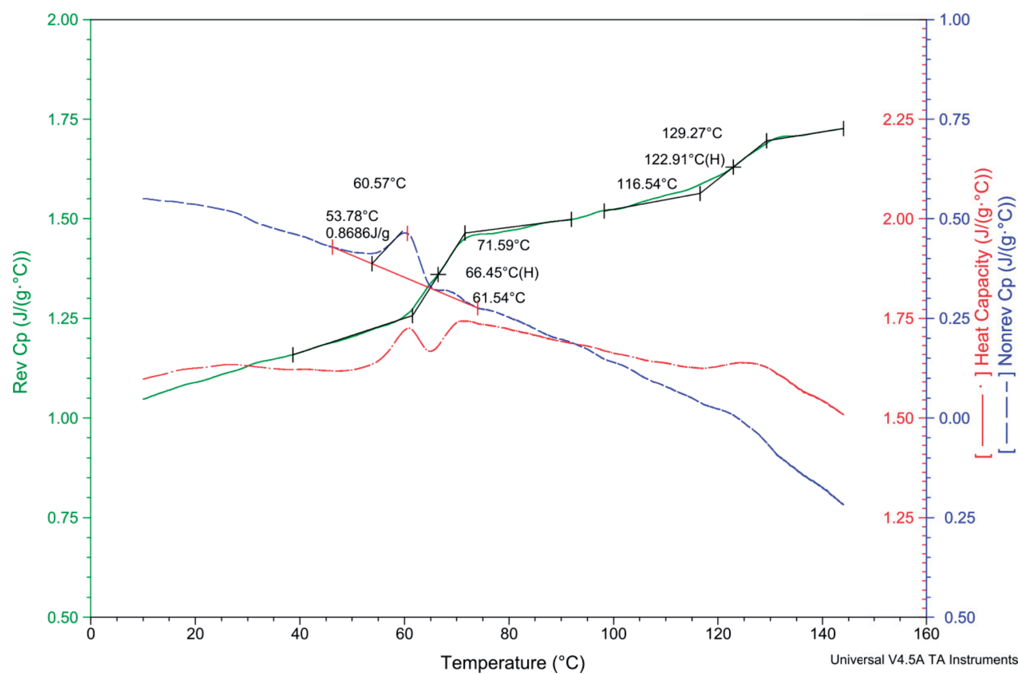

Fig. S5. MDSC signals showing the reversible C_p (green, solid line), total C_p (red, stapled and dotted line), and non-reversible C_p (blue, stapled line), as well as the glass transitions of the epoxy and PMMA cores (in reversible signal) and endothermic relaxation peaks (in non-reversible signal) of a 100Ag sample.

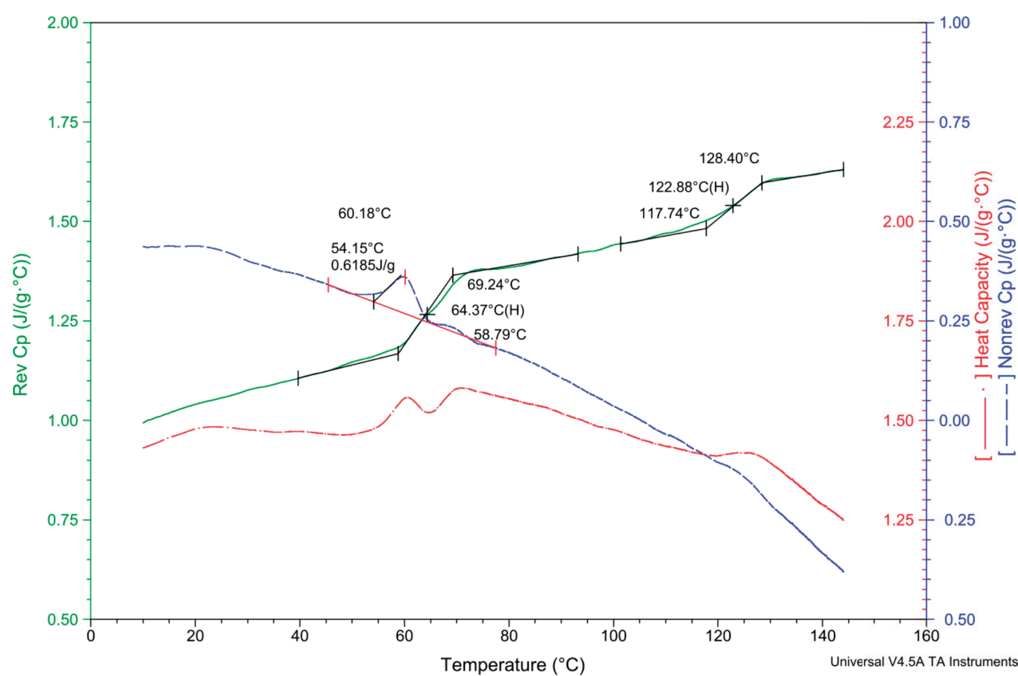

Fig. S6. MDSC signals showing the reversible C_p (green, solid line), total C_p (red, stapled and dotted line), and non-reversible C_p (blue, stapled line), as well as the glass transitions of the epoxy and PMMA cores (in reversible signal) and endothermic relaxation peaks (in non-reversible signal) of a 150Ag sample.

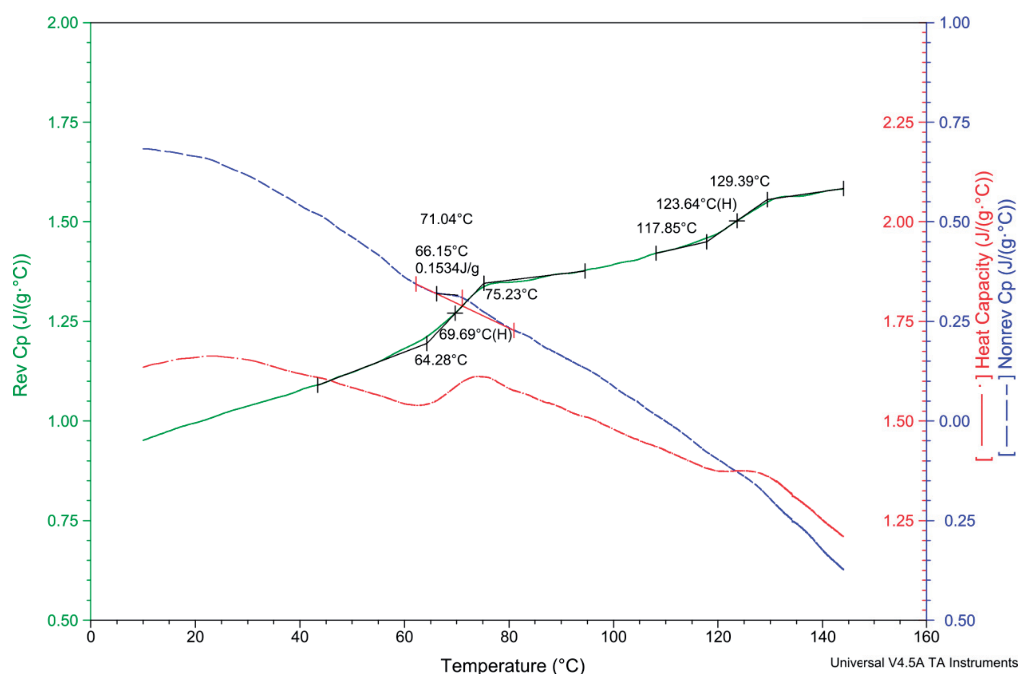

Fig. S7. MDSC signals showing the reversible C_p (green, solid line), total C_p (red, stapled and dotted line), and non-reversible C_p (blue, stapled line), as well as the glass transitions of the epoxy and PMMA cores (in reversible signal) and endothermic relaxation peak (in non-reversible signal) from a second heating cycle on the same 150Ag sample shown in Fig. S6. Notice a slight increase in the Tg of the epoxy, perhaps caused by additional cross-linking of the epoxy during the first heating, as well as the much smaller endothermic relaxation peak.

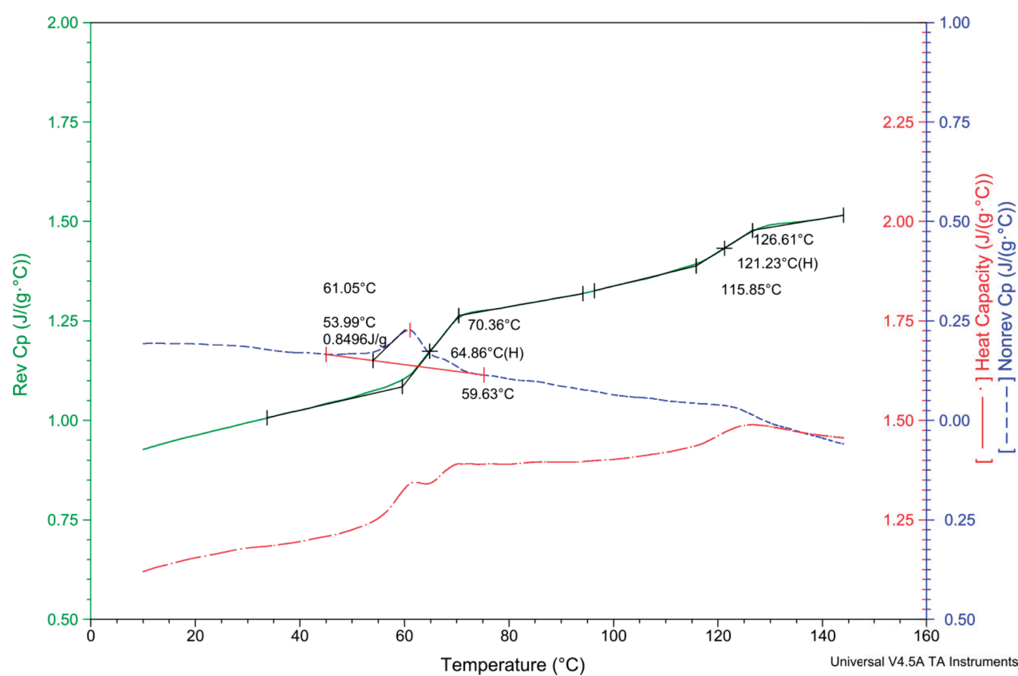

Fig. S8. MDSC signals showing the reversible C_p (green, solid line), total C_p (red, stapled and dotted line), and non-reversible C_p (blue, stapled line), as well as the glass transitions of the epoxy and PMMA cores (in reversible signal) and endothermic relaxation peaks (in non-reversible signal) of a 270Ag sample.

Supplementary material to Investigation of thermal transport in polymer composites with percolating networks of silver thin films by the flash diffusivity method

PhD Publication list

DEPARTMENT OF STRUCTURAL ENGINEERING
NORWEGIAN UNIVERSITY OF SCIENCE AND TECHNOLOGY

N–7491 TRONDHEIM, NORWAY
Telephone: +47 73 59 47 00

"Reliability Analysis of Structural Systems using Nonlinear Finite Element Methods",
C. A. Holm, 1990:23, ISBN 82-7119-178-0.

"Uniform Stratified Flow Interaction with a Submerged Horizontal Cylinder",
Ø. Arntsen, 1990:32, ISBN 82-7119-188-8.

"Large Displacement Analysis of Flexible and Rigid Systems Considering Displacement-Dependent Loads and Nonlinear Constraints",
K. M. Mathisen, 1990:33, ISBN 82-7119-189-6.

"Solid Mechanics and Material Models including Large Deformations",
E. Levold, 1990:56, ISBN 82-7119-214-0, ISSN 0802-3271.

"Inelastic Deformation Capacity of Flexurally-Loaded Aluminium Alloy Structures",
T. Welo, 1990:62, ISBN 82-7119-220-5, ISSN 0802-3271.

"Visualization of Results from Mechanical Engineering Analysis",
K. Aamnes, 1990:63, ISBN 82-7119-221-3, ISSN 0802-3271.

"Object-Oriented Product Modeling for Structural Design",
S. I. Dale, 1991:6, ISBN 82-7119-258-2, ISSN 0802-3271.

"Parallel Techniques for Solving Finite Element Problems on Transputer Networks",
T. H. Hansen, 1991:19, ISBN 82-7119-273-6, ISSN 0802-3271.

"Statistical Description and Estimation of Ocean Drift Ice Environments",
R. Korsnes, 1991:24, ISBN 82-7119-278-7, ISSN 0802-3271.

"Properties of concrete related to fatigue damage: with emphasis on high strength concrete",
G. Petkovic, 1991:35, ISBN 82-7119-290-6, ISSN 0802-3271.

"Turbidity Current Modelling",
B. Brørs, 1991:38, ISBN 82-7119-293-0, ISSN 0802-3271.

"Zero-Slump Concrete: Rheology, Degree of Compaction and Strength. Effects of Fillers as Part Cement-Replacement",
C. Sørensen, 1992:8, ISBN 82-7119-357-0, ISSN 0802-3271.

"Nonlinear Analysis of Reinforced Concrete Structures Exposed to Transient Loading",
K. V. Høiseth, 1992:15, ISBN 82-7119-364-3, ISSN 0802-3271.

"Finite Element Formulations and Solution Algorithms for Buckling and Collapse Analysis of Thin Shells",
R. O. Bjærum, 1992:30, ISBN 82-7119-380-5, ISSN 0802-3271.

"Response Statistics of Nonlinear Dynamic Systems",
J. M. Johnsen, 1992:42, ISBN 82-7119-393-7, ISSN 0802-3271.

"Digital Models in Engineering. A Study on why and how engineers build and operate digital models for decisison support",
J. Høyte, 1992:75, ISBN 82-7119-429-1, ISSN 0802-3271.

"Sparse Solution of Finite Element Equations",
A. C. Damhaug, 1992:76, ISBN 82-7119-430-5, ISSN 0802-3271.

"Some Aspects of Floating Ice Related to Sea Surface Operations in the Barents Sea",
S. Løset, 1992:95, ISBN 82-7119-452-6, ISSN 0802-3271.

"Modelling of Cyclic Plasticity with Application to Steel and Aluminium Structures",
O. S. Hopperstad, 1993:7, ISBN 82-7119-461-5, ISSN 0802-3271.

"The Free Formulation: Linear Theory and Extensions with Applications to Tetrahedral Elements with Rotational Freedoms",
G. Skeie, 1993:17, ISBN 82-7119-472-0, ISSN 0802-3271.

"Høyfast betongs motstand mot piggdekkslitasje. Analyse av resultater fra prøving i Veisliter'n",
T. Tveter, 1993:62, ISBN 82-7119-522-0, ISSN 0802-3271.

"A Nonlinear Finite Element Based on Free Formulation Theory for Analysis of Sandwich Structures",
O. Aamlid, 1993:72, ISBN 82-7119-534-4, ISSN 0802-3271.

"The Effect of Curing Temperature and Silica Fume on Chloride Migration and Pore Structure of High Strength Concrete",
C. J. Hauck, 1993:90, ISBN 82-7119-553-0, ISSN 0802-3271.

"Failure of Concrete under Compressive Strain Gradients",
G. Markeset, 1993:110, ISBN 82-7119-575-1, ISSN 0802-3271.

"An experimental study of internal tidal amphidromes in Vestfjorden",
J. H. Nilsen, 1994:39, ISBN 82-7119-640-5, ISSN 0802-3271.

"Structural analysis of oil wells with emphasis on conductor design",
H. Larsen, 1994:46, ISBN 82-7119-648-0, ISSN 0802-3271.

"Adaptive methods for non-linear finite element analysis of shell structures",
K. M. Okstad, 1994:66, ISBN 82-7119-670-7, ISSN 0802-3271.

"On constitutive modelling in nonlinear analysis of concrete structures",
O. Fyrileiv, 1994:115, ISBN 82-7119-725-8, ISSN 0802-3271.

"Fluctuating wind load and response of a line-like engineering structure with emphasis on motion-induced wind forces",
J. Bogunovic Jakobsen, 1995:62, ISBN 82-7119-809-2, ISSN 0802-3271.

"An experimental study of beam-columns subjected to combined torsion, bending and axial actions",
A. Aalberg, 1995:66, ISBN 82-7119-813-0, ISSN 0802-3271.

"Scaling and cracking in unsealed freeze/thaw testing of Portland cement and silica fume concretes",
S. Jacobsen, 1995:101, ISBN 82-7119-851-3, ISSN 0802-3271.

"Damping of water waves by submerged vegetation. A case study of laminaria hyperborea",
A. M. Dubi, 1995:108, ISBN 82-7119-859-9, ISSN 0802-3271.

"The dynamics of a slope current in the Barents Sea",
Sheng Li, 1995:109, ISBN 82-7119-860-2, ISSN 0802-3271.

"Modellering av delmaterialenes betydning for betongens konsistens",
Ernst Mørtsell, 1996:12, ISBN 82-7119-894-7, ISSN 0802-3271.

"Bending of thin-walled aluminium extrusions",
Birgit Søvik Opheim, 1996:60, ISBN 82-7119-947-1, ISSN 0802-3271.

"Material modelling of aluminium for crashworthiness analysis",
Torodd Berstad, 1996:89, ISBN 82-7119-980-3, ISSN 0802-3271.

"Estimation of structural parameters from response measurements on submerged floating tunnels",
Rolf Magne Larssen, 1996:119, ISBN 82-471-0014-2, ISSN 0802-3271.

“Numerical modelling of plain and reinforced concrete by damage mechanics”,
Mario A. Polanco-Loria, 1997:20, ISBN 82-471-0049-5, ISSN 0802-3271.

“Nonlinear random vibrations - numerical analysis by path integration methods”,
Vibeke Moe, 1997:26, ISBN 82-471-0056-8, ISSN 0802-3271.

“Numerical prediction of vortex-induced vibration by the finite element method”,
Joar Martin Dalheim, 1997:63, ISBN 82-471-0096-7, ISSN 0802-3271.

“Time domain calculations of buffeting response for wind sensitive structures”,
Ketil Aas-Jakobsen, 1997:148, ISBN 82-471-0189-0, ISSN 0802-3271.

"A numerical study of flow about fixed and flexibly mounted circular cylinders",
Trond Stokka Meling, 1998:48, ISBN 82-471-0244-7, ISSN 0802-3271.

“Estimation of chloride penetration into concrete bridges in coastal areas”,
Per Egil Steen, 1998:89, ISBN 82-471-0290-0, ISSN 0802-3271.

“Stress-resultant material models for reinforced concrete plates and shells”,
Jan Arve Øverli, 1998:95, ISBN 82-471-0297-8, ISSN 0802-3271.

“Chloride binding in concrete. Effect of surrounding environment and concrete composition”,
Claus Kenneth Larsen, 1998:101, ISBN 82-471-0337-0, ISSN 0802-3271.

“Rotational capacity of aluminium alloy beams”,
Lars A. Moen, 1999:1, ISBN 82-471-0365-6, ISSN 0802-3271.

“Stretch Bending of Aluminium Extrusions”,
Arild H. Clausen, 1999:29, ISBN 82-471-0396-6, ISSN 0802-3271.

“Aluminium and Steel Beams under Concentrated Loading”,
Tore Tryland, 1999:30, ISBN 82-471-0397-4, ISSN 0802-3271.

"Engineering Models of Elastoplasticity and Fracture for Aluminium Alloys",
Odd-Geir Lademo, 1999:39, ISBN 82-471-0406-7, ISSN 0802-3271.

"Kapasitet og duktilitet av dybelforbindelser i trekonstruksjoner",
Jan Siem, 1999:46, ISBN 82-471-0414-8, ISSN 0802-3271.

“Etablering av distribuert ingeniørarbeid; Teknologiske og organisatoriske erfaringer fra en norsk ingeniørbedrift”,
Lars Line, 1999:52, ISBN 82-471-0420-2, ISSN 0802-3271.

“Estimation of Earthquake-Induced Response”,
Símon Ólafsson, 1999:73, ISBN 82-471-0443-1, ISSN 0802-3271.

“Coastal Concrete Bridges: Moisture State, Chloride Permeability and Aging Effects”
Ragnhild Holen Relling, 1999:74, ISBN 82-471-0445-8, ISSN 0802-3271.

”Capacity Assessment of Titanium Pipes Subjected to Bending and External Pressure”,
Arve Bjørset, 1999:100, ISBN 82-471-0473-3, ISSN 0802-3271.

“Validation of Numerical Collapse Behaviour of Thin-Walled Corrugated Panels”,
Håvar Ilstad, 1999:101, ISBN 82-471-0474-1, ISSN 0802-3271.

“Strength and Ductility of Welded Structures in Aluminium Alloys”,
Miroslaw Matusiak, 1999:113, ISBN 82-471-0487-3, ISSN 0802-3271.

“Thermal Dilation and Autogenous Deformation as Driving Forces to Self-Induced Stresses in High Performance Concrete”,
Øyvind Bjøntegaard, 1999:121, ISBN 82-7984-002-8, ISSN 0802-3271.

“Some Aspects of Ski Base Sliding Friction and Ski Base Structure”,
Dag Anders Moldestad, 1999:137, ISBN 82-7984-019-2, ISSN 0802-3271.

"Electrode reactions and corrosion resistance for steel in mortar and concrete",
Roy Antonsen, 2000:10, ISBN 82-7984-030-3, ISSN 0802-3271.

"Hydro-Physical Conditions in Kelp Forests and the Effect on Wave Damping and Dune Erosion. A case study on Laminaria Hyperborea",
Stig Magnar Løvås, 2000:28, ISBN 82-7984-050-8, ISSN 0802-3271.

"Random Vibration and the Path Integral Method",
Christian Skaug, 2000:39, ISBN 82-7984-061-3, ISSN 0802-3271.

"Buckling and geometrical nonlinear beam-type analyses of timber structures",
Trond Even Eggen, 2000:56, ISBN 82-7984-081-8, ISSN 0802-3271.

”Structural Crashworthiness of Aluminium Foam-Based Components”,
Arve Grønsund Hanssen, 2000:76, ISBN 82-7984-102-4, ISSN 0809-103X.

“Measurements and simulations of the consolidation in first-year sea ice ridges, and some aspects of mechanical behaviour”,
Knut V. Høyland, 2000:94, ISBN 82-7984-121-0, ISSN 0809-103X.

”Kinematics in Regular and Irregular Waves based on a Lagrangian Formulation”,
Svein Helge Gjøsund, 2000-86, ISBN 82-7984-112-1, ISSN 0809-103X.

”Self-Induced Cracking Problems in Hardening Concrete Structures”,
Daniela Bosnjak, 2000-121, ISBN 82-7984-151-2, ISSN 0809-103X.

"Ballistic Penetration and Perforation of Steel Plates",
Tore Børvik, 2000:124, ISBN 82-7984-154-7, ISSN 0809-103X.

"Freeze-Thaw resistance of Concrete. Effect of: Curing Conditions, Moisture Exchange and Materials",
Terje Finnerup Rønning, 2001:14, ISBN 82-7984-165-2, ISSN 0809-103X

"Structural behaviour of post tensioned concrete structures. Flat slab. Slabs on ground",
Steinar Trygstad, 2001:52, ISBN 82-471-5314-9, ISSN 0809-103X.

"Slipforming of Vertical Concrete Structures. Friction between concrete and slipform panel",
Kjell Tore Fosså, 2001:61, ISBN 82-471-5325-4, ISSN 0809-103X.

"Some numerical methods for the simulation of laminar and turbulent incompressible flows",
Jens Holmen, 2002:6, ISBN 82-471-5396-3, ISSN 0809-103X.

“Improved Fatigue Performance of Threaded Drillstring Connections by Cold Rolling”,
Steinar Kristoffersen, 2002:11, ISBN: 82-421-5402-1, ISSN 0809-103X.

"Deformations in Concrete Cantilever Bridges: Observations and Theoretical Modelling",
Peter F. Takâcs, 2002:23, ISBN 82-471-5415-3, ISSN 0809-103X.

"Stiffened aluminium plates subjected to impact loading",
Hilde Giæver Hildrum, 2002:69, ISBN 82-471-5467-6, ISSN 0809-103X.

"Full- and model scale study of wind effects on a medium-rise building in a built up area",
Jónas Thór Snæbjørnsson, 2002:95, ISBN82-471-5495-1, ISSN 0809-103X.

"Evaluation of Concepts for Loading of Hydrocarbons in Ice-infested water",
Arnor Jensen, 2002:114, ISBN 82-417-5506-0, ISSN 0809-103X.

"Numerical and Physical Modelling of Oil Spreading in Broken Ice",
Janne K. Økland Gjøsteen, 2002:130, ISBN 82-471-5523-0, ISSN 0809-103X.

"Diagnosis and protection of corroding steel in concrete",
Franz Pruckner, 20002:140, ISBN 82-471-5555-4, ISSN 0809-103X.

"Tensile and Compressive Creep of Young Concrete: Testing and Modelling",
Dawood Atrushi, 2003:17, ISBN 82-471-5565-6, ISSN 0809-103X.

"Rheology of Particle Suspensions. Fresh Concrete, Mortar and Cement Paste with Various Types of Lignosulfonates",
Jon Elvar Wallevik, 2003:18, ISBN 82-471-5566-4, ISSN 0809-103X.

"Oblique Loading of Aluminium Crash Components",
Aase Reyes, 2003:15, ISBN 82-471-5562-1, ISSN 0809-103X.

"Utilization of Ethiopian Natural Pozzolans",
Surafel Ketema Desta, 2003:26, ISSN 82-471-5574-5, ISSN 0809-103X.

"Behaviour and strength prediction of reinforced concrete structures with discontinuity regions",
Helge Brå, 2004:11, ISBN 82-471-6222-9, ISSN 1503-8181.

"High-strength steel plates subjected to projectile impact. An experimental and numerical study",
Sumita Dey, 2004:38, ISBN 82-471-6282-2 (printed version), ISBN 82-471-6281-4 (electronic version), ISSN 1503-8181.

"Alkali-reactive and inert fillers in concrete. Rheology of fresh mixtures and expansive reactions."
Bård M. Pedersen, 2004:92, ISBN 82-471-6401-9 (printed version), ISBN 82-471-6400-0 (electronic version), ISSN 1503-8181.

"On the Shear Capacity of Steel Girders with Large Web Openings".
Nils Christian Hagen, 2005:9 ISBN 82-471-6878-2 (printed version), ISBN 82-471-6877-4 (electronic version), ISSN 1503-8181.

"Behaviour of aluminium extrusions subjected to axial loading".
Østen Jensen, 2005:7, ISBN 82-471-6873-1 (printed version), ISBN 82-471-6872-3 (electronic version), ISSN 1503-8181.

”Thermal Aspects of corrosion of Steel in Concrete”.
Jan-Magnus Østvik, 2005:5, ISBN 82-471-6869-3 (printed version), ISBN 82-471-6868 (electronic version), ISSN 1503-8181.

”Mechanical and adaptive behaviour of bone in relation to hip replacement.” A study of bone remodelling and bone grafting.
Sébastien Muller, 2005:34, ISBN 82-471-6933-9 (printed version), ISBN 82-471-6932-0 (electronic version), ISSN 1503-8181.

“Analysis of geometrical nonlinearities with applications to timber structures”.
Lars Wollebæk, 2005:74, ISBN 82-471-7050-5 (printed version), ISBN 82-471-7019-1 (electronic version), ISSN 1503-8181.

“Pedestrian induced lateral vibrations of slender footbridges”,
Anders Rönnquist, 2005:102, ISBN 82-471-7082-5 (printed version), ISBN 82-471-7081-7 (electronic version), ISSN 1503-8181.

“Initial Strength Development of Fly Ash and Limestone Blended Cements at Various Temperatures Predicted by Ultrasonic Pulse Velocity”,
Tom Ivar Fredvik, 2005:112, ISBN 82-471-7105-8 (printed version), ISBN 82-471-7103-1 (electronic version), ISSN 1503-8181.

“Behaviour and modelling of thin-walled cast components”,
Cato Dørum, 2005:128, ISBN 82-471-7140-6 (printed version), ISBN 82-471-7139-2 (electronic version), ISSN 1503-8181.

“Behaviour and modelling of selfpiercing riveted connections”,
Raffaele Porcaro, 2005:165, ISBN 82-471-7219-4 (printed version), ISBN 82-471-7218-6 (electronic version), ISSN 1503-8181.

”Behaviour and Modelling og Aluminium Plates subjected to Compressive Load”,
Lars Rønning, 2005:154, ISBN 82-471-7169-1 (printed version), ISBN 82-471-7195-3 (electronic version), ISSN 1503-8181.

”Bumper beam-longitudinal system subjected to offset impact loading”,
Satyanarayana Kokkula, 2005:193, ISBN 82-471-7280-1 (printed version), ISBN 82-471-7279-8 (electronic version), ISSN 1503-8181.

“Control of Chloride Penetration into Concrete Structures at Early Age”,
Guofei Liu, 2006:46, ISBN 82-471-7838-9 (printed version), ISBN 82-471-7837-0 (electronic version), ISSN 1503-8181.

“Modelling of Welded Thin-Walled Aluminium Structures”,
Ting Wang, 2006:78, ISBN 82-471-7907-5 (printed version), ISBN 82-471-7906-7 (electronic version), ISSN 1503-8181.

”Time-variant reliability of dynamic systems by importance sampling and probabilistic analysis of ice loads”,
Anna Ivanova Olsen, 2006:139, ISBN 82-471-8041-3 (printed version), ISBN 82-471-8040-5 (electronic version), ISSN 1503-8181.

“Fatigue life prediction of an aluminium alloy automotive component using finite element analysis of surface topography”.
Sigmund Kyrre Ås, 2006:25, ISBN 82-471-7791-9 (printed version), ISBN 82-471-7791-9 (electronic version), ISSN 1503-8181.

”Constitutive models of elastoplasticity and fracture for aluminium alloys under strain path change”,
Dasharatha Achani, 2006:76, ISBN 82-471-7903-2 (printed version), ISBN 82-471-7902-4 (electronic version), ISSN 1503-8181.

“Simulations of 2D dynamic brittle fracture by the Element-free Galerkin method and linear fracture mechanics”,
Tommy Karlsson, 2006:125, ISBN 82-471-8011-1 (printed version), ISBN 82-471-8010-3 (electronic version), ISSN 1503-8181.

“Penetration and Perforation of Granite Targets by Hard Projectiles”,
Chong Chiang Seah, 2006:188, ISBN 82-471-8150-9 (printed version), ISBN 82-471-8149-5 (electronic version), ISSN 1503-8181.

“Deformations, strain capacity and cracking of concrete in plastic and early hardening phases”,
Tor Arne Hammer, 2007:234, ISBN 978-82-471-5191-4 (printed version), ISBN 978-82-471-5207-2 (electronic version), ISSN 1503-8181.

“Crashworthiness of dual-phase high-strength steel: Material and Component behaviour”,
Venkatapathi Tarigopula, 2007:230, ISBN 82-471-5076-4 (printed version), ISBN 82-471-5093-1 (electronic version), ISSN 1503-8181.

“Fibre reinforcement in load carrying concrete structures”,
Åse Lyslo Døssland, 2008:50, ISBN 978-82-471-6910-0 (printed version), ISBN 978-82-471-6924-7 (electronic version), ISSN 1503-8181.

“Low-velocity penetration of aluminium plates”,
Frode Grytten, 2008:46, ISBN 978-82-471-6826-4 (printed version), ISBN 978-82-471-6843-1 (electronic version), ISSN 1503-8181.

“Robustness studies of structures subjected to large deformations”,
Ørjan Fyllingen, 2008:24, ISBN 978-82-471-6339-9 (printed version), ISBN 978-82-471-6342-9 (electronic version), ISSN 1503-8181.

“Constitutive modelling of morsellised bone”,
Knut Birger Lunde, 2008:92, ISBN 978-82-471-7829-4 (printed version), ISBN 978-82-471-7832-4 (electronic version), ISSN 1503-8181.

“Experimental Investigations of Wind Loading on a Suspension Bridge Girder”,
Bjørn Isaksen, 2008:131, ISBN 978-82-471-8656-5 (printed version), ISBN 978-82-471-8673-2 (electronic version), ISSN 1503-8181.

“Cracking Risk of Concrete Structures in The Hardening Phase”,
Guomin Ji, 2008:198, ISBN 978-82-471-1079-9 (printed version), ISBN 978-82-471-1080-5 (electronic version), ISSN 1503-8181.

“Modelling and numerical analysis of the porcine and human mitral apparatus”,
Victorien Emile Prot, 2008:249, ISBN 978-82-471-1192-5 (printed version), ISBN 978-82-471-1193-2 (electronic version), ISSN 1503-8181.

“Strength analysis of net structures”,
Heidi Moe, 2009:48, ISBN 978-82-471-1468-1 (printed version), ISBN 978-82-471-1469-8 (electronic version), ISSN1503-8181.

“Numerical analysis of ductile fracture in surface cracked shells”,
Espen Berg, 2009:80, ISBN 978-82-471-1537-4 (printed version), ISBN 978-82-471-1538-1 (electronic version), ISSN 1503-8181.

“Subject specific finite element analysis of bone – for evaluation of the healing of a leg lengthening and evaluation of femoral stem design”,
Sune Hansborg Pettersen, 2009:99, ISBN 978-82-471-1579-4 (printed version), ISBN 978-82-471-1580-0 (electronic version), ISSN 1503-8181.

“Evaluation of fracture parameters for notched multi-layered structures”,
Lingyun Shang, 2009:137, ISBN 978-82-471-1662-3 (printed version), ISBN 978-82-471-1663-0 (electronic version), ISSN 1503-8181.

“Modelling of Dynamic Material Behaviour and Fracture of Aluminium Alloys for Structural Applications”
Yan Chen, 2009:69, ISBN 978-82-471-1515-2 (printed version), ISBN 978-82 471-1516-9 (electronic version), ISSN 1503-8181.

“Nanomechanics of polymer and composite particles”
Jianying He 2009:213, ISBN 978-82-471-1828-3 (printed version), ISBN 978-82-471-1829-0 (electronic version), ISSN 1503-8181.

“Mechanical properties of clear wood from Norway spruce”
Kristian Berbom Dahl 2009:250, ISBN 978-82-471-1911-2 (printed version) ISBN 978-82-471-1912-9 (electronic version), ISSN 1503-8181.

“Modeling of the degradation of TiB_2 mechanical properties by residual stresses and liquid Al penetration along grain boundaries”
Micol Pezzotta 2009:254, ISBN 978-82-471-1923-5 (printed version) ISBN 978-82-471-1924-2 (electronic version) ISSN 1503-8181.

"Effect of welding residual stress on fracture"
Xiabo Ren 2010:77, ISBN 978-82-471-2115-3 (printed version) ISBN 978-82-471-2116-0 (electronic version), ISSN 1503-8181.

"Pan-based carbon fiber as anode material in cathodic protection system for concrete structures"
Mahdi Chini 2010:122, ISBN 978-82-471-2210-5 (printed version) ISBN 978-82-471-2213-6 (electronic version), ISSN 1503-8181.

"Structural Behaviour of deteriorated and retrofitted concrete structures"
Irina Vasililjeva Sæther 2010:171, ISBN 978-82-471-2315-7 (printed version) ISBN 978-82-471-2316-4 (electronic version) ISSN 1503-8181.

"Prediction of local snow loads on roofs"
Vivian Meløysund 2010:247, ISBN 978-82-471-2490-1 (printed version) ISBN 978-82-471-2491-8 (electronic version) ISSN 1503-8181.

"Behaviour and modelling of polymers for crash applications"
Virgile Delhaye 2010:251, ISBN 978-82-471-2501-4 (printed version) ISBN 978-82-471-2502-1 (electronic version) ISSN 1503-8181.

"Blended cement with reducted CO_2 emission – Utilizing the Fly Ash-Limestone Synergy",
Klaartje De Weerdt 2011:32, ISBN 978-82-471-2584-7 (printed version) ISBN 978-82-471-2584-4 (electronic version) ISSN 1503-8181.

"Chloride induced reinforcement corrosion in concrete" Concept of critical chloride content – methods and mechanisms.
Ueli Angst 2011:113, ISBN 978-82-471-2769-9 (printed version) ISBN 978-82-471-2763-6 (electronic version) ISSN 1503-8181.

"A thermo-electric-Mechanical study of the carbon anode and contact interface for Energy savings in the production of aluminium".
Dag Herman Andersen 2011:157, ISBN 978-82-471-2859-6 (printed version) ISBN 978-82-471-2860-2 (electronic version) ISSN 1503-8181.

"Structural Capacity of Anchorage Ties in Masonry Veneer Walls Subjected to Earthquake". The implications of Eurocode 8 and Eurocode 6 on a typical Norwegain veneer wall.
Ahmed Mohamed Yousry Hamed 2011:181, ISBN 978-82-471-2911-1 (printed version) ISBN 978-82-471-2912-8 (electronic ver.) ISSN 1503-8181.

"Work-hardening behaviour in age-hardenable Al-Zn-Mg(-Cu) alloys".
Ida Westermann , 2011:247, ISBN 978-82-471-3056-8 (printed ver.) ISBN 978-82-471-3057-5 (electronic ver.) ISSN 1503-8181.

"Behaviour and modelling of selfpiercing riveted connections using aluminium rivets". Nguyen-Hieu Hoang, 2011:266, ISBN 978-82-471-3097-1 (printed ver.) ISBN 978-82-471-3099-5 (electronic ver.) ISSN 1503-8181.

“Fibre reinforced concrete”.
Sindre Sandbakk, 2011:297, ISBN 978-82-471-3167-1 (printed ver.) ISBN 978-82-471-3168-8 (electronic ver) ISSN 1503:8181.

“Dynamic behaviour of cablesupported bridges subjected to strong natural wind”.
Ole Andre Øiseth, 2011:315, ISBN 978-82-471-3209-8 (printed ver.) ISBN 978-82-471-3210-4 (electronic ver.) ISSN 1503-8181.

“Constitutive modeling of solargrade silicon materials”
Julien Cochard, 2011:307, ISBN 978-82-471-3189-3 (printed ver). ISBN 978-82-471-3190-9 (electronic ver.) ISSN 1503-8181.

“Constitutive behavior and fracture of shape memory alloys”
Jim Stian Olsen, 2012:57, ISBN 978-82-471-3382-8 (printed ver.) ISBN 978-82-471-3383-5 (electronic ver.) ISSN 1503-8181.

“Field measurements in mechanical testing using close-range photogrammetry and digital image analysis”
Egil Fagerholt, 2012:95, ISBN 978-82-471-3466-5 (printed ver.) ISBN 978-82-471-3467-2 (electronic ver.) ISSN 1503-8181.

“Towards a better under standing of the ultimate behaviour of lightweight aggregate concrete in compression and bending”,
Håvard Nedrelid, 2012:123, ISBN 978-82-471-3527-3 (printed ver.) ISBN 978-82-471-3528-0 (electronic ver.) ISSN 1503-8181.

“Numerical simulations of blood flow in the left side of the heart”
Sigrid Kaarstad Dahl, 2012:135, ISBN 978-82-471-3553-2 (printed ver.) ISBN 978-82-471-3555-6 (electronic ver.) ISSN 1503-8181.

“Moisture induced stresses in glulam”
Vanessa Angst-Nicollier, 2012:139, ISBN 978-82-471-3562-4 (printed ver.) ISBN 978-82-471-3563-1 (electronic ver.) ISSN 1503-8181.

“Biomechanical aspects of distraction osteogensis”
Valentina La Russa, 2012:250, ISBN 978-82-471-3807-6 (printed ver.) ISBN 978-82-471-3808-3 (electronic ver.) ISSN 1503-8181.

“Ductile fracture in dual-phase steel. Theoretical, experimental and numerical study”
Gaute Gruben, 2012:257, ISBN 978-82-471-3822-9 (printed ver.) ISBN 978-82-471-3823-6 (electronic ver.) ISSN 1503-8181.

“Damping in Timber Structures”
Nathalie Labonnote, 2012:263, ISBN 978-82-471-3836-6 (printed ver.) ISBN 978-82-471-3837-3 (electronic ver.) ISSN 1503-8181.

“Biomechanical modeling of fetal veins: The umbilical vein and ductus venosus bifurcation”
Paul Roger Leinan, 2012:299, ISBN 978-82-471-3915-8 (printed ver.) ISBN 978-82-471-3916-5 (electronic ver.) ISSN 1503-8181.

“Large-Deformation behaviour of thermoplastics at various stress states”
Anne Serine Ognedal, 2012:298, ISBN 978-82-471-3913-4 (printed ver.) ISBN 978-82-471-3914-1 (electronic ver.) ISSN 1503-8181.

“Hardening accelerator for fly ash blended cement”
Kien Dinh Hoang, 2012:366, ISBN 978-82-471-4063-5 (printed ver.) ISBN 978-82-471-4064-2 (electronic ver.) ISSN 1503-8181.

“From molecular structure to mechanical properties”
Jianyang Wu, 2013:186, ISBN 978-82-471-4485-5 (printed ver.) ISBN 978-82-471-4486-2 (electronic ver.) ISSN 1503-8181.

“Experimental and numerical study of hybrid concrete structures”
Linn Grepstad Nes, 2013:259, ISBN 978-82-471-4644-6 (printed ver.) ISBN 978-82-471-4645-3 (electronic ver.) ISSN 1503-8181.

“Mechanics of ultra-thin multi crystalline silicon wafers”
Saber Saffar, 2013:199, ISBN 978-82-471-4511-1 (printed ver.) ISBN 978-82-471-4513-5 (electronic ver). ISSN 1503-8181.

“Through process modelling of welded aluminium structures”
Anizahyati Alisibramulisi, 2013:325, ISBN 978-82-471-4788-7 (printed ver.) ISBN 978-82-471-4789-4 (electronic ver.) ISSN 1503-8181.

“Combined blast and fragment loading on steel plates”
Knut Gaarder Rakvåg, 2013:361, ISBN978-82-471-4872-3 (printed ver.) ISBN 978-82-4873-0 (electronic ver.). ISSN 1503-8181.

“Characterization and modelling of the anisotropic behaviour of high-strength aluminium alloy”
Marion Fourmeau, 2014:37, ISBN 978-82-326-0008-3 (printed ver.) ISBN 978-82-326-0009-0 (electronic ver.) ISSN 1503-8181.

“Behaviour of threated steel fasteners at elevated deformation rates”
Henning Fransplass, 2014:65, ISBN 978-82-326-0054-0 (printed ver.) ISBN 978-82-326-0055-7 (electronic ver.) ISSN 1503-8181.

“Sedimentation and Bleeding”
Ya Peng, 2014:89, ISBN 978-82-326-0102-8 (printed ver.) ISBN 978-82-326-0103-5 (electric ver.) ISSN 1503-8181.

“Impact against X65 offshore pipelines”
Martin Kristoffersen, 2014:362, ISBN 978-82-326-0636-8 (printed ver.) ISBN 978-82-326-0637-5 (electronic ver.) ISSN 1503-8181.

“Formability of aluminium alloy subjected to prestrain by rolling”
Dmitry Vysochinskiy, 2014:363,, ISBN 978-82-326-0638-2 (printed ver.) ISBN 978-82-326-0639-9 (electronic ver.) ISSN 1503-8181.

“Experimental and numerical study of Yielding, Work-Hardening and anisotropy in textured AA6xxx alloys using crystal plasticity models”
Mikhail Khadyko, 2015:28, ISBN 978-82-326-0724-2 (printed ver.) ISBN 978-82-326-0725-9 (electronic ver.) ISSN 1503-8181.

“Behaviour and Modelling of AA6xxx Aluminium Alloys Under a Wide Range of Temperatures and Strain Rates”
Vincent Vilamosa, 2015:63, ISBN 978-82-326-0786-0 (printed ver.) ISBN 978-82-326-0787-7 (electronic ver.) ISSN 1503-8181.

“A Probabilistic Approach in Failure Modelling of Aluminium High Pressure Die-Castings”
Octavian Knoll, 2015:137, ISBN 978-82-326-0930-7 (printed ver.) ISBN 978-82-326-0931-4 (electronic ver.) ISSN 1503-8181.

“Ice Abrasion on Marine Concrete Structures”
Egil Møen, 2015:189, ISBN 978-82-326-1034-1 (printed ver.) ISBN 978-82-326-1035-8 (electronic ver.) ISSN 1503-8181.

“Fibre Orientation in Steel-Fibre-Reinforced Concrete”
Giedrius Zirgulis, 2015:229, ISBN 978-82-326-1114-0 (printed ver.) ISBN 978-82-326-1115-7 (electronic ver.) ISSN 1503-8181.

“Effect of spatial variation and possible interference of localised corrosion on the residual capacity of a reinforced concrete beam”
Mohammad Mahdi Kioumarsi, 2015:282, ISBN 978-82-326-1220-8 (printed ver.) ISBN 978-82-1221-5 (electronic ver.) ISSN 1503-8181.

“The role of concrete resistivity in chloride-induced macro-cell corrosion”
Karla Horbostel, 2015:324, ISBN 978-82-326-1304-5 (printed ver.) ISBN 978-82-326-1305-2 (electonic ver.) ISSN 1503-8181.

“Flowable fibre-reinforced concrete for structural applications”
Elena Vidal Sarmiento, 2015-335, ISBN 978-82-326-1324-3 (printed ver.) ISBN 978-82-326-1325-0 (electronic ver.) ISSN 1503-8181.

“Development of chushed sand for concrete production with microproportioning”
Rolands Cepuritis, 2016:19, ISBN 978-82-326-1382-3 (printed ver.) ISBN 978-82-326-1383-0 (electronic ver.) ISSN 1503-8181.

“Withdrawal properties of threaded rods embedded in glued-laminated timer elements”
Haris Stamatopoulos, 2016:48, ISBN 978-82-326-1436-3 (printed ver.) ISBN 978-82-326-1437-0 (electronic ver.) ISSN 1503-8181.

“An Experimental and numerical study of thermoplastics at large deformation”
Marius Andersen, 2016:191, ISBN 978-82-326-1720-3 (printed ver.) ISBN 978-82-326-1721-0 (electronic ver.) ISSN 1503-8181.

"Modeling and Simulation of Ballistic Impact"
Jens Kristian Holmen, 2016:240, ISBN 978-82-326-1818-7 (printed ver). ISBN 978-82-326-1819-4 (electronic ver.) ISSN 1503-8181.

"Early age crack assessment of concrete structures"
Anja B. Estensen Klausen, 2016:256, ISBN 978-82-326-1850-7 (printed ver). ISBN 978-82-326-1851-4 (electronic ver.) ISSN 1503-8181.

"Uncertainty quantification and sensitivity analysis for cardiovascular models"
Vinzenz Gregor Eck, 2016:234, ISBN 978-82-326-1806-4 (printed ver.) ISBN 978-82-326-1807-1 (electronic ver.) ISSN 1503-8181.

"Dynamic behaviour of existing and new railway catenary systems under Norwegain conditions"
Petter Røe Nåvik, 2016:298, ISBN 978-82-326-1935-1 (printed ver.) ISBN 978-82-326-1934-4 (electronic ver.) ISSN 1503-8181.

"Mechanical behaviour of particle-filled elastomers at various temperatures"
Arne Ilseng, 2016:295, ISBN 978-82-326-1928-3 (printed ver.) ISBN 978-82-326-1929-0 (electronic ver.) ISSN 1503-8181.

"Nanotechnology for anti-icing application: From superhydrophobic surfaces to super-low ice adhesion surfaces"
Zhiwei He, 2016:348, ISBN 978-82-326-2038-8 (printed ver.) ISBN 978-82-326-2039-5 (electronic ver.) ISSN 1503-8181.

"Conduction mechanisms in conductive adhesives with metal-coated polymer spheres"
Sigurd Rolland Pettersen, 2016:349, ISBN 978-82-326-2040-1 (printed ver.) ISBN 978-82-326-2041-8 (electronic ver.) ISSN 1503-8181.